High Repetition-Rate Laser-Driven Particle Generation – Towards High Flux Fast Neutron Sources

Zur Erlangung des Grades eines Doktors der Naturwissenschaften (Dr. rer. nat.)
Genehmigte Dissertation von Franziska Sarah Treffert aus Bad Honnef
Tag der Einreichung: 20. Dezember 2022, Tag der Prüfung: 25. Januar 2023

1. Gutachten: Prof. Dr. Markus Roth
2. Gutachten: Prof. Dr. Siegfried Glenzer
Darmstadt, Technische Universität Darmstadt

TECHNISCHE UNIVERSITÄT DARMSTADT

Physics Department
Institut für Kernphysik
Laser- und Plasmaphysik

High Repetition-Rate Laser-Driven Particle Generation – Towards High Flux Fast Neutron Sources

Accepted doctoral thesis by Franziska Sarah Treffert

Date of submission: 20. Dezember 2022
Date of thesis defense: 25. Januar 2023

Darmstadt, Technische Universität Darmstadt

Erklärungen laut Promotionsordnung

§ 8 Abs. 1 lit. c PromO

Ich versichere hiermit, dass die elektronische Version meiner Dissertation mit der schriftlichen Version übereinstimmt.

§ 8 Abs. 1 lit. d PromO

Ich versichere hiermit, dass zu einem vorherigen Zeitpunkt noch keine Promotion versucht wurde. In diesem Fall sind nähere Angaben über Zeitpunkt, Hochschule, Dissertationsthema und Ergebnis dieses Versuchs mitzuteilen.

§ 9 Abs. 1 PromO

Ich versichere hiermit, dass die vorliegende Dissertation selbstständig und nur unter Verwendung der angegebenen Quellen verfasst wurde.

§ 9 Abs. 2 PromO

Die Arbeit hat bisher noch nicht zu Prüfungszwecken gedient.

Darmstadt, 20. Dezember 2022

F. Treffert

Abstract

High-flux, high repetition-rate pulsed neutron sources are of interest for probing studies such as neutron-induced damage processes in materials employed and considered for shielding purposes in fusion reactors. Simulating the effect an intense neutron flux has on such materials will ultimately guide designs for future fusion reactors. Laser-driven neutron sources employing petawatt laser systems show great potential to fulfill the need for such a neutron source. One of the most common approaches for neutron generation utilizing lasers as drivers is the pitcher–catcher geometry in which a directional ion beam is generated from a pitcher target and impinges on a catcher target producing neutrons through nuclear reactions within the catcher material. Despite the fact that neutron generation using such setups have only recently gained attention, it has so far shown the highest neutron yields using short-pulse lasers. To date, experiments predominantly studied neutron generation on a single shot basis, especially since the development of a high repetition-rate laser-driven neutron source faces a variety of challenges.

In this thesis, the individual components of a successful high repetition-rate laser-driven neutron source were investigated and developed. The focus of this work was especially the development of a stable target system compatible with high repetition-rate laser operations, the development of a design for the catcher target, allowing for optimization of ion beam-catcher overlap, and an efficient ion and neutron beam detection platform.

For this work, a robust version of the SLAC-developed converging liquid microjet target delivery systems was designed and fielded. This system was successfully implemented at two different laser facilities, surviving more than 1000 shots on target with no apparent damage to the nozzle or degradation of the liquid target. The liquid microjet system was implemented to study high repetition-rate deuteron acceleration from heavy water microjet targets at the ALEPH laser facility reaching average fluxes of 1×10^{12} deuterons/sr/min at a repetition rate of 0.5 Hz. Stable deuteron acceleration over 60 shots was observed at varying laser energies on target, suggesting a more favorable scaling of the ion beam cut-off energy than currently established in the literature.

A flexible, repetition-rate compatible neutron generation platform was designed around a stackable catcher target, which can be adjusted based on laser parameters and experimental conditions. This specific design aims at enhancing the generation of high-flux, directional neutron beams. A flexible detector setup simultaneously monitors the ion and neutron beam emission characteristics to study their individual shot-to-shot parameter changes and the correlations between them. Employing cryogenic or ambient-temperature liquid jet targets as a pitcher enables high-repetition-rate operation.

This novel platform was successfully tested using cryogenic liquid deuterium jet targets at the Texas Petawatt laser facility demonstrating efficient generation of forward directed neutron beams with fluxes reaching 7.2×10^{9} neutrons/sr within a narrow divergence angle of $\pm20^{\circ}$. As such, this work lays the foundation for future high-repetition-rate experiments towards pulsed, high-flux, fast neutron sources for radiation-induced effect studies relevant for fusion science and applications that require neutron beams with short pulse duration for the probing of fast evolving processes complementary to X-rays.

Zusammenfassung

Neutronenquellen mit hohen Fluss- und Repetitionsraten sind interessant für Anwendungen im Bereich der Materialwissenschaften, speziell Fusionsforschung, um den Effekt von hohen Neutronenflüssen in fusionsrelevanten Materialien zu simulieren. Petawatt-Lasergetriebene Neutronstrahlen haben die nötigen Eigenschaften und das Potential solche Studien zu ermöglichen. Die sogenannten "Pitcher-Catcher"-Konfiguration erzeugt gerichtete Ionenstrahlen mit Hilfe des Pitcher-Targets, die dann Neutronen durch nukleare Reaktion im Catcher-Targetmaterial produzieren. Obwohl die Neutronenproduktion in dieser speziellen Konfiguration erst seit kurzem genauer untersucht wird, erreicht sie bis heute die höchste gemessenen Neutronenausbeute mit Kurzpulslasern. Studien dazu sind hauptsächlich auf Einzelschussbasis durchgeführt worden und folglich sind mehrere Hürden auf dem Weg zu einer Laserneutronenquelle mit hoher Repetitionsrate zu überkommen.

Thema dieser Arbeit ist die Entwicklung der einzelnen Komponenten einer funktionstüchtigen Laserneutronenquelle mit hoher Repetitionsrate, mit Fokus auf der Entwicklung eines stabilen, kompatiblen Targetsystems, eines Catcher-Targets, welches die Optimierung der Neutronenproduktion erlaubt, und einer effizienten Detektorplatform für Ionen und Neutronen.

Im Rahmen dieser Arbeit wurde ein robustes Targetsystem, basierend auf einem SLAC-entwickelten System, für konvergierende, flüssige Jets entwickelt. Dieses System wurde erfolgreich in zwei unterschiedlichen Hochleistungslasereinrichtungen getestet, ohne Anzeichen von Schäden am Targetsystem oder Degradierung der Qualität des Targets. Das Jet-Targetsystem wurde am ALEPH Laser zur Beschleunigung von Deuteronen aus schwerem Wasser mit einer Repetitionsrate von 0.5 Hz und einer mittleren Flussdichte von 1×10^{12} Deuterons/sr/min verwendet. Gemessenen Spektren erreichten vergleichbare Enegien und Flüssen über 60 konsekutive Schüsse für drei unterschiedliche Laserenergien. Eine Skalierungsmessung mit den durchschnittlichen Deuteronenspektren für die unterschiedlichen Laserenergien zeigt eine abweichende, möglicherweise günstigere Skalierung der maximalen Deuteronenenergie als bereits etablierte Skalierungen.

Ein anpassbarer Catcher für Neutronengeneration ist der zentrale Baustein einer flexiblen Neutronengenerationsplatform für hohe Repetitionsraten. Das Catcherdesign kann basierend auf Lasereigenschaften und experimentspezifische Konstellationen angepasst und geändert werden und ist optimiert für die Generation von gerichteten Neutronenstrahlen mit hohen Flussraten. Der flexible Detektorenaufbau vereinfacht die gleichzeitige, durchgängige Messung von Ionen- und Neutronenstrahlen und die Identifizierung von Korrelationen zwischen Ionen- und Neutronenstrahlemissionscharakteristiken. Hohe Repetitionsraten werden durch die Verwendung von kryogenen und flüssigen Jettargets als Pitcher-Target ermöglicht.

Die entwickelte Neutronenproduktionsplatform wurde erfoglreich mit kryogenen Deuteriumjetargets am Texas Petawatt Lasersystem getestet. Effiziente Neutronenproduktion mit einer gerichteten Komponente und maximalem Fluss von 7.2×10^{9} Neutronen/sr und niedrigem Öffnungswinkel von $\pm20^{\circ}$ wurden gemessen. Damit legt diese Arbeit den Grundstein für Experimente mit hohen Repetitionsraten auf dem Weg zur Realisierung einer gepulsten schnellen Neutronenquelle mit hoher Flussdichte und kurzer Pulsdauer. Diese Quelle wird Studien im Bereich der Fusionsforschung ermöglichen und zusätzlich als Diagnostik komplementär zu Röntgenstrahlen einsetzbar sein um kurzlebige Prozesse zu messen.

Contents

Abbreviations

ALEPH	Advanced Laser for Extreme PHotonics (Fort Collins, USA)	p. 19
ASE	Amplified Spontaneous Emission	p. 6
CAD	Computer Aided Design	p. 27
CCD	Charge Coupled Device	p. 26
CPA	Chirped-Pulse Amplification	p. 6
CSU	Colorado State University (Fort Collins, USA)	p. 31
ELI	Extreme Light Infrastructure (Dolní Břežany, Czech Republic)	p. 105
ESS	European Spallation Source (Lund, Sweden)	p. 51
FOV	Field Of View	p. 25
FWHM	Full Width at Half Maximum	p. 46
He-Ne	Helium-Neon	p. 6
HPLC	High Performance Liquid Chromatography	p. 23
ICF	Inertial Confinement Fusion	p. 2
IP	Image Plate	p. 34
LANSCE	Los Alamos Neutron Science CEnter (Los Alamos, USA)	p. 51
Laser	Light Amplification by Stimulated Emission of Radiation	p. 1
LCLS	Linear Coherent Light Source (Menlo Park, USA)	p. 21
LLE	Laboratory for Laser Energetics (Rochester, USA)	p. 52
LLNL	Lawrence Livermore National Laboratory (Livermore, USA)	p. 52
LTE	Local Thermal Equilibrium	p. 9
Maser	Microwave Amplification by Stimulated Emission of Radiation	p. 1
MCP	MicroChannel Plate	p. 34
MEC-U	Matter in Extreme Conditions Upgrade	p. 105
Nd:glass	Neodymium doped Glass	p. 6
NIF	National Ignition Facility (Livermore, USA)	p. 52
nTOF	Neutron Time-Of-Flight	p. 70
OD	Optical Density	p. 83

PIC	Particle In Cell	p. 18
PMT	Photomultiplier tube	p. 72
PSL	Photo-Stimulated Luminescence	p. 37
PW	PetaWatt	p. 7
QL	Quantum Level	p. 83
RAL	Rutherford Appleton Laboratory (Didcot, UK)	p. 105
RCF	Radiochromic Film	p. 66
ROI	Region Of Interest	p. 25
SLAC	SLAC National Accelerator Laboratory (Menlo Park, USA)	p. 21
SSRL	Stanford Synchrotron Radiation Lightsource (Menlo Park, USA)	p. 21
TCC	Target Chamber Center	p. 28
Ti:Sa	Titanium doped Sapphire	p. 6
TNSA	Target Normal Sheath Acceleration	p. 5
TP	Thomson Parabola	p. 31
TPW	Texas PetaWatt (Austin, USA)	p. 19

Symbols

A_{spot}	focal spot size	m^2
a_0	laser field amplitude	-
B_0	magnetic field amplitude	T
$\vec{B}$	magnetic field	T
γ	relativistic Lorentz factor	-
c_s	sound speed	$\mathrm{m\,s^{-1}}$
$c_{s,ion}$	ion speed in the target	$\mathrm{m\,s^{-1}}$
d	target thickness	m
E_0	electric field amplitude	$\mathrm{V\,m^{-1}}$
$\vec{E}$	electric field	$\mathrm{V\,m^{-1}}$
$\mathcal{E}_{\mathrm{ion}}$	binding energy	J or eV
$E_{\mathrm{p,max}}$	maximum proton (cut-off) energy	J or eV
E_{L}	laser pulse energy	J
$e_{\mathrm{x}}, e_{\mathrm{y}}, e_{\mathrm{z}}$	cartesian unit vectors	m
f	laser to electron conversion efficiency	-
$\vec{F}_{\mathrm{L}}$	Lorentz force	$\mathrm{kg\,m\,s^{-2}}$
f_{p}	ponderomotive force	$\mathrm{kg\,m\,s^{-2}}$
I_{L}	laser pulse intensity	$\mathrm{W\,cm^{-2}}$
k	laser wave vector	$\mathrm{m^{-1}}$
L	plasma scale length	m
λ_{L}	laser wavelength	m
λ_{D}	Debye length	m
l_{s}	skin depth	m
m_i	ion mass	kg
n	refractive index	-
n_{c}	critical density	$\mathrm{m^{-3}}$
N_{D}	Number of particles in Debye sphere	-
n_{e}	electron number density	$\mathrm{m^{-3}}$

$n_{\mathrm{e},0}$	electron number density of the unperturbed plasma	m^{-3}
ω_{L}	laser frequency	s^{-1}
ω_{p}	plasma frequency	s^{-1}
$\vec{p}$	momentum vector	$\mathrm{kg\,m\,s}^{-1}$
$\vec{r}$	position vector	m
r_{L}	focal spot radius	m
S_{sheath}	TNSA sheath area	m^2
t	time	s
τ_{L}	laser pulse length	s
t_{acc}	TNSA acceleration time	s
T_{e}	electron temperature	K or eV
$\vec{v}_{\mathrm{e}}$	electron velocity	$\mathrm{m\,s}^{-1}$
v_{D}	electron drift velocity	$\mathrm{m\,s}^{-1}$
v_{os}	electron quiver velocity	$\mathrm{m\,s}^{-1}$
x, y, z	cartesian coordinates	m
Z	ion charge number	-
z_{R}	Rayleigh length	m

Constants

a_B	Bohr radius	$5.292 \times 10^{-11}\,\mathrm{m}$
e_N	Euler number	$2.718\,28$
c	speed of light	$2.998 \times 10^{8}\,\mathrm{m\,s^{-1}}$
e	electron charge	$1.602 \times 10^{-19}\,\mathrm{C}$
ϵ_0	vacuum permittivity	$8.854 \times 10^{-12}\,\mathrm{A\,s\,V^{-1}\,m^{-1}}$
E_a	atomic binding strength	$1.602 \times 10^{-19}\,\mathrm{C}$
I_a	atomic intensity	$5.1 \times 10^{9}\,\mathrm{V\,m^{-1}}$
k_B	Boltzmann constant	$1.381 \times 10^{-23}\,\mathrm{m^2\,kg\,m^{-2}\,K^{-1}}$
m_e	electron mass	$9.109 \times 10^{-31}\,\mathrm{kg}$

1. Introduction

Breakthrough discoveries are usually motivated by enhancing existing technology enabling applications that are better, faster and easier to field or, in science, to study small-scale phenomena of the world and universe we live in with unprecedented precision. These often times trigger the development of new technology branches and the discovery of so far unexplored scientific fields. One example is the Microwave Amplification by Stimulated Emission of Radiation (Maser) invented in 1954 and a few years later the Light Amplification by Stimulated Emission of Radiation (Laser) in 1960 [1, 2]. To better serve the field of physics for the study of short-lived micro- and macro-scale phenomena, lasers were further developed to obtain short pulses carrying large amounts of energy. The invention of chirped pulse amplification by Strickland and Mourou in 1985 [3], which received the Nobel prize in 2018, was another breakthrough on the way to achieve petawatt (10^{15} Watts) laser systems. These lasers find application in medicine, as a tool used in surgeries, and in machining, on the macro- and the micro-scale. At the physics frontier, a heavily studied field to date is the interaction of such high-energy, short-pulse lasers with matter, which combines concepts of laser, plasma, nuclear and condensed matter physics.

Early experiments studying the interaction of a high-power short-pulse laser with matter discovered the generation of secondary particles such as electrons, ions and X-rays [4–6]. Particularly the generation of directional, high-flux ion beams using high-power short-pulse lasers has received significant interest from a variety of fields and their unique ion beam parameters have lead to developments for applications in medicine, specifically tumor therapy [7–12], plasma diagnostics [13–15], inertial confinement fusion [7, 16], hybrid accelerator designs [17, 18], and laser-driven secondary neutron sources [19–22]. Until now, research towards such applications was limited to low repetition rates predominantly due to cooling limitations of the laser system and the lack of compatible target systems. Recent advances in laser technology, leading to the commissioning and successful operation of multiple high-repetition-rate petawatt lasers, promise to overcome past restrictions [23]. Combined with progress in delivery of continuous targets [24–26], repetition rates of laser-driven ion sources beyond 1 Hz or greater have become achievable. When employing high repetition-rate, high-power short-pulse lasers, such ion beam sources can reach high peak and high average ion fluxes at pulse duration of nanoseconds, which are uniquely suited to generate high-flux, short bursts of neutrons.

Due to their interaction with atoms through the strong force rather than the electromagnetic force, neutron beams are a versatile, sensitive probe of the atomic structure of a material. Directional, high-flux neutron beams are of wide interest for applications including fusion energy science [19, 21], fundamental physics research [27], materials science [20, 28], homeland security [29], and medicine [30]. Especially the field of high energy-density physics can greatly benefit from neutron beams with short pulse duration and a high flux. Due to the short-lived nature and presence of strong magnetic and electric fields, neutron probing offers a new way to measure material structure or ion temperature and velocity non-destructively in dense plasmas [27, 31]. Neutron sources also find application in the study of radiation-induced effects in fusion science such as damage cascades or neutron-induced transmutations relevant for fusion reactor materials and astrophysical scenarios (e.g., to study the s- and r-processes) [32]. These studies are important to advance designs and construction of internationally-supported fusion pilot plants such as the ITER and DEMO projects [33–36].

Over the past decades different approaches have investigated the development of a neutron source suitable for aforementioned applications. Conventional neutron sources including nuclear reactors or spallation sources are established neutron generation approaches, while neutron generation utilizing lasers has only recently regained attention. High-flux neutron beams required for applications are routinely produced by nuclear reactors or spallation sources. They rely either on the generation of neutrons through nuclear fission or spallation reactions induced by a $\sim$ GeV proton beam impinging on a high-Z target. While reactors and spallation sources are able to achieve high average neutron fluxes of up to 10^{15} neutrons/(cm^2 s), their applications are limited by inflexible probing setups, relatively long pulse duration (hundreds of ns or greater) [37, 38], and their large footprint and operational cost. These limitations have motivated the development of alternative drivers for high repetition-rate, high flux ion and neutron sources.

Recently, high-power laser systems have demonstrated their utility as drivers of high-flux neutron sources through Inertial Confinement Fusion (ICF) and the pitcher–catcher approach. In the ICF scheme, neutrons are produced by heating a target to temperatures exceeding tens of keV while simultaneously compressing it to pressures in the hundreds of Gbar [39, 40]. This way, peak fluxes up to 10^{27} neutrons/(cm^2 s) can be achieved through indirect drive of a fusion capsule implosion [41–44]. However, these systems are limited to low shot rates, resulting in a comparably low average neutron flux. The pitcher–catcher approach commonly utilizes high-power short-pulse laser systems, which have the potential to reach much higher repetition rates than their long pulse laser counter parts.In this scheme, two targets, the pitcher for ion acceleration and the catcher for neutron generation, are implemented in the target chamber. Neutrons are created through nuclear reactions between the energetic ions and catcher atoms [27, 45, 46]. The inherently short duration of such laser-driven neutron beams, on the order of a nanosecond, gives them the potential to become unique probes of fast-evolving processes, which requires high flux, directional neutron beams. Until this work, peak fluxes of up to 10^{19} neutrons/(cm^2 s) have been demonstrated, but shot rates were still limited to repetition-rates of $\sim$1 shot/hour by the laser capabilities and the target replenishing times, resulting in a low average neutron flux [47].

The advent of high repetition-rate short-pulse laser systems has opened up the path towards particle sources that could exceed the repetition rates of conventional accelerators. This thesis takes the first steps towards the development of high-flux laser-driven neutron sources and investigates the physics of high repetition-rate laser-target interactions in the pitcher–catcher approach. The key components of such a laser-driven neutron source are the high repetition-rate short-pulse laser, the fast-replenishing target, high-flux directional deuteron beams, an optimized neutron converter design, and an efficient detection platform to measure the generated ion and neutron beam spectra. This work focuses on the demonstration of stable, high repetition-rate ion acceleration based on advanced target concepts and the generation of high-flux directional neutron beams. Key to this is the stability and control of the pitcher target, which was investigated for two different types of self-replenishing jets. Furthermore, an ion and neutron detector setup was developed to distinguish between the directional neutron beam generated within the converter from neutrons produced elsewhere.

Chapter 2 presents the state of the art of short-pulse lasers and describes important fundamental physical concepts of short-pulse laser matter interactions. These are initially introduced by considering a single free charged electron and then expanded to the concept of laser interaction with the bulk target. Laser-target interaction ultimately results in the phenomenon of laser-driven ion acceleration which is explained based on the established Target Normal Sheath Acceleration mechanism. The targets utilized in this work, an ambient-temperature liquid microjet target and a cryogenic liquid jet target, are discussed in Chapter 3. It also includes the development and design of the new ambient-temperature liquid jet system. Additionally, the essential monitoring diagnostics are described for the individual jet targets. The ambient-temperature liquid jet target was fielded using heavy water at the ALEPH laser facility at Colorado State University for the purpose of studying the acceleration of deuterium ions at high repetition-rate. Chapter 4 describes the

experimental setup and the experimental results obtained at a repetition rate of 0.5 Hz. The results feature the first demonstration of deuteron acceleration reaching a peak flux of up to 2×10^{11} deuterons/MeV/sr and an average flux of 3×10^{11} deuterons/MeV/sr/min.

In a next step, the possible ways of neutron generation are explored. Chapter 5 gives an overview of conventional and laser-based neutron sources. Based on experimental and theoretical data, an adjustable converter concept is designed. Possible options of implementation at high-power laser facilities are discussed at the end of the chapter. To be able to diagnose the ion and neutron beams and draw conclusions about correlations of ion and neutron beam parameters, a characterization platform consisting of ion and neutron detectors is presented in Chapter 6. Different detectors and their operational principles are explained as well as shielding consideration for measurements with optimized signal to noise ratios. The optimized converter and characterization platform was subsequently implemented at the Texas Petawatt laser facility at the University of Texas at Austin. Results of this experiment are presented in Chapter 7. Data from various shots are presented and the respective ion and neutron beam data are analyzed in terms of the ion beam-converter overlap, the resulting neutron beam properties and the primary neutron generation location within the experimental setup (i.e. the catcher target versus the target chamber wall). Chapter 7 outlines future experiments and next steps in terms of outstanding analysis and comparison with modeling. Chapter 8 concludes this thesis, summarizing the results and gives an outlook on the future applications of high repetition-rate particle beams and the implementation of machine learning algorithms to further optimize laser-driven neutron sources.

2. Short-Pulse Laser Matter Interaction

Soon after the successful demonstration of the first laser by Theodore Maiman in 1960 [2], the interaction of such lasers, focused to high intensity, with matter was investigated [48, 49]. These studies observed the generation of a plasma upon irradiation of a material accompanied by the emission of energetic particles. Since then the field of laser-matter interaction has grown exponentially thanks to advances in laser technology which has lead to a rapid increase in laser intensities on target. One of the key invention, allowing laser pulses to contain more energy and reach high intensities on target, the Chirped Pulse Amplification technique [3], was awarded the Nobel prize in physics in 2018. Nowadays lasers with a large variety of parameters such as pulse duration, energy delivered to the target and intensity on target are available, giving access to explore the large parameter space of laser-matter interactions. Short-pulse laser are a subcategory of lasers and their interaction with matter and subsequent acceleration of energetic ions is an extensive field of study [5, 6, 50], and subject of this thesis.

When a short-pulse laser interacts with a target, the target material, independent of its state (solid, liquid, gas), will be rapidly ionized and a plasma will be generated. The free electrons and ions of the plasma are directly subjected to the laser field. Through this interaction of the laser field with free charged particles they can be efficiently accelerated to high energies through different mechanisms depending on laser intensity and wavelength and the target parameters. This chapter will focus on the interaction of high-intensity short-pulse laser systems with matter. Starting with the generation of a plasma by the incident laser pulse, a subsequent discussing will address the interaction and propagation of the laser pulse with the formed plasma. Important parameters will be explained including the plasma frequency, the ponderomotive force and the principle of relativistic transparency.

During the interaction of a laser with the preformed plasma, laser-driven effects within the target can ultimately lead to acceleration of ions. The phenomenon of laser-driven ion acceleration will be introduced based on the well-studied Target Normal Sheath Acceleration (TNSA) mechanism. Advanced target concepts such as structured targets, solid foams or gas, liquid and cryogenic jet targets have enabled the exploration of the wide parameter space of laser-driven ion acceleration regimes. Since the discovery of TNSA many new single mechanism or hybrid regimes have been studied theoretically and experimentally. A brief overview of alternative acceleration regimes will be provided at the end of this chapter.

2.1. High-Intensity Short-Pulse Laser Systems

Central to understanding the interaction of a high-power short-pulse laser is the fundamental knowledge of basic operational principles of short-pulse laser systems. This includes the formation of the high-power laser beam starting with an initial low energy pulse and the resulting characteristics of high-power short laser pulses. The operation of high repetition-rate capable short pulse lasers will be briefly explained, as this is of importance to this work.

Lasers operate on the principle of amplifying stimulated or spontaneous emission of light by a gain medium. Placing a mirror at either end of the gain medium creates a cavity which allows light to travel back and forth and gain energy on every round trip. Depending on the length of the cavity a certain subset of wavelengths exists as standing waves and will therefore be amplified, resulting in the emission of coherent light. Each wavelength at which positive interference is achieved in a round-trip through the laser medium is called a mode. Typical gain media for short pulse lasers are Titanium doped Sapphire (Ti:Sa) or mixed Neodymium doped Glass (Nd:glass), a mix of neodymium doped silicate and phosphate glass. Their advantage over other standard gain media such as Helium-Neon (He-Ne) is a wider gain bandwidth, the range of wavelengths that are efficiently amplified in the gain medium. For Ti:Sa and mixed Nd:glass lasers the gain bandwidth spans a larger range of wavelengths compared to standard gain media. Through induction of a fixed-phase relationship between the different modes, called mode-locking, it is possible to amplify a large set of wavelengths, within the gain bandwidth of the medium which in turn allows for the generation of short-duration laser pulses. Here, the minimum duration of the pulse is inversely proportional to the width of amplified wavelength range. Consequently, a wider gain bandwidth enables shorter pulses. The obtained pulse duration of short-pulse lasers ranges from sub-femtosecond (10^{-16} s) to picosecond (10^{-12} s). To achieve high energies within the laser pulse it is send through additional amplification stages. The invention of Chirped-Pulse Amplification (CPA) ([3]) ultimately enabled high-power short-pulse lasers by stretching the pulse before and recompressing it after the amplification stage. This way higher pulse energies are achievable without causing damage to the laser optics and hardware. Stat-of-the-art pulsed laser systems consist of an oscillator, a stretcher, an amplifier and a compressor and routinely achieve peak laser intensities of the order of 10^{19} - 10^{23} on target [51–58].

For laser matter interactions the temporal profile of the laser pulse is of importance as it deviates from a Gaussian pulse shape. A schematic of the temporal profile of a short pulse laser is shown in Figure 2.1. The Gaussian laser pulse, with a temporal width of less than a picosecond, is shown in green and often refered to as the main laser pulse. Current laser systems generate a pedestal that precedes and succeeds the main laser pulse. One distinguishes between two pedestal time scales that result due to different phenomena. The nanosecond-scale pedestal (ns-pedestal, yellow) is a result of Amplified Spontaneous Emission (ASE) in the

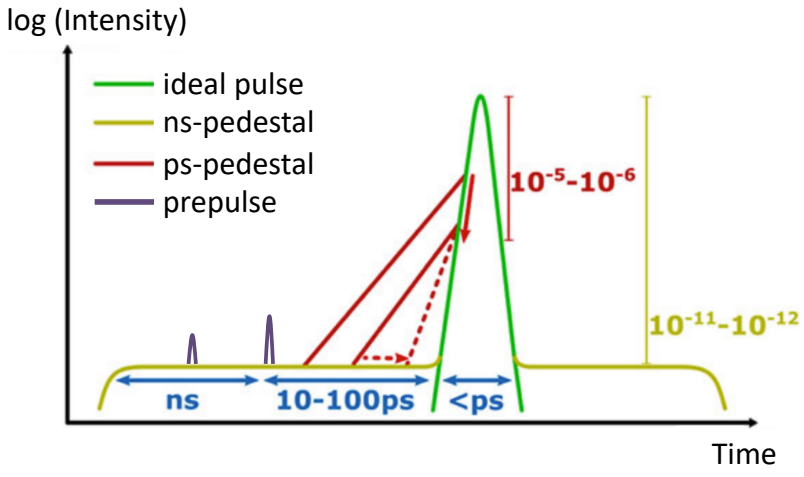

Figure 2.1.: Schematic of a short pulse laser temporal profile. In addition to the main pulse (green), short pulse laser systems generate long pedestals (yellow and red) before and after the main pulse. Short prepulses (purple) with higher intensity than the pedestal can also be observed. Adapted from Ref. 59.

gain medium of the laser. On a shorter timescale one can observe a picosecond-scale pedestal (ps-pedestal, red). The ps-pedestal is caused by spectral width narrowing of the laser pulse during the amplification process [60]. This can be the result of the limited bandwidth of optics used in the laser line. During the compression stage, a pulse with a narrow spectrum cannot be temporally compressed as much as a pulse with a large spectral bandwidth. Additionally, prepulses (purple), which are short compressed pulses of light with an intensity higher than the pedestal, are routinely observed in the laser temporal profile. Those prepulses can for example be generated by postpulses through compression [61], but can also be generated due to optical leakage in the laser chain.

The intensity of the prepulses and pedestals is commonly compared to the intensity of the main pulse. Rather than giving the intensity of both, the typical parameter referring to the prepulse intensity is the contrast, which is the ratio between the intensity of the pedestal or prepulse and the main laser pulse. The contrast for the ns-pedestal is usually on the order of 10^{-11}, while the contrast for prepulses and ps-pedestals can be on the order of 10^{-5}. For laser matter interactions, especially laser-driven ion acceleration, a contrast better than 10^{-8} is preferred.

2.1.1. High Repetition-Rate Lasers

The repetition rate of a laser system refers to the frequency at which a laser pulse can be delivered to the target. Depending on the laser system, repetition rates can range from one shot every few hours up to thousands of shots a second (kHz). The determining factor that limits the repetition rate in most laser systems is the cooling rate of the amplifiers. Low-power laser systems, delivering energies from 10's of mJ up to a few Joules on target, have been able to achieve few Hz to kHz repetition rate as the heat created in the amplifiers during operation is low enough to successfully cool them with air or liquid cooling flows. For high-power laser systems, where amplifiers need to increase the laser power significantly during a single pass, cooling rates are a key issue. During the amplification of a laser pulse, excess energy generates heat, which does not dissipate fast enough and consequently impacts the performance of the system. In extreme cases, the excess heat can even lead to damages of the amplifier. Thus, cooling times limit the repetition rate at which high-power laser system operate. New cooling techniques achieve reduced wavefront degradation due to thermal effects [62, 63]. Changing traditional flashlamp pump lasers with diodes to pump the gain medium further reduce the waste heat deposited in the gain medium since diode lasers produce a pump spectrum more closely matched to the gain spectrum of the amplifier medium [64]. These recent developments in laser technology have been essential to the commissioning of high repetition-rate PetaWatt (PW) class systems [65].

2.2. Laser Induced Ionization Processes

When a high-intensity short-pulse laser interacts with a target, a plasma is generated. A plasma is a state of matter that is microscopically charged but macroscopically neutral, which means that the electrons are separated from the atomic core, but have not escaped the target. To fully understand how a target can arrive in such a state, one can study the interaction of laser light with a single atom and its' subsequent ionization.

The laser induced ionization is explained based on the easiest case, the hydrogen atom. The atom will be ionized when the electric field strength of the laser exceeds the binding strength E_a of the electron, which is given by

$$E_a = \frac{e}{4\pi\epsilon_0 a_B^2} \quad , \tag{2.1}$$

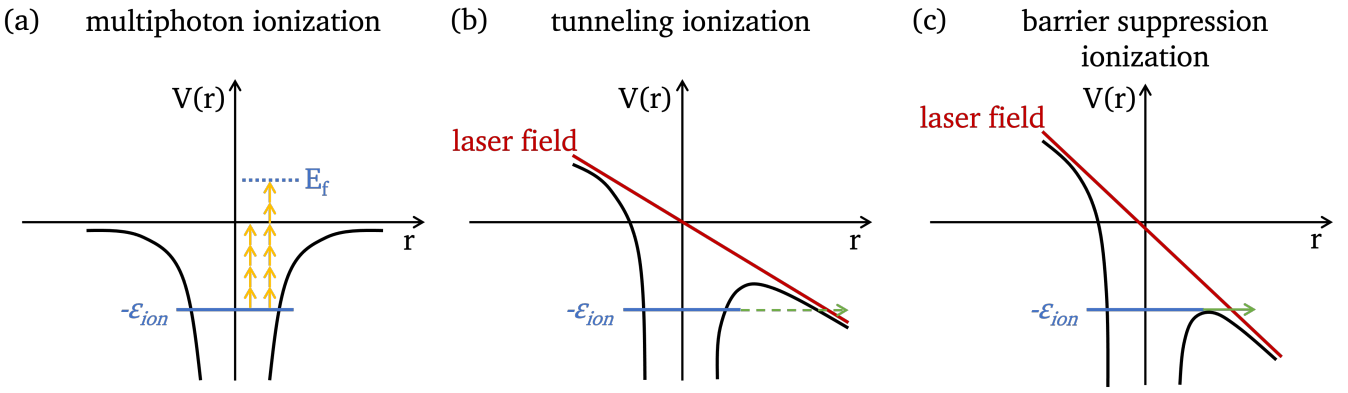

Figure 2.2.: Overview of laser induced ionization of an atom, where ϵ_{ion} is the binding energy of the electron. When the laser intensity is much lower than the binding strength of the electron, the atom can be ionized through multiphoton ionization (a). If the atom absorbs more photons than necessary to free the electron, its' kinetic energy is given by E_f. If the laser intensity is equal to the atomic intensity, an electron can be freed through tunnel ionization (b). Finally, barrier suppression ionization (c), is achieved when the laser intensity is larger than the binding strength. Adapted from Ref. 66.

where e is the electron charge, ϵ_0 is the vacuum permittivity and $a_B = 5.3 \times 10^{-9}$ cm the Bohr radius. The atomic intensity I_a, when the laser electric field matches the binding strength of the electron, is then given by

$$I_a = \frac{\epsilon_0 c E_a}{2} \simeq 3.51 \times 10^{16} \frac{\mathrm{W}}{\mathrm{cm}^2} \tag{2.2}$$

with c being the speed of light. For any target, the ionization of the atoms is guaranteed when the laser intensity I_L is larger than the atomic intensity I_a. I_L can be calculated following

$$I_L = \frac{E_L}{\tau_L A_{spot}} \quad , \tag{2.3}$$

where E_L is the laser pulse energy, τ_L is the laser pulse length and A_{spot} is the laser spot size [66].

Upon interaction of the laser with the front surface of the target, the laser electric field ionizes local atoms. To ionize an atom and thus free an electron, the transferred energy needs to be large enough for the electron to reach the continuum outside of the potential. Depending on the intensity of the laser three different ionization processes are distinguished:

- multiphoton ionization
- tunneling ionization
- barrier suppression ionization .

While multiphoton ionization can occur at any given laser intensity, above a threshold of 10^{10} W/cm^2 the ionization rate is large enough to have a significant impact. Similar to the absorption of a single high-frequency photon, an atom can also be ionized by absorbing several lower frequency photons. One distinguishes two different cases as shown in Figure 2.2 (a). In the first case, the total energy of the absorbed photons equals ϵ_{ion}, thus only transferring enough energy to ionize the atom. Another possibility is the absorption of more photons than necessary for ionization, which leaves the free electron with a kinetic energy E_f. This process

is called above-threshold ionization and often the predominant ionization channel during the interaction of X-ray free electron lasers with matter [67].

At laser intensities approaching the binding strength of the electron, two additional ionization processes have to be considered: tunnel ionization and barrier suppression ionization. A commonly considered simple model to describe the two types of ionization is that of a stationary homogeneous electric field overlapped with the Coulomb potential of the atom. This model has proven to be fairly accurate despite it's simplistic approach [66]. As shown in Figure 2.2 (b) and (c) the laser field distorts the Coulomb potential of the atom, lowering it on the right hand side. If the maximum value of the distorted potential on the right side is larger than the binding energy at small distances r but drops to below ϵ_{ion} at a larger distance, quantum mechanics allows the electron to tunnel through the barrier (green dashed arrow). This process occurs with a finite probability. Finally, when the maximum value of the potential on the right hand side drops below ϵ_{ion} the electron can escape spontaneously as it is not bound by the potential anymore (solid green arrow in (c)).

The considered model allows for the calculation of the appearance intensity for barrier suppression, which is a species-dependent value, but can be approximated as 1×10^{14} W/cm^2. Tying back to short pulse laser systems and their challenges to maintain a high contrast, this intensity limit can be problematic, as prepulses or even pedestals can have a high enough intensity to significantly ionize the target before the main pulse arrives.

If the target is of solid density, a dense surfaces plasma is created through field ionization in the electromagnetic field of the laser pulse during the first few cycles of the laser through the three processes presented above. After the release of initial electrons, once the number of electrons is high enough, electron impact ionization will take over to further ionize the target. In the process of electron impact ionization an energetic electron interacts with an atom to free a additional electrons [68]. The energy initially absorbed by the electrons is redistributed through electron-electron, ion-ion or phonon-phonon collisions until the local area thermalized to a Local Thermal Equilibrium (LTE). However, this state takes a comparably long time to establish. Thus, high-temperature plasmas are often ion a non-LTE state where the electron temperature is different from the bulk temperature. For short-pulse laser create such plasma states where energetic (hot) electrons are present and a single bulk temperature can no longer be defined.

2.3. Free Charge in the Laser Field

Once the target has been sufficiently ionized, the target electrons and ions are subject to the laser field directly. The descriptions of plasma behavior are based on the motion of these individual particles of the plasma. It is therefore important to consider the interaction of the laser field with a free charge before considering the interaction of the laser field with the plasma.

The easiest starting point is the consideration of a single free electron interacting with an infinite electromagnetic wave. For further simplicity we will consider a linearly polarized electromagnetic wave with wavelength λ_L propagating along the z-axis. The respective electric and magnetic field can be described by

$$\vec{E}(\vec{r},t) = E_0(\vec{r})cos\left(\omega_L t - kz\right) \cdot \vec{e_x} \quad , \tag{2.4}$$

$$\vec{B}(\vec{r},t) = B_0(\vec{r})cos\left(\omega_L t - kz\right) \cdot \vec{e_y} \quad . \tag{2.5}$$

Corresponding variables for the equations above are the time t, the spatial coordinate of the electron $\vec{r}$, the laser angular frequency $\omega_L = 2\pi c/\lambda_L$, the speed of light c, the laser wave vector $k = 2\pi/\lambda_L$ and the unit vectors $\vec{e_x}$ and $\vec{e_y}$. The equation of motion for electrons in this field is then described by the Lorentz equation

as

$$\vec{F_L} = \frac{d\vec{p}}{dt} = -e\left(\vec{E} + \vec{v_e} \times \vec{B}\right) = -e\left(\vec{E} + \frac{\vec{v_e}}{c} \times \left[\vec{e_z} \times \vec{E}\right]\right) \tag{2.6}$$

with the electron charge e, the electron velocity $\vec{v_e}$ and the electron momentum $\vec{p} = \gamma m_e \vec{v_e}$ with the relativistic Lorentz factor $\gamma = \left(1 + v^2/c^2\right)^{-1/2}$ [66]. In the last step Maxwell's third equation ($\nabla \times \vec{E} = -\partial\vec{B}/\partial t$) was used to further simplify the expression.

This equation can be solved for two different scenarios, when the speed of the electron is considered non-relativistic, i.e. $|\vec{v_e}| \ll c$, and for relativistic speeds. In the case of a non-relativistic electron speed, the effect of the magnetic field can be neglected. As a consequence, the solution to Equation 2.6 is given by

$$\vec{v_e} = \frac{eE_0}{m_e\omega} sin\left(\omega_L t\right) + v_i \tag{2.7}$$

$$= v_{os}\ sin\left(\omega_L t\right) + v_i \tag{2.8}$$

with the electron quiver velocity v_{os} and the initial velocity v_i. By dividing the quiver velocity v_{os} by the speed of light c one obtains the dimensionless normalized laser amplitude a_0, which can also be linked to the laser wavelength and intensity following

$$a_o = \frac{v_{os}}{c} = \frac{eE_0}{m_e\omega c} = \sqrt{\frac{I_L[\mathrm{W/cm^{-2}}]\ \lambda_L^2[\mu\mathrm{m}^2]}{1.37 \cdot 10^{18}\mathrm{W/cm^{-2}}\mu\mathrm{m}^2}} \tag{2.9}$$

with the laser intensity I_L and the laser wavelength λ_L. The threshold between non-relativistic and relativistic regime is given by $I_L\lambda_L^2 = 1.37 \cdot 10^{18}\mathrm{W/cm^{-2}}\mu\mathrm{m}^2$ or $a_0 = 1$ [69]. Below this threshold the electron motion is treated non-relativistically, but above this threshold it needs to be treated relativistically and the magnetic field in Equation 2.6 can no longer be neglected. In this case, the electron starts to drift along the z-axis with an average momentum $\overline{p_z} = a_0^2/4$ which results in a drift velocity v_D, derived from relativistic solution of the equation of motion in the laboratory frame, that scales with the normalized laser amplitude a_0 as follows

$$v_D = c \cdot \frac{\overline{p_z}}{\overline{\gamma}} = c \cdot \frac{a_0^2}{4 + a_0^2}\vec{e_z} \quad , \tag{2.10}$$

where the overscore represents values averaged over a rapidly varying electromagnetic phase $\phi = \omega_L t - kz$. Looking at the individual components of this equation, we can determine, that this drift is only a constant meaning that the electron is effectively only changing position and not gaining energy. This is a result of the starting point of an infinite electromagnetic wave and is described by the Lawson-Woodward theorem [70].

2.3.1. Ponderomotive Force

While the description of electron motion in a plane laser field proves to be useful, it does not completely describe the details of electron motion caused by a finite laser pulse. Equation 2.4 and 2.5 can be adapted by adding a time-varying function $f(t)$ which is considered to vary slowly compared to the laser frequency [66]. This time dependent function can effectively be incorporated in the field amplitude to obtain $E(\vec{r}, t)$ and $B(\vec{r}, t)$. Short pulse lasers in particular generate strong radial intensity gradients due to the small focal spots and ultrashort timescale of the pulse duration.

Considering an electromagentic wave propagating in the positive z direction with a radial intensity dependence, which is typically observed in the small focal spots of short-pulse lasers, the equation of motion for the non-relativistic case for an electron can be written as

$$\frac{\partial v_x}{\partial t} = -\frac{e}{m_e} E_x(\vec{r}) \tag{2.11}$$

Taylor expansion of the electric field using the substitution $\phi = \omega_L t - kz$ yields

$$E_x(\vec{r}) \simeq E_0(x)cos(\phi) + x\frac{\partial E_0(x)}{\partial x}cos(\phi) + ... \quad . \tag{2.12}$$

Inserting the first order term into Equation 2.11 we obtain

$$x^{(1)} = \frac{v_{os}}{\omega_L}cos(\phi) \tag{2.13}$$

with the quiver velocity defined in Equation 2.8. Similarly we can solve the equation of motion for the second order term of the Taylor expansion of the electric field. By using our previously determined first order term, we arrive at

$$\frac{\partial v_x^{(2)}}{\partial t} = -\frac{e^2}{m_e^2 \omega_L^2} E_0 \frac{\partial E_0(x)}{\partial x} cos^2(\phi) \quad . \tag{2.14}$$

The ponderomotive force acting on the electron can then be calculated by taking the cycle-average yield and multiplying by the electron mass m_e yielding

$$F_P = m_e \overline{\frac{\partial v_x^{(2)}}{\partial t}} = -\frac{e^2}{4 m_e \omega_L} \frac{\partial}{\partial x} E_0^2 \quad . \tag{2.15}$$

Effectively, the ponderomotive force pushes electrons out of regions of local intensity maxima towards lower intensity regions. This is facilitated by a lower restoring force in regions of lower intensity, which pushes the electrons less efficiently back towards its equilibrium state.

2.4. Laser-Target Interaction

Once the target is sufficiently ionized it can be treated as a plasma. This quasineutral state of charged and neutral particles exhibit collective behavior as a whole [71]. The term collective behavior means that the motion of a particle in the plasma not only depends on the local conditions of its' position but also on the state of the plasma in nonlocal regions. The reason for this behavior is the accumulation or movement of charges which induces electric or magnetic fields that affect other charged particles in the plasma. For a full understanding of the plasma state of the target additional variables determining the dynamics of the interaction of the laser with the plasma need to be explained. Important parameters describing the plasma are the Debye length, the plasma frequency and the critical electron density. Following the definition of these parameters, the energy transfer from the laser to the target electrons is explained, which can occur through a variety of mechanisms, collectively those processes are called electron heating.

2.4.1. Debye Sphere and Plasma Frequency

One characteristic of a plasma is the ability to efficiently shield out electric fields. If an electric potential is introduced to the plasma, the charge particles of the plasma shift accordingly to then efficiently shield the potential. Effectively this is achieved by the accumulation of charges around the introduced charge and the length of this shielding cloud can be characterized by the Debye length λ_D which is given by

$$\lambda_D = \sqrt{\frac{\epsilon_0 k_B T_e}{n_e e^2}} \tag{2.16}$$

with the permittivity of vacuum ϵ_0, the Boltzmann constant k_B, the electron temperature T_e and the electron density n_e. This particular distance refers to the point at which the strength of the introduced potential drops to 1/e of its initial value. The number of particles in the shielding or Debye sphere N_D is given by

$$N_D = \frac{4\pi}{3}\lambda_D^3 n_e \quad . \tag{2.17}$$

Eventhough the plasma can be considered globally quasineutral, there are still local areas where charge inhomogeneities exist. Those result in a displacement of the electrons relative to the uniform background of ions and consequently to the build up of electric fields aiming to restore neutrality by pulling the electrons back to their original position. Due to the inertia of the electrons, they will overshoot that original position and oscillate around their equilibrium positions with a characteristic frequency ω_p known as the plasma frequency and given by

$$\omega_p = \sqrt{\frac{e^2 n_e}{m_e \epsilon_0}} \tag{2.18}$$

with the electron mass m_e [71]. A plasma is characterized by $N_D \gg 1$, $\lambda_D < L$ with the pre-plasma scale length $L = c_s \tau_L$ calculated using the sound speed c_s and $\omega_p \sim \omega_L$.

2.4.2. Critical Density

Due to the laser-induced plasma generation on the surface of the target, the laser is no longer propagating in vacuum. As a result, we need to consider the dispersion relation for electromagnetic waves propagating in a plasma. The dispersion relation for electromagnetic waves is given by

$$\omega_L^2 = \omega_p^2 + c^2 k^2 \tag{2.19}$$

and the refractive index given by $n = ck/\omega_L$. Applying the dispersion relation to the refractive index equation leads to

$$n = \sqrt{1 - \frac{\omega_p^2}{\omega_L^2}} \quad . \tag{2.20}$$

This equation shows that the laser light is able to penetrate the plasma when the laser frequency ω_L is larger than the plasma frequency ω_p. In this case the plasma is called underdense. It needs to be taken into account, that the plasma frequency ω_p is proportional to the electron density n_e, see Equation 2.18. The threshold density at which the laser cannot penetrate the plasma anymore is call the critical density and is given by

$$n_c = \frac{\omega_L^2 \epsilon_0 m_e}{e^2} \simeq 1.1 \times 10^{21} \left(\frac{\lambda}{\mu\text{m}}\right)^{-2} \text{cm}^{-3} \quad . \tag{2.21}$$

When the laser cannot penetrate the plasma anymore, it is called overdense and instead of propagating within the plasma, the field decays exponentially behind the boundary layer with the maximum spatial reach given by the skin depth $l_s = c/\omega_p$.

The explained relationship is valid for the non-relativistic case. However, if the electrons are relativistic, i.e. $\gamma > 1$, the formula for the critical density n_c needs to be modified by the factor γ and effectively increases and allows the laser to propagate into the plasma further than classically possible. This phenomenon is called the relativistic transparency regime and is especially relevant in a variety of laser-driven acceleration regimes.

2.4.3. Electron Heating

Electron heating is a seed for other processes including ion acceleration, which will be the main topic of this work. Here, a few common mechanisms of electron heating will be discussed as efficient electron generation is important for laser-driven ion acceleration. Previously the mechanism of laser-induced ionization was discussed in Section 2.2, particularly focusing on the interaction of the laser field with a single atom and the eventual transfer of energy to other atoms through collisions. While this model builds a good basis for many standard short-pulse laser-matter interaction simulations, experiments have shown, that this type of mechanism is not the only one that needs to be taken into account in terms of electron heating.

For intensities above 10^{15} W/cm^2 the plasma temperature rises significantly such that collisions become ineffective during the laser-target interaction, as the collision frequency scales with $T_e^{-3/2}$ [66, 72, 73]. The high absorption observed in experiments for laser intensities higher than 10^{15} W/cm^2 can be explained by collissionless absorption processes. While the ponderomotive force as an electron heating mechanisms has already been explained in Section 2.3.1, the principle of some of the other most common collissionless absorption processes will be explained here. However for a more detailed description of electron heating in the collissionless regime, the reader is referred to other literature such as Reference 66.

Resonant absorption relies on resonantly driving a plasma wave at the critical density interface over a number of laser periods and thus coupling energy into the plasma. This mechanism can occur when the incoming laser light is p-polarized and interacts with a rising density gradient. After energy gain over multiple laser periods the plasma wave is eventually damped either by collisions or by particle trapping and wave breaking [66]. Resonant absorption stops to be one of the dominant absorption mechanisms, when the density gradient becomes too steep.

Brunel heating is a mechanisms that predominantly takes place when the target shows a very steep density gradient on the laser facing side. It can be divided into two steps. During the first step a thermal electron with the right momentum positioned near the edge of the target is accelerated out of the target by the laser field. The distance up to where it is accelerated is well beyond the Debye length λ_D. When the field reverses, the momentum of the electron reverses and it is consequently accelerated into the target plasma. Due to the overcritical density of the plasma, the laser will only reach to the skin depth c/ω_p into the target. As a result the accelerated electron can travel unaffected further into the target where it eventually is absorbed through collisions.

$\vec{J} \times \vec{B}$ *heating* as a mechanism is similar to Brunel heating as electrons are directly accelerated by the incident laser field. The driving force of the acceleration is the $\vec{v} \times \vec{B}$ component of the Lorentz force (see Equation 2.6). This mechanism occurs for any polarization except for circular polarized light. For an incident linearly polarized wave, it gives rise to a longitudinal force term that is composed of the pondoromotive force and the $\vec{J} \times \vec{B}$ heating term, which oscillates at twice the laser frequency. Normal incidence is the most efficient for this type of heating mechanism and it becomes significant at relativistic quiver velocities [66].

Direct laser acceleration relies heavily on the optimal injection of electrons into the laser field. The two criteria are a far enough distance from the critical density to gain a significant amount of energy and the injection at the ideal phase of the laser. This results in requirements for the initial velocity and position of the accelerated electron relative to the laser electric field phase. As a consequence electrons can only gain a significant amount of energy when they are injected during the accelerating half cycle of the laser pulse and can escape into the target bulk before the onset of the decelerating half cycle. For relativistic laser intensities, a laser phase velocity and electron velocity close to the speed of light c is required for the electrons to experience a significant positive acceleration from the wave over an extended distance [74].

Each different mechanism can be used to predict a resulting electron temperature and the scaling with laser intensity can vary largely based on the underlying mechanism. This work will focus on relativistic laser plasma interactions. We will therefore follow the approach as described in Reference 75 where the hot electron temperature is proportional to the ponderomotive potential. This dependence is a result of the $\vec{J} \times \vec{B}$ heating mechanism and predicts a hot electron temperature scaling following

$$T_e \simeq 511 \left[\left(1 + 0.73 I_{18} \lambda_\mu^2\right)^{1/2} - 1 \right] \text{keV} \tag{2.22}$$

with the laser intensity I_{18} in 10^{18} W/cm^2 and the laser wavelength λ_μ in micrometers [66].

Once a population of hot electrons is successfully generated, they can establish large enough electric fields to efficiently generate and accelerate ions from the target surface or the bulk, which will be discussed in greater detail in the next section.

2.5. Laser-Driven Ion Acceleration

Experiments, investigating the interaction of high intensity lasers with matter, showed efficient acceleration of electrons, protons and ions [4,5,50,76,77]. Compared to particle beams produced by conventional accelerators the laser-accelerated particle beams exhibit unique properties such as high brightness, high spectral cut-off, high directionality, low emittance and microsecond duration [78].The most widely-studied mechanism for laser-driven ion acceleration is the TNSA [5, 6, 50]. Subsequent studies have explored alternative mechanism both theoretically and experimentally [79–84]. Several of those studies have demonstrated enhanced acceleration performance from ultrathin (submicron thick) targets irradiated by high-contrast laser systems as a result of relativistic transparency effects [79, 80, 84–86]. The effect of relativistic transparency was previously discussed in Section 2.4.2.

2.5.1. Target Normal Sheath Acceleration

The efficient acceleration of ions from the interaction of a tightly focused high-power laser with a solid-density target was first observed twenty years ago [4, 5, 77]. The first identified mechanism of ion acceleration was named Target Normal Sheath Acceleration (TNSA), due to the emission of ions normal to the target surface. TNSA was for the first time theoretically explained by Wilks et al. [6]. To date TNSA is the most studied mechanism of laser-driven ion acceleration and is well known due to its robustness, directionality of the accelerated ions and high particle yield.

TNSA arises when a petawatt laser pulse interacts with a thick, solid density target. Figure 2.3 illustrates the different stages of this interaction. In the first step, shown in (a), the target front surface is rapidly ionized by the pedestal or rising edge of the laser pulse. During this first ionization stage, free electrons are created.

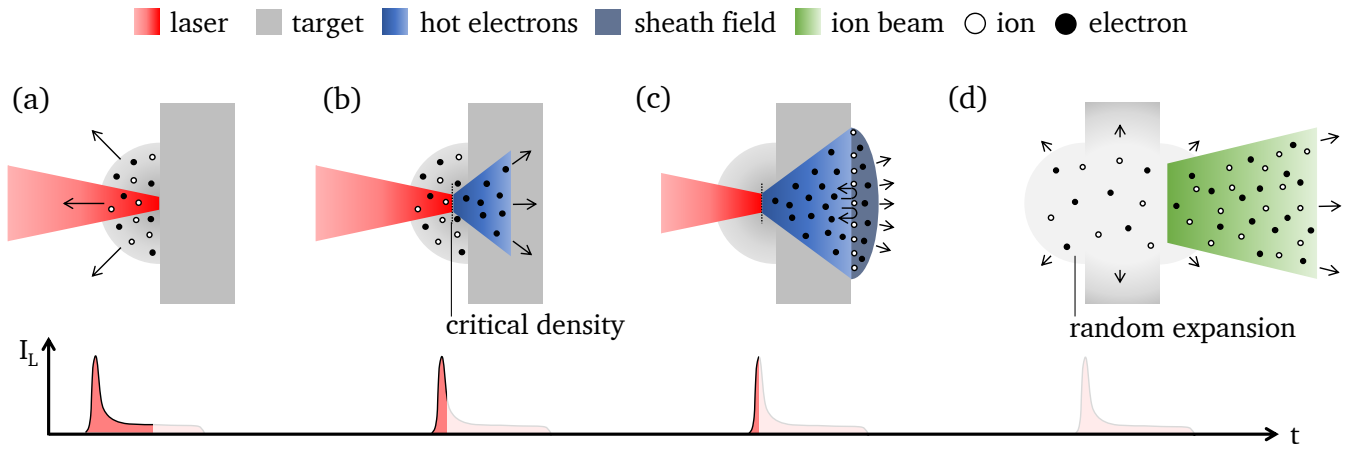

Figure 2.3.: (a) Upon interaction of a high-power short pulse laser with a solid target, the front surface of the target is ionized and a preplasma is formed. (b) When the main pulse arrives at the target, electrons are accelerated to MeV energies penetrating the target. (c) Hot electrons begin to reflux in the target, establishing an electrostatic sheath field at the target backside, that ionizes atoms in the surface layer. (d) A forward directed ion beam is driven by the electric sheath field, accelerating ions to MeV energies, while electrons copropagate alongside. The target expansion occurs on much longer time scales than the laser pulse, leading to a random expansion after the end of the laser pulse.

When the main laser pulse interacts with the preheated target, (b), the freed electrons begin to oscillate in the electromagnetic field of the laser and are accelerated into the target at relativistic velocities, mainly through the ponderomotive force or relativistic mechanisms like $\vec{J} \times \vec{B}$ heating [72]. The forward driven hot electrons have an average energy on the order of several MeV. Due to their high kinetic energy their collisional range is much larger than typical target thicknesses of 10 - 25 µm. The beam of hot electron propagates to the rear side of the target, where the relativistic electrons will leave the target and escape into vacuum. This triggers a return current of cold (less energetic) electrons towards the positive ions at the front side of the target. Electrons returning to the front surface are accelerated back into the target. Sufficiently energetic electrons, break through the backside of the target as shown in (c), but are then pulled back into the target due to space charge confinement. The energetic electrons that temporarily leave the target before refluxing, or permanently escape the target, establish a strong electrostatic sheath field on the back side of the target extending over a length approximately equivalent to a Debye length λ_D from the initially unperturbed rear surface [87]. The electrostatic field is sustained by continuously refluxing electrons with high enough energies. The strength of the electric field can be calculated using

$$E = \frac{k_B T_e}{e c_{s,ion} t} \tag{2.23}$$

where $c_{s,ion} = \sqrt{Z T_e / m_i}$ denotes the ion speed in the target [6]. Electric fields around TV/m are generated through this process, which are orders of magnitude higher than the ionization threshold of atoms, and as a consequence are sufficient to instantaneously ionize a thin layer at the rear surface of the target. Here, the maximum charge state found under the accelerated ions is a measure of the maximum field strength that appeared at the rear surface of the target. The ions generated at the rear surface are accelerated away from the target bulk, normal to the surface, reaching energies up to tens of MeV. The generated ion beam expands isotropically in all directions as the ion trajectories depend on the local orientation of the expanded rear

surface as well as the electric field lines driven by the time dependent electron density distribution. In principle any ion species present in the rear surface layer of the target can be accelerated through TNSA, however, the acceleration of light ions is preferred, especially protons due to their high charge-to-mass ratio. These light ions usually originate from a contamination layer on the rear surface of the target [5, 6, 88, 89]. For single species continuously refreshing targets, as used during later presented experiments, such a contamination layer is not formed and as a result ions of the target bulk material are accelerated. The resulting ion beam exhibits a broadband energy spectrum with an exponential profile up to a high cut-off energy that is dependent on the hot electron temperature. The opening angle of the emitted beam is energy dependent. Protons with the highest energy are emitted with the smallest opening angle up to a few degrees half angle. If the protons have less energy, the opening angle is consequently larger. Below about 30% of the maximum energy, the opening angle reaches a maximum and stays constant for lower energies [4–6, 89, 90].

While the presented scaling proves useful in a lot of scenarios, especially Equation 2.23 fails to describe the physics of TNSA both at early times as the electric field strength E diverges for $t \to 0$ and long times $t \gg \tau_L$ since the electric field quickly decays after the laser pulse ends. The performance of TNSA in terms of maximum achievable ion energy is limited by two factors, the cooling of the hot electrons and the increase in scale length [6]. As the strength of the accelerating field is inversely proportional to the scale length of the plasma $c_s t$, the acceleration performance degrades as the scale length increases. By requiring the scale length to always be smaller than the Debye length λ_D. Mora et al. established a scaling law for the maximum proton energy following

$$v_{p,max} \simeq 2\sqrt{\frac{Zk_BT_e}{m_i}} ln\left(\tau + \sqrt{\tau^2+1}\right) \tag{2.24}$$

$$E_{p,max} \simeq 2Zk_BT_e \left[ln\left(\tau + \sqrt{\tau^2+1}\right)\right]^2 \tag{2.25}$$

with $\tau = \omega_{pi} t/\sqrt{2e_N}$, where $e_N = 2.71828$ is the Euler number, and the ion plasma frequency $\omega_{pi} = \sqrt{n_{e,0}Ze^2/(m_i\epsilon_0)}$ with the electron density of the unperturbed plasma $n_{e,0}$ [88, 91, 92]. This equation is still dependent on the acceleration time t as a free parameter and thus effectively not limiting the maximum achievable proton energies. Experiments however observed a sharp cut-off energy for ions accelerated through the TNSA mechanism. To accommodate the fact, that the electron temperature is not constant over the full duration of the target evolution, Fuchs et al. [78, 93] introduced a finite acceleration time t_{acc} to substitute t in Equation 2.25. Two different cases are distinguished based on two classes of laser architectures with different laser pulse duration τ_L following

$$t_{acc} = \begin{cases} 1.3\tau_L & \text{for } \tau_L = (0.15 - 10)\text{ps} \\ \alpha(\tau_L + t_{min}) & \text{for } \tau_L = (30 - 100)\text{fs} \end{cases} \tag{2.26}$$

where α varies between 3 ($I_L = 2 \times 10^{18}$ W/cm^2) to 1.3 ($I_L = 3 \times 10^{19}$ W/cm^2) and $t_{min} = 60$ fs as the minimum energy transfer time between electrons and ions for short laser pulse durations.

While this approach resolves the dependence of the proton cut-off energy on the laser parameters, the target thickness is not taking into account, but has been shown to have an impact on the proton energy spectrum [78, 94–97]. Over the past years a variety of theoretical models have been proposed in order to attempt to fully describe TNSA [98]. In an early attempt to build an analytical model Fuchs et al. [78] established the dependence of the cut-off proton energy on the target parameters through the hot electron density, which in his model is given by

$$n_{e,0} = \frac{fE_L/T_e}{c\tau_L S_{sheath}} \quad \text{and} \tag{2.27}$$

$$S_{sheath} = \pi\left(A_{spot} + d\ tan(\theta)\right)^2 \tag{2.28}$$

with the laser to hot electron conversion efficiency f, the laser pulse energy E_L, the laser pulse duration τ_L, the sheath area S_{sheath}, the laser spot size A_{spot}, the target thickness d_T and the electron divergence half angle θ. Additional works have tried to establish analytical scaling laws of ion cut-off energy with target and laser parameters [78, 95, 99–101]. While all of those models can describe the presented data very well, their applicability to data sets from other facilities is very limited. This is due to the complexity of the generated system, which requires models to make phenomenological assumptions or simplifications to be able to solve the equations of motion.

Zimmer et al. bridged the gap between different experiments and data sets by establishing an empirical scaling of the proton energy with the four parameters (laser energy E_L, laser pulse duration τ_L, laser spot size A_{spot} and target thickness d) using experimental data from many different laser facilities [102]. The presented scaling relies on choosing a reference data point, from an experiment in the vicinity of the parameters of interest, as a basis for the prediction of the cut-off energy following

$$E_{max} = E^r_{max} \cdot \left(\frac{E_L}{E^r_L}\right)^{0.59} \left(\frac{\tau_L}{\tau^r_L}\right)^{-0.09} \left(\frac{A_{spot}}{A^r_{spot}}\right)^{-0.58} \left(\frac{d}{d}\right)^{-0.16} \tag{2.29}$$

with the reference values marked with the label r. The exponents indicate a stronger dependence on laser energy and spot size compared to the laser pulse duration and target thickness.

In general, two main criteria for optimizing the laser-target interaction conditions have been identified over the past years from simulations and experiments. First, the laser system should have a high contrast, which will result in a smaller preplasma that is generated at the target front surface. However, as electron heating benefits from the formation of a preplasma, it is challenging to choose the optimal laser contrast. To precisely tailor the preplasma, two pulse schemes have been successfully implemented [103]. In addition to that, it is important to optimize the target thickness. It should be thick enough to avoid disturbance of the back surface caused by the shock wave launched into the target by the laser. On the other hand, it needs to be thin enough to limit scattering of the hot electron beam. An unperturbed beam is important to maximize the field established on the back side of the target. Typically effective target thicknesses range between hundreds of nanometers to several micrometers [87]. Higher cut-off energies are observed for longer (>ps) laser pulses. Thus it is recommended that experimental campaigns perform scans of the parameter space around chosen laser and target conditions as for each laser facility individual parameters to optimize the maximum proton energy for a specific facility. It is important to point out, that all those scalings, analytical or empirical, are solely applicable to the regime of TNSA. Once a transition to a different acceleration regime occurs, new scaling models would need to be established and followed.

2.5.2. Enhanced Target Normal Sheath Acceleration

Although very robust and predictable, the TNSA mechanism faces some limitations, that can be more or less severe depending on the application of the laser-driven ion beam. To mention a few limitations, the relatively low cut-off energy that is achievable is a limiting factor for applications that use ions to penetrate matter such as for tumor treatment using laser-driven sources [104]. The energy limitation, sets an upper boundary for the maximum depth at which a tumor can be treated. Additionally, the large bandwidth of energies of the TNSA ion beam can be complicated for applications that prefer a smaller bandwidth beams.

The need for different ion beam properties has driven the exploration of novel acceleration regimes theoretically and experimentally. Among the identified regimes are Collisionless Shockwave Acceleration [81–83], Radiation Pressure Acceleration [79], Breakout Afterburner [80] and Enhanced Target Normal Sheath Acceleration [84].

The interested reader is referred to the publications listed for the first three mechanisms, which are less relevant to the presented work. This section will focus on the enhanced TNSA mechanism. Mishra et al. studied the interaction of a high power laser with a cryogenic hydrogen target, which is especially of relevance for the second experiment that is part of this work, as it utilized a cryogenic jet target.

The enhances TNSA mechanism is based on relativistic transparency, which occurs during the irradiation by the laser and enables the laser to penetrate the target further than initially possible by lowering the target density due to relativistic effects as explained in Section 2.4.2. The TNSA mechanism limit in terms of maximum cut-off energy is caused by the accelerated ions, that leave the target surface, pulling the hot electrons back and cooling them in the process. Effectively, this results in a decrease in the sheath electric field. If the electron energy in the sheath region is continuously replenished, the electric sheath field will decay much slower. This reheating of electrons occurs during relativistic transparency of the target. In this regime the group velocity of the laser is much smaller than the speed of light c when the laser crosses the near critical density plasma. As a result the laser interacts with the expanding target over an extended period of time. It is to be noted, that the time at which the target becomes relativistically transparent is of great importance with regards to the maximum cut-off energy of the ion beam. If relativistic transparency occurs too early, the TNSA field will be weak and the laser will cross the target bulk without significantly heating the expanding electron population. In the other extreme case, if relativistic transparency occurs too late in time, only a small fraction of the laser energy will reach the rear side of the target and thus prevents significant energy coupling into reheating the hot electron population.

Using an analytical model, validated by extensive Particle In Cell (PIC) simulations, Mishra et al. found a criterion for the minimum laser pulse duration τ_L based on other laser and target parameters to achieve maximal cut-off energies of the laser-driven ion beam. The relativistic gamma factor γ for a p-polarized laser is defined as $\gamma = \sqrt{1 + a_0^2/2} \approx a_0/\sqrt{2}$ for the normalized laser potential $a_0 \gg 1$. Starting with the simplified assumption of a 1D-like expansion and a fast electron temperature defined by the laser ponderomotive scaling we obtain

$$n_{e0} d_0 = n_e d \tag{2.30}$$

$$k_B T_{hot} = \left(\sqrt{1 + \frac{a_0^2}{2}} - 1 \right) m_e c^2 \approx \frac{a_0}{\sqrt{2}} m_e c^2 \tag{2.31}$$

with the initial target thickness d_0 and the expanded target thickness d. The thickness evolution throughout laser irradiation can be approximated by $d \simeq d_0 + c_s t$, where $c_s = \sqrt{Z k_B T_{hot}/m_i}$. Relativistic transparency occurs when $n_e = \gamma n_c \approx a_0/\sqrt{2} n_c$, ideally this transition occurs at the peak of the laser pulse intensity, adding the requirement $t \approx \tau_L/2$. For a high laser intensity ($a_o \gg 1$), we can utilize the expressions above together with the assumption that by the time the laser peak intensity reaches the target it is significantly pre-expanded such that $d \gg d_0$. Equation 2.30 can then be rewritten to obtain an expression for the optimal areal density of the target as a function of the laser parameters

$$\frac{n_{e0}}{n_c} d_0 \approx c \tau_L \sqrt{\frac{a_0^3}{2^{2/3}} \frac{Z m_e}{m_i}} \approx 0.59\ c\ \tau_L \sqrt{a_0^3 \frac{Z m_e}{m_i}} \quad . \tag{2.32}$$

This equation relies on the fact, that the target is initially opaque to the laser and eventually becomes transparent during irradiation. We therefore can add further requirements to the model for the initial density n_{e0} and the target thickness d_0

$$n_{e0} > \gamma n_c \quad \text{and} \tag{2.33}$$

$$d_0 > \sqrt{\gamma} c/\omega_p \quad . \tag{2.34}$$

This results in a condition for the normalized vector potential a_0 as follows

$$a_0 < min\left[\sqrt{2}n_{e0}/n_c\ ,\ 5\times10^3(d_0(\mu\mathrm{m})^2)n_{e0}(10^{23}\mathrm{cm}^{-3})\right] \quad . \tag{2.35}$$

Additionally the laser pulse duration is required to be larger than the time it takes for the initial density to drop to the relativistic transparency threshold. Using Equation 2.30 and the approximated thickness evolution we obtain

$$\tau_L > \frac{d_0}{2c_s}\left(\frac{\sqrt{2}n_{e0}}{a_0 n_c} - 1\right) \tag{2.36}$$

which can be simplified for $n_{e0}/n_c \gg a_0/\sqrt{2}$ to

$$\tau_L > \frac{d_0}{c}\frac{n_{e0}}{a_0^{3/2}n_c}\sqrt{\frac{m_i}{\sqrt{2}Zm_e}} \quad . \tag{2.37}$$

As an example for a laser pulse with $a_0 \sim 10$ and a 1 µm thick cryogenic hydrogen target ($n_{e0} \approx 40n_c$) the minimum required pulse duration to observe enhanced TNSA is 125 fs.

This equation can be used to predict whether in the experiments conducted at the Advanced Laser for Extreme PHotonics (Fort Collins, USA) (ALEPH) and Texas PetaWatt (Austin, USA) (TPW) laser facilities, presented in this work, enhanced TNSA is expected to be responsible for the acceleration of ions from the target. Table 2.1 summarizes the laser and target parameters observed during the experiment used as input for the calculation including the laser intensity, the target thickness and the target electron density. The second-last column shows the minimum required pulse duration for both laser facilities for enhanced TNSA to play a roll in the acceleration process. The last column shows the measured laser pulse duration for each system. While the pulse duration of the ALEPH laser, 45 fs, is much smaller than the necessary 1020 fs to observe enhanced TNSA effects, the pulse length of the TPW laser is more than three times the threshold of enhanced TNSA. It is therefore expected, that enhanced TNSA played no role during experiments at the ALEPH laser, but it likely occurred during ion acceleration using the TPW laser.

Laser facility	laser intensity (a_0)	target thickness (µm)	target electron density (n_c)	min. pulse duration (fs)	laser pulse duration (fs)
ALEPH	12	5	50	1020	45
TPW	31	1.2	40	40	137

Table 2.1.: Summary of laser and target parameters of the ALEPH and TPW laser facilities. The minimum required pulse duration to observe enhanced TNSA is shown in column 5. Enhanced TNSA can be expected to occur for the experiment conducted at the TPW laser, but is unlikely to have been responsible for ion acceleration during the experiment at the ALEPH laser facility.

3. Continuously Replenishing Jet Targets

There are two components to laser-driven ion acceleration, the laser system delivering the laser pulses and the target delivery system. Traditionally, single solid foils have been used for laser-driven ion acceleration experiments. Once the shot rate of high power lasers increased, multi-target holders were developed to make use of advancing laser capabilities. However, the transition current to high repetition-rate capable laser systems now require faster replenishing targets which has led to significant development in this area.

Requirements for such fast replenishing target systems are the stability of the target itself and the ability to operate at repetition rates of multiple Hz to kHz. In order to make use of these laser system capabilities, targetry systems need to be developed that can match and even exceed the laser repetition rate. A large variety of systems has been developed over the past decade based on different materials ranging from tapes [105–107] to cryogenic [108,109] and liquid jets [110–114]. Jet targets specifically are promising fast replenishing target systems as they can reach target thicknesses of sub to several micrometer. Cryogenic and ambient-temperature liquid jet targets are developed and continuously improved at SLAC National Accelerator Laboratory (Menlo Park, USA) (SLAC).

In this chapter, the technical details of those two targetry systems and the parameters of the targets they generate will be explored. Additionally, the implementation in a vacuum chamber and the target related diagnostics setup will be explained with regards to the two experiments that delivered the core data of this thesis. The ambient-temperature liquid jet platform will be explained first, as this target was used for the later presented experiment conducted at the ALEPH laser at Colorado State University, presented in Chapter 4. Subsequently, the cryogenic jet system will be explained, which was implemented at the Texas Petawatt laser facility at the University of Texas at Austin, presented in Chapter 7.

3.1. Ambient-Temperature Liquid Jet Targets

Ambient temperature liquid jet targets have been developed and studied at SLAC for the past few years [111,113,115]. Their primary applications are found within biology and chemistry, where liquids or structures dissolved in a liquid are studied at the Linear Coherent Light Source (Menlo Park, USA) (LCLS) free electron laser or the Stanford Synchrotron Radiation Lightsource (Menlo Park, USA) (SSRL). Due to the low laser and X-ray intensities on target, the jet forming nozzles have been historically machined from glass. Those designs are however not strong enough to withstand the harsh environments encountered in high-power laser-matter interactions.

In the course of this thesis, a new design was developed and machined out of tungsten, a more robust material that is more resistant to heat and shock strain. The developed two-piece microfluidic nozzle assemble, shown in Figure 3.1, is based on the same principle as the successfully tested and implemented glass nozzles. The design consists of two initially identically “blank” plates, a “top plate” and a “bottom plate” as shown in (a). A 1.6 mm diameter through hole is machined into the top plate as the liquid inlet, which is feeding liquid

into the 25 μm deep converging microfluidic channel etched into the bottom plate. The channel extends all the way to the bottom of the plate, where the liquid is injected into the vacuum chamber to form the target. The right channel geometry was determined by testing glass proto-types with different channel geometries prior to the experiment. For optimal ion acceleration, a liquid jet thickness of around 1 μm and below is preferred. The corresponding output channel geometry of 100 × 25 μm was then laser cut into the bottom plate [111, 116]. A 500 nm thick layer of gold, coated onto the bottom plate around the channel, enhances the seal created using four high-strength stainless steel fasteners, one in each corner of the assembly, which are exerting uniform pressure across the sealing surface. Once the nozzle is sealed and assembled, the output surface on the bottom is polished to create a smooth transition from one plate to the other at the nozzle exit. This ensures that the jet emerges perpendicular to the nozzle output surface to facilitate alignment of the jet and ensure reproducibility of the jet position when nozzle assemblies are exchanged.

The liquid jet target is formed by a converging channel geometry with the underlying principle of jet formation illustrated in Fig. 3.1(c). Due to the converging geometry of the nozzle, opposing, high-speed flows are generated along the channel wall. These flows converge at the nozzle exit and flatten the liquid from the center of the channel to form a sheet perpendicular to the channel plane [111, 115, 117]. The lateral expansion of the sheet is limited by the surface tension, which will ultimately overcome the fluid inertia and collapse the edges into rims with diameters of several tens of μm. While the length of the primary sheet (1–5 mm) is linearly dependent on the flow rate, the width is limited to ∼0.7 mm. The highest speed flows are found within the rims, which ultimately causes the sheet to narrow again and recombine. Analogous to the sheet formation at

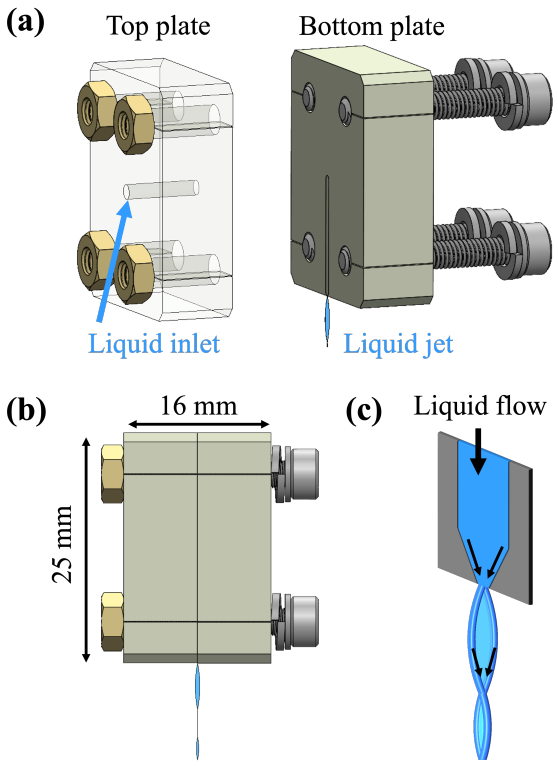

Figure 3.1.: (a) Exploded-view of the top and bottom plate showing the liquid inlet channel and the microfluidic channel etched into the bottom plate. (b) Side view of the collapsed nozzle design and liquid jet that is formed perpendicular to the sealing plane. (c) Schematic illustration of the nozzle geometry and the formation of the jet sheets, arrows indicate flows with maximum speeds.

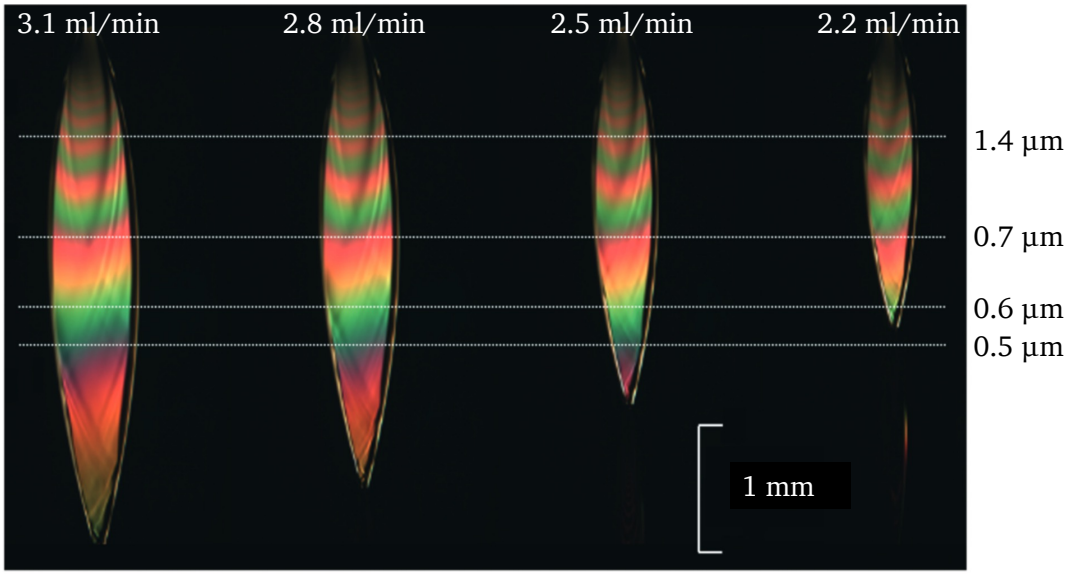

Figure 3.2.: Thickness gradient along first sheet ranging from multiple µm to 100s of nm for a glass prototype nozzle [115]. The thickness gradient is shown at different flow rates from 3.1 ml/min to 2.2 ml/min. The thickness gradient is stationary in space, while increasing flow rates results in larger and wider sheets, consequently giving access to a larger thickness range.

the nozzle exit, a second sheet, which is smaller than the predecessor sheet, is formed perpendicular to the first sheet. This recombination and subsequent sheet formation process repeats to form successively smaller sheets as energy is dissipated through viscous effects in the "fluid chain" geometry [118,119]. After generation of five consecutive sheets with alternating orientation the rims eventually no longer separate and the jet collapses into a cylinder.

Converging liquid jets exhibit a thickness gradient across the individual sheets with decreasing thickness for larger distances to the nozzle output. This thickness gradient is observed for each individual sheet. An example of a thickness gradient for a glass nozzle proto-type is shown in Figure 3.2, where the same nozzle was operated at increasing flow rate settings resulting in increasing sheet sizes. The thickness gradient is stationary in space as it is set by the nozzle geometry, this is illustrated by the dashed white lines at set thicknesses across the four different flow rates. As the flow rate through the assembly is increased, the sheet grows in length and width and generated addition target regions with sub-micrometer thicknesses. This principle is valid until the flow rate reaches a maximum above which the primary sheet begins to fray into a spray of droplets and the subsequent fluid chain cannot form [115]. For details on the measurement of the thickness, see Section 3.1.2.

3.1.1. Water Jet Operation

The stability of the water target is influenced by the percentage of air present in the water and the stability of the flow rate at different points along the liquid line, Peek tubing (1/8 in. outer diameter). To ensure optimized stability of the water target, additional components are added to the liquid line before the water is injected into the target chamber. The liquid is pumped through the whole line shown in Figure 3.3 by a High Performance Liquid Chromatography (HPLC) pump (LC-20AD, Shimadzu Scientific Instruments), which applies a constant flow rate across the full water line. The pump draws liquid from a reservoir, where

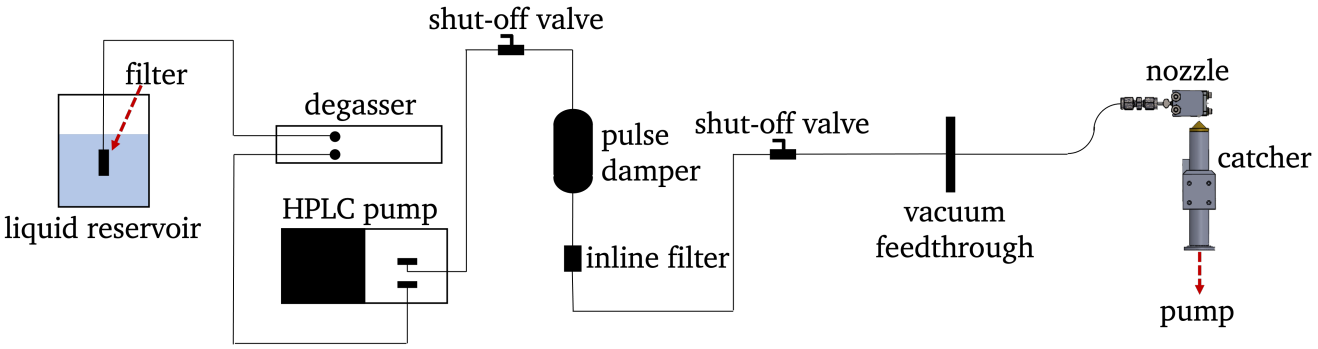

Figure 3.3.: Schematic of liquid water line to the jet nozzle. The liquid is stored in a liquid reservoir and pumped through the line by a HPLC water pump. Several filters, a degasser and a pulse damper ensure a stable flow without any contaminants or flow fluctuations. The liquid is injected into the vacuum chamber through the nozzle and collected by a catcher a few millimeters below the nozzle, which is connected to a vacuum pump.

large impurities and particles are prevented to enter the water line by a filter. Before entering the pump, a degasser eliminates air bubbles in the water flow. After the dual plunger HPLC pump, the liquid passes a pulse damper, which compensates for small flow rate fluctuations to prevent the target from pulsing with the plunger frequency of the pump. This pulse damper is realized using an water filled reservoir with a compressible air bubble. A second filter in the line prevents large particles to enter and clog the nozzle assembly. The liquid passes the vacuum feedthrough and is then injected into the vacuum chamber through the nozzle. Two shut-off valves are located along the liquid inlet line to enable shut-off of the liquid flow when required, while maintaining sufficient pressure and liquid in the line to easily restart operation.

To mitigate the influence of the vapor, that surrounds the target at all times, on the vacuum quality during operation, a heated catcher system evacuated the liquid from the target chamber by intercepting the jet at the convergence point of the first sheet, i.e. when the first sheet has collapsed into a cylinder. The tip of the catcher assembly is made from copper and narrows to a ⌀500 µm orifice at the top. Heating the catcher tip and cylindrical body beyond 100° C ensures that the liquid does not freeze when coming in contact with the catcher body, but instead vaporizes and is immediately evacuated from the catcher body. Metal vacuum tubing connects the interior of the catcher to an oil-free small scroll pump, Leybold SCROLLVAC or equivalent, with liquid and cold traps installed before the pump. The scroll pump creates a pressure difference between the interior of the catcher, where the pressure equals the vapor pressure of the liquid, above 15 mbar, at the set temperature and the liquid and cold traps outside the chamber, a few mbar. This pressure difference allows for efficient evacuation of the liquid vapor, which is reliquefied and collected in the liquid and cold traps.

For implementation during the experiment the nozzle was mounted on a 6-axis motorization stage including x-y-z motion, rotation and tip/tilt of the target. This allowed for precision alignment of the target in the focal plane of the laser. The presented setup including the catcher line was able to operate for up to one hour without interruption. However, the presented evacuation system was sensitive to local temperature and pressure differences. Changes in temperature and pressure could lead to a reduction of the efficiency of the system, which resulted in a lower pressure in the cold trap outside of the target chamber. Once this pressure drop was observed, the issue could be solved by stopping and restarting the liquid jet as well as venting the catcher line outside of the target chamber, which took roughly 10 - 15 minutes. Additional efforts are currently focusing on the improvement of the system based on these complication, to implement a more robust system in the future.

3.1.2. Water Jet Diagnostics

During operation, except for on shot, the jet is monitored continuously by four different imaging lines, two low-resolution large Field Of View (FOV) imaging systems, a high resolution laser focus and jet imaging system and a medium resolution thickness measurement through a white light interferometry line. All four imaging lines were blocked on shot to prevent damages to the imaging systems and cameras. Figure 3.4 shows the setup of the four imaging lines with respect to the jet target. For each imaging line exemplary images show the Region Of Interest (ROI) of each imaging system.

The FOV imaging systems consist of a camera and objective, which can be a fixed or adjustable focal length objective depending on the setup. The main constraints are the size of the field of view, at least 4×4 cm and a resolution of at least 10 µm. During the experiment presented in Chapter 4, the angle between the two large FOV imaging lines was 110°, in general an angle close to 90° is recommended. The two large FOV imaging lines allow for millimeter precision positioning of the jet near the target chamber center (TCC) and relative alignment of the catcher to the jet throughout the whole duration of the experiment, to ensure efficient evacuation of the water by the catcher, see FOV1 and FOV2 in Figure 3.4.

A high resolution (0.3 µm per pixel) imaging system is set up in the laser forward direction used an f/1.6 lens, equivalent to a magnification of 20. This imaging systems serves two purposes, primarily it can be used to inspect and optimize the laser focus. Additionally it can monitor the laser target overlap and enables the precise positioning of the jet in the laser focal plane using features on the rear surface of the jet. In Figure 3.4 the laser spot on the liquid sheet can be seen as the dark spot inbetween the two converging liquid rims.

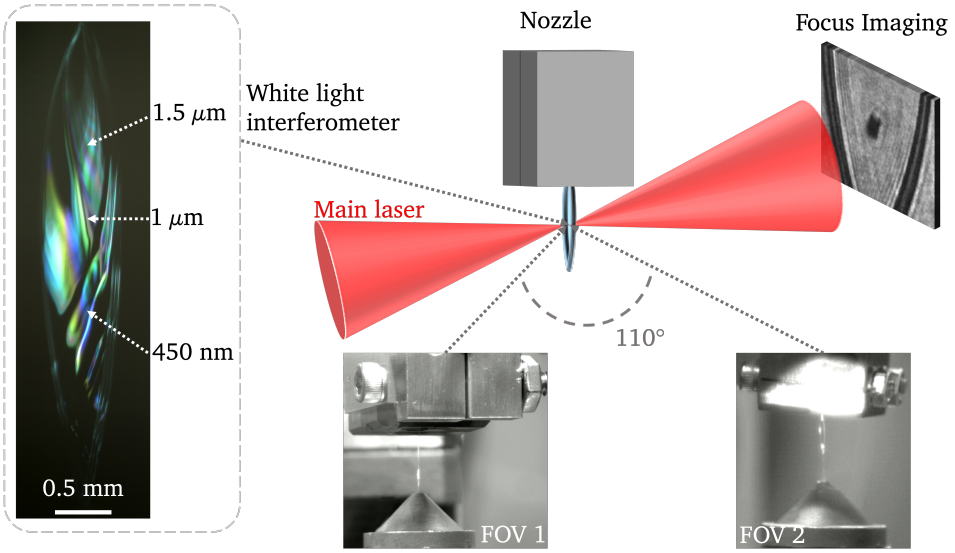

Figure 3.4.: Optical setup for monitoring the ambient-temperature liquid jet target. The jet and laser-target overlap are diagnosed using the focus imaging system. A dark spot is observed where the laser interacts with the target and it turns opaque to the light due to a change in density. Two large FOV imaging lines at 110° from each other image the nozzle, the jet and the liquid catcher using surrounding light. White light interferometry set up in reflection mode using a collimated white light source measures the thickness of the jet, see inset on the left. The working principle of the white light interferometry is explained in the text below.

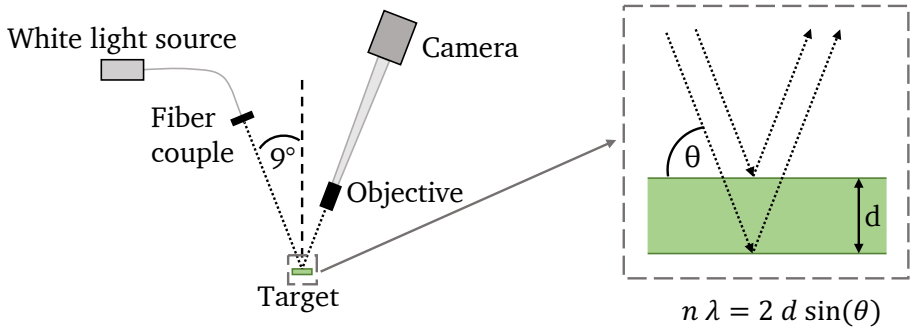

Figure 3.5.: Setup for the white light thin film interferometry measurement. A white light source paired with a fiber couple illuminates the target at an angle of 9°. The reflected light is collected by an objective and imaged using a camera. Following Bragg's law (see inset on the right) two waves interfer constructively if the distance travelled by the wave penetrating the target is equal to n times the wavelength of the light. For this particular setup θ is 81° and the incident wavelengths span the visible spectrum. Bragg's law is only fulfilled for a small subset of wavelengths of one color given a particular target thickness.

White Light Thin Film Interferometry

The thickness of the jet is measured using white light interferometry set up in reflection at an angle of 9° from the target normal as shown in the setup sketch in Figure 3.5. A collimated, continuous white light source, Ocean Optics HL-2000-HP or equivalent, illuminates the target. The reflected light is collected by an objective, in this specific setup using a magnification of 10x, and imaged using a Charge Coupled Device (CCD) camera. Based on the thickness of the target, different wavelengths fulfill Bragg's law stated in the inset in Figure 3.5. If the distance travelled within the target is equal to multiples of the wavelength, the light will interfer constructively. For incident white light and the thickness gradient across the primary sheet this results in different constructively interfering wavelengths at different locations on the liquid sheet, leading to the observed rainbow pattern. The high resolution imaging line has a field of view that accommodates the full length of the liquid sheet, in this case 5 mm.

It is important to note, that this technique is especially useful for thicknesses around and below 1 µm and becomes ineffective above a few micrometer. Figure 3.4 shows an example of a white light interferometry image. As can be seen in the image, the sheet shows different colors at different distances from the nozzle (top of the image). Those colors can then be related to a thickness of the sheet in that specific location. Three different thicknesses are identified as an example, to give the reader an idea of the thickness range of the jet. Additionally, dark areas are observed in the captured interference image. These areas correspond to areas of high surface roughness, which leads to an uncollimated reflection of the light and a decreased intensity of the positively interfering reflected light.

3.2. Cryogenic Jet Targets

Micron-scale, cryogenically-cooled, and fast replenishing jet targets have been developed at SLAC over the past decade [26, 120, 121]. While the cryogenic jet was initially operated with hydrogen, the repertoire of sample cases has been extended to many higher Z gases such as CH_4, CO_2, Ne, Ar and Kr. For the presented work in this thesis, the focus will be on low-Z, hydrogen and deuterium, cryogenic jets. This section will

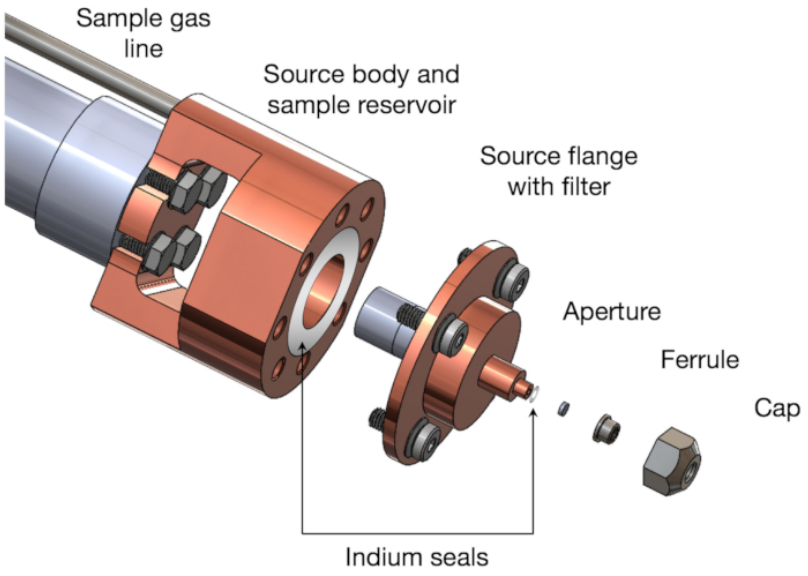

Figure 3.6.: The in-vacuum hardware of the cryogenic jet source assembly consists of a source body, a source flange and a cap. The sample gas is liquefied in the source body and injected into the vacuum chamber through the aperture held by the cap [26].

therefore focus on the operational principles of jets using these two gases.

The main jet hardware consists of a liquid-helium continuous-flow cryostat which cools a hollow copper assembly, called the source, mounted in the vacuum chamber. Figure 3.6 shows an exploded Computer Aided Design (CAD) image of the source assembly. It consists of the source body with the sample reservoir, the source flange with the filter and finally the cap that holds and seals the aperture to the source flange. The low-Z gas is injected into the reservoir in the cold copper assembly, where it is cooled to cryogenic temperatures. When the reservoir is filled, the pressure in the gas line pushes the liquid through the aperture and injects it into the vacuum chamber at speeds around 100 m/s [108]. The aperture, located at the lower end of the source, determines the shape of the jet as it enters the vacuum chamber. Depending on the exact injection speed, the liquid jet solidifies through evaporative cooling a few millimeters below the nozzle. Since the target forms directly inside the vacuum chamber from ultra-high purity gas, cryogenic jets are contaminant-free, single-species and near-critical density targets.

The jet stability, quantified in terms of jitter, is directly influenced by the jet backing pressure and injection temperature. Under stable operating conditions in a laminar flow regime, the jitter increases linearly with the distance from the nozzle [120]. Its position stability was previously characterized at a distance of 10 mm from the aperture to range from 3 to 12 μm [122]. Recently, significantly improved jet stability was shown after optimization of the jet operational parameters and improved vacuum conditions [26]. Vacuum conditions were improved by adding a liquid jet catcher assembly located a few millimeters below the laser-target interaction point. It captures and evacuates the majority of the cryogenic jet target before vaporization to ensure a sufficient vacuum level ($\leq 10^{-3}$ mbar).

To date, three different types of cryogenic jet targets have been demonstrated using the source assembly shown above. As mentioned before, different target geometries are obtained by changing the aperture geometry and aspect ratio. Planar jets are formed using rectangular shaped apertures, cylindrical and droplet targets

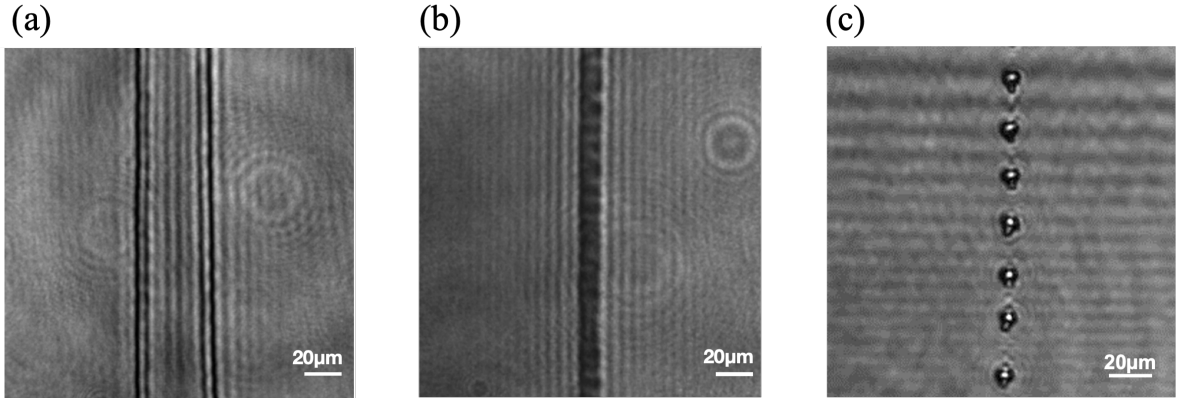

Figure 3.7.: Shadowgraphy images show the three currently available cryogenic jet configurations. (a) Planar jets with accessible dimension of (10 – 40) $\times$ (0.5 – 4) μm. (b) Cylindrical jets with diameters ranging from 2 – 10 μm. (c) Droplet jets with droplet diameters between 10 – 19 μm.

utilize circular apertures. The different target types are displayed in Figure 3.7, with a planar jet shown in (a) and a cylindrical and droplet jet shown in (b) and (c) respectively. Using different aspect ratios for the nozzles, planar jets with dimensions between (10 – 40) $\times$ (0.5 – 4) μm, cylindrical jets from 2 – 10 μm, and droplet jets with diameter from 10 – 19 μm have be generated. For the presented work in Chapter 7, rectangular apertures with an aspect ratio of 4 $\times$ 20 μm were used to produce planar cryogenic deuterium jets. For further details on the characterization and thickness estimated for the analyzed shots, please refer to Chapter 7 directly.

3.2.1. Cryogenic Jet Diagnostics

The cryogenic jet is continuously monitored between shots using four imaging systems with three separate purposes. Two low magnification large FOV imaging lines at 90° from each other monitor a larger section of the cryogenic jet. The focus imaging set up in laser forward direction monitors the jet position in the laser plane and the laser target overlap. Using the same imaging line as the focus imaging, a Michelson interferometer determines the thickness of the planar sheet and the rims of the jet. Figure 3.8 shows an overview of the different imaging lines with example images from the experiment presented in Chapter 7. All four imaging lines are blocked on shot to prevent damages to the imaging lines and cameras.

The low magnification large FOV imaging systems have a magnification of (2 - 5)x, where one imaging system usually has a slightly larger magnification than the other, set at a relative angle of 90°. The FOV is usually on the order of 500 $\times$ 500 μm with the images shown in Figure 3.8 only showing the ROI while the full images is roughly four to five times larger than the ROI. These imaging systems monitor the jet during cool down and the initial liquifying process. For this, the catcher is moved up vertical such that it is visible in the bottom of the frame for both imaging systems and the nozzle is moved down to be visible on the top of the frames. Once the jet has stabilized, the catcher is moved to it's final position and the two FOV imaging lines are used to position the jet at the Target Chamber Center (TCC) which coincides with the focal position of the laser.

The focus imaging set up in laser forward direction is a high resolution (sub-μm per pixel) imaging system using an f/1.6 lens, equivalent to a magnification of 15 - 20. Without the jet, this system is used to inspect and optimize the laser focus and with an operating jet, it allows for precise positioning of the target at the laser focal plane and to monitor the laser focal overlap. Figure 3.4 shows the Texas Petawatt laser focal spot,

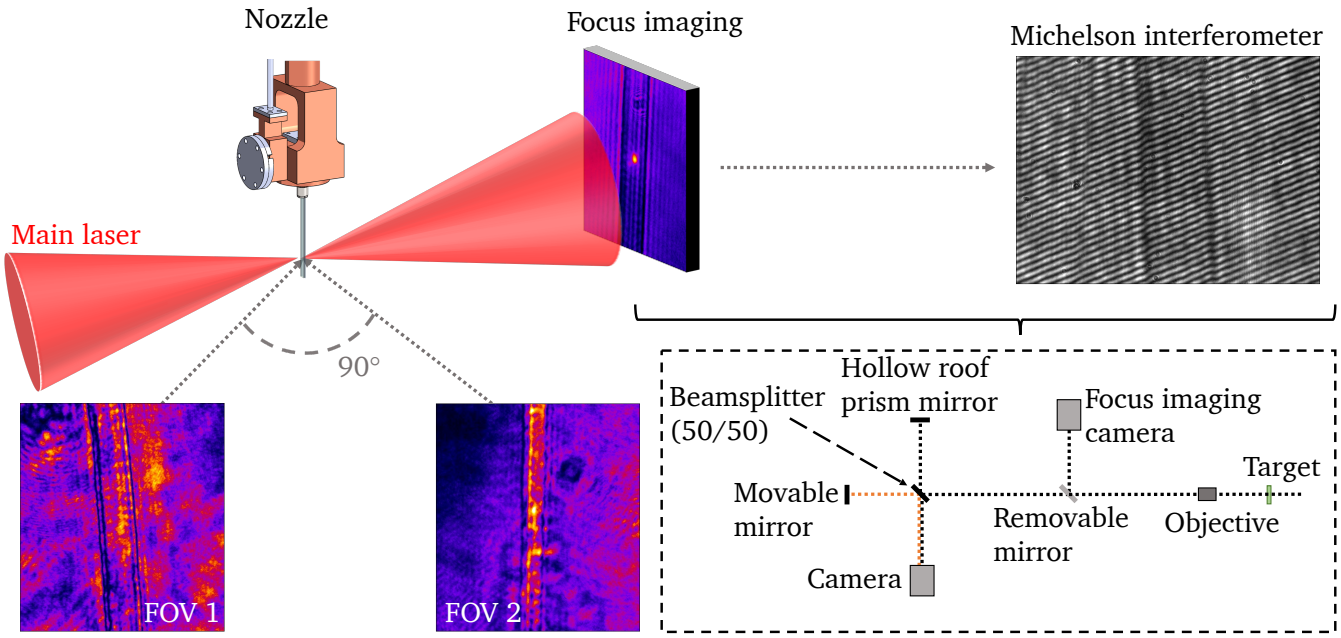

Figure 3.8.: The cryogenic jet is diagnosed using the focus imaging, two larger field of view (FOV) imaging lines at 90° from each other use low power pulses off-harmonic laser to backlight the target. The focus imaging line, which also served the Michelson interferometer, uses either a low amplified focused main beam to inspect the laser focal spot and laser-target overlap or the pinched main laser beam at low amplification as a backlighter for the interferometer measurement. A removable mirror allows switching between the two different diagnostics.

bright spot in the center of the planar cryogenic jet target. A removable mirror enables switching between the focus imaging camera and the Michelson interferometer setup, which is shown in the inset of Figure 3.8.

The Michelson interferometer setup uses a fraction of the image line of the focus imaging. The beam is redirected to the Michelson interferometer setup by removing a mirror in the optical setup. The beam is then split into two beams using a 50/50 beam splitter. The two beam travel along the two independent arms of the interferometer, depicted as black and orange beam paths in the figure. On one arm, the beam is reflected by a movable mirror, while on the other arm, it is reflected using a hollow roof prism mirror. The two beams are overlapped after passing through the beam splitter again. If the two beam paths are exactly the same length, the interference is constructive and fringes are formed as seen in Figure 3.8. The evolution of the spacing and shape of the fringes across the jet allows to measure the thickness of the rims and the planar sheet inbetween the two rims. For angles of incidence close to 90° the phase shift Δ introduced by the jet can be approximated by

$$\Delta = 2\left(\frac{2\pi n d}{\lambda} - \frac{2\pi d}{\lambda}\right) \tag{3.1}$$

with the wavelength λ, the thickness d and the refractive index n [123]. Since the wavelength and the density of the target are known quantities, the phase change can be directly related to the thickness of the target.

4. High Repetition-Rate Deuteron Acceleration from Heavy Water Jets

A key achievement on the way to efficiently using laser-driven ion beams for diagnostics application of short-lived processed or secondary particle generation is the stable acceleration of ions across minutes to hours. This increases the signal-to-noise ratio and the resolution in probing applications and increases the average flux of secondary particle sources. With regards to upcoming high repetition-rate PW laser systems, there is a need to develope and optimize stable target systems that can be efficiently operated at high repetition rates and laser powers.

Using an ambient-temperature liquid heavy water microjet, described in Section 3.1, high repetition-rate (0.5 Hz) laser-driven deuteron acceleration was investigated using the frequency-doubled, high contrast ALEPH laser [124] at Colorado State University (Fort Collins, USA) (CSU). A high repetition-rate compatible Thomson Parabola (TP) spectrometer in target normal direction measured the spectrum of the accelerated deuteron ion beam. Data for three different laser energies on target, 5.5 J, 3.2 J and 1.5 J, was recorded over 60 consecutive shots (2 min) respectively. At a laser energy on target of 5.5 and 3.2 J the shot-to-shot stability of the laser-driven deuteron beam was studied. The stability of the ion beam is quantified using the accuracy of a linear increase of the cummulative sum of the ion beam flux at a given energy by calculating the coefficient of determination R^2. Average deuteron ion spectra for all three laser energies on target were used to investigate the ion beam parameter scaling with laser energy.

In the following, the experimental setup and the working principle of the Thomson parabola as a key diagnostic will be explained. Subsequently, the experimental data will be discussed and compared with existing publications on high repetition-rate laser-driven ion acceleration studies in terms of the ion energy cut-off scaling. The experimental results presented in this chapter have been published in Reference 125 and 116. A short outlook section compares the scaling of the ion cut-off energy extracted from Particle In Cell (PIC) simulations as a function of target thickness and discusses the potential of the ambient-temperature liquid jet target as a suitable platform to study these scalings at high repetition-rate.

4.1. Experimental Setup

The design of the experimental implementation of the liquid heavy water jet target at the ALEPH laser at Colorado State University (CSU) builds on the experimental platform developed for cryogenic liquid jet targets [15, 122, 126–129]. Figure 4.1 shows a simplified schematic of the setup. The frequency-doubled ALPEH Ti:Sapphire laser (400 nm, up to 5.5 J, 45 fs, 0.5 Hz, 7% shot-to-shot energy stability) is focused to a spot size of 1.8 μm (FWHM) diameter using an f/2 off-axis parabola (OAP). Intensities reached up to 1.2×10^{21} W/cm^2 on target, corresponding to a normalized vector potential $a_0 \simeq 12$. A laser contrast of 10^{-12} at -25 ps was achieved through laser pulse cleaning prior and fielding of a laser frequency doubling stage after the compressor.

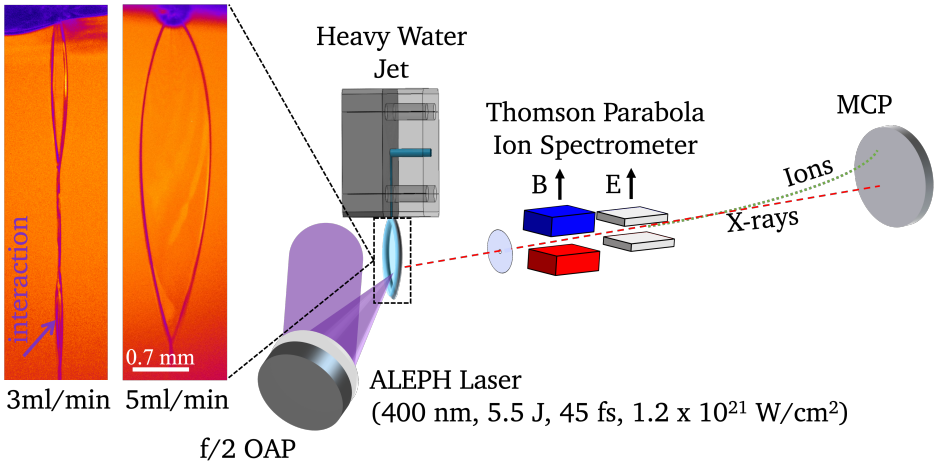

Figure 4.1.: Simplified schematic of the experimental setup for 0.5 Hz deuteron acceleration from a heavy water jet using the frequency-doubled ALEPH laser. A Thomson parabola equipped with a high repetition-rate compatible microchannel plate (MCP) detector was positioned in the laser forward direction.

The heavy water, deuterium oxide (MilliporeSigma (formerly Sigma Aldrich), 99.9%), jet is generated using the tungsten nozzle assembly presented in Section 3.1. It is irradiated by the laser at an incident angle of 45°. To prevent occlusion of the incoming laser by the nozzle assembly, the laser-target interaction point was located 4 mm below the output surface of the nozzle. A primary sheet of this length is generated at a flow rate of around 5 ml/min, which presents a large load on vacuum pumps connected to the chamber. To investigating the behavior and survivability of these nozzles for the first time while minimizing the risk of damaging laser or vacuum equipment, the flow rate was limited to around 3 ml/min. For this given flow rate, the laser interacts with the center of the third consecutive sheet along the fluid chain. Figure 4.1 shows examples of liquid jets at the two different flow rates with the laser-target interaction point marked by the purple arrow. The thickness at the interaction point on the third sheet was inferred to be (5 ± 1) µm. This value was obtained by estimating the jet thickness as a function of nozzle output dimensions using a study conducted by Crissman et al. (Ref. 115) using the same nozzle channel geometry fabricated in glass. Crissman et al. thickness measurment together with insitu shadowgraphy measurements of the liquid jet target and the principle of conversation of flow allowed to determine the thickness on the third sheet. A differentially pumped Thomson Parabola (TP) ion spectrometer, set up in the target normal direction, was used as the primary diagnostic during this experiment to distinguish between different ion energies and charge-to-mass ratios of the accelerated ions.

4.2. Thomson Parabola Spectrometer

Originally developed as a mass spectrometer, a Thomson parabola (TP) spectrometer employs electric and magnetic fields to disperse ions according to their charge-to-mass ratios and energies. These detectors are well suited to measure the energy spectrum and flux of different isotopes in a laser-driven ion beam. To maintain a high resolution, TPs sample a small solid angle, typically a few µsr. The solid angle is determined by the entrance pinhole of the Thomson parabola. Ions passing through the pinhole are displaced by parallel or antiparallel static homogeneous magnetic and electric fields, see Figures 4.1 and 4.2 and drift the distance to the detector assembly after leaving the fields.

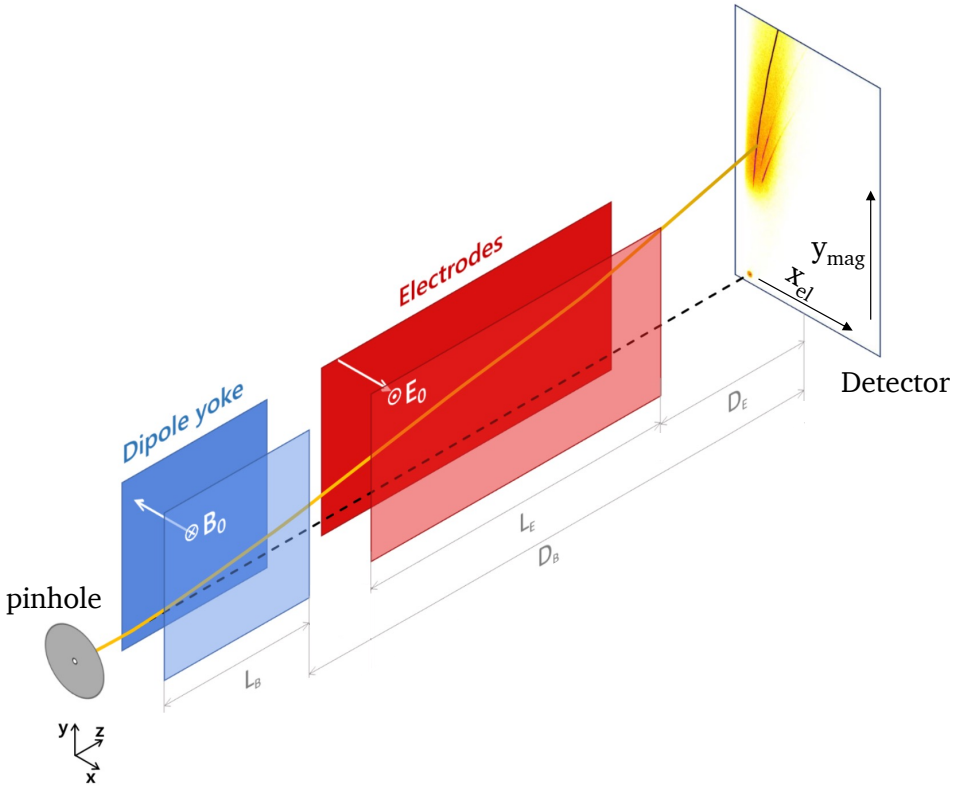

Figure 4.2.: A Thomson parabola consists of a pinhole and as shown here antiparallel, or parallel, electric and magnetic fields. Ions of the different charge-to-mass ratio trace different parabolas in the detector plane. The ions deflected to positions further away from the zero point (dashed line) on the detector have lower kinetic energy, while the deflection of higher kinetic energy ions is smaller. Figure adapted from Ref. 130.

The magnetic field is generated by a permanent magnet and causes a deflection of the charged particle perpendicular to the field lines according to

$$\vec{F}_B = q \cdot \vec{v} \times \vec{B} \quad , \tag{4.1}$$

where q is the ion charge, $\vec{v}$ the ion velocity and $\vec{B}$ the magnetic field. Contrary to that the deflection by the electric field, typically generated using two parallel electrodes, is parallel to the field lines following

$$\vec{F}_E = q \cdot \vec{E} \tag{4.2}$$

with the ion charge q and the electric field $\vec{E}$. Assuming z as the beam axis and the magnetic field and the electric field oriented anti-parallel along the x-axis (see Figure 4.2), the decoupled deflection for the electric and magnetic component are described by

$$x_{\text{el}} = \frac{Z\, e\, E\, L_E \cdot \left(D_E + \frac{L_E}{2}\right)}{2\, E_{\text{kin}}} \quad \text{and} \tag{4.3}$$

$$y_{\text{mag}} = \sqrt{\frac{Z^2\, e^2\, B^2\, L_B^2 \cdot \left(D_B + \frac{L_B}{2}\right)^2}{2\, m\, E_{\text{kin}}}} \quad \text{with} \tag{4.4}$$

the ion charge state Z, the electron charge e, the ion mass m, the kinetic energy of the ion E_{kin}, the magnitude of the magnetic (B) and electric (E) field, the length of the magnetic (L_B) and electric (L_E) field, the drift length after the magnetic (D_B) and electric (D_E) field.

Following equations 4.3 and 4.4 ions with the same charge-to-mass ratio $q/m = Ze/m$ will trace the same parabola in the detection plane. The reference point for the deflection measurement, called zero point, is defined by the interaction point of the trajectory of all neutral particles and photons through the field with the detector, see dashed line in Figure 4.2. Since the deflection scales inversely with the kinetic energy of the ions, higher energetic particles experience a smaller deflection. Consequently, high energy particles will appear closer to the zero point, while low energy ions are deflected further away from the zero point. The drift section between the magnetic and electric assembly and the detector plane determines the magnitude of the deflection and with this the length of the parabolas on the detector. Shorter drift sections are typically used to resolve energies on the order of a few MeV, while larger drift sections are employed to resolve energies in the range of 10's of MeV.

The parabolas observed in the detection plane can be recorded using different types of detector units, which are typically chosen based on the need of the experiment. For single shot experiments, ion traces are usually recorded using an Image Plate (IP) [131]. However, IPs must be read out using a nonconfocal phosphor scanner, such as the Typhoon FLA 7000, and are consequently not suitable for high-repetition-rate operation. To adapt to high repetition-rate operation, a combination of a MicroChannel Plate (MCP) with a scintillator and a fast, gated camera are commonly used. These types of detectors are limited in repetition-rate by the dead time of the detector unit and the frame rate of the optical camera, but can sustain repetition rates beyond the 10 Hz level. In the experiments presented in this work both types of detector units were employed to measure the deflected ion beam. Their individual detection principles are explained below.

4.2.1. Microchannel Plate Detector Assembly

A MCP is a cluster of 10^4-10^7 individual miniature electron multipliers that are oriented parallel to one another as shown in Figure 4.3. The channels are angled 8° with respect to the surface normal direction and each of the channels of the Hamamatsu model (F1942-04) used in this work has a diameter of 25 µm. The channel matrix is usually fabricated from lead glass and treated to optimize the secondary electron emission characteristics.

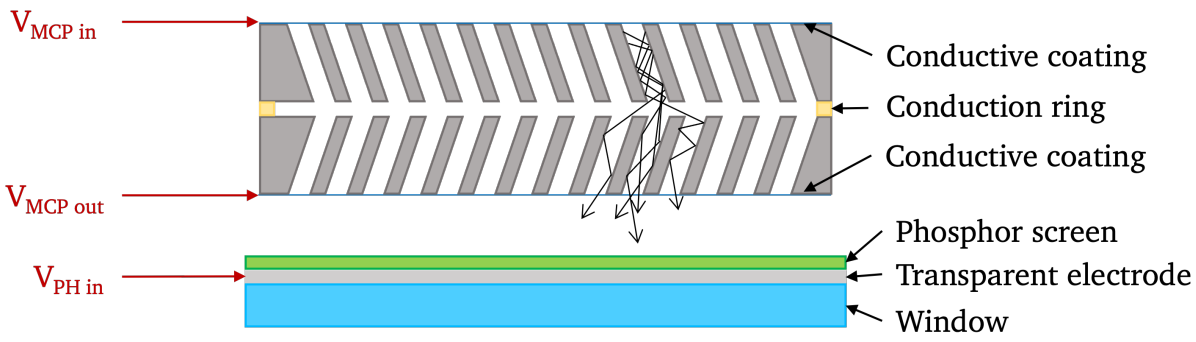

Figure 4.3.: A MCP is an assembly of many electron multipliers. When an ion hits the MCP material several electrons are liberated, which are amplified in one of the electron multiplier channels starting an electron cascade that is detected as an output signal at the end of the channel. Figure adapted from Ref. 132.

Furthermore, the channel walls are semiconducting to allow charge to replenish from an external voltage source applied to the front and back of the MCP assembly ($V_{MCP\ in}$ and $V_{MCP\ out}$). MCPs can be purchased as a single stage amplifier, or a multi-stage amplifier unit. The MCP used for the presented experiments is a double stage MCP with two channel matrices mounted in a chevron configuration, meaning the channels of the second stage are tilted the opposite way compared to the first stage. This configuration reduces background noise in the MCPs, which are directly sensitive to charged particles and energetic photons.

When an ion impinges on a channel wall it causes the emission of secondary electrons, which are accelerated by a voltage applied across the MCP. This voltage is typically varied between 1-5 kV. On their way through the channel the electrons multiply by generation of additional secondary electrons in the channel wall through a cascade process as illustrated in Fig. 4.3. Based on this principle the minimum signal gain of the MCP is 10^4 for an applied voltage of 1 kV. The precise gain for given experimental conditions is dependent on the applied voltage, the operation temperature and vacuum of the MCP assembly. After an electron cascade has depleted all the electrons of predominantly the last 20% of the channel wall along the channel, the channel takes time to recover/ recharge before it can detect another signal. This time interval is called dead time and is usually on the order of 10^{-2} s for each channel. Since an MCP consists of an average of 10^5-10^6 channels, the effective dead time of the plate is $10^{-7} - 10^{-8}$ s [133]. In addition to a fast recovery time, MCPs also exhibit excellent timing properties in terms of response, which is due to the short transit time of electrons through the channel, only a few nanoseconds. This is much faster than decay times of phosphor screens or read out speeds of CCD cameras [133–136].

After the electrons leave the MCP, they gain energy due to a potential generated by the voltage ($V_{PH\ in}$) applied to the electrode connected to the phosphor screen, an inorganic scintillator. The valence band and the conduction band of an inorganic scintillator are separated by forbidden states which are never occupied, i.e. the band gap. Small amounts of impurities, activators, are added to the lattice. These activator centers locally modify the band structure of the crystal by adding allowed energy states in the band gap, see Fig. 4.4. When the electrons generated in the MCP impinge on the scinitillator, electron-hole pairs are formed. These pairs either travel through the scintillator separately or as an exciton, a bound electron-hole pair. For independent migration of the electron and hole, the hole can ionize an activator center. Once a free electron encounters such an ionized activator it drops into this activator site. The created excited activator state decays under emission of a scintillation photon of a given wavelength. Typical half-lives of any excited activator state are 50 - 500 ns. [134, 135, 137]. The scintillation light emission spectrum is determined by the energy structure of the activator. Usually the transition energy is around 3 eV, as a consequence the emitted light is part of

Figure 4.4.: An inorganic scintillator has a valence and a conduction band. Additional energy levels are made available in the band gap through doping the material with so called activators. These levels are usually passed when deexcition of the atom from the conduction band occurs in the local impurity regions of the activators. The transitions between the added energy levels in the band gap are the scintillation transitions, that result in the emission of a scintillation photon, that is later detected by the CCD camera. Figure adapted from Reference 134.

the visible spectrum [134]. One distinguished two different types of scintillation namely fluorescence and phosphorescence. Fluorescence describes the prompt emission of visible or ultraviolet (UV) radiation from a material. Phosphorescence generally shows slower emission of light and longer wavelength of the emitted light. To capture all emitted scintillation photons, the acquisition time window of the camera used to capture the light therefore needs to accommodate for the different decay times.

Note, that each individual combination of scintillator/MCP and camera for a given experimental setup requires a separate response calibration to be able to relate the number of incident ions to the recorded pixel value.

4.2.2. Image Plate

For single shot experiments, where repetition-rate compatible detector units are not essential, the deflected ion beam is commonly detected using image plates (IPs) (Fujifilm, Tokyo, Japan) [138–140]. The size and shape of the detector is adaptable as they can be purchased in larger size and then cut to the desired format. Typically, BAS-MS (multipurpose standard) and BAS-TR (tritium) image plates are used for ion detection with four (BAS-MS) or three (BAS-TR) layers total. Table 4.1 gives an overview of the different layers and their composition, density and thickness. The sensitive layer of image plates is the europium-ion (E^{2+}) doped phosphor layer. Incoming ions transfer energy to the Eu^{2+} dopant, which creates a free electron and Eu^{3+}. The free electron is then trapped by FBr or FI to form the metastable state FBr^{-} and FI^{-} respectively. The number of created electrons and thus metastable states is proportional to the energy loss of the ionizing particle in the sensitive layer and consequently to the total number of incident particles. Compared to the BAS-TR type mage plate, the BAS-MS image plate has an added protective layer which prevents protons with energies lower than 650 keV to reach the sensitive layer [141, 142]. A magnetic layer at the back of each image plate facilitates mounting for readout purposes.

Due to the difference in the thickness of the sensitive layer, the response of the BAS-MS image plate is roughly a factor of 2-4 higher than the response of the BAS-TR image plate [143]. On the other hand, due to the additional protective layer, the sensitivity of the BAS-MS image plate to protons with energies below 10 MeV starts to decline and drops to 0 at an incident proton energy of 650 keV. BAS-TR image plates benefit from the lack of this protective layer and show a constant sensitivity across the few MeV proton energy range [143]. For both image plates an energy dependent sensitivity, with a rapidly decreasing sensitivity towards higher

	TR			MS		
	composition	density [g/cm^3]	thickness [μm]	composition	density [g/cm^3]	thickness [μm]
Protective				C_2H_2O	1.66	9
Phosphor	C_{ph}	2.85	50	C_{ph}	3.31	115
Support	C_2H_2O	1.66	250	C_2H_2O	1.66	190
Magnetic	C_{mag}	2.77	160	C_{mag}	2.77	160

$C_{ph} = BaFBr_{0.85}I_{0.15}:Eu^{2+}$
$C_{mag} = ZnMn_2Fe_5NO_{40}H_{15}C_{10}$

Table 4.1.: Composition and thicknesses of BAS-MS and BAS-TR image plate layers [141]. Both detectors consist of a magnetic, a support, and a phosphor (ion sensitive) layer. The BAS-MS image plate has an additional protective layer.

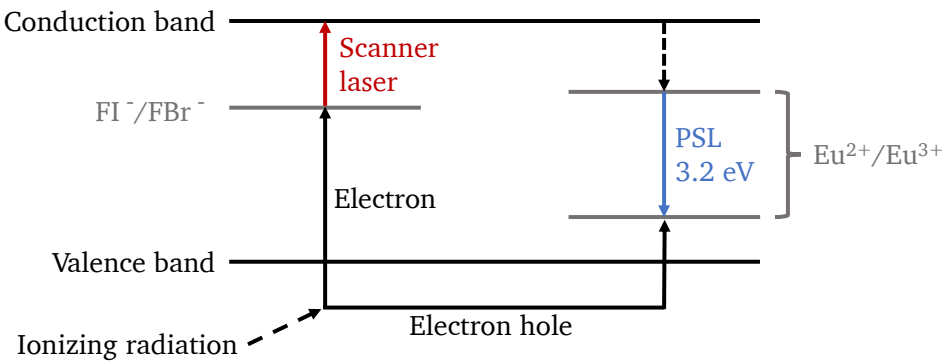

Figure 4.5.: Ionizing radiation incident on the active layer of an image plate generates an electron-hole pair. The hole further ionizes a europium ion to Eu^{3+} while the electron is trapped in a metastable FBr^{-} and FI^{-} state. When illuminated with the red scanner laser light, the electron is lifted into the conduction band and will deexite at a europium ion location under emission of a 3.2 eV Photo-Stimulated Luminescence (PSL) photon.

incident proton energies ($>$ 100 MeV) is observed. Due to the higher sensitivity in the few MeV range, BAS-TR image plates are commonly used as detector units in laser-driven ion acceleration experiments [144].

The spatially encoded signal recorded by the image plates is read out using the principle of photo-stimulated luminescence (PSL). When the previously exposed image plate is illuminated with coherent light (635 nm, 2.1 eV), the electrons trapped in the meta-stable FBr^{-} and FI^{-} states are excited to the conduction band. Upon encounter of an ionized dopant Eu^{2+} or Eu^{3+} electrons from the conduction band will deexcite under emission of a PSL photon (3.2 eV, 390 nm). A non-confocal phosphor scanner, such as the Typhoon FLA 7000, is used to illuminate the image plate and collect the emitted light with a given resolution. Here, the number of PSL read by the scanner is directly related to the number of impinging particles in each pixel. During the readout process the scanner rasters the surface using a chosen resolution setting, as small as 25 x 25 μm^2. A photomultiplier collects the emitted light and records and saves the value to the pixel to a readout file. In order to minimize the loss of the PSL induced by white light, the measurements are carried out in a dark room. Additionally, the time interval between image plate irradiation with ions and the scanning of the IP is recorded to account for the fading of the signal. After the measurement the IPs are erased through exposure to white light [141, 142].

4.2.3. Thomson Parabola Setup during this Experiment

During the experiment described in this chapter, the Thomson parabola used a 500 μm diameter pinhole located 1.1 m away from the target with a corresponding solid angle of 0.16 μsr. A 0.53 T magnetic field and a 0.83 kV/m electric field separated the accelerated ions based on their charge-to-mass ratio and energy. In the detector plane, the ion signal was recorded using an MCP detector assembly. For our geometry and field strengths, the minimum resolvable deuteron energy is $\sim$0.2 MeV, constrained by the size of the MCP.

The absolute response of the TP was calibrated using a solid state nuclear track detector, allyl diglycol carbonate (CR-39). A 1 mm thick piece of the nuclear track detector CR-39, cut into a series of 2 mm wide bars separated by 2 mm wide gaps, was placed 4 cm in front of the MCP for a single shot. Ions impinging on the bars of the CR-39 leave a track of broken molecular chains along their trajectory through the material [145, 146]. The signal of the ions passing through the gaps is recorded using the MCP assembly. Exposing the irradiated

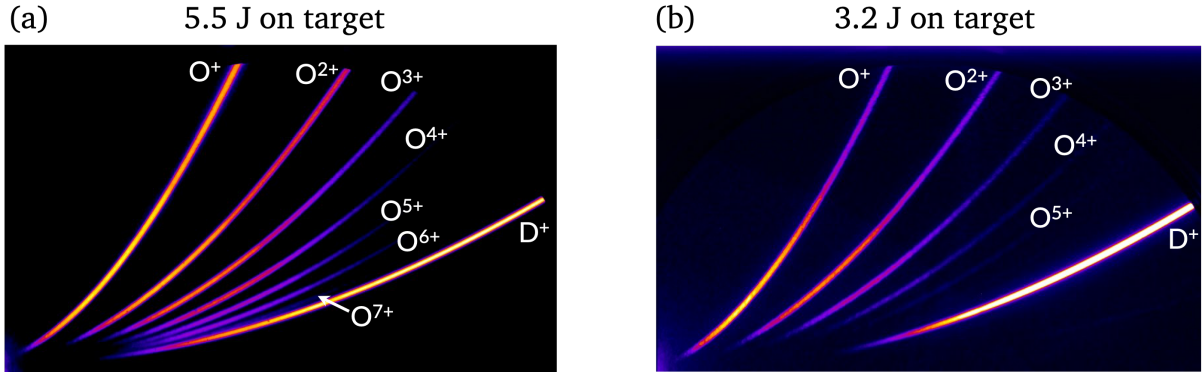

Figure 4.6.: Sum of all 60 consecutive raw TP images for 5.5 J, (a), and 3.2 J, (b), on target. Oxygen charge states up to O^{7+} are accelerated for 5.5 J on target while a maximum oxygen charge state of O^{5+} is observed for 3.2 J on target.

CR-39 to sodium hydroxide post experiment slowly dissolved the plastic polymer in undamaged spots, while damaged spots are etched away faster, identifiable as dark pits [147]. The total number of ions is counted on each bar allowing to calculate the impinging flux of ions on the CR-39 [148]. Comparing the ion numbers detected on the CR-39 with the signal levels on the MCP establishes an ion energy dependent conversion factor from particles to counts. This established conversion factor can then be applied to the signal level detected by the MCP to convert count levels to ion flux with an uncertainty of 20%.

4.3. Experimental Results

For a laser energy of 5.5 and 3.2 J on target, 60 consecutive shots were recorded in laser forward direction at a repetition-rate of 0.5 Hz. Summing over all raw recorded TP images on shot for the two laser energies shows the degree of ionization of the target and the accelerated species. The sum of the raw TP images for the two runs are shown in Figure 4.6. As can be seen, the different charge-to-mass ratios trace different parabolas on the camera image and consequently allow to distinguish between different charge states of oxygen and deuterons. The zero point of the TP is located outside of the frame shown in the figure, but was previously recorded for precise energy determination of the pixels along the individual parabolas.

Oxygen charge states up to O^{6+} are routinely detected for 5.5 J on target while O^{7+} is only observed on a limited number of shots, see arrow in Figure 4.6 (a). The degree of ionization of the oxygen atoms present in the target decreased as expected with the laser energy on target. Figure 4.6 (b) shows oxygen charge states up to O^{5+} for a laser energy of 3.2 J on target.

For further evaluation, the presence of O^{8+} needs to be investigated. Due to the same charge-to-mass ratio of O^{8+} and D^{+}, the two ions would trace the same parabola in the detection plane. Since O^{8+} is much heavier than D^{+}, the oxygen ions would be deflected much less and artificially increase the cut-off energy measured when taking the lineout of the D^{+} trace. The raw TP images in Figure 4.6 suggest, that O^{8+} ions were not present in the accelerated ion beam. This was confirmed by the CR-39 calibration measurement, which can distinguish between different ion species. Due to their higher mass, O^{8+} ions will create larger tracks on the CR-39, which allows us to tell O^{8+} and D^{+} ions apart. Figure 4.7 on the right shows one of the etched bars of the CR-39 corresponding to a center deuteron energy of 0.49 MeV. The observed tracks are all the same size and can solely be attribute to deuterium. The contribution of O^{8+} is therefore considered negligible.

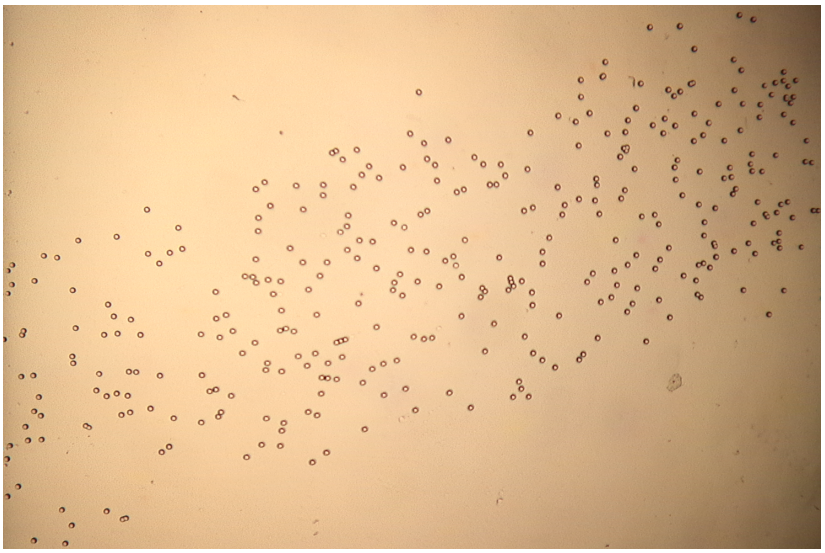

Figure 4.7.: Microscope image of one bar of the CR-39 after four hours of etching. Observed tracks are all the same size and can be attributed to deuterons ($\sim$ 0.49 MeV) with no presence of O^{8+}.

The shot-to-shot stability of the deuteron spectrum is investigates using a waterfall plot, see Fig. 4.8, which displays the 60 consecutive deuteron spectra for both 5.5 J (120 TW) and 3.2 J (70 TW) on target. For the 5.5 J laser energy on target run, one can distinguish between a high yield, high energy range, shot 15 to 40, and a lower yield, lower energy range for the remaining shots. Deuteron cut-off energies up to 4.4 MeV and fluences up to 2×10^{11} deuterons/MeV/sr are consistently observed for high yield shots. Low yield shots reach cut-off energies of up to 2.0 MeV and fluences just below 1×10^{11} deuterons/MeV/sr. The observed fluctuations in deuteron cut-off energy and fluence indicate a change in the laser-target interaction. A possible explanation for this could be target instabilities, either influenced by short-lived vacuum fluctuations or by the nozzle quality. At lower laser energy on target, 3.2 J for the subsequent run, improved stability at lower cut-off energies (1.25 MeV) and fluence ($< 1\times10^{11}$ deuterons/MeV/sr) is observed. For shots 1 to 50, the cut-off energy and fluence of the deuteron beam fluctuates by only a small amount, while a decrease in cut-off energy and peak deuteron fluence is observed for shots 50 to 60. Similar to the previous run, this suggests a change in the interaction conditions of the laser with the target. Both data sets show fluences of around 10^{10} deuterons/MeV/sr per shot for energies up to 40% of the cut-off energy. At a repetition-rate of 0.5 Hz, this single shot fluence corresponds to an average fluence of 3×10^{11} deuterons/MeV/sr/min.

An ideal pulsed deuteron source maintains a stable fluence of particles at a certain energy over minutes to hours. This enhances the predictability of the total delivered charge and minimizes measurement uncertainties due to fluence fluctuations. This fluctuation in fluence can be quantified by calculating the cummulative yield across the acquired shots, which should linearly increase with time for the case of an ideal source. For the two previously presented runs at 5.5 and 3.2 J on target the cummulative sum was calculated at deuteron energies of 0.25 and 1 MeV. Figure 4.9(a) and (b) show the cummulative sum (black), the corresponding linear fit (red for 5.5 J and blue for 3.2 J), and the 2σ confidence interval (grey). At a deuteron energy of 0.25 MeV a narrow confidence interval supports the assumption of an ideal pulsed source. For 1 MeV deuteron energy, (b), the cumulative sum diverges more significantly from the desired linearly increasing trend, as shown by the fluctuating cummulative sum and the resulting larger confidence interval. The measured deuteron fluence appears to oscillate between a low- and a high-yield mode across the full spectrum, especially visible for deuteron energies close to the cut-off. The long oscillation period of about 1.5 min, as can be seen in

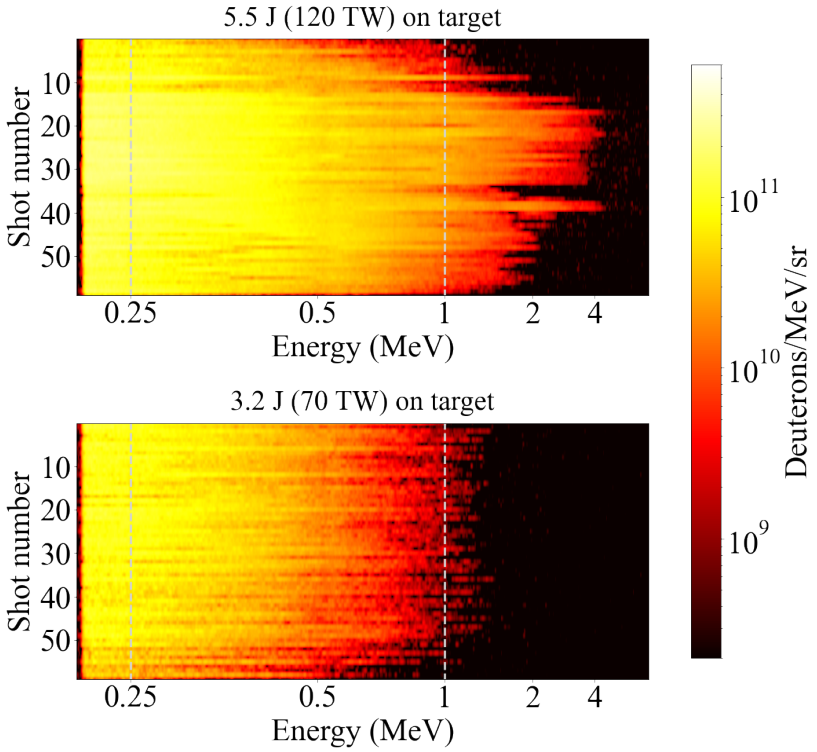

Figure 4.8.: Deuteron energy spectra for laser energy of 5.5 J (top) and 3.2 J (bottom) on target for 60 consecutive shots recorded at 0.5 Hz. The fluence in units of deuterons/MeV/sr is indicated by the color bar. For 5.5 J laser energy on target, maximum cut-off energies and peak fluences of up to 4.4 MeV and 2×10^{11} deuterons/MeV/sr are reached. A lower laser energy on target of 3.2 J results in lower cut-off energies up to 1.25 MeV and fluences below 1×10^{11} deuterons/MeV/sr. Fluctuations in terms of deuteron energies and peak fluences are likely caused by a change in the laser-target interaction.

the left plot of Fig. 4.9 (b), cannot be attributed to noise or measurement uncertainties. As pointed out before, they are likely caused by changing target orientation or thickness fluctuations of the liquid sheet resulting in a change in the laser-target interaction. Future efforts will focus on exploring different machining techniques, nozzle materials and designs for access to different water jet thicknesses and enhanced target and thus deuteron beam stability.

For a more quantitative assessment of the accuracy of the assumption of a linear increase of the cumulative sum, we calculate the coefficient of determination

$$R^2 = 1 - \frac{\sum_i (y_i - f_i)^2}{\sum_i (y_i - \overline{y})^2} \quad , \tag{4.5}$$

where y_i are the data values, f_i are the linear fit values and $\overline{y}$ is the average value of the data in Figure 4.9 (c). Data points above 3 MeV (marked red squares) for 5.5 J on target were excluded from the respective fit, as more than 75% of the shots delivered no dose at those energies. The experimental data shows an $R^2 > 0.96$ for deuteron energies up to 0.75 MeV for both laser energies on target. While the R^2 value for 3.2 J on target stays almost constant below 60% of the average cut-off energy for that run, the R^2 value for 5.5 J on target starts decreasing notably at 10% of the average cut-off energy. The drop-off in stability towards higher

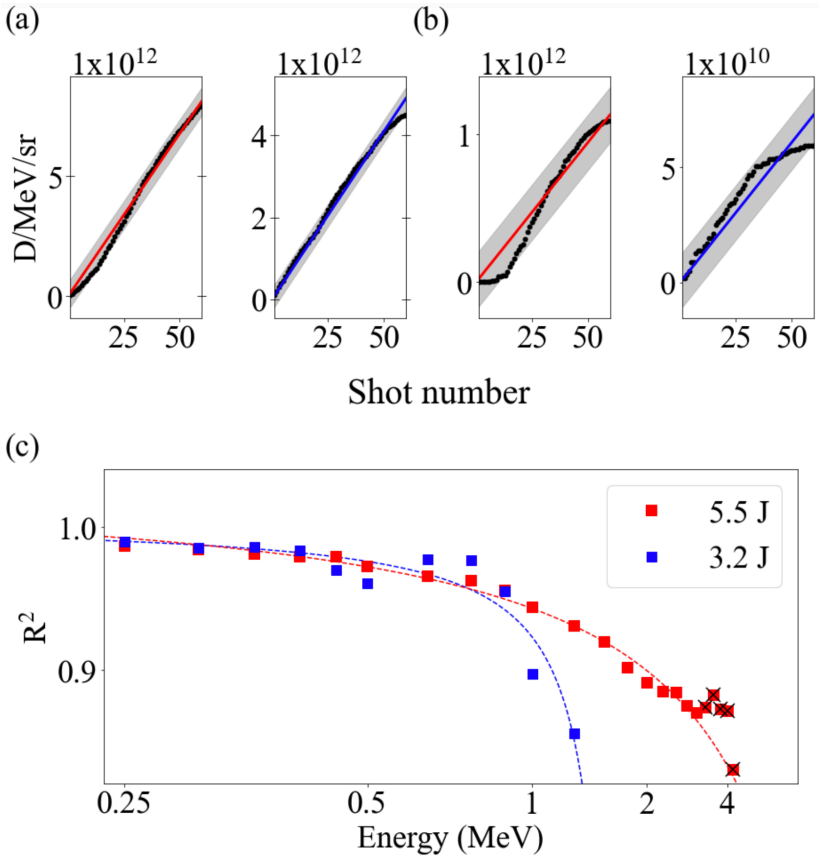

Figure 4.9.: Cumulative sum of deuterons at (a) 0.25 MeV, and (b) 1 MeV for 60 consecutive shots (black). The solid red and blue lines are linear fits for 5.5 and 3.2 J on target, respectively. A grey shaded region indicates the 95% confidence limits of each fit. (c) Characterization of the accuracy of a linear fit as a function of energy for 5.5 (red) and 3.2 J on target (blue) using the coefficient of determination R^2.

energies is much more gradual than the sharp drop off in stability for the 3.2 J on target run. This supports the conclusion of a more stable run for 3.2 J laser energy on target.

An additional run of 60 consecutive shots at a repetition rate of 0.5 Hz recorded the deuteron spectrum for 1.5 J laser energy on target. The evolution of the deuteron cut-off energy was studied as a function of the incident laser power by calculating the average deuteron energy spectrum for laser energies on target of 1.5 J (35 TW), 3.2 J (70 TW), and 5.5 J (120 TW) for 60 consecutive shots. The fast replenishing nature of the heavy water jet and ability to operate the jet target for multiple individual consecutive measurements without interruption enabled continuous data acquisition to ensure the target parameters were comparable between measurements. Fig. 4.10 shows the average spectrum and the fluence and standard error at selected deuteron energies for the three consecutively recorded runs. For all laser energies on target the spectrum exhibits a semi-Maxwellian distribution with deuteron cut-off energies of 0.6, 1.25 and 4.4 MeV for 1.5, 3.2 and 5.5 J on target respectively. The calculated error bars for the low-power laser shots (35 TW, orange) are larger compared to higher laser power on target. This can be explained by the low signal levels on the MCP, which are close to the noise threshold, making signal discrimination more difficult. Calculated as a percentage of the average fluence, the standard error at a sample energy of 0.25 MeV is 21% for 1.5 J, 2% for 3.2 J and 4% for 5.5 J on target and at a sample energy of 1 MeV it is 9% for 3.2 J and 12% for 5.5 J.

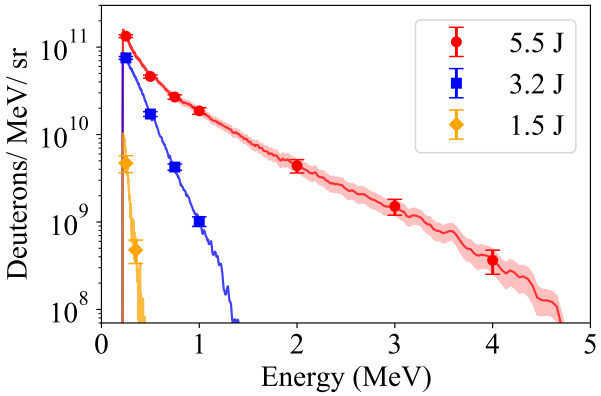

Figure 4.10.: Average fluence for 5.5 (red), 3.2 (blue) and 1.5 J (orange) laser energy on target calculated from 60 consecutive shots at 0.5 Hz. The error bars and shaded regions depict the standard error range of the shot series for each energy.

Previous single shot experiments using Ti:sapphire laser systems with comparable parameters ($<10^{21}$ W/cm^2 on target ($a_0<12$), 30 fs pulse duration and micrometer thick solid-density targets) have investigated the dependence of proton cut-off energies as a function of laser energy on target [149, 150]. Table 4.2 gives details of the individual experimental parameters for the three experiments. While laser pulse duration and energy on target vary within the same order of magnitude, the main differences in terms of laser parameters on target are the laser wavelength, the intensity on target and the picosecond laser contrast. This work used a frequency-doubled Ti:Sa laser, the other two studies used the fundamental laser wavelength at 800 nm. Furthermore the intensity on target and laser contrast differed by up to two and four orders of magnitude respectively. However, as the laser amplitude a_0 shows, the maximum value achieved during experiments is an a_0 of 12 with the same maximum laser amplitude for the work bei Zeil et al. and this work. Another main difference are the target composition and thicknesses. Zeil et al. used metal foils of 5 µm thickness, while Noaman-ul-Haq used VHS (plastic) tape with 15 µm thickness.

For each individual experiment the laser intensity on target I_L was varied by adjusting the laser energy while keeping the laser spot size constant. The individual data points for the three experiments are plotted in Figure 4.11. For better comparison, the data is shown as a function of the laser intensity and the wavelength squared ($I_L\lambda^2$) to account for the difference in wavelength and intensity of the individual experiments. We observe

	this work [125]	Zeil 2010 [95]	Noaman-ul-Haq 2018 [150]
laser wavelength [nm]	400	800	800
laser pulse duration [fs]	45	30	30
laser energy [J]	1.5 – 5.5	0.3 – 3	0.3 – 1.5
laser intensity [W/cm^2]	$<1.2\times 10^{21}$	$<3.1\times 10^{20}$	$<5\times 10^{19}$
laser amplitude a_0	<12	<12	<5
picosecond laser contrast	10^{-12}	5×10^{-9}	10^{-8}
target (thickness)	D_2O (5±1 µm)	metal foils (5 µm)	VHS (15 µm)

Table 4.2.: On target laser and target parameters of experiments comparable to this work.

a difference in terms of cut-off energy for given laser intensities between previously published work. This discrepancy can in parts be explained by the different wavelengths of the laser as 400 nm laser light has a lower coupling efficiency than 800 nm. Additionally the exceptionally high laser contrast of the frequency-doubled ALEPH laser can be beneficial in cases, however a small prepulse has also been shown to boost the ion cut-off energy [151]. Additionally, this work employs a target with a slightly lower density compared to the other two works.

To investigate the scaling of the ion cut-off energy, the data sets were fit separately using a scaling with the normalized laser amplitude a_0 following $E_{max} \propto a_0$. This scaling was deduced from the theoretical works by Mora and Wilks et al. [6, 88]. Following Mora's model of expansion of a plasma into vacuum, the maximum achievable ion energy E_{max} can be calculated using

$$E_{max} \simeq E_0 \left[ln(2\tau)\right]^2 \quad \text{with} \tag{4.6}$$

$$E_0 = Zk_BT_e \quad \text{and} \quad \tau = \omega_{pi}t/\sqrt{2e} \tag{4.7}$$

with Z the ion charge number, k_B the Boltzmann constant, T_e the electron temperature, ω_{pi} the ion plasma frequency, e the electric charge [88]. Consequently the maximum ion energy is proportional to the hot electron temperature T_e. Wilks et al. found a dependence of the hot electron temperature on the poderomotive potential U_p, which in turn depends on the normalized laser amplitude a_0 following

$$T_e \simeq mc^2 \left(1 + \frac{2U_p}{mc^2}\right)^{1/2} \quad \text{with} \tag{4.8}$$

$$U_p[\text{eV}] = 9.33 \times 10^{-14} I[\text{W/cm}^2]\lambda^2[\mu\text{m}^2] \quad \text{and} \tag{4.9}$$

$$a_o = \sqrt{\frac{I_L[\text{W/cm}^2]\ \lambda_L^2[\mu\text{m}^2]}{1.37 \cdot 10^{18}\text{W/cm}^2\mu\text{m}^2}} \tag{4.10}$$

with the laser intensity I_L and laser wavelength λ. Combining equations 4.6 - 4.10 we find that the ion maximum energy E_{max} scales linearly with a_0 through $E_{max} \propto T_e \propto a_0$ [6, 72, 88].

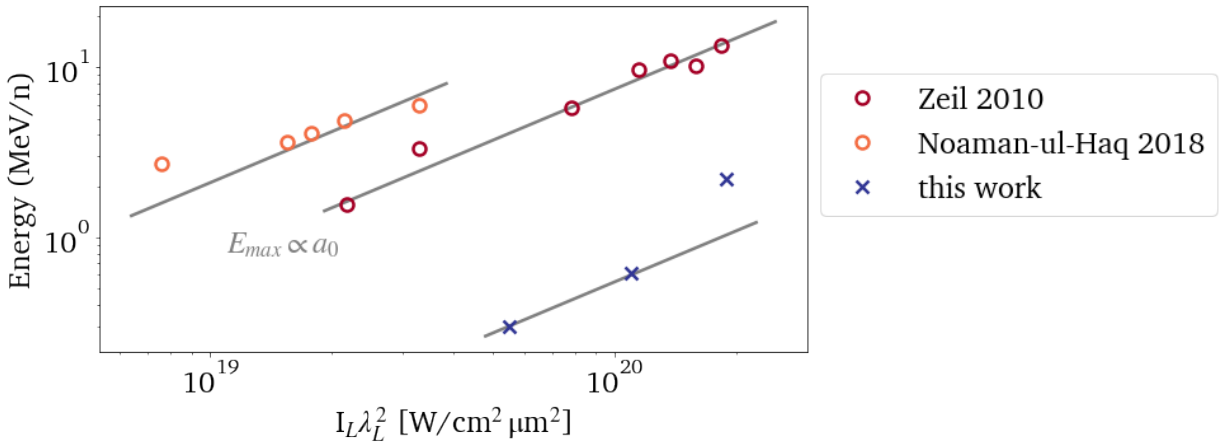

Figure 4.11.: The cut-off energies (MeV/nucleon) in this work (blue cross) shows a more favorable trend with laser intensity compared to other observed scalings in by Zeil et al. [95] and Noaman-ul-Haq et al. [150] using similar laser parameters. Grey lines are fits scaling with the normalized laser amplitude a_0.

The three data sets were individually fitted using that linear dependency on a_0 and resulting fits are shown in grey in Figure 4.11. Comparing the scaling of cut-off energies with laser intensities on target, a linear trend and good agreement with the $E_{max} \propto a_0$ scaling can be observed for the works of Zeil and Noaman-ul-Haq. While the two data points at lower energy for this work also agree with this scaling, the high laser energy on target data point shows a significant deviation from that trend and indicates a more favorable, potentially more exponential than linear, trend with increasing normalized laser amplitude. Future investigations will aim to understand the relative discrepancies in terms of cut-off energies compared to other studies using comparable laser parameters and an optimized target thickness.

Focusing more specifically on the high repetition-rate aspect of this experiment, Table 4.3 presents a summary of previously published work on high repetition-rate laser-driven ion acceleration. They are sorted by year and compared based on the laser parameters, second column, including repetition rate, energy and intensity on target. The third column summarizes the ion beam acceleration performance by stating the accelerated ion species, the maximum achieved energy and the average flux. Dashed lines in the flux column represent uncalibrated ion data which prevents a flux calculation.

As can be observed in the table, this work presents the first stable, 0.5 Hz deuteron source delivering 5×10^{10} deuterons/sr/pulse (1.5×10^{12} deuterons/sr/min) over 60 shots (two minutes) and a maximum deuteron energy of 4.4 MeV using a 120 TW laser. All other studies reporting on high repetition-rate ion acceleration have so far solely investigated the acceleration of protons using various laser systems and varying laser parameters. Previous experiments at higher repetition rate but significantly lower (sub-J) laser energies on target resulting in sub-MeV proton energies [114, 152] reach comparable average fluxes to the ones presented here. Another experiments reaching similar fluxes is presented by Gauthier et al. [126], where the same average flux is achieved at a higher repetition rate of 1 Hz using cryogenic liquid jet targets to produce protons up to 6 MeV. The data presented earlier demonstrates consistently higher peak ion flux at MeV energies, exceeding the flux presented by Gauthier et al. [126] by a factor 1.5 per shot and thus promise higher average fluxes when operated at a higher repetition-rate.

Paper details			Laser parameters			Ion parameters		
Year	First author	Journal	Rep. rate (Hz)	Energy (J)	Intensity (W/cm^2)	Species	Max. energy (MeV)	Flux (#/sr/ min)
2002	P. McKenna	Rev. Sci. Instrum.	<10	< 0.2	$< 10^{19}$	H^+	1.5	$* \sim 10^{10}$
2003	T. Fujii	Appl. Phys. Lett.	<10	0.088	6.8×10^{18}	H^+	1.2	–
2003	I. Spencer	Physical Review E	2	0.2	$< 10^{19}$	H^+	1.5	$* \sim 10^{10}$
2009	B. Hou	Appl. Phys. Lett.	500	0.003	2×10^{18}	H^+	0.5	$\sim 10^{12}$
2009	A. S. Pirozkhov	Proc. of SPIE	1	1	1×10^{20}	H^+	4	$* \sim 10^{11}$
2017	M. Gauthier	Appl. Phys. Lett.	1	3	5×10^{20}	H^+	6.5	$\sim 10^{12}$
2017	M. Noaman-ul-Haq	Phys. Rev. Accel. Beams	0.2	2	$\sim 6 \times 10^{19}$	H^+	6	–
2017	S. Goede	Phys. Rev. Lett.	1	3	5×10^{20}	H^+	6.5	$\sim 10^{12}$
2018	J. T. Morrison	New J. Phys.	1000	0.011	5×10^{18}	H^+	2	$\sim 10^{11}$
2018	M. Noaman-ul-Haq	Nuclear Inst. and Methods in Physics Research	0.2	1.5	5×10^{19}	H^+	6	–
2018	M. Noaman-ul-Haq	Nuclear Inst. and Methods in Physics Research	~ 1	2	$\sim 10^{20}$	H^+	4.5	–
2019	B. Aurand	Phys. Plasmas	5	0.7	10^{20}	H^+	0.065	$* \sim 10^{12}$
2019	Y. Gershuni	Nuclear Inst. and Methods in Physics Research	0.2	0.5	$\sim 10^{19}$	H^+	2	$\sim 10^{11}$
2022	P. Puyuelo-Valdes	Plasma Phys. Control Fusion	< 1	4	4×10^{19}	H^+	3.5	$* \sim 10^{11}$
2022	F. Treffert	Appl. Phys. Lett.	0.5	5.5	1.2×10^{21}	D^+	4.4	$\sim 10^{12}$

* estimated from spectrum in published work

Table 4.3.: Summary of previously published work on high repetition-rate laser-driven ion acceleration [105, 112, 126, 150, 152–161].

4.4. Ion Beam Optimization

Converging liquid jets present an ideal platform for methodical ion acceleration performance optimization by leveraging the accessibility of thicknesses ranging from 10s of micrometer down to sub-micrometer. The liquid jet thickness range of interest can be adjusted by changing the appropriate channel geometry [111, 115]. Along the liquid sheet different thicknesses can be accessed by vertical translation of the liquid jet nozzles. This capability provides access to different ion acceleration regimes and the experimental exploration of their performance to generate ion beams with high ion energy and flux [84, 162]. 2D particle-in-cell simulations were performed by H.-G. Jason Chou (SLAC, Stanford) using the PIC code OSIRIS and will be presented here as an outlook on future planned experimental campaigns using this target [116].

Two dimensional (2D) PIC simualtions were performes using a simulation box size with a longitudinal (x_1) width of 800 c/ω_0 (∼50 µm) and a transverse (x_2) width of 200 c/ω_0 (≈ 13 µm). The simulations use 36 particles per cell per species and a spatial resolution of 0.4 c/ω_{pe} in each direction, where $\omega_{pe} = \sqrt{4\pi e^2 n_0/m_e}$ is the electron plasma frequency. The time step is chosen according to the Courant–Friedrichs–Lewy condition, which ensures convergence when numerically solving partial differential equations. Open (absorbing) boundary conditions for both particles and fields are used in the longitudinal direction. The transverse boundary conditions are periodic. A laser pulse (400 nm, 10 J, 45 fs, 1.2 µm Full Width at Half Maximum (FWHM) spot size) with frequency ω_0 corresponding to a wavelength of 400 nm is launched along the x_1 direction (coincidental with target normal) irradiating a planar sheet of fully-ionized H_2O and D_2O. The target density is 1 g/cm^3 (approximately 50 n_c) with an initial electron temperature $T_e = 100$ eV and no pre-expansion. Different resolutions and numbers of particles per cell were tested to ensure convergence of the results and

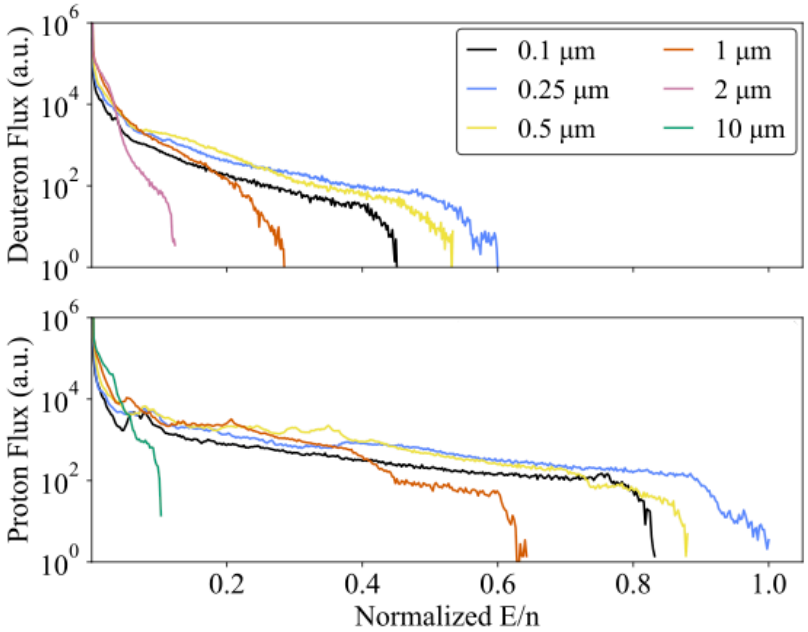

Figure 4.12.: Ion beam spectra obtained from PIC simulations are plotted as a function of the energy per nucleon (E/n), normalized to the maximum observed value. D_2O liquid target spectra for different target thicknesses (0.1, 0.25, 0.5, 1, 2 µm) are shown in the top plot. The spectra for an H_2O liquid target of different thicknesses (0.1, 0.25, 0.5, 1, 10 µm) are shown in the bottom plot. Both plots show a distinct increase in cut-off energy with decreasing target thickness and a decrease after reaching on optimum between 0.5 and 0.1 µm.

have used a third order particle interpolation scheme for improved numerical accuracy. The resulting ion spectra for D_2O and H_2O jets of variable thickness are displayed in Figure 4.12. For a better comparison, the energy is given in energy per nucleon and normalized to the maximum detected value among the H_2O and D_2O data sets.

For both H_2O and D_2O jets an increase in peak ion energy is observed as the target thickness decreases. It reaches a maximum close to a thickness of 250 nm and decreases again with decreasing thicknesses. A variety of theoretically and experimentally studies have investigated this observed increases in cut-off energies with decreasing target thickness. An explanation for this phenomenon is the reduce transverse spread of hot electrons as a result of the decreased target thickness. This improves the hot electron recirculation, thus increasing the rear-surface sheath field strength [163, 164]. Furthermore, high-contrast laser systems enable controlled or even eliminate pre-expansion of ultrathin (submicron) targets and have been used to explore relativistic transparency effects, which can further enhance the ion acceleration process [79, 80, 84–86]. The possibility of an acceleration regime transition is supported by density plots of longitudinal (p1) and transverse (p2) momenta for each target thickness in Figure 4.13. As can be observed, the ion emission pattern changes from thin (100 nm) to thick (2 μm) D_2O targets. Thinner targets show discrete lobes equivaent to high transverse momenta. Thicker targets show a more constant momentum distribution with a predominantly forward directed ion beam. This change in density distribution could be an indication of an entirely different acceleration regime or the interplay of two acceleration mechanisms. Future experiments utilizing sub-micrometer thick liquid jet targets will be able to test the presented simulation results and allow to compare observed spectral shapes and cut-off energies trends as a function of target thickness.

Furthermore liquid jet's capacity for in-situ thickness tuning the interaction point, makes it a promising target platform for studying the transition between different regimes of laser-driven ion acceleration and

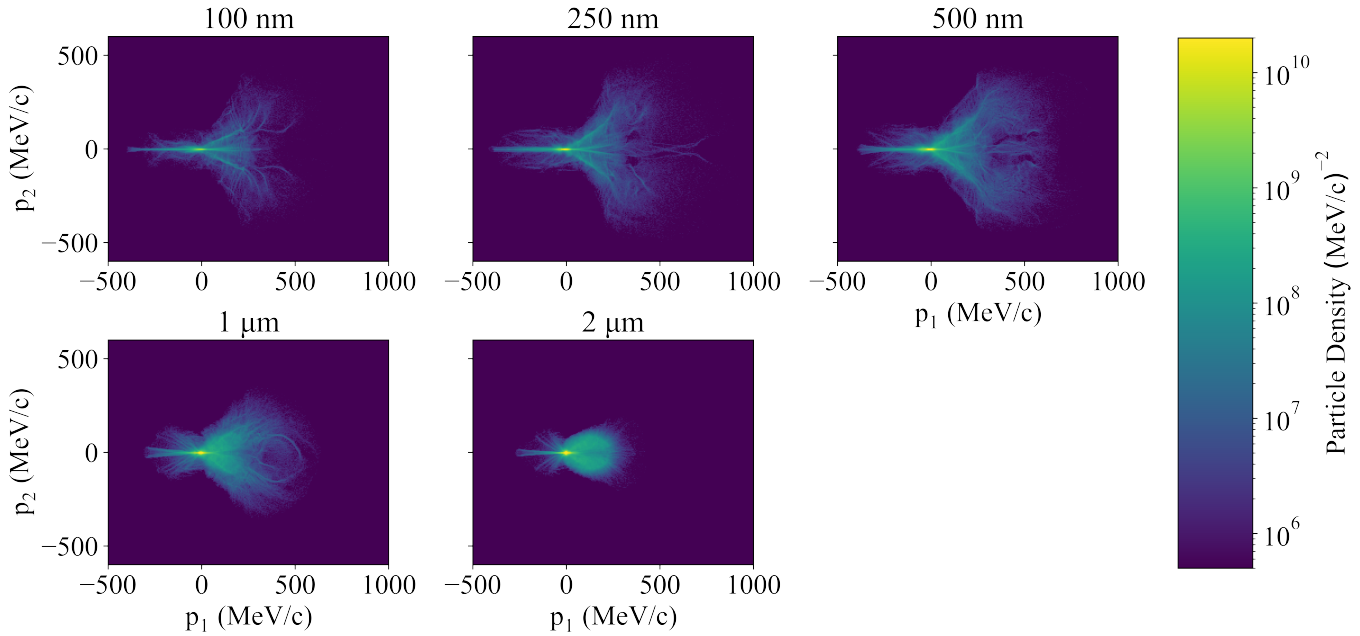

Figure 4.13.: Density plots of simulated ion momenta (p_2 vs. p_1) for various thicknesses of a D_2O target. With decreasing target thickness the density map drastically changes in shape from a confined angular emission for 2 μm to a large opening angle emission for 500 nm to finally a lobe like structure for lower target thicknesses.

optimization studies at PW laser facilities, focusing on peak and average flux as well as ion cut-off energies. A future experiment, awarded through LaserNetUS at the ALEPH laser at Colorado State University will optimize the deuteron beam generated from a sub-micron heavy water jet target. This optimized deuteron source can then be employed for secondary particle beam generation. Of particular interest in the context of this work is the generation of laser-driven secondary fast neutron beams in a pitcher-catcher setup.

5. Neutron Generation Platform Design

This Chapter focuses on the essentials to build an efficient laser-driven neutron generation platform. Since neutrons have a short, 15 min, life time [165], they cannot be generated, stored and recirculated in storage rings like ions and electrons. As a consequence, neutron beams are regularly generated on demand in fission processes or spallation reactions.

To develop an optimized laser-driven neutron source, standard sources are compared in the following based on the neutron generation mechanism at play and the parameters of the obtained neutron beam parameters. Furthermore the state of the art for laser-driven short-pulse neutron sources is summarized. Based on higher achievable fluxes, the pitcher-catcher setup was chosen for the presented platform. By investigating ion driven neutron generation reactions, the deuteron was identified as the ideal driver ion, settling on a deuterium jet target as a pitcher target. The composition of the catcher target is decided by considering neutron generation cross sections as well as simulation and experimental data investigating the neutron yield from lithium and beryllium.

In a final step the converter design is adapted for implementation at the Texas Petawatt laser facility and overall experimental considerations are presented. The majority of the presented work has been published by the author of this thesis in Reference 22.

5.1. Conventional and Laser-Based Neutron Sources

Common conventional and laser-based neutron sources supplying neutron beams operate on one of three fundamental neutron generation mechanisms:

- nuclear fission
- spallation
- and nuclear fusion.

These three fundamentally different processes require unique environments for efficient neutron generation and generate neutron beams with varying properties in terms of energy spectrum and emission profile. In the following the three different processes will be explained. Note, that neutron sources are not limited to the ones presented below and the interested reader is referred to References 166–168. In the frame work of this thesis, the focus lies on large scale facilities producing neutron beams with peak fluxes beyond 10^{15} n/cm^2/s. Reactor-based fusion sources, accelerator based spallation sources and laser-based fusion sources are discussed in detail. Figure 5.1 illustrates the neutron generation process for the different processes and the resulting energy spectra.

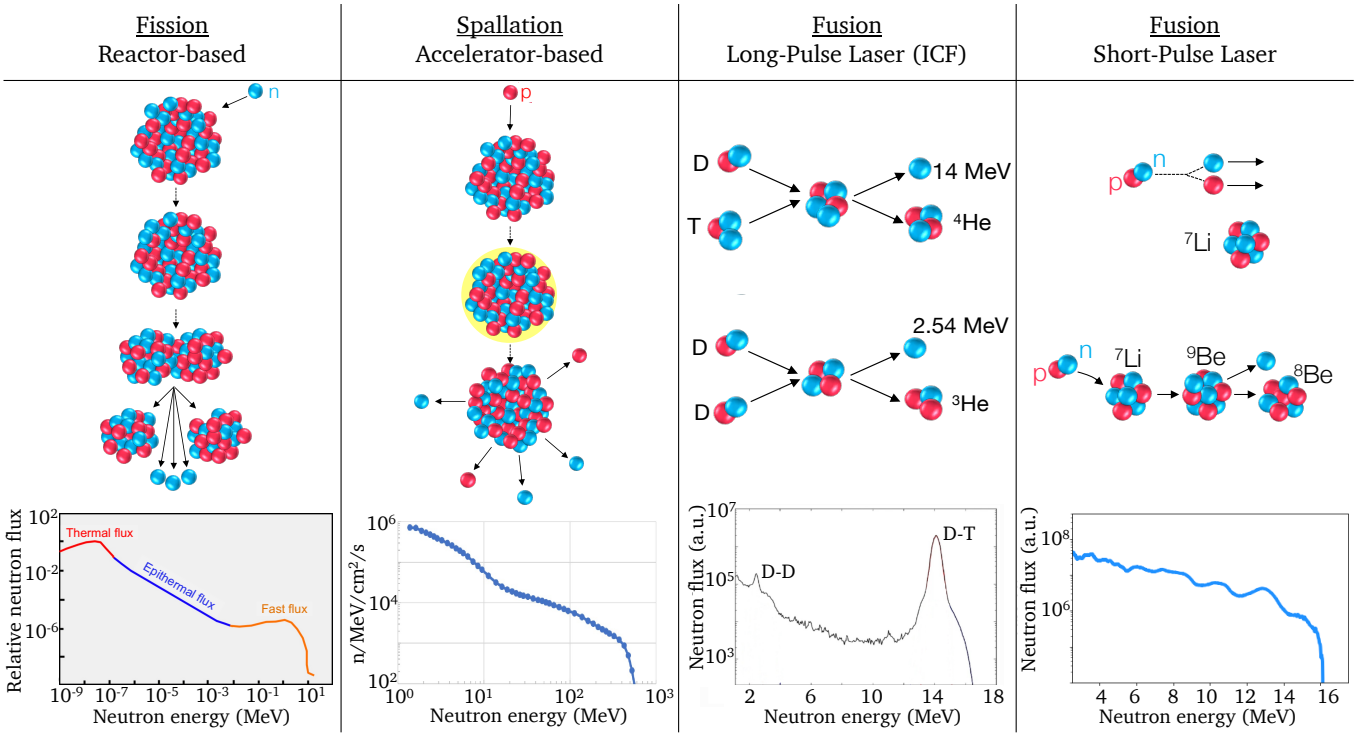

Figure 5.1.: In reactor-based fission (far left) multiple neutrons can be produced when an excited nucleus decays by splitting into at least two smaller nuclei. Maximum neutron energies reach around 10 MeV with a large epithermal and thermal tail. Accelerator-based spallation sources (center left) generate neutrons through internuclear cascades and deexcitation through evaporation which results in the emission of multiple neutrons. Energies of spallation neutrons range up to multiple 100s of MeV. Laser-based fusion sources are distinguished by laser pulse length (right). Long-pulse lasers are predominantly used to generate neutrons through deuterium-deuterium or deuterium-tritium fusion with energies up to 14 MeV. Short-pulse lasers have been efficiently used to drive neutron generation through interaction of energetic protons or deuterons with low-Z materials such as lithium or beryllium. The resulting energy spectrum can reach up to multiple 10s to 100 MeV. Energy spectra for fission, spallation and long-pulse laser fusion are adapted from References 169–171. The spectrum for short-pulse laser fusion experiments was recorded during shot 12359 of the experiment conducted at the Texas Petawatt laser facility presented in Chapter 7.

5.1.1. Reactor-Based Fission

The term nuclear fission describes the possibility of a nucleus made of Z protons and N neutrons ($A = Z + N$) to split into two or more lighter elements. Nuclear fission can be divided into spontaneous fission and neutron induced fission. The nuclear fissility parameter x given by

$$x \approx Z^2/50.88A\left(1 - \eta I^2\right) \quad \text{with} \tag{5.1}$$

$$I = (N - Z)/A \quad \text{and} \quad \eta = 1.7826 \tag{5.2}$$

quantifies the likelihood of a nucleus to undergo spontaneous fission. For values $x > 1$ the nucleus is unstable and nuclear fission can occur spontaneously. Actinides and transactinides, $A \geq 89$, are heavy nuclei that are unstable due to this criterion and undergo spontaneous fission characterized by the time it takes for half of

the population of the sample to undergo fission $\tau_{1/2}$ [172]. Well known actinides are uranium and plutonium, which are commonly used in fission fuels, or americium, a standard material used in smoke detectors.

Reactor-based fission sources typically harness neutron induced fission reactions using ^{235}U, ^{233}U, ^{241}Pu or ^{239}Pu, out of these ^{235} is most commonly used as the mother nucleus due to its natural abundance [172]. After the absorption of a neutron, the mother nucleus splits into predominantly two daughter nuclei of comparable, but slightly different, size under the emission of at least one neutron [173]. Figure 5.1 illustrates this process on the far left. Daughter nuclei always have a higher binding energy, so an energetically more favorable state, than the mother nucleus. Unlike other radioactive decays such as α (emission of a He^{2+} ion), β (emission of an electron) or γ (emission of a electromagnetic radiation), a mother nucleus can decay into a variety of daughter nuclei combinations. Furthermore, a mother nucleus can undergo multiple fission and decay processes until it reaches it's final state. After the first initial fission reaction has taken place, free neutrons are available within the reactor core and trigger additional fission reactions. Through a sustained chain reaction and additional lower energetic neutrons from ^{238}U fission, the number of free neutrons in the reactor core rapidly multiplies, achieving high flux neutron beams on the surface of the reactor structure.

The free neutrons produced during fission reactions are emitted homogeneously with energies on the order of a few MeV. On the way through the reactor structure these neutrons interact with their surroundings and effectively loose energy. Depending on where in the reactor core the neutrons are generated, they lose some or the majority of their initial energy. As a result, the energy spectrum of the emitted neutrons on the surface of the reactor structure is a convoluted spectrum with a high thermal neutron flux at meV energies (thermal), a Maxwellian spectrum for eV – keV neutron energies (epithermal) and another peak at MeV neutron energies (fast).

5.1.2. Accelerator-Based Spallation

Spallation refers to the process of ejection of fragments of material by an object as a consequence of impact or stress. In the context of neutron production, this more specifically means the ejection of nuclear fragments from a target nucleus when an ion beam impinges on it. This implies, that not only neutrons are ejected during this process, but instead a variety of different nuclei are ejected with variable momentum and energy distributions. Accelerator-based spallation sources accelerate predominantly protons to energies around 1 GeV, which are then directed onto a high Z target, typically tantalum or tungsten. These targets can range in size from multiple centimeters, like in the first design of the Los Alamos Neutron Science CEnter (Los Alamos, USA) (LANSCE) [174], to multiple meters as designed for the European Spallation Source (Lund, Sweden) (ESS) [175].

Neutrons are produced and emitted isotropically in two separate stages. In the first stage, the intra-nuclear cascade, high energy, 20 MeV to 100s of MeV, particles, typically protons, neutrons and α-particles, are generated and escape the nucleus. The exact cut-off energy of the neutron spectrum produced during this stage is dependent on the cut-off energy of the proton beam spectrum. These particles generated during the first stage have high enough energies to trigger a second, inter-nuclear, cascade by causing additional nuclear reactions in neighbouring nuclei. In this second stage, predominantly low energy ($<$ 20 MeV) particles are emitted during nucleus relaxation processes exhibiting a Maxwellian distribution [176, 177]. An exemplary spectrum of a spallation source is shown in Figure 5.1 on the center left column. This spectrum recorded at an instrument of the LANSCE facility illustrates the Maxwellian distribution of the neutron beam reaching up to several 100s of MeV. The contributions from the intra- and inter-nuclear cascades can be distinguished as total neutron spectrum is the sum of the two Maxwellian neutron spectra generated through the two types of cascades.

5.1.3. Laser-Driven Fusion

Using high-power lasers following the schemes of laser indirect drive or laser direct drive, neutrons are produced through fusion reactions. Two different approaches have been successfully demonstrated in the past. The first approach, inertial confinement fusion (ICF) utilizes millimeter-scale spherical target capsule that consist of an exterior ablator layer, for example high density carbon (HDC) and a thin interior cryogenic deuterium-tritium ice layer, on the order of tens of micrometer. The rest of the capsule is filled with a deuterium-tritium gas mixture, also called fusion fuel [44, 178]. Drivers for such neutron sources using these capsule targets are long-pulse (ns–10 ps), high-power, single shot lasers (1–5 shots/day) such as the National Ignition Facility (Livermore, USA) (NIF) at the Lawrence Livermore National Laboratory (Livermore, USA) (LLNL) and the OMEGA laser at the Laboratory for Laser Energetics (Rochester, USA) (LLE) at the University of Rochester.

The necessary conditions to achieve fusion in the capsule target were first described by Lawson et al. and have since been extended by a temperature dependence and are combined in what is today know as the Lawson criterion [180]. This criterion sets a lower limit for the product of density, confinement time and temperature of plasma, which are required to overcome the Coulomb repulsion of the two nuclei participating in the so-called thermonuclear fusion reaction in order to initiate fusion reactions. The necessary conditions are achieved by first heating the outer surface of of the capsule by a laser (direct drive) of laser produced X-rays (indirect drive), see Figure 5.2 (a) on the left. Consequently, the outer surface of the capsule is ablated, which results in an implosion reaching velocities around 300 km/sec [44]. The fuel that is accelerated towards the center of the capsule by the implosion ultimately stagnates by the high pressures formed in the center of the implosion, creating a compressed shell of fuel around a lower density area in the center. Upon stagnation, the kinetic energy of the imploding fuel is converted into internal energy, heating the central, low density region of the capsule, called the hot spot. Ultimately, keV temperatures and pressures in the hundreds of Gbar are reached within this hot spot region are sufficient for fusion reactions to be initiated [39, 40, 44, 181],

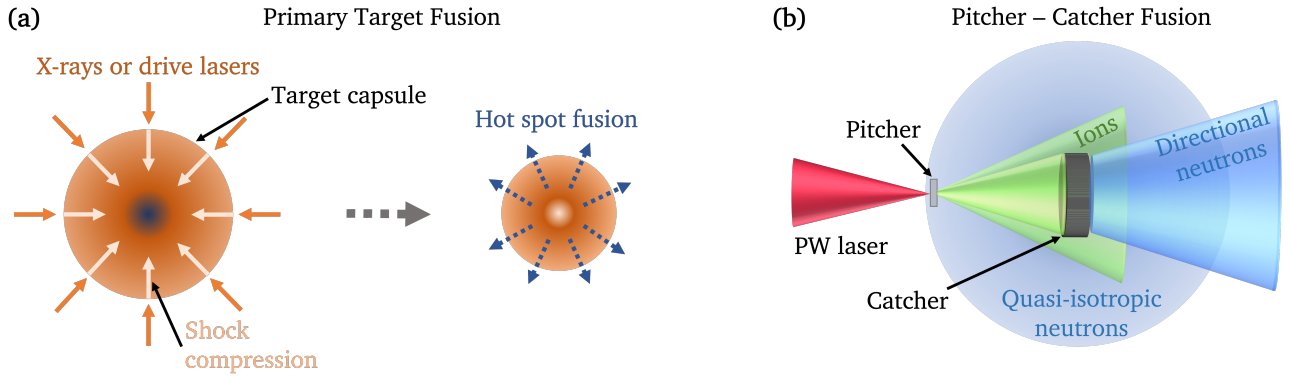

Figure 5.2.: In the laser-based approach neutrons are generated in two different setups. In the primary target fusion setup, (a), the target is irradiated either directly with multiple long-pulse laser beams or by laser-generated X-rays. The laser beams or X-rays heat and compress the material eventually generating a hot spot in its center. Neutrons are produced through nuclear reactions in the hot spot region and emitted isotropically. Short-pulse lasers efficiently generate neutrons in the pitcher-catcher configuration. The high power laser irradiates the pitcher target to produce a directional ion beam that subsequently impinges on the catcher material. Neutrons are emitted quasi-isotropic with an added directional component, aligned with the direction of travel of the ion beam. (a) adapted from Ref. 179.

as shown in Figure 5.2 (a) on the right. The two main fusion reactions of interest in this approach are deuterium-deuterium (DD) and deuterium-tritium (DT) fusion:

$$ {}^{2}_{1}D + {}^{2}_{1}D \longrightarrow {}^{3}_{2}He + n^{0} \ (2.45 \text{ MeV}) \tag{5.3} $$

$$ {}^{2}_{1}D + {}^{3}_{1}T \longrightarrow {}^{4}_{2}He + n^{0} \ (14.1 \text{ MeV}) \tag{5.4} $$

in which a free neutron is generated with a kinetic energy of 2.45 and 14.1 MeV respectively. If the areal density and ion temperature within the hot spot is high enough, the hot spot will 'ignite' fueled by generated α-particles (^{4}He) that deposit their energy locally. For fuel areal density above 1 g/cm^2 the surrounding high density cold fuel will be heated significantly driven by the energy deposition of generated α-particles and electron conduction. Consequently, a larger volume of fuel ignites and "burns" to produce more neutrons and α-particles that drive a burn wave propagating into the outer layers of cold fuel until the whole system explodes and rapidly cools off [43, 44, 181–183].

The second approach, predominantly employing short-pulse lasers, relies on a pitcher–catcher geometry consisting of two targets separated by up to 5 cm, see Figure 5.2 (b). The pitcher target (pitcher), usually sub-micrometer thick, is irradiated by the short (sub ps) laser pulse and an ion beam is generated and emitted from the backside of the target. A centimeter-size catcher target (catcher/converter) captures the ion beam close to the pitcher, and neutrons are created through nuclear (fusion) reactions between the ions and catcher atoms [27, 45, 46].

Figure 5.1 shows two examples of interactions between a deuterium ion and a lithium nucleus. The deuteron can either undergo break-up in the potential of the lithium nucleus (seen on the top) or is absorbed by the lithium nucleus and the generated beryllium nucleus decays to a stable state through emission of a neutron. In this scenario neutrons are emitted quasi-isotropically with an additional direction component as seen in Figure 5.2 (b). Neutron cut-off energies are highly dependent on those of the ion drive beam with maximum neutron energies up to 100 MeV observed in the past [21].

The setup for neutron generation presented developed and presented in this work follows this pitcher–catcher approach using deuterium ions as neutron production drivers. Subsequent sections will focus on the state of the art of such sources, the different neutron generation mechanisms and neutron converter design considerations.

5.1.4. Neutron Source Performance Comparison

Different neutron sources are best compared in terms of their characteristics with respect to potential applications. Such applications require certain neutron beam properties like the neutron energy and spectrum, the peak neutron flux, the average neutron flux and linked to that the repetition rate of the source as well as the bunch duration of the neutron beam. One can distinguish between applications involving stationary and stable objects or systems and applications with fast evolving states.

Applications such as diagnostics for fuel cell [184] or medical cancer treatment [185] among others [186, 187] don not necessarily require a high peak flux or a short bunch duration, but rely on high average flux and high repetition rate in order to accumulate a large enough dose to achieve necessary results or resolutions. Other applications focusing on diagnosing fast evolving processes such as for example shock imaging [188–190] on the other hand require a high peak flux and a short bunch duration in order to achieve the spatial and temporal resolution necessary. Table 5.1 summarizes the properties of neutron beams from different neutron sources presented above in terms of flux at the sample, bunch duration and repetition rate.

While currently conventional neutron sources such as fission reactors and spallation sources still out-perform laser-driven sources in terms of average flux at the sample, they are severely limited to a specific set of

Neutron source	Peak flux $\left(\frac{\text{n}}{\text{cm}^2\text{s}}\right)$	Average flux $\left(\frac{\text{n}}{\text{cm}^2\text{s}}\right)$	Repetition rate (Hz)	Bunch duration
Reactor [191]	$\sim 10^{15}$	$\sim 10^{15}$	continuous	continuous
Spallation [191]	$\sim 10^{16}$	$\sim 10^{12}$	60	$\sim 1\,\mu$s
Current lasers [21, 192, 193]	10^{18} - 10^{19}	5 x 10^{5} - 5 x 10^{6}	5 x 10^{-4}	~ 1 ns
Future PW lasers [194, 195]	$>10^{19}$	$>10^{10}$	10	~ 1 ns
Laser fusion (ICF) [44]	10^{27}	10^{11}	4 x 10^{-6}	~ 100 ps

Table 5.1.: Overview of the characteristics of presently-available conventional (reactor- or accelerator-based) and laser-based neutron sources. Based on properties important for applications, neutron sources are characterized by peak and average flux at the sample, repetition rate and bunch duration. (adapted from [32])

applications with static conditions or slowly evolving states due to their long bunch duration. This fact prevents probing of dynamically evolving systems with sufficient temporal resolution. Since a chain reaction cannot be easily stopped once initiated, the majority of fission reactors are continuous sources of neutrons with peak fluxes up to 10^{15} n/cm^2/s. Spallation sources produce pulses of neutrons at a comparable peak flux but reduced average flux with a bunch duration of hundreds of ns up to ms [37, 38], at a repetition rate that is dictated by the ion accelerator and can range up to 60 Hz [191]. Overall setups for reactor and accelerator-based sources lack flexibility due to overall shielding and experimental instrument location restrictions. Additionally, the isotropic emission of neutrons, even into the 100s of MeV regime (spallation), requires large scale shielding geometries to protect personnel and ensure high fidelity measurements with low background noise. As such, these neutron sources are large scale facilities that require large operations budgets and workforce to stay operational.

The advent of high-power laser systems, enabled by CPA, resulted in the development of novel laser-based neutron sources. The inherently short duration of laser-driven ion beams produces neutron bunches with pulse durations on the order of a nanosecond, giving such neutron sources the potential to become unique probes of fast-evolving processes. Long-pulse laser-based sources deliver high neutron flux, on the order of 10^{27} neutrons/(cm^2 s), emitted isotropically through direct or indirect drive of implosions triggered by shock waves into the target [41, 42]. However these sources are limited in repetition rate to a around one shot a day, due to the cooling requirements of the flash-lamp pumped high energy glass laser.

A promising alternative to those systems are short-pulse laser-based pitcher-catcher sources, which have demonstrated peak fluxes of up to 10^{19} n/cm^2/s, outperforming reactor and spallation sources by multiple orders of magnitude. Their inherently short pulse duration at or even below 1 ns can enable the use of those neutron beams to diagnose fast evolving dynamic systems. Although average fluxes are still well below those achieved by conventional sources, the development of high repetition-rate capable high-power laser systems such as the ELI L3 beamline [194] will allow to close the gap to conventional sources. Additionally, the compact and flexible setup of short-pulse laser-driven pitcher-catcher setups allows for the accommodation of a variety of sample setups and geometries, eventually promising to enable the development of a movable high flux neutron source.

Year	E_L on target [J]	Pitcher target	Ion species	Catcher target	Neutron energy [MeV]	Neutron flux [1/sr]
1999 [196]	30	bulk CD	H^+/D^+	bulk CD	–	1×10^7
2004 [45]	80	Mylar/ Cu	H^+	LiF (3.4 mm)	2.1	3×10^8
[197]	200-300	Mylar/ Au/ Al	H^+	B (3 mm)	–	1×10^9
2010 [27]	127	Cu	H^+/D^+	LiF (0.9 mm)	–	1×10^8
2011 [198]	360	CD	H^+/D^+	LiF (1.8 mm)	18	8×10^8
[46]	6	Mylar-CD	H^+/D^+	bulk CD	4	5×10^3
2013 [199]	6	Cu-D_2O	H^+/D^+	bulk D_2O	–	4×10^5
[21]	80	CH/ CD	H^+/D^+	Be (50/60 mm)	100	1×10^{10}
[200]	1	Cu-D_2O	H^+/D^+	LiF (8.5 mm)	16.8	1×10^7
[201]	60	Si_3N_4-Al	H^+	Li (4.5 mm)	2.9	1×10^7
[202]	80	CH/ CD	H^+/D^+	Be (50 mm)	80	4.4×10^9
[203]	50	CH/ CD/ DLC	H^+/D^+	Be (50 mm)	–	1×10^9
2015 [204]	62	Au	H^+	Li (4 mm)	5	1×10^9
2016 [205]	200	CD	H^+/D^+	CD (2 mm)	25	5×10^8
[28]	80	CH/ CD	H^+/D^+	Be (30 mm)	80	1.5×10^9 / 9×10^8
2018 [206]	140 - 175	CD	H^+/D^+	Be (33 mm)	–	1×10^{10}
2019 [47]	80	CH/ CD	H^+/D^+	Be (40 mm)	55	$>1\times 10^{10}$

Table 5.2.: Summary of previously published work on the characterization of short-pulse laser-driven neutron sources predominantly in the pitcher-catcher geometry. Experiments utilizing only one single target are distinguished by adding *bulk* to the catcher material specification. *DLC* in the target section stands for diamond-like-carbon. Experimental results are compared based on laser energy E_L on target, the accelerated ion species and the resulting maximum neutron energy and flux. Past experiments have employed predominantly plastic based pitcher targets with lithium or beryllium as a converter material, reaching up to 100 MeV neutrons at a flux of 1×10^{10} neutrons per steradian.

5.2. State of the Art of Laser-Driven Neutron Sources

Over the past two decades numerous studies have investigated the efficient generation of fast neutrons using short pulse lasers and a variety of combinations of pitcher and catcher targets. Table 5.2 gives an overview of all previously published works until today, specifying the laser energy E_L on target, the pitcher material and accelerated ion species, the catcher material and the resulting neutron cut-off energy and peak flux.

Only a few studies were able to accelerate single species ion beams and the majority of the conducted studies accelerated a mixed proton and deuteron beam with varying fractions of protons with respect to the accelerated deuteron numbers. While the overall yield of neutron generation, for the studies achieving neutron generation within the primary target bulk material, is limited to a maximum achieved flux of 1×10^{7} n/sr, pitcher-catcher neutron sources regularly achieve higher peak fluxes. The highest neutron flux from a laser-driven pitcher-catcher source was recorded by Roth et al. in 2013 with a peak flux of 1×10^{10} n/sr in the direction of the ion beam propagation and cut-off energies up to 100 MeV [21]. This particular setup used a deuterated plastic foil as a pitcher target and a beryllium target as a catcher target.

A scaling of neutron flux with incident laser power is observed, as the neutron number directly depends on the number of ions incident on the converter material. This scaling agrees with trends observed for TNSA ion acceleration [93, 95, 100]. Paired with the development and comissioning of high power laser facilities and the advances in laser technology, culminating in the recent commissioning and successful operation of multiple high-repetition-rate petawatt lasers [23], peak and average neutron fluxes are projected to significantly increase over the next few years by leveraging new laser capabilities. When combining these laser capabilities with recent significant progress in delivery of continuous, debris-free targets [24–26], neutron generation with repetition rates of 1 Hz or greater are achievable, promising to close the gap in average neutron flux between laser-based and conventional sources.

In this work, a platform is presented that is based on fast self-replenishing targets and promises to be able to provide the necessary tools to achieve higher neutron fluxes in future studies. Before going into detail of the experimental platform, the principle of neutron generation in a pitcher-catcher setup will be explained.

5.3. Pitcher-Catcher Neutron Generation

For the selection of the right combination of pitcher and catcher target, one has to consider the efficiency of laser-to-ion coupling in the pitcher target as well as the efficiency of ion-induced neutron generation in the catcher target. As discussed in Section 2.5, light ions, especially protons and deuterons, are most efficiently accelerated through the TNSA mechanism. While protons are more efficiently accelerated due to their lower charge-to-mass ratio, deuterons offer additional neutron generation channels. In the work presented here, high purity cryogenic deuterium jets were used as a pitcher target, in the following the discussion will therefore focus on deuteron-specific neutron generation channels.

When deuterons impinge on a converter material, neutrons are produced through three different mechanisms: complete fusion (compound formation followed by neutron emission), elastic breakup, and incomplete fusion (inelastic breakup or deuteron stripping) [207–209]. These three interaction channels can be grouped into two different types of nuclear reactions. Compound nuclear reactions are complete fusion reactions that occur for any type of incident ion, for example protons. Direct nuclear reactions group together elastic breakup and incomplete fusion and are interaction paths unique to deuterons.

5.3.1. Compound Nuclear Reaction

During complete fusion, the deuteron and the target atom form a short-lived compound state as shown in Figure 5.3 for the example of a deuteron impinging on ^{7}Li. Here, a deuteron is absorbed by a ^{7}Li atom to form a short lived ^{9}Be state, that decays into ^{8}Be under emission of a neutron:

$$^{7}\mathrm{Li} + \mathrm{d} \longrightarrow ^{8}\mathrm{Be} + \mathrm{n} \quad . \tag{5.5}$$

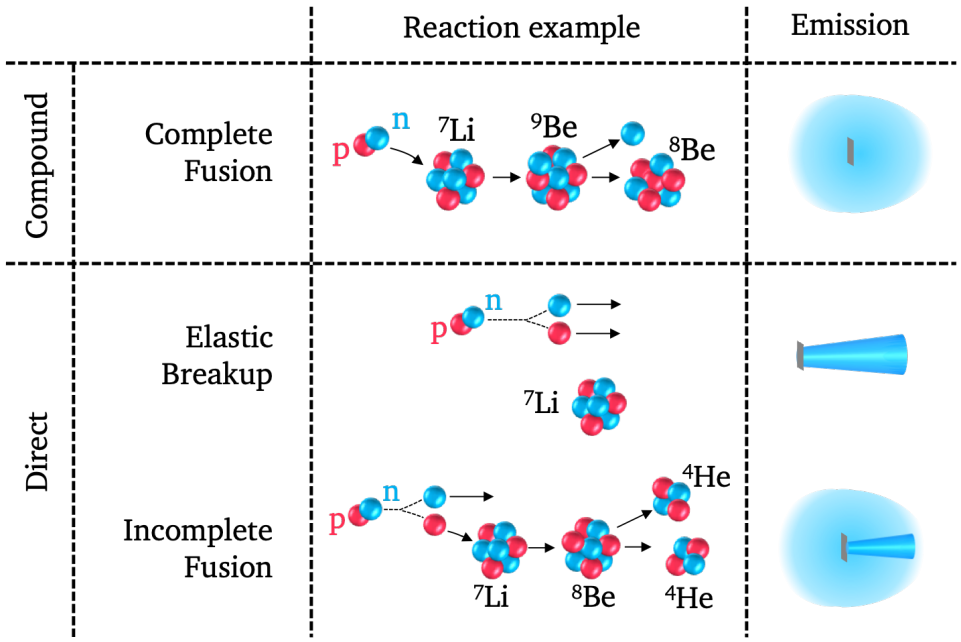

Figure 5.3.: Nuclear reactions of deuterons with a converter material can be divided into compound and direct nuclear reactions. Compound reactions are complete fusion processes with the example of post-equilibrium neutron generation shown here and the resulting isotropic emission. Direct nuclear reactions, specific to deuterons, distinguish between elastic breakup and incomplete fusion. During elastic breakup the deuteron splits up within the atom's Coulomb potential maintaining the forward directed momentum of the deuteron. Incomplete fusion is a combination of breakup and fusion and results in a quasi-isotropic emission of neutrons with a forward directed component.

Two cases are distinguished by the time of the neutron emission after the excitation of the nucleus. Neutrons can be emitted before (pre-) or after (post-) equilibration of the nucleus. The properties of the emitted neutron vary based on whether it is emitted pre or post equilibration. Pre-equilibration emission [210–213] occurs for high-energy ions impinging on the converter material, in particular, for kinetic energies larger than the binding energy of the converter nucleus. In this scenario the energy of the incoming ion is not fully transmitted to the formed compound nucleus, keeping it from reaching equilibrium. As a consequence information about the incoming ion velocity vector and value is partially maintained throughout the interaction. This results in an emission of neutrons with a quasi-isotropic distribution and a more forward directed component and higher energies compared to post-equilibration neutron emission [213].

Post-equilibrium neutron emission occurs when the compound nucleus has been fully formed and reached equilibrium. At that point all information about the incoming ion properties has been lost. The evaporation-like neutron spectrum obtained for this interaction can reach maximum ion energies of

$$E_{n,max} \approx E_{ion} + Q \tag{5.6}$$

with the reaction Q-value [214]. The specific decay channels of the compound nucleus are solely dictated by the probability of each individual channel and quasi-monoenergetic neutrons are emitted isotropically. As a result the overall spatial emission profile for compound interactions is a superposition of an isotropic profile and a quasi-isotropic, more forward direction, emission profile as shown in Figure 5.3 on the top for the example of a deuteron impinging on a lithium atom.

5.3.2. Direct Nuclear Reaction

Compared to compound nuclear reactions, direct nuclear reactions specific to deuterons, occur on a much shorter time scale and can be subdivided into elastic breakup and incomplete fusion, also referred to as stripping. The threshold for these reaction is given by the binding energy of the deuteron $E_B = 2.225$ MeV [215]. Figure 5.3 shows an example of elastic breakup and incomplete fusion for a deuteron impinging on a lithium converter and the resulting emission profile.

Elastic breakup occurs in the vicinity of a converter atom, which does not partake in the reaction, shown below for deuteron breakup in lithium

$$^{7}\mathrm{Li} + \mathrm{d} \longrightarrow ^{7}\mathrm{Li} + \mathrm{n} + \mathrm{p} \quad . \tag{5.7}$$

Deuterons approaching the nucleus are decelerated in the Coulomb potential of the converter atoms. Once the Coulomb force becomes larger than the binding energy E_B of the deuteron, it dissociates producing a proton and a neutron. It is important to note that the trajectory of the neutron and proton pair is conserved. Assuming that the proton and neutron receive the same amount of energy upon dissociation, the energies of the proton E_p and neutron E_n can be calculated using

$$E_n = \frac{1}{2}\left(E_d - \frac{1}{4\pi\epsilon_0}\frac{Ze^2}{R} - E_B\right) \tag{5.8}$$

$$E_p = \frac{1}{2}\left(E_d + \frac{1}{4\pi\epsilon_0}\frac{Ze^2}{R} - E_B\right) \tag{5.9}$$

with the deuteron energy E_n and the energy-loss $\frac{1}{4\pi\epsilon_0}\frac{Ze^2}{R}$ in the Coulomb potential with the dissociation distance R [216]. Since the proton directly interacts with the Coulomb potential it gets accelerated after dissociation, which leads to a change in the sign of the energy-loss term. The neutron beam has a continuous energy spectrum similar to that of the incoming ion beam and is forward-directed due to conservation of momentum.

While the process of elastic breakup is very efficient for high-Z catcher materials due to an increased cross-section value, deuterons in low-Z materials predominantly generate neutrons through stripping or incomplete fusion [214, 217, 218]. In this scenario, elastic breakup occurs close enough to the converter atom and the liberated proton or neutron is captured by the target atom. This is a result of the smaller radius of the low-Z atoms, resulting in deuteron breakup much closer to the nucleus. If the resulting intermediate compound state is unstable, it can decay via emission of another neutron. For the example of deuteron impinging on lithium, a proton is absorbed after deuteron breakup. An intermediate unstable ^{8}Be nucleus is formed, that decays into two ^{4}He nuclei:

$$^{7}\mathrm{Li} + \mathrm{d} \longrightarrow ^{7}\mathrm{Be} + ^{4}\mathrm{He} + ^{4}\mathrm{He} \quad . \tag{5.10}$$

Consequently, neutrons produced by incomplete fusion have a directed component from deuteron stripping and a quasi-isotropic component from complete fusion, with an energy spectrum given by the sum of the quasi-monoenergetic and continuous spectra produced from the two underlying processes.

Of these three mechanisms, elastic breakup and incomplete fusion are often preferred for laser-driven neutron beam applications due to their higher reaction cross sections, depending on the catcher material, and the directionality of the neutron beam. In the following the converter designed for the experiment at the Texas Petawatt laser facility will be discussed based on this knowledge and tabulated deuteron interaction cross sections with common catcher materials [219, 220].

5.4. Neutron Converter Design

The overall neutron yield, spatial distribution and energy spectrum are not only dependent on the impinging ion beam but also on the choice of the converter material. In principle any material can generate neutrons and a reaction cross-section with deuterons for neutron generation can be measured. For an efficient laser-driven neutron source design, it is important to maximize the energy transfer from laser to ions and from ions to neutrons. Therefore a converter material with a high interaction cross-section for neutron generating reaction channels, especially deuteron breakup and stripping, and a low neutron scattering or absorption cross section is ideal. For efficient neutron production through breakup and stripping impinging ions need to have a high energy (> 2.225 MeV), which is routinely achieved through TNSA at high power lasers. Since TNSA-accelerated ion beams exhibit highest fluxes for low ion energies, it is additionally important to choose a converter material with a high cross section especially below 10 MeV, such materials are usually low-Z materials. Two materials that fullfill these requirements and are ideally suited for deuteron-driven neutron generation are lithium and beryllium [21, 45, 201, 214].

The converter composition was determined by considering the deuteron stripping (d,n), deuteron elastic breakup (d,n+p), and fusion nuclear reactions (d,n+x), where x can be α, n, or t, of the most abundant

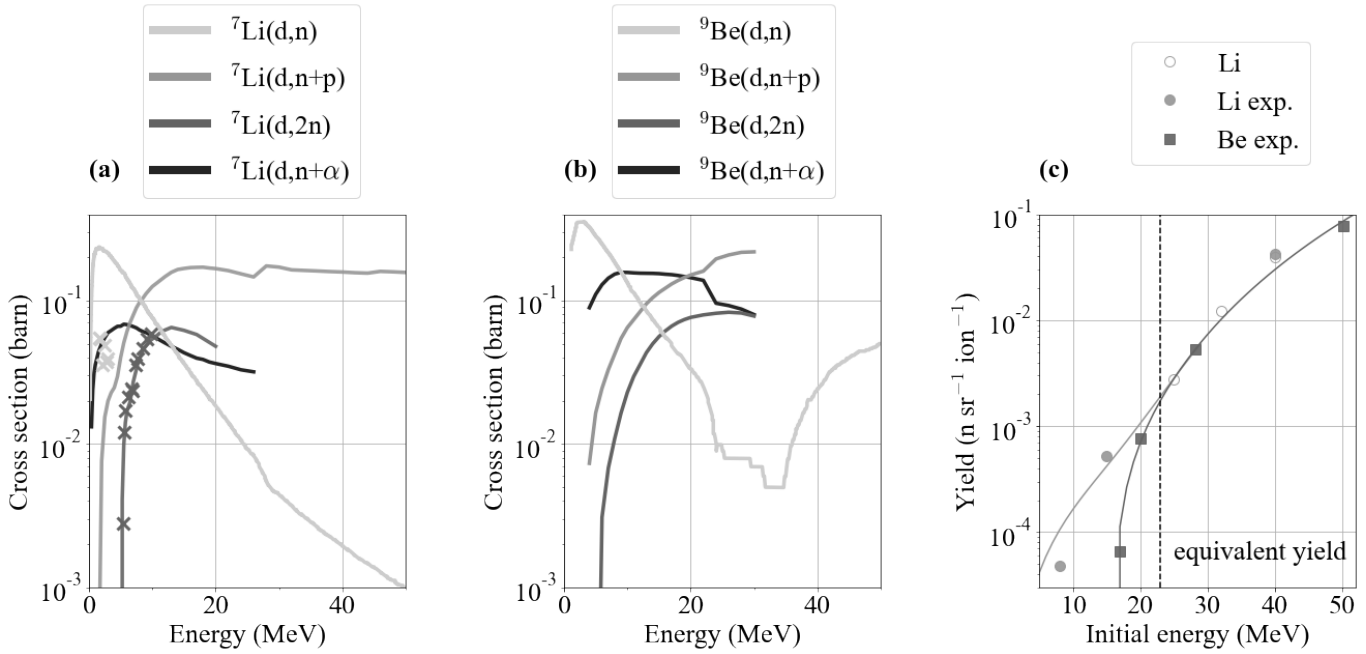

Figure 5.4.: (**a**) Neutron production cross sections for lithium (^{7}Li) including simulations (solid lines) [219–221] and corresponding experimental data (crosses) [222–224]. (**b**) Beryllium (^{9}Be) specific simulated neutron production cross sections [219–221, 225]. (**c**) Comparison of neutron yields for lithium and beryllium with experimental neutron yields (full circles) for lithium (8, 12, and 15 MeV [226], 40 MeV [227]) and for beryllium (squares) from [228]. Experimental data wss obtained by measuring the neutron yield from a monoenergetic deuteron beam produced by an accelerator impinging on a thick converter target. Simulation studies using Monte Carlo codes are added as empty circles [229, 230]. The plotted lines are a guide to the eye for the two different materials. To the right of the dashed line lithium and beryllium show equivalent neutron yield for incident deuterons with the same energy. (adapted from [214]).

isotope of beryllium (^{9}Be) and lithium (^{7}Li). Figure 5.4 plots the corresponding cross-sections for lithium, (a), and beryllium, (b). Experimentally measured interaction cross sections are depicted by crosses in the plot, confirming simulated neutron production cross sections. Figure 5.4 (c) visualizes the overall yield per impinging deuteron as a function of the initial deuteron energy for both beryllium and lithium consisting predominantly of experimental data using monoenergetic deuteron beams to generate neutrons.

Let us first consider the individual cross sections between deuterons and lithium and beryllium shown in (a) and (b). For both converter material candidates the cross sections for the following reactions are displayed

- A(d,n) – deuteron stripping
- A(d,n+p) – deuteron breakup
- A(d,2n)
- A(d,n+α)

where A is a placeholder for either ^{7}Li or ^{9}Be. Interaction cross sections for deuterium with beryllium, such as (d,n+t), are not shown in this plot because they are lower by one order of magnitude compared to the displayed cross section and are thus neglected during further considerations.

Neutron generation cross sections of fusion reaction channels, such as (d,2n) and (d,n+α), for lithium and beryllium attain maximum values of tens of mb [219, 220], much lower than deuteron stripping or breakup cross sections. An exception is the ^{9}Be(d,n+α) reaction which becomes dominant over deuteron stripping or breakup in the 10–20 MeV energy range. The ^{7}Li(d,n) (stripping) reaction shows a high reaction cross section for energies ranging from $\sim$100 keV to $\sim$10 MeV [221]. For higher energies, deuteron breakup (^{7}Li(d,n+p)) becomes significant due to a higher reaction cross section value with a maximum of $\sim$150 mb (1 barn 1×10^{-24} cm^2) at around 15 MeV [219]. Simulations predict a similar behavior for beryllium where deuteron stripping dominates at lower energies and the breakup cross section reaches a maximum over 100 mb for energies around 30 MeV. Comparisons between simulations and experiments studying deuteron breakup in lithium and beryllium show good agreement and measure the cross section to be on the order of 100s of mb for energies above 10 MeV for both materials [218, 231].

Experimental results and simulations for the total neutron yield using monoenergetic ion beams incident on lithium and beryllium confirm this assumption as shown in Figure 5.4 (c). Here, the neutron yield per incident ion per steradian is plotted as a function of the energy of an incident monoenergetic deuteron beam. Experimental data is shown as solid markers, squares for beryllium and circles for lithium, and simulation data for lithium are shown as empty circles. To identify a trend in neutron generation as a function of energy, lines are plotted for both materials to guide the eye. A similar neutron yield per incident deuteron is observed for lithium and beryllium and deuteron energies above 23 MeV; this threshold is indicated by the dashed line and corresponds to the energy at which the beryllium breakup cross section surpasses the breakup cross section of lithium. For lower energies, the neutron yield for lithium drops more gradual than for beryllium. Based on these experimentally measured yields and simulated cross sections, lithium will yield higher neutron fluxes for the low energy tail of TNSA-like ion beams compared to beryllium. For higher incident deuteron energies (> 23 MeV) the experimental data does not suggest a big neutron yield difference between lithium and beryllium. However especially the breakup cross section for beryllium presented in (b) surpass the lithium cross section and indicate a trend towards consistently higher values for energies above 23 MeV. This leads to the conclusion that above 23 MeV beryllium and lithium show comparable neutron yields. It has to be noted that in the framework of this work the determination of transition between lithium and beryllium did not include a dedicated study of the neutron yield as a function of penetration depth and incident ion energy. As ions lose energy on their way through the converter, the incident energy is not necessarily equivalent to

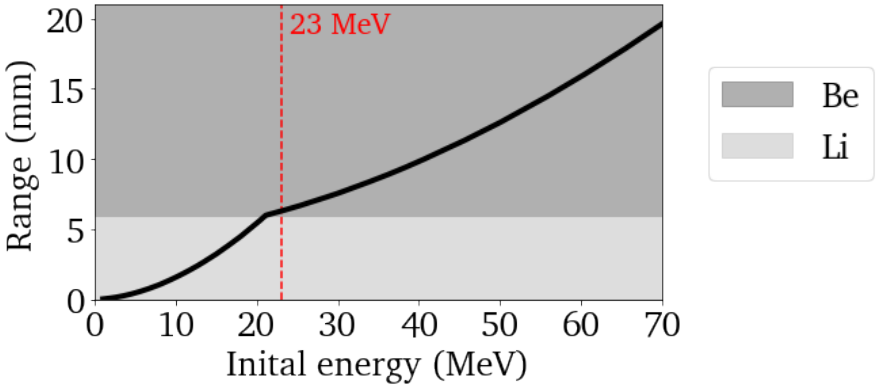

Figure 5.5.: Exemplary stacked converter design with a 6 mm layer of lithium followed by 15 mm of beryllium with the overlaid range of deuterons with energies up to 70 MeV. The transition between lithium and beryllium occurs at roughly 23 MeV.

the energy of the deuteron when it participates in a neutron generating reaction. Future optimizations may include a study taking this into account to maximize the conversion efficiency from deuterons to neutrons.

For implementation of a converter material during the experiment, the goal is to maximize the conversion efficiency from ions to neutrons. Due to the continuous ion spectra typically generated during TNSA-like ion acceleration, a high neutron generation cross section across all ion energies is important. Since lithium exhibits a higher neutron generation ability for lower energies, but beryllium has the potential to generate an even higher neutron yield for higher energies, a combination of lithium and beryllium was chosen for the converter in this study. To realize this, 6 mm of lithium is chosen to precede beryllium in a stacked converter design. For a detailed theoretical study of this design, see Ref. [232].

The converter is designed as a stackable assembly, which means that multiple pieces of beryllium with different thicknesses (1.25, 5 and 10 mm) are available to obtain the desired total thickness of the converter. The precise necessary thickness of the beryllium layer of the converter is estimated by calculating the range of the most energetic deuteron ions measured in the experiment within the converter using stopping power tables provided by SRIM [233]. Figure 5.5 shows the range of deuterons with energies up to 70 MeV in the stacked converter configuration. The transition between lithium and beryllium occurs roughly at the predetermined threshold of 23 MeV. When determining the thickness of the beryllium layer and building the converter, the neutron absorption cross section (above 100 mb) of beryllium needs to be taken into account. Yield losses due to scattering in the converter itself can be minimized by keeping the design to its minimum thickness to ensure both efficient ion stopping and a predominantly unperturbed neutron beam. The more specific design for the experiment conducted at the Texas Petawatt laser facility will be presented below.

5.5. Converter Setup at a High Power Short Pulse Laser Facility

The converter design for implementation at a high-power short-pulse laser facility was finalized based on two considerations: (1) the converter shape and width and (2) the pitcher-to-converter distance. Conversion efficiency of a TNSA-like deuteron beam to neutrons is maximized when matching the cone-like emission of the ion beam. The ideal shape of the converter is consequently a cone, which can complicate implementation of the converter itself or other necessary diagnostics around it. The closest shape to a cone is a cylinder, which was chosen for the converter with a transverse width of 1 inch (2.54 cm), to match the circular cross section

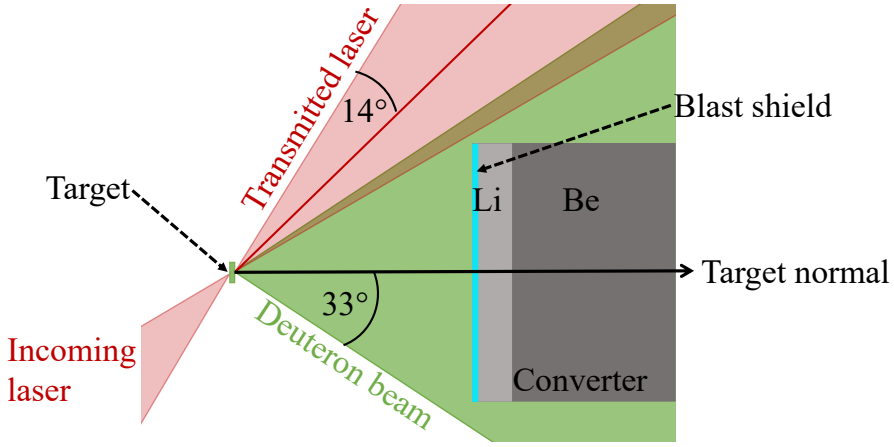

Figure 5.6.: Top view of the setup (target size not to scale). The converter is placed in the target normal direction to capture the ion beam and at a large enough distance to avoid damages by the laser to the converter material.

of the cone-like spatial emission profile of the ion beam at a distance of a few centimeters away from the pitcher target.

Once the shape and size of the converter is determine, we need to determine the distance between the pitcher and the converter. With the same objective of maximizing the neutron yield, the first aspect to consider is the opening angle of the ion beam. In previous experiments using the cryogenic jet, the opening angle of the TNSA-like beam was found to be $\sim 33^\circ$ half angle taking into account the low energy part (MeV energies) of the spectrum. A short distance between pitcher and catcher is favorable due two three important aspects. Firstly, a short distance enables capturing the majority of the accelerated deuteron beam. Additionally, the smaller the distance between pitcher and catcher, the smaller the spatial cross section of the accelerated ion beam and the resulting source size of the neutron beam. Lastly, the short distance results in a smaller energy spread (chirp) of the ion beam and therefore a smaller pulse duration of the ion beam, as a direct consequence the pulse duration of the neutron beam is short and will increase with increasing distance between the pitcher and converter.

On the other hand, especially for high-power short-pulse lasers that routinely reach intensity on the order of 10^{21} W/cm^2, the possible damage to the converter caused by laser light transmitted through or past the mass-limited pitcher jet target has to be assessed. The primary measure of limiting the potential for damage to the converter is to rotate the target by 45° relative to the laser's forward direction and place the converter on the target normal axis. However, due to the large opening angle of the emitted ion beam, an overlap of the transmitted laser light cone with the deuteron beam can remain, which further constrains placement options of the converter. Figure 5.6 illustrates this issue for an $f/2$ final focusing optic, like available at the Texas Petawatt laser facility. The intensity of the transmitted laser light stays beyond or near the damage threshold of most materials, typically on the order of 10^{11}–10^{13} W/cm^2, for several centimeter behind the target. Considering an $f/2$ focusing optic and a laser energy on the target of 10–100 J, a distance on the order of tens of centimeters is necessary to ensure no damages to the converter material.

A compromise between maximizing the total number of ions captured by the converter and minimizing the potential damage by laser light can be found by placing the converter as close as possible to the pitcher while still remaining outside the transmitted laser light cone. As an additional safety measure, a blast shield is added to the front of the converter that will deflect away any incident scattered laser light. It consists of a No.

1.5 borosilicate glass microscope cover slip (170–250 µm thick) with a 40 nm thick aluminium coating. In the presented configuration but also depending on the laser intensity on target and the focal length of the final focusing optic at different laser facilities, this allows the distance between pitcher and converter to be reduced to x=5 cm. At this distance, the converter covered a deuteron beam half opening angle of 15°, fully capturing deuteron with energies above approximately 30 MeV, while lower energy deuterons still partially miss the converter. These will produce neutrons upon interacting with either the chamber wall or other components in the target chamber.

A maximized neutron yield is achieved when the traces of higher-energy deuterons are centered on the axis of the converter. Few studies have investigated the possibility of tracking the ion beam within the converter to date. Techniques to track the ion beam pointing in the converter include wrapping the converter material with imaging plates, copper plates [132], or RCF in the converter [206]. Such tracking layers yield measurements of the ion beam flux and spatial distribution at a certain depth within the converter corresponding to a specific ion energy and are limited to single-shot use due to read-out requirements. To implement a rep-rated ion beam pointing diagnostic within the converter, a thin scintillator screen could be installed in front of the converter that is imaged by a camera and monitors the beam position relative to the converter body. Another option would be to drill an open slit cross section into the converter bulk material. This will allow implementation of a thin scintillator layer at a certain depth, corresponding to higher ion energies. The scintillator signal can be monitored from the rear side of the converter.

5.5.1. Implementation at the Texas Petawatt Laser Facility

Due to spatial constraints of the experimental setup at the Texas Petawatt laser facility, given by the laser propagation path and the target characterization platform, it was not possible to rotate the pitcher and converter axis. Therefore the laser forward direction and target normal direction are coinciding in this experimental setup as shown in Figure 5.7. To avoid any damage to the converter material in this scenario, the converter was placed at a distance of 4.75 cm behind the cryogenic jet pitcher target, with low enough intensity of the transmitted laser light and minimal ablation concerns. To fully eliminate the concern of ablating the converter material, the blast shield was implemented at an angle of 20° in this setup to deflect transmitted and scattered laser light. As a consequence the transmitted laser beam was send into open space allowing it to expand significantly before being incident on any other experimental components and fully eliminating

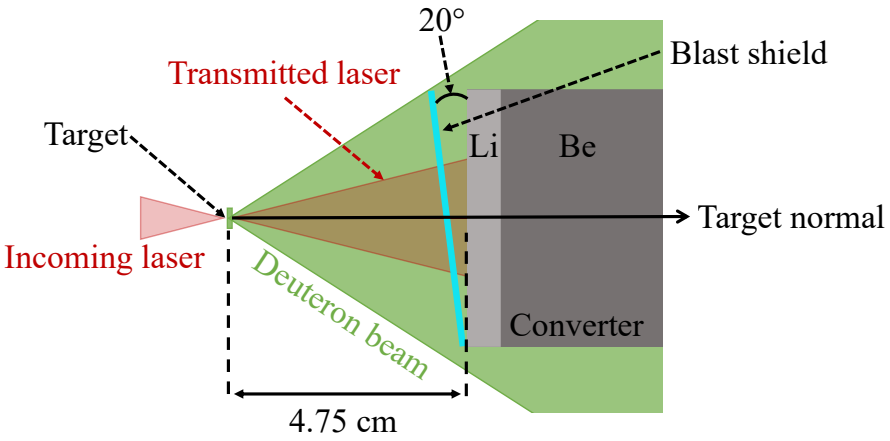

Figure 5.7.: Top view of the setup (target size not to scale). The converter is placed in the target normal direction to capture the ion beam but outside the transmitted laser cone ($f/2$) to avoid damages.

any concerns of laser induced damage to any of the components of the setup. The detailed converter setup, in terms of total length, for the experiment conducted at the Texas Petawatt laser facility will be presented in Chapter 7.

In order to adapt the converter length to the maximum energy of the accelerated ion beam during each individual experiment, it is important to closely monitor and fully characterize the deuteron ion beam. Additionally it is important to characterize the neutron beam spectrum to enhance the understanding of the dominant neutron generation processes. An optimized platform for full ion and beam characterization, generated from a cryogenic deuterium jet pitcher target and the above presented converter, is presented in the following Chapter.

6. Laser-Driven Particle Beam Characterization Platform for Cryogenic Jets

For implementation of an optimized converter in terms of thickness it is important to characterize the laser-produced ion beam energy and spatial profile, to ensure that all ions are stopped within the converter. Once the converter is implemented in the experimental target chamber, the ion detector setup is used to characterize and monitor the acceleration physics performance upon laser-target interaction. Additionally, it is important to fully characterize the neutron beam energy spectrum and the spatial distribution profile. These measurements enable identification of the correlation of the ion beam and the neutron beam parameters and the identification of dominant neutron generation mechanisms.

For this purpose an experimental platform for ion beam and neutron beam characterization was developed for implementation at a high power laser facility. The details of this platform are presented below and are divided into a section about ion diagnostics and a section about neutron diagnostics. The majority of the content presented in this chapter has been published in Reference 22.

6.1. Ion Beam Characterization Platform

In the following the different detection methods for ions will be explained especially with a focus on the characteristics of ion stopping in matter. The diagnostic based on this principle is the ion beam imager, which will be discussed. Finally an exemplary setup implementing Thomson parabolas and an imager for ion beam characterization is presented, this setup has been optimized for a cryogenic jet target.

6.1.1. Detection of Ions

On their way through a material, ions continuously interact with the surrounding electrons through the Coulomb force. Depending on the distance between the ion and the electron it is interacting with, the electron is either excited to a higher shell (atomic excitation) or fully removed from the atomic potential (atomic ionization). In the process the ion loses energy, which is transferred to the electron, with the maximum transferable energy per interaction given by 1/500 of the ion energy per nucleon [234]. This initial energy transfer can be detected by ion detectors such as MCPs or IPs, which are detector types typically used for TPs. Section 4.2 has already introduced the principle of ion beam detection by a Thomson parabola spectrometer based on the creation of knock-on electrons.

While some detectors can rely on this single ion-electron interaction mechanism, others require a larger energy transfer from ion to matter, which is why it is beneficial to consider the path of an ion through matter until it loses all its energy. This occurs during a multitude of such single electron interactions on the ions' way through matter. Since ions are not deflected greatly from their initial path through matter, one can define a range based on ion energy and material. This range defines the depth beyond which no particle with the

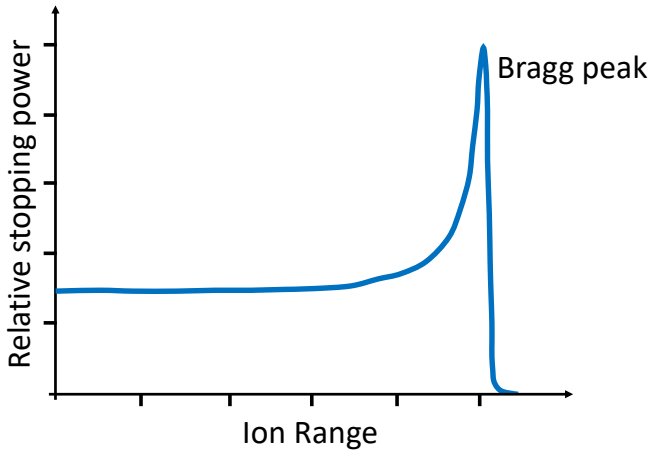

Figure 6.1.: Ions lose energy in matter following the Bragg curve, with low stopping power and energy loss at the start of their path. The stopping power then increases with decreasing ion energy resulting in the Bragg peak just before the end of the ion range.

same incident energy can penetrate any further. Another way of quantifying how a particle loses energy in a material is by defining the stopping power S which is given by the specific energy loss -dE/dx along an ion trajectory [234]. The value of the stopping power can be calculated using the Bethe-Bloch formula

$$S = -\frac{dE}{dx} = \frac{Z_1^2 Z_2^2 e^4}{4\pi\epsilon_0^2 m_e v_i^2} L\,\Delta L \quad \text{with} \tag{6.1}$$

$$L = ln\left(\frac{2m_e v^2}{I}\right) \quad \text{and} \quad \Delta L = \left(-ln\left[1-\beta^2\right]-\beta^2\right) \tag{6.2}$$

with the atomic charge state Z_2, the ion charge state Z_1, the electron mass m_e, the ion velocity v_i and the ionization energy I and the relativistic correction ΔL with $\beta = \frac{v}{c}$ [235].

One can plot the specific energy loss along a trajectory of an ion in matter and will obtain Figure 6.1, which is also know as the Bragg curve. As can be seen, the specific energy loss stays nearly constant for the majority of the propagation of the ion through matter. Towards the end, the specific energy loss or stopping power increases as the ion velocity decreases until it reaches a maximum close to the range of the ion and then quickly falls off. This peak at the end of the ions range is called the Bragg peak [234]. As a result of the increase in stopping power, the majority of the energy of the ion is deposited in the material at the position of the Bragg peak. Such a behavior is different compared to the energy loss of X-rays in matter, which lose the majority of their energy at the start of their trajectory. Detectors such as ion imagers make use of the unique stopping behavior of ions in matter by using the range to identify different energies. The detailed concept of an ion imager will be discussed in the next section.

6.1.2. Ion Imager

Ion imagers are used as a complementary diagnostic to the small sampling angle TPs to record the energy-resolved spatial profile and fully characterize the accelerated deuteron beam. While they are able to capture the full or a large fraction of the accelerated ion beam, the spectrum is measured with a lower resolution compared to TPs. Single shot Radiochromic Film (RCF) is commonly used for this purpose. These films are

	HD-V2	MD-V3	EBT-3
Active layer (μm)	12	15	28
Number of protective layers	1	2	2
Protective layer (μm)	96	120	125

Table 6.1.: Composition of the three types of RCF, HD-V2, MD-V3 and EBT-3, routinely used during experiments.

based on a radiation-sensitive dye that allows to measure absorbed doses of high-energy photon or ionizing radiation like ions and electrons up to the order of 10^4 Gy. As a comparison, standard cancer treatments reach total doses of tens of Gray delivered over the course of multiple appointments. During this work Gafchromic^{TM} HD-V2, MD-V3 and EBT-3 films were used, which are suitable for a different range of doses based on the composition of the different types of film, which is shown in Table 6.1. The HD-V2 film consists of an active layer, 12 μm thick, which is coated on a 97 μm thick polyester substrate. For the MD-V3 film a 15 μm thick active layer is sandwiched between two 120 μm thick layers of polyester. EBT films use the same sandwich structure with a 28 μm thick active layer between two 125 μm thick polyester layers. The suitability of these film for different incident doses is determined by the thickness and chemical composition of the active layer. While HD films are best suited for high doses, MD is better suited for moderate dose and EBT films are ideally used for low doses. The order of the active layer and protective layer (polyester substrate) is shown in Figure 6.2 (a) for the example of an MD-V3 film.

The main component of these colorless films is a thin ,transparent polycrystalline 'active' layer on a clear polyester base. Upon exposure to ionizing radiation the sensitive diacetylene monomer in the active layer undergoes a radiation-induced, auto-catalytic polymerization and forms a dye polymer [236]. As a result absorption bands at 618 nm and 676 nm, red light, are developed which leads to a change in color. The darkness (optical density) of the film is directly proportional to the deposited dose in that particular area and thus proportional to the number of incident ions. RCFs can be read out using film scanners, where the response of the films is generally strongest for scanners with red light sources. During the readout process it is important to maintain a high dynamic range to resolve even small color changes. The spatial resolution of the film is at most 5 μm which is influenced by the grain size of the radiation-sensitive components of approximately $2 \times 2\,\mu m^2$ [151, 236, 237]. Before readout it is advisable to store the films in a light-tight box for at least 24 hours as the polymerization process can take a few hours after exposure. Additionally, RCFs are sensitive to ultraviolet light with wavelengths below 300 nm and should not be handled in sun light.

RCFs not only allow for extraction of incident particle numbers based on optical density but can also resolve the spatial distribution at different ion beam energies through stacking of multiple films [109, 239, 240]. Figure 6.2 (b) shows a sketch of an exemplary RCF stack imaging the beam profile at energies E_1 - E_8. The energy interval covered by the RCF stack can be expanded by using filters, copper or aluminium, in between the different layers of RCF. Since ions lose the majority of their energy at a certain range, or depth in the RCF stack, a simplified assumption is that the discoloring of the film was predominantly caused by ions with a range that coincides with the position of the active layer of the investigated RCF. The ion range is a function of the type of material, the ion type and the ion energy. Using tools such as ion range calculators like the SRIM software [233], allow for precise determination of the ion energies stopped in a particular RCF layer. An example of an RCF stack used during the Texas Petawatt laser experiment is shown in Figure 6.2 (c) including nine layers of HD film with 100 μm thick aluminium filters in front of each film, five MD films combined with a 150 μm copper filter in front each and eight EBT films stacked with 300 μm copper in front of the film. The graph shows the energy deposited in each RCF layer as a function of incident deuteron energy. Considering the first MD layer for example, we can see, that no energy is deposited in the RCF for deuteron

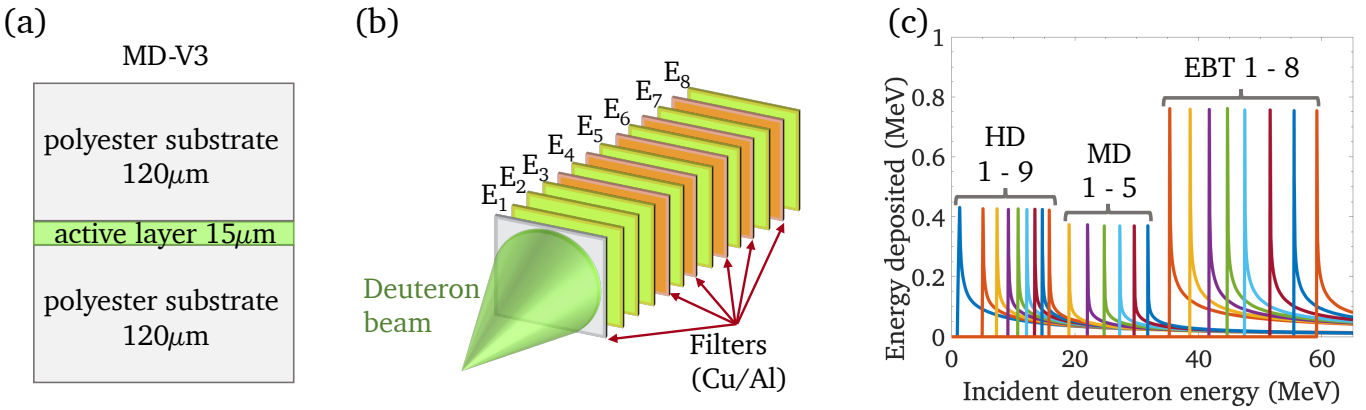

Figure 6.2.: (a) The MD-V3 film consists of an active layer of the thickness of 15 μm sandwiched between two layers of polyester with a thickness of 120 μm. It is suitable for a dynamic dose range of 1 Gy up to 100 Gy [238]. (b) RCFs can be stacked to obtain an energy-resolved spatial profile of the beam. Copper or aluminium filters can be inserted to extend the covered energy range. (c) Thee calculated energy deposited in an exemplary RCF stack is shown utilizing HD, MD and EBT films. Each color coded curve shows the energy deposited in a specific RCF based on the incident deuteron energy. As can be seen higher energy deuterons deposit energy in every layer they penetrate. However, that energy deposition is small compared to the energy deposited by ions with energies that correspond to a range and Bragg peak which falls into the active layer of the RCF, see peaks in (c). Details are discussed in the text.

energies below $\sim$ 19 MeV, which refers to the energy of particles which are completely stopped in the MD layer. Higher energy deuterons however also contribute to the discoloring to the film by depositing energy in the film, which is significantly lower than the energy deposited by the particles which are stopped in the layer. This means, that for precise evaluation of the RCF stack layers in terms of number of stopped ions at the given range/energy it is important to subtract the contribution of higher energy deuterons to the total deposited energy in a given RCF layer.

While RCF stacks are reliable detectors, that are extensively used in laser-driven ion acceleration experiments, their single shot nature is limiting their usage. As the repetition-rate of laser and target delivery systems increases it is important to develop detector systems that can match these repetition rates. For this purpose scintillator-based ion imagers are under active development in order to provide energy-resolved ion beam spatial profiles at high repetition rates. Two approaches are being followed in this effort and will be briefly presented here. The first method relies on energy resolution through stacking of thin scintillators to obtain energy resolution. On possibility is to stack different types of scintillators emitting different wavelengths imaged from the stack rear side [241, 242] or stacking the same type of scintillator at an angle and imaging the individual scintillators from the side [243]. Another method only uses one scintillator in combination with an absorber mesh, achieving energy resolution by periodically varying the thickness of the absorber on the mesh [244–246]. The spatial resolution of such setups is usually limited by the absorber mesh pixel size, the ion transverse scattering, and the grain size and lateral photon spread of the scintillator. A recent effort investigated the improvement of the spatial resolution of the scintillators through division of the bulk material into individual scintillators with smaller volume (pixelation) [247].

6.1.3. Detector Placement

Before a converter is implemented for neutron generation measurements, the laser-accelerated deuteron beam is characterized in terms of the total ion yield, the energy distribution and cut-off energy, and the spatial distribution. A standard setup to measure those characteristics contains Thomson parabola (TP) spectrometer detectors and an ion imager as shown in Figure 6.3 for the "without converter"-option.

As explained in Section 4.2, Thomson parabolas measure the energy spectrum of the fraction of the accelerated ion beam that passes through the aperture; typically capturing a very small percentage, 1 ‰= 1×10^{-4}%, of the ion beam. Three Thomson parabolas measure the ion energy distribution at different angles counter-clockwise with respect to the target normal direction to enhance the understanding of the ion acceleration characteristics of a particular cryogenic jet target. A TP in the target normal direction measures the ion beam spectrum and its directional high-energy component that will be incident on the Li/Be converter. The second TP, at 30° from target normal, measures the ion beam at the transition between the directional and the non-directional component. Monitoring the change in the ion cut-off energy across multiple shots at this location also helps maintaining consistent target alignment of the cryogenic jet. A third TP at 120° from target normal, of particular importance for mass-limited targets with a 360° ion acceleration component, measures the non-directional component of the ion beam. The ion imager is positioned at 10° clockwise from the target normal direction at a distance of around 5 cm from the target, to capture the majority of the directional ion beam. The close proximity of the 0° TP and the ion imager enables cross-calibration of the signals.

After completion of the initial ion beam characterization the converter is implemented in the setup. There are multiple possibilities to make the setup compatible with the converter, one will be discussed here. To enable the continued measurement of the ion spectrum by the target normal TP, a small hole (∼0.5 mm) can be drilled along the axis of the converter. The ion imager can be placed around the converter to track the lower-energy part of the directional ion beam, which allows to still closely monitor the ion beam-converter overlap. The three TPs and the ion imager then monitor the ion acceleration performance by comparing beam parameters to previously obtained references, which enables neutron yield predictions and benchmarking of neutron generation simulations. The ultimate goal of this setup is the identification of the dominant neutron production channel and the estimation of the conversion efficiency from deuterons to neutrons. For this purpose, it is additionally important to fully characterize the emitted neutrons. In the next section the principles of neutron detection, the platform for neutron characterization and its individual components will be discussed.

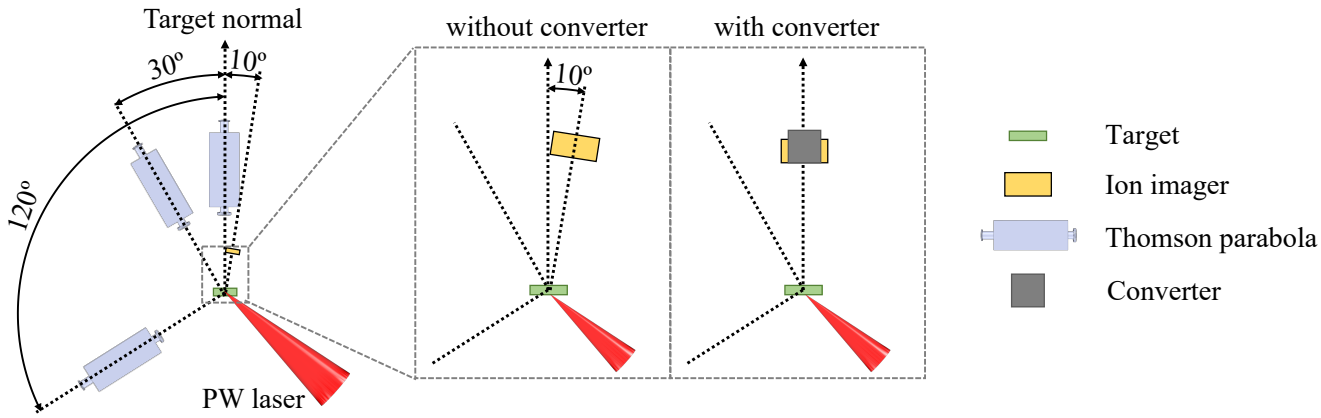

Figure 6.3.: Ion beam diagnostics, three Thomson parabolas and an ion imager, placed around the converter during neutron generation, are set up at various angles from the target normal.

6.2. Neutron Emission Characterization Platform

A detector platform consisting of bubble detectors and Neutron Time-Of-Flight (nTOF) was developed for the purpose of fully characterizing the emitted neutrons in terms of directionality, total flux distribution, and local energy spectra. Before going in detail about the individual detectors and their placement it is important to understand how neutrons interact with matter and how they can be detected. This section will therefore give a quick introduction about neutron detection techniques followed by an explanation of the operation of the chosen detectors and finally the placement of the detectors on and at larger distances from the chamber chamber wall.

6.2.1. Detection of Neutrons

Neutrons are uncharged particles, that do not interact with surrounding atoms through the Coulomb force. Instead, they predominantly interact directly with the nucleus of the target material through the strong force. The main interaction channels for neutrons are scattering and absorption. These can be further divided into elastic and inelastic scattering and electromagnetic, charged, neutron and fission interactions for absorption. Table 6.2 shows examples of reactions for the individual processes. The probability of each of those interactions is energy dependent with absorption interactions occurring more likely for lower energy (sub to few MeV) and scattering interactions gaining in significance for higher neutron energies. Since in this work the detection of fast neutron, tens of MeV energies, is of interest, their interaction with matter will be considered.

In a collision of a fast neutron with an atom, the neutron can transfer a significant amount of energy and a secondary particle, a recoil nucleus, is created. The recoil nucleus, for neutron detection typically protons [234], picks up a significant amount of energy to make it detectable following interactions explained in Section 6.1.1. The highest energy transfer is achieved for hydrogen-rich materials or other light elements, making those the most suitable detector materials for fast neutron detection.

6.2.2. Bubble Detectors

Neutron flux is commonly measured using bubble detectors [249], a dosimetry detector that is sensitive to a specific neutron energy range and insensitive to gamma radiation. For this work the specific detector employed is the BD-PND bubble detector manufactured by Bubble Technology Industries (Chalk River, Canada). BD-PND detectors have an approximate detection threshold of 100 keV and are sensitive to neutrons of few to tens of MeVs [202]. These detectors rely on the expansion of superheated liquid droplets to visually detectable

Scattering		Absorption			
elastic	inelastic	electromagnetic	charged	neutral	fission
(n,n')	(n,n')	(n,γ)	(n,p) (n,α) (n,d) etc.	(n,2n) (n,3n) (n,4n) etc.	(n,f)

Table 6.2.: Summary of neutron interactions with matter grouped by scattering and absorption mechanisms. While absorption interactions occur predominantly for sub-MeV energy neutrons, fast neutrons with energies of several MeV interact predominantly through scattering interactions [248].

size upon formation of recoil ions by incident neutrons and subsequent energy deposition of those recoil ions within the superheated bubble [250, 251].

For efficient detection, around 10^4 - 10^5 droplets of superheated liquid with a size of roughly 20 μm in diameter are dispersed in a clear, elastic polymer [249]. These small superheated bubbles can be seen as tiny black dots in the detector polymer as the pre-exposure picture shows in Figure 6.4. The sensitivity of the detector is determined by the detailed composition of the fluid and the polymer. Superheated liquids refer to liquids which exist in the liquid state above their boiling point. This can be achieved by suppressing the boiling process through immersion in a second immiscible phase, the polymer used for the bubble detector. In this scenario, the liquid can remain in it's liquid phase until it reaches its superheat limit at which point it undergoes homogeneous nucleation. As a result of nucleation the bubble vaporized to form a visible bubble within the detector volume [249].

For fast neutrons the predominant mechanism of nucleation of superheated bubbles is the generation of energetic recoil ions close to the location of a superheated bubble. The created recoil ions lose energy on their way through the superheated bubble. If the energy deposited within a time frame of 10^{-3} s surpassed the energy necessary to heat the fluid to its superheated limit, it will vaporize entirely. Figure 6.4 shows a cartoon in the center illustrating the generation of recoil ions and the resulting bubble growth. This energy threshold makes bubble detectors insensitive to gamma rays, produced during a short pulse laser-target interaction, as the deposited energy in a bubble is insufficient for nucleation. It is important to note, that during the detection process any information about the incident neutron is lost. Additionally, the size of the bubble is independent on the neutron flux through the detector, but instead directly dependent on the volume of the superheated fluid available [249].

The number of bubbles is proportional to the total deposited energy dose, given as a calibration of bubbles to mrem, which allows conversion to the number of incident neutrons. Multiple groups have investigated the

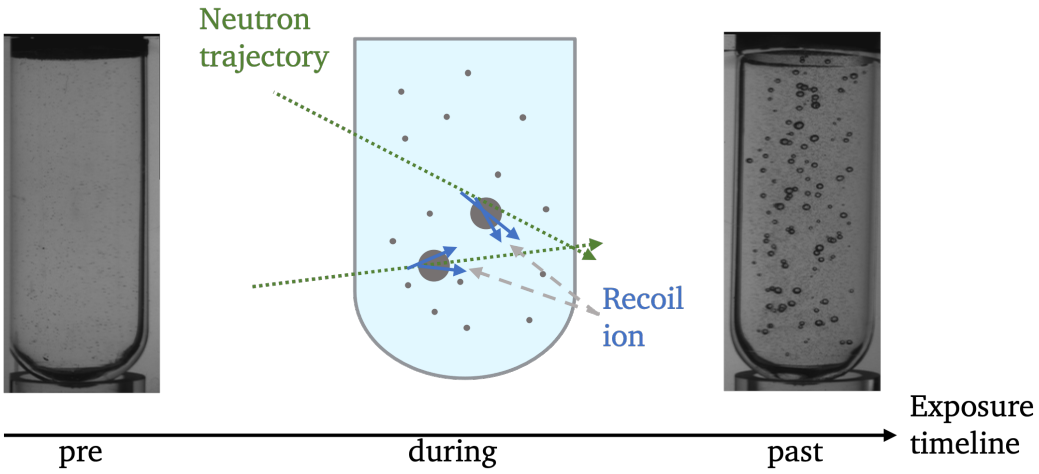

Figure 6.4.: Pre-exposure (left), during bubble formation (center) and post-exposure (right) bubble detectors. The small superfluid bubbles are barely visible for the eye before exposure to neutrons. During exposure, recoil ions deposit energy in the bubbles leading to their vaporization and expansion. Post-exposure the expanded bubbles are visible to the eye and can be counted and converted to neutron numbers. Pictures correspond to data of shot 12357 (E_L =73 J), Section 7.8.1, from the experiment conducted at the Texas Petawatt laser presented in Chapter 7.

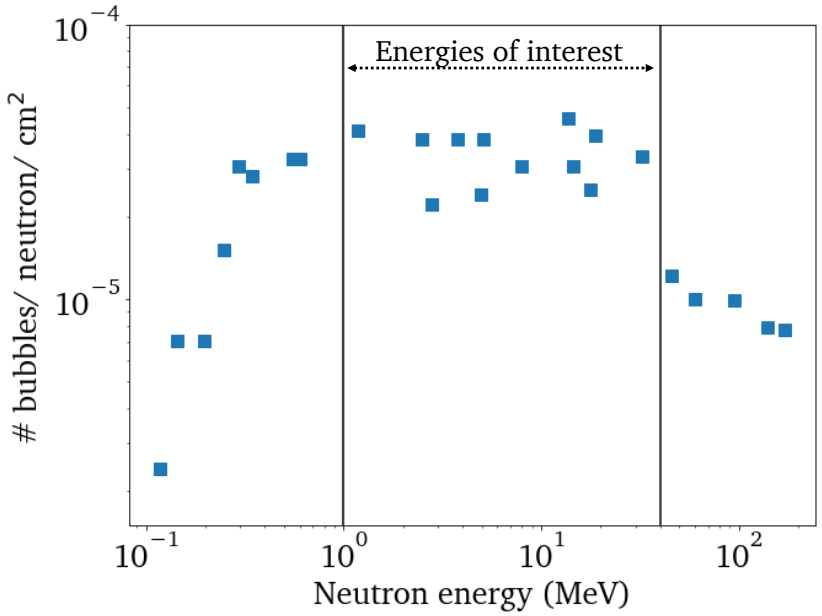

Figure 6.5.: Response of a BD-PND bubble detector to neutrons of varying incident energies. Outside of the energies of interest, the response drops of quickly as energy deposition decreases. Within the interval of interest the response remains mostly flat with an average response of 3.3$\times$ 10^{-5} bubbles/neutron/cm^2 [202, 252, 253].

sensitivity of bubble detectors with a response normalized to 1 bubble/mrem for all energies as a function of incident neutron energy [252, 253]. The combined data is shown in Figure 6.5 with the energy interval of interest for this work indicated by the dashed arrow and the two black lines. For the evaluation of experimental data a average response of the bubble detector is calculated in the energy range of interest which obtains a response of 3.3$\times$ 10^{-5} bubbles/neutron/cm^2. Outside this interval the response of the bubble detector drops off quickly as recoil ions do not deposit enough energy in the superheated fluids anymore to cause vaporization. The average response of the bubble detector in the energy range of interest is 3.3$\times$ 10^{-5} bubbles/neutron/cm^2.

While the manufacturer-stated calibration has been proven to differ from the actual response of the detector by up to 20% [254, 255], those uncertainties can be mitigated by performing a separate calibration measurement with a neutron source of known flux. Single-shot compatible bubble detectors can be reused by recompression of the formed bubbles when applying external pressure to the polymer and the superheated bubbles. It is recommended to do so as soon as possible after counting the number of bubbles generated during a shot or shot series, as bubbles can grow to a size where they are no longer recompressible when left uncompressed [249]. For precise neutron flux measurements at high repetition rates, this detector can easily be adapted, for example by monitoring the bubble count in the detector in real time over the course of a shot sequence, as bubble formation only takes a few milliseconds [256]. ^{3}He-based or other proportionally counting dosimetry detectors are other alternatives for high repetition-rate experiments [257, 258].

6.2.3. Neutron Time of Flight Detectors

Neutron time-of-flight (nTOF) detectors can measure the full neutron energy spectrum along a single line of sight in an experiment, sampling a small solid angle of the overall generated neutrons. Typically, these devices consist of a fast-decaying (a few ns) scintillator, such as organic plastic, which is coupled to a Photomultiplier

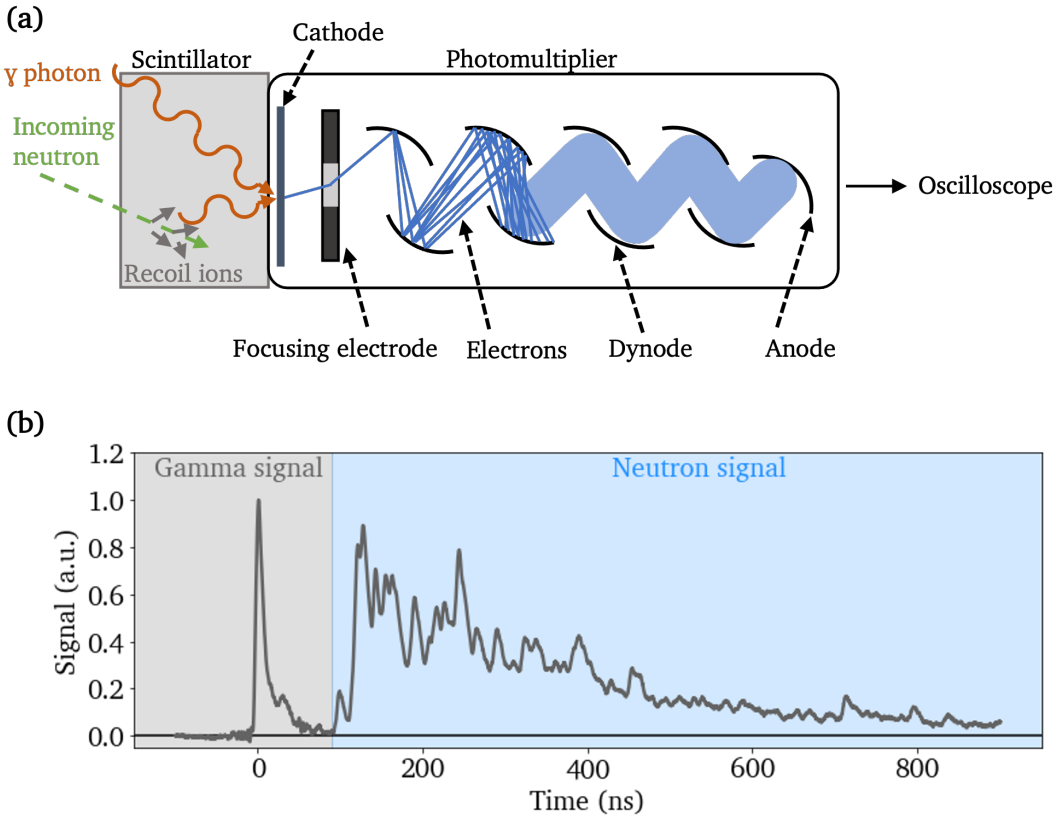

Figure 6.6.: (a) Setup of an nTOF detector, consisting of a scintillator and a photomultiplier. The whole assembly is sensitive to gamma radiation generated outside of the detector and photons triggered by recoil ion generation within the scintillator. Photons impinging on the cathode free an electron that is accelerated and multiplied in a series of dynode stages. The signal is then readout at the anode and recorded by an oscilloscope. (b) Raw nTOF detector trace recorded for a pitcher–catcher configuration located 7.2 m away with 27 cm lead shielding in front of the nTOF. The trace recorded on shot 12359 with a laser energy on target of 73 J, experimental results presented in Section 7.9.1, shows a gamma peak component followed by the neutron signal.

tube (PMT) for signal conversion and amplification. Contrary to bubble detectors, nTOF detectors are sensitive to any kind of ionizing radiation, including gamma radiation produced during the interaction of the high-power laser with the pitcher. Since PMTs are sensitive to any light, it is important to wrap the scintillator and the connection between scintillator and PMT with light tight tape such that only signal originating from gamma radiation or photons created within the scintillator is detected.

Figure 6.6 (a) shows a sketch of an nTOF detector setup. Gamma radiation (orange) generated upon laser-target interaction, travels at the speed of light, and reaches the detector shortly after the interaction. While gamma radiation can generate a free electron directly in the cathode of the photomultiplier tube, non-ionizing radiation, such as neutron radiation (green), is detected indirectly through creation of recoil protons in the scintillator material. These recoil protons excite scintillator atoms to an unstable higher energy state through energy transfer. This state then decays via emission of light, which is collected by the PMT and converted into an electronic signal through the photoelectric effect at the surface of the cathode. The generated electrons are accelerated towards a dynode where the electron signal is amplified through generation of secondary

electrons. Multiple dynode stages amplify the signal with a gain of around 10^6 before the signals is read out at the anode. The electronic output signal is recorded as a function of time using a fast sampling rate ($\geq$1 GHz) oscilloscope.

Figure 6.6 (b) shows a exemplary raw nTOF trace, normalized to the peak value of the gamma signal, recorded during shot 12359 of the experiment conducted at the Texas Petawatt laser facility. The response of the detector based on the incident gamma radiation is indicated by the grey shaded area, while the neutron signal is detected over a much longer timescale after the initial gamma signal triggered response as shown by the blue shaded area. The time of the initial laser–pitcher interaction (t_0) is given by the gamma signal and the γ photon's time of flight to the nTOF detector. After determination of t_0, the neutron time-of-flight can be calculated for any data point along the signal. Using this time-of-flight value in combination with the measured distance from the neutron source to the detector, the energy of the neutrons incident on the detector is calculated. Due to the electronic read-out and fast decay time of the scintillator, these detectors are naturally suited for high-repetition-rate operation.

Due to the direct detection of gamma radiation by the scintillator, nTOF detectors are more sensitive to gamma radiation than they are to indirectly detected neutrons, which oftentimes results in the saturation of the detector by incident gamma radiation. A clear temporal separation between the fast gamma and slower neutron signal (Figure 6.6 (b)) can be achieved for sufficiently large distances between detector and the neutron source. For quasi-directional to quasi-isotropic neutron emission neutron fluxes and consequently signal levels decrease with the square of the distance between source and detector. For the optimal detector placement one therefore has to strike the balance between sufficient temporal separation between gamma and neutron signals and high enough incident neutron flux above the background noise. For this reason, neutron detectors are typically placed $\sim$1–8 m from the interaction, where the exact distance depends on the expected neutron fluxes and the detection efficiency of the detector. To then achieve a clear separation between gamma and neutron signal as shown in Figure 6.6 (b), shielding is added to the front of the detector to attenuate the gamma signal.

Detector Shielding

To identify well-suited shielding materials it is necessary to study the attenuation of gamma radiation and neutrons in different materials. For the purpose of shielding the gamma radiation generated during a

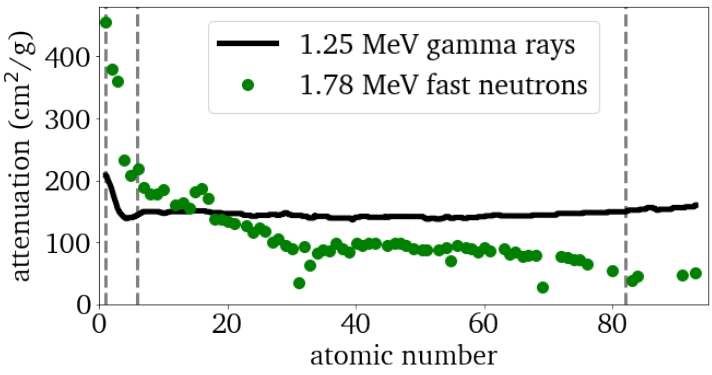

Figure 6.7.: Mass attenuation coefficient as a function of atomic number. Neutrons are best attenuated by low atomic number materials, while the opposite is valid for gamma radiation. Dashed lines indicate hydrogen (A=1), carbon (A=6) and lead (A=82). Adapted from [259].

short-pulse laser-matter interaction experiment, an efficient gamma ray absorber is required. However, the material should not have a high attenuation coefficient for neutrons, as the detected neutrons should remain predominantly undisturbed. Figure 6.7 displays the mass attenuation coefficient for high-energy gamma rays and high-energy neutrons as a function of atomic number. While gamma rays are most efficiently attenuated by high atomic number materials, fast neutrons are most efficiently attenuated by lower atomic number materials.

Out of all high atomic number materials, lead (Pb) is a standard choice as a gamma shielding material due to its high attenuation of gamma radiation. A typical neutron shielding material is polyethylene, which is a mixture of carbon and hydrogen, showing a higher attenuation for neutrons due to a lower mass number. To investigate the behavior of the attenuation coefficient of X-rays as a function of energy for the two commonly used shielding materials for gammas and neutrons, 6.8 (a) plots the attenuation coefficient as a function of photon energy. Due to the higher density of lead compared to polyethylene, the attenuation coefficients differ by up to three orders of magnitude depending on the X-ray energy. To achieve a clear separation such as the one shown in Figure 6.6 (b), the thickness of the lead shielding is adjusted between approximately 5–30 cm, depending on the level of gamma radiation present during a short-pulse laser-matter interaction experiment.

To prevent scattered neutrons from entering the scintillator, additional neutron shielding, made of 5 cm thick high-density polyethylene (HDPE), modeled as CH_2, is added to the sides and part of the front of the detector, leaving a circular hole in the shielding of the same diameter as the scintillator. This ensures that only neutrons on a direct flight path from the neutron source to the detector are measured. HDPE has a low mean free path for neutrons, see Figure 6.8 (b), effectively preventing scattered, lower-energy neutrons from being detected in the scintillator. To estimate the shielding thickness necessary to block these scattered neutrons, one needs to consider the mean free path of neutrons in the shielding material and the number of collisions necessary to reduce the energy of the incident neutron to a specific value. The main difference in shielding thickness is determined by the number of collisions n given by

$$n = \log \frac{E_n}{E_0} \Big/ \log \frac{A^2+1}{(A+1)^2}, \tag{6.3}$$

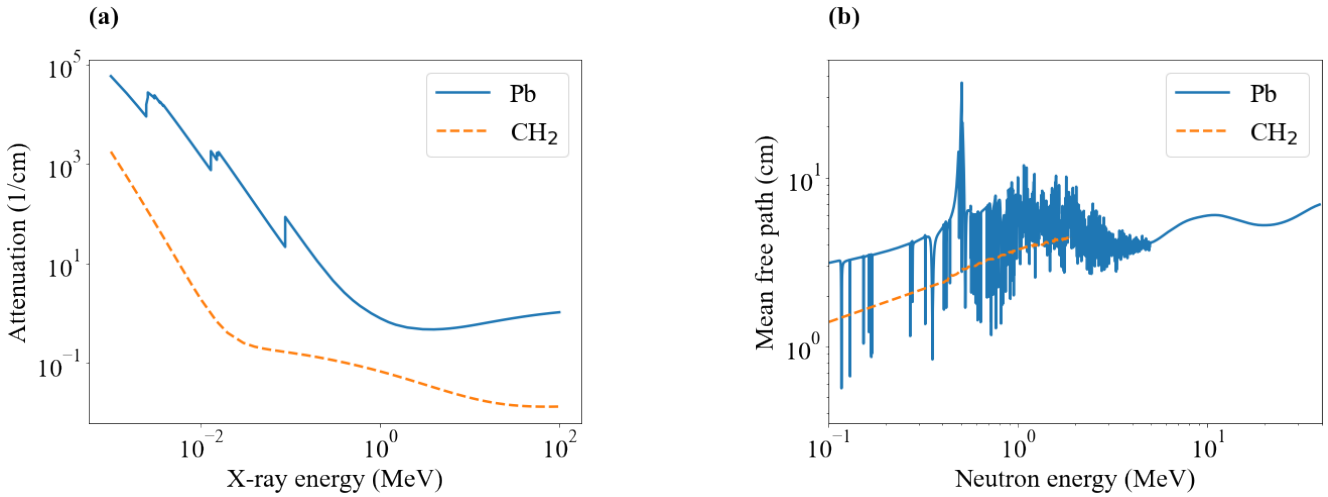

Figure 6.8.: (a): X-ray attenuation coefficient (1/cm) shows superior x-ray attenuation up to three orders of magnitude in lead (Pb) over polyethylene (CH_2) [260]; (b): Neutron mean free path in lead and polyethylene show a lower mean free path for polyethylene [219, 221, 261, 262].

where E_0 is the initial neutron energy, E_n is the final neutron energy and A is the atomic mass number [248]. The final neutron energy E_n can be chosen as the drop-off in detection sensitivity of the nTOF detector at $\sim$1 MeV. Considering a neutron with 5 MeV initial energy, the number of necessary collisions to downscatter the neutron to a final energy of 1 MeV for the different materials are:

$$n_H = 3, \qquad n_C = 11, \qquad n_{CH_2} = \frac{1}{3}\, n_C + \frac{2}{3}\, n_H \approx 6, \qquad n_{Pb} = 169. \tag{6.4}$$

The combination of a similar mean-free path of neutrons in lead and polyethylene and a factor of $\sim$30 higher number of collisions necessary for lead makes polyethylene is a superior neutron-shielding material. It is important to note that this calculation is only an estimate of the shielding thickness; for more precise values, it would be necessary to take into account diffusion in the material and the energy loss of the neutron along its path. Furthermore it has to be noted, that neutron shielding material close to the detector should be kept short in thickness as extended shielding walls can result in a source of background counts close to the detector due to enhanced scattering interactions of the neutrons with the shielding material. As a result the neutron shielding was chosen to be 5 cm to allow for stopping of low energy neutrons while only resulting in single to few scattering events for higher energy neutrons.

Calibration

nTOF detectors are initially not calibrated, which means that the relation between the measured signal (e.g., Volts) and the incident neutron numbers on the detector as a function of energy is unknown. To establish the relation between measured signal and incident neutron numbers, it is important to know what mode the detector was operated in. For low incident neutron fluxes, the detector can be operated in counting mode. Here, individual peaks can be detected with preserved signal height and timing such that single neutrons can be resolved. In this case, the total number of neutrons incident on the detector as well as the signal per incident neutron can be determined, taking into account the detection efficiency of the scintillator. While the counting mode is preferred for its high single-neutron detection efficiency, it cannot be sustained during laser-driven neutron generation. In such experiments the incident neutron flux the neutron flux is much higher and as a consequence multiple neutrons are detected at once, referred to as Campbelling or mean square voltage (MSV) mode. In this mode, both the signal mean and variance are proportional to the event rate [263, 264]. Consequently, the response of the detector becomes nonlinear and is not directly proportional to the incident neutron flux.

It is therefore necessary to calibrate the response of the detector to neutrons, preferably in an environment similar to the high-radiation environment present during laser-matter interactions. This calibration measurement can be conducted offline at a neutron source with a well-characterized spectrum such as LANSCE (0.1 - 400 MeV, up to 0.1 $\frac{\mathrm{n}}{\mathrm{cm}^2\ \mathrm{MeV\ s}}$) [125]. Such a measurement additionally enables the identification of gain settings and neutron fluxes at which the signal of the scintillator/PMT assembly becomes independent of the incident neutron flux (i.e., saturation limits).

6.2.4. Detector Placement

Studying underlying neutron production mechanisms and governing ion or laser beam parameters and their effect on neutron yield or the energy distribution requires a thorough characterization of emitted neutron directionality, total flux, and energy distribution. Using bubble detectors and nTOF detectors described above a neutron diagnostics platform was developed and will be presented here. Figure 6.9 shows the location of

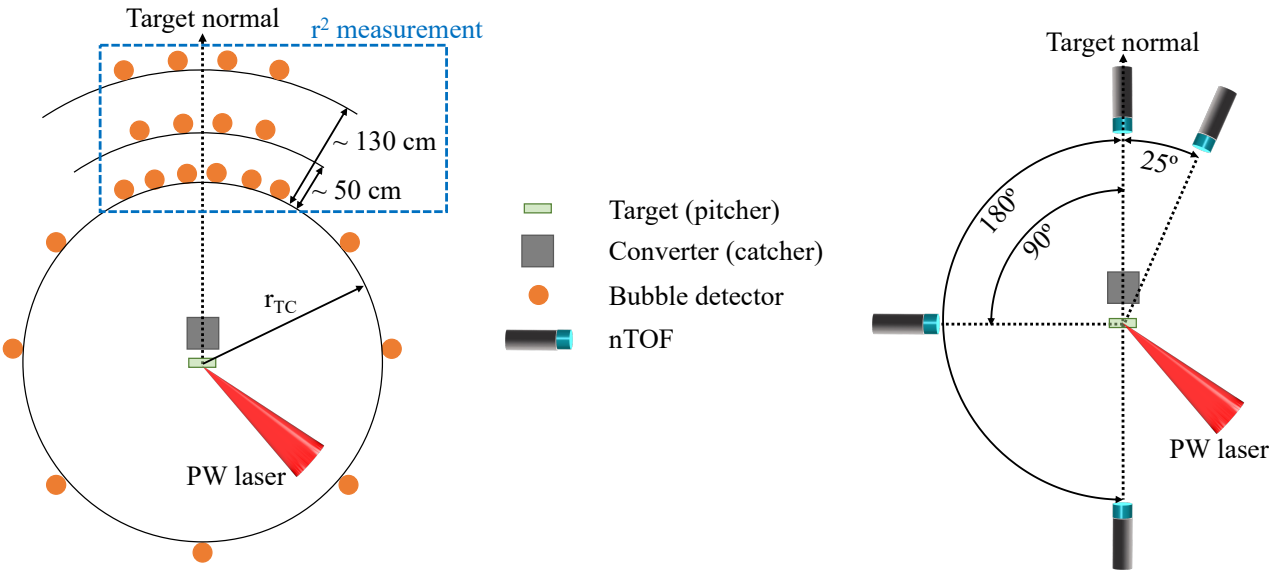

Figure 6.9.: Setup for the neutron flux measurement in the laser plane using bubble detectors (left). Characterization in 360° enables identification of a directional component of the neutron emission profile. The r^2 measurement setup allows to identify the dominant neutron source in the setup. The energy spectrum is measured using neutron time-of-flight detectors at selected angles (right).

the bubble detectors (left) and nTOF detectors (right) in the laser plane. Additional placement of bubble detectors or nTOF detectors out of plane enables to investigate the emission characteristics of neutrons in 3D.

An ensemble of bubble detectors (BD-PND) measures the neutron numbers at a specific location to provide insight into the spatial variation of generated fast neutrons. The setup covers the full 360° in the laser plane, with the majority of the detectors mounted on the target chamber outside wall at a distance r_{TC} from the pitcher (Figure 6.9). To resolve the transition from the predicted breakup and stripping dominated high-yield directional component to the isotropic emission, bubble detectors are mounted closer together in the target normal direction and spaced out at larger angles from target normal. The assessment of the isotropic emission from the bubble detectors at large angles allows estimating the contribution of the directed neutron beam to the overall yield. Placing bubble detectors outside of the laser plane also allows to investigate the widely made assumption of a rotational symmetric emission profile.

While bubble detectors with different material compositions can be used to sample a portion of the energy spectrum as part of a bubble detector spectrometer [249], their sensitivity drops significantly for energies above 10 MeV. Additionally their large sensitivity range does not allow to distinguish between different incident neutron energies. Neutron energy distributions are commonly measured by employing nTOF detectors at different angles. In this setup, four nTOF detectors are placed in target normal direction, at 25°, 90°, and 180° from target normal.

Assuming a dominant neutron source, typically the converter, and calculating the distance from each detector to the converter, a flux per solid angle can be calculated and compared across diagnostics. This however requires the identification of the primary neutron source with high enough fidelity. Depending on the distance between the pitcher and the converter and the emission profile of the ion beam, not all the deuterons are fully stopped in the converter and can generate neutrons in other components within the target chamber or the chamber wall. Distinguishing between the different neutron sources and determining the main source

location is especially important to determine the source size of the forward-directed neutron beam and its opening angle and for more precise predictions of deuteron-to-neutron conversion efficiency.

r^2 Measurement

A dedicated setup was developed for the purposed of determining the dominant neutron source using bubble detectors in the target normal direction and laser plane at various distances (0 cm, 50 cm and 130 cm) from the target chamber wall; see blue dashed box in Figure 6.9. The formula of the solid angle Ω is given by $\Omega = A/r^2$, where A is the cross-sectional area of the bubble detector and r is the distance from the neutron source. As the formula shows, the relative solid angle sampled by a bubble detector is proportional to the square of the distance r from a neutron source. Thus, the measured neutron number per solid angle is directly sensitive to the relative placement of the detectors with respect to the neutron origin.

Assuming a source location and taking the neutron numbers measured at the chamber wall, the neutron numbers can be predicted at 50 cm and 130 cm using the r^2-scaling following

$$\frac{N_1}{N_2} = \frac{r_2^2}{r_1^2} \tag{6.5}$$

with the neutron numbers N_1 and N_2 at two different respective distances r_1 and r_2. These predictions are then compared to the experimentally detected neutron numbers. If the numbers match within the margin of error given by the experimental values, the assumed source is the dominant source for neutron generation in target normal direction. The main uncertainty of this method is given by the inherent uncertainty in the response of the bubble detectors ($\sim$20%) [265], with a smaller contribution due to measurement uncertainties of the distance from detector to the assumed source location ($\leq$ 1%). The contribution of neutrons generated in different locations such as the chamber wall is minimized by placing the bubble detectors in the ”shadow” of the converter. In this region, no deuterons will interact with the chamber wall directly adjacent to the bubble detectors, thus enhancing the accuracy of the r^2 measurement. Comparing the neutron signal detected outside of the converter shadow allows to estimate whether the overall dominant neutron source, responsible for the quasi-isotropic neutron emission, is the converter or the chamber wall.

7. High Flux Directional Fast Neutron Beams using Cryogenic Deuterium Jets

For applications such as material composition studies, neutron beams with high directionality ensured a constant neutron flux across the full sample. Paired with a high flux, measurements can achieve a high signal-to-noise ratio, ultimately enabling single shot studies of short-lived phenomena. Neutron-induced damage studies for fusion energy science require high neutron fluxes comparable to fusion environments. Laser-driven directional neutron beams produced by deuteron breakup reactions, showing peak fluxes around 10^{19} neutrons/cm^2/s close to the converter, are promising to achieve the necessary fluxes for such experiments. However, the implemented multi-component experimental setups increase the operational parameter space that needs to be optimized for efficient neutron generation and introduce additional uncertainties with regards to the origin of the detected neutrons. Minimizing the number of parameters and limiting uncertainties is a key step towards the development of a reliable laser-driven high-flux directional fast neutron source, which has not been studied in detail in the past.

The pitcher–catcher neutron generation platform developed in this work combines the converter design, presented in Chapter 5, with the detector platform for ion and neutron beam generation, described in Chapter 6. It is well suited to study the feasibility of such a source as a function of

- the stability and controllability of the pitcher target and the generated deuteron beam
- the contribution of different neutron generation locations to the directional neutron beam.

Utilizing the cryogenic liquid deuterium jet as a pitcher target, this setup was implemented for an experiment at the Texas Petawatt (TPW) laser facility at the University of Texas at Austin to study directional neutron beam generation.

In the following, the experiment concept is presented followed by a discussion of the laser and target characteristics affecting the laser-target interaction. Two subsequent sections introduces the ion diagnostic setup and examples of measured deuteron beam spectra and discuss the ability to control target stability and orientation. The optimized converter designs for the presented shots are explained, followed by the introduction of the neutron diagnostics setup. Prior to the discussion of the experimental results, a concept for different cases of deuteron beam-converter overlap is explained. Four consecutive neutron generation shots are analyzed, distinguishing between full and partial ion beam overlap with the converter and resulting dominant neutron source locations. Directional neutron beams generated in the converter are observed for full ion beam-converter overlap, while partial or minimal ion beam-converter overlap leads to an isotropic emission profile generated in the chamber wall. Remaining analysis tasks are discussed following the presentation of the collected data. Next steps towards a follow-up experiment are briefly laid out at the end of the chapter.

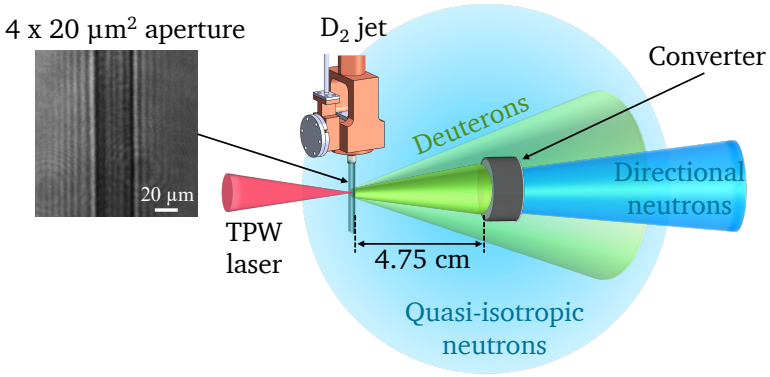

Figure 7.1.: The Texas Petawatt laser is focused on the planar cryogenic liquid D_2 jet target for deuteron acceleration. A shadowgraphy image of the planar cryogenic deuterium jet target is shown in the inset. Deuterons are accelerated as a directional beam with a TNSA-like spectrum. This beam impinges on the converter 4.75 cm behind the pitcher target and produces neutrons through nuclear reactions. The neutron beam has a quasi-isotropic and a directional component.

7.1. Experimental Concept

The Texas Petawatt laser, with a wavelength of 1057 nm, was focused on the planar cryogenic liquid jet target at an incident angle of 0°, generated using a rectangular aperture (4×20 µm^2), using an f/3 final focusing optic. For laser pulse cleaning and contrast enhancement a plasma mirror was implemented 4.2 cm in front of the target, which was position at the target chamber center (TCC). Plasma mirrors transition from non-reflective to reflective at an ultrafast timescale through ionization and formation of an overcritical surface plasma upon high-intensity laser irradiation. Consequently, prepulses or the pedestal of laser pulses are only partially reflected while the main pulse is reflected completely, enhancing the overall pulse contrast. For efficient ion generation using a near-critical density cryogenic jet target, laser intensities on target exceeding 10^{18} W/cm^2 and a laser-pulse temporal contrast exceeding 10^{10} (10^8) in the multiple (sub)-picosecond window before arrival of the main laser pulse are crucial [94, 164, 266]. A reflectivity of the plasma mirror of 76% was determined prior to the experiment.

The ion beam is accelerated from the backside of the cryogenic target with a TNSA-like emission profile. Neutrons are generated when the pure deuteron beam impinges on the converter. It is placed 4.75 cm away from the pitcher target along the laser forward direction in the cone of the expanding deuteron beam. At this distance, a 14° half angle subset of the deuteron beam is fully captured by the converter, as shown by the lighter shaded green cone in Figure 7.1. Considering the half opening angle and following TNSA-like emission characteristics, we can estimate that all deuteron ions with energies above approximately 30 MeV are captured by the converter. Due to the characteristics of different neutron generation channels responsible for neutron production, the neutrons are emitted both quasi-isotropically and directionally as explained in Section 5.3.

7.2. Laser-Target Interaction

The first step in the neutron generation process using a pitcher-catcher setup is the ion acceleration from the pitcher target. This section will briefly discuss the laser parameters of the TPW laser and the average geometry of the planar cryogenic deuterium jet during the conducted experiment. Table 7.1 summarized the laser parameters on target for the individual shots presented in this chapter. On average the laser delivered

Shot No.	Pulse duration (fs)	focal spot diameter (μm)	Energy (J)	Peak intensity (W/cm^2)	Average intensity (W/cm^2)
12355	138	6.8	76	1.2×10^{21}	3.8×10^{20}
12357	156	6.4	73	1.1×10^{21}	3.7×10^{20}
12359	135	5.7	72	1.2×10^{21}	5.2×10^{20}
12365	133	6.2	75	1.3×10^{21}	4.7×10^{20}

Table 7.1.: Individual laser parameters on target, as measured by the on-shot laser diagnostics. The focal spot is given by the diameter enclosing 50% of the laser energy. Average intensities are calculated across the focal spot area.

74 J on target reaching peak intensities over 1×10^{21} W/cm^2 across a 6.2 μm FWHM diameter focal spot with an average pulse duration of 140 fs. The experimental setup was designed such that the laser was focused onto the target at an incident angle of 0° and coinciding laser forward and target normal directions.

The thickness of the cryogenic liquid deuterium jet target was measured prior to each shot using the Michelson interferometer setup presented in Section 3.2.1. Average dimensions of the cryogenic deuterium jet were calculated for all measurements using a 4×20 μm^2 nozzle. The jet consists of a thin, flat region in the center, that is on average 10 μm wide and 1.2 μm thick, see Figure 7.2. While the width of the rims was determined to be 6.7 μm, a thickness was challenging to obtain from the interferometry measurement due to diffraction and refraction effects through and around the rims. Based on fluid dynamics, the two columns framing the planar region are predicted to be circular as such a shape is energetically more favorable. We therefore assume that the thickness of the rims is also equal to 6.7 μm.

Since the laser focal spot diameter and the width of the planar sheet of the target are on the same order of magnitude with pointing jitters on the order of a few micrometers, high control over the target and laser pointing for maximal laser-target overlap is important. Interaction between the TPW laser and the cryogenic target can be distinguish as a 'centered interaction' and a 'off-center interaction'. In a 'centered interaction', as shown in Figure 7.2 on the left, the laser focal spot overlaps completely with the planar sheet section of the

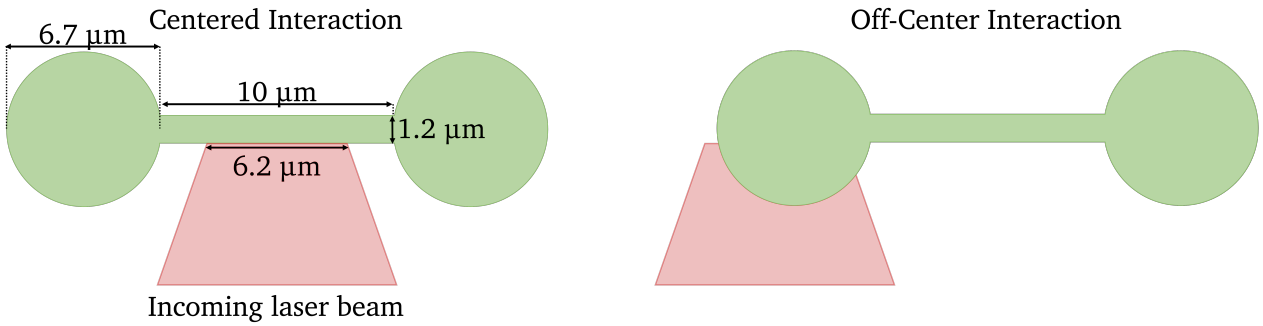

Figure 7.2.: The planar region of the cryogenic liquid jet was on average 10 μm wide and 1.2 μm thick. Two 6.7 μm wide rims framed the planar center sheet. The incoming laser beam was focused to an average spot size of 6.2 μm diameter containing 50% of the laser energy. Interactions are distinguished between center interactions (left), where the laser beam interacts with the planar sheet, and off-center interactions (right), where the laser interacts predominantly with one rim.

cryogenic jet target. 'Off-center interaction' includes shots where either a portion of the laser light misses the target, as depicted in Figure 7.2 on the right, the primary interaction with one of the rims or the interaction of the laser beam with part of the rim and part of the planar sheet. A centered interaction is the most favorable as it results in a TNSA-like ion emission. The probability of such a centered interaction was maximized by minimizing lateral shifts of the cryogenic jet through optimized operation parameters, as described by Curry et al. in Ref. 109. Correlation between the pointing of an unamplified test shot and the main laser shot enabled increased pointing stability by applying strategic corrections to mirror positions prior to the shot.

Additionally to the laser-target overlap, the relative angle between the laser propagation axis and the target normal are of importance. While enhanced control of the jet position and orientation was demonstrated during this experiment [109], vacuum fluctuations or pressure differences within the sample gas delivery line can result in the jet geometry oscillating between different stable target orientations. Target manipulation stages were used leading up to each shot to correct the rotation and repositioning of the target in the laser focal plane. Using lateral translation motors, the overlap between the target and the laser focal plane can be ensured at all time, while target orientation changes just before a shot were not always recoverable in time. Ongoing research is dedicated towards understanding and controlling these fluctuations in geometry based on operational parameters to enable precision ion beam steering. In the case of a deliberately rotated target, the focal plane of the laser is only partially overlapping with the target which results in changes in the focal spot size and intensity on target as a function of position. To determine whether such changes play a role in the laser-target interaction one has to consider the Rayleigh length z_R of the laser focus. It corresponds to the distance from the focal plane to the location at which the cross-sectional area of the laser beam has doubled in size. The Rayleigh length can be calculated using the laser focal spot radius r_L and the laser wavelength λ_L following

$$z_R = \frac{\pi r_L^2}{\lambda_L} \quad . \tag{7.1}$$

For the TPW laser the Rayleigh length is 26.8 μm. For a hypothetical angle of incidence of 45°, the furthest point of laser target interaction is 10 μm away from the laser focal plane, well within the Rayleigh range of the laser. We can therefore neglect this effect. In the experiment, the orientation of the target on shot can be estimated based on the emission profile and detected spectra of the accelerated deuteron beam.

7.3. Ion Diagnostics Setup

The mass-limited nature of the target results in an acceleration of ions in 360° in addition to the directional ion beam component. This 360° component of the ion acceleration usually shows a lower flux and cut-off energy than the directional component [122]. Due to the ion emission normal to the target surface in the TNSA regime, the ion beam is send away from laser forward for angles of incidence smaller than 90°. This effect can be used to manipulate and steer the ion beam pointing by rotating the jet target. For all shots on target, the relative orientation of the target with respect to the laser forward direction on shot can be indirectly diagnosed by measuring the directionality and profile of the accelerated ion beam.

Three Thomson parabolas (0°, 30°, 122°) monitored the deuteron acceleration prior to implementation of the converter in the experimental setup. Figure 7.3 shows the ion diagnostics setup on the left including all three TPs. The TPs at 0 and 30° are dedicated to measure the directional TNSA-like component of the deuteron acceleration. Using the TP at 122°, the 360° component of the deuteron acceleration is monitored. Once the converter is implemented in the chamber, the TP in laser forward direction is removed and RCF layers within the converter monitor the deuteron acceleration at chosen energy intervals in this direction.

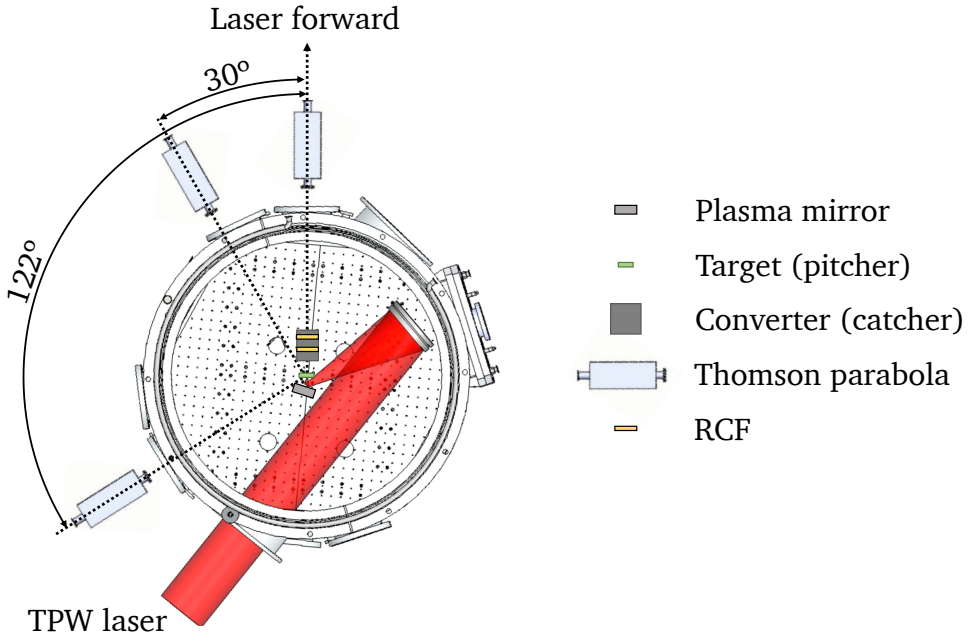

Figure 7.3.: Ion diagnostics setup consisting of three Thomson parabolas and RCFs placed between converter layers.

The exact placement of the RCF layers within the converter is presented in Section 7.5. Since RCFs detect a larger cross-section of the accelerated deuteron, the recorded signal enables a more precise target rotation and deuteron beam pointing estimate than with only TPs.

7.3.1. Ion Detector Data Evaluation

The ion beam spectra were recorded using image plate detectors, BAS-TR (Fujifilm, Tokyo, Japan) [267–269], located in each TP. After exposure of the image plates, they were read out using a GE Typhoon FLA 7000 image plate reader (GE Healthcare, USA). For each image plate the fading of the signal was taken into account by recording the time of exposure and the time of the read-out. A calibration measurement using the decay of the radioactive ^{14}C isotope via the emission of an electron relates the initially recorded Quantum Level (QL) values to photo-stimulated luminescence (PSL) values. These PSL values can then be converted to impining deuteron flux using the experimental measurement from Alejo et al., see Reference 268, and the simulation results presented by Lelasseux et al. [269].

The RCFs were evaluated post-exposure by scanning them using an Epson Perfection V750 Pro scanner (Epson, Japan) and converting counts to Optical Density (OD) using the self-reference technique described in Reference [109]. The film dependent calibration curves published by Curry et al ([109]) then allow for conversion to deposited dose given in Gray. While ultimately the conversion from Gray to deuteron numbers detected by the RCF is of importance, as part of the future analysis presented in Section 7.10, the analysis presented here will focus the determination of the ion beam pointing and opening angle.

7.4. Deuteron Acceleration from Planar Cryogenic Deuteron Jets

Prior to removing the laser forward TP from the target chamber, the pointing stability of the deuteron jet and the resulting deuteron beam was tested and optimized across five individual shots. While it was possible to keep the position of the jet stable, the deuterium jet could flip between two stable rotation positions with an oscillation period of tens of seconds up to a few minutes. The high position stability of the cryogenic jet was achieved by precisely controlling the flow and the temperature of the cryogenic jet. The temperature stabilized using a proportional-integral-derivative (P-I-D) temperature controller (LakeShore Cryotronics, USA) with fluctuations below 0.1 K. A high precision mass flow controller (MKS Instruments, USA) ensured a constant pressure and flow of gas along the supply line. Prior to each shot the temperature and pressure settings were scanned to optimize the operational parameters for a given background pressure and nozzle geometry. Reasons for the rotational instability of the jet could be contamination in the nozzle, which resulted in small fluctuations in the cryogenic flow, or small fluctuations in the vacuum pressure of the target chamber leading up to the shot.

Two examples of deuteron spectra for separate shots with a rotated jet target are shown in Figure 7.4. On the left, a higher energy beam component is observed by the TP at 30° from laser forward direction. Deuteron energies reach up to 44 MeV and deuteron fluxes of just under 10^{13} neutrons/MeV/sr are observed. Around half of that cut-off energy, 18 and 23 MeV, and an order of magnitude less in peak deuteron flux up to 10^{12} neutrons/MeV/sr are measured by the TPs at 0° and 122°. The spectra measured at 0° and 122° can be attributed to the 360° acceleration of deuteron based on the mass-limited nature of the target. The higher deuteron energies and flux observed at 30° corresponds to a TNSA-like accelerated deuteron beam. We can therefore conclude that a 'centered interaction' occurred. The target was likely rotated counter-clockwise by close to 30°, as illustrated by the cartoon inset. On the right, it has to be noted that a CR-39 detector, explained in Section 4.2.3, was implemented in front of the image plate of the TP positioned at 30°, which results in the observed dips in the spectrum. Peak deuteron fluxes measured by all three TPs reach up to around 10^{12}

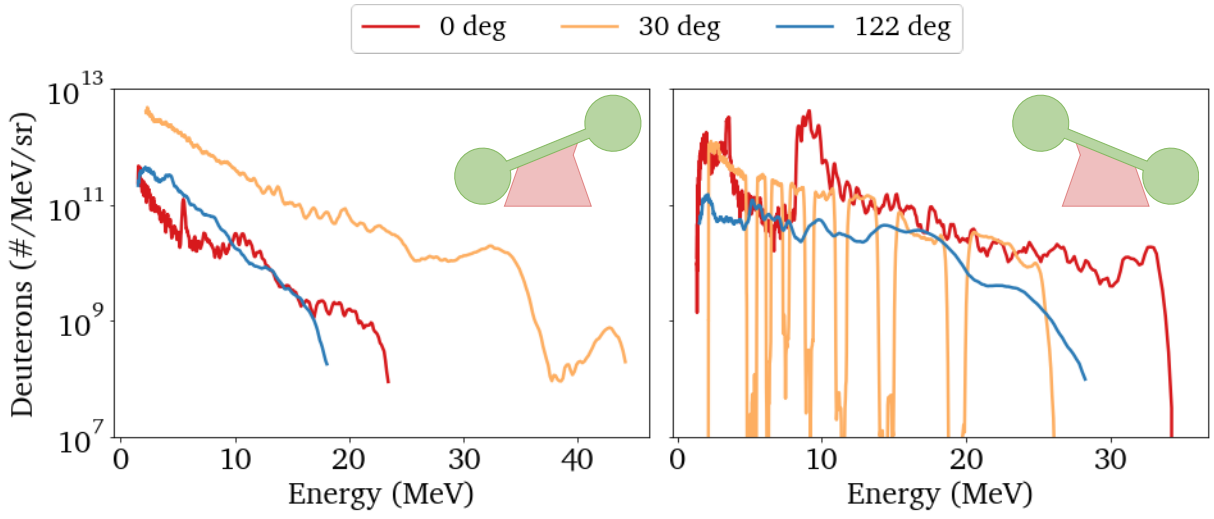

Figure 7.4.: Exemplary Thomson parabola traces for a counter-clockwise (left) and clockwise (right) rotated target. On the left a higher energy and flux component is observed by the TP placed at 30°. On the right similar fluxes and small variations in cut-off energy are observed between the three TPs. On this shot a CR-39 detector with slots was placed in front of the image plate of the TP at 30° resulting in the dips in the spectrum.

neutrons/MeV/sr. Slightly higher cut-off energies of 35 MeV are measured in laser forward direction, with 27 and 28 MeV for the 30° and 122° TP respectively. Based on the similarity of the three measured spectra, an off-centered interaction can be ruled out, as in this case a higher flux in laser forward direction would be expected. The observed spectra are rather a measurement of the 360° component of deuteron acceleration from the mass-limited target, which was rotated clockwise. These shots show, that a high control over the laser-target overlap was possible in this experiment, leading to TNSA-like deuteron beam acceleration for the majority of the shots. Future tests will studying the dependency and fluctuation of the target rotation on environmental conditions to eliminate the uncertainty of the deuteron beam pointing on shot.

7.5. Converter Designs

After optimizing the deuteron acceleration performance, the converter design was adjusted to maximize the neutron yield as presented in Chapter 5. The length of the full converter stack was determined such that deuterons with previously measured maximum deuteron cut-off energies would be completely stopped within the converter assembly. Two different designs for the converter compositions, as shown in Figure 7.5, were used during the four shots discussed in this chapter. Both designs consist of a blast shield and a lithium layer preceeding the beryllium layer. The blast shield is made of 170 µm glass coated with 40 nm of aluminium, angled at 20° to deflect incident laser light. A 6 mm thick disk of lithium is wrapped in 6.4 µm thick kapton tape to protect the lithium from interacting with oxygen in the air. The converter stack was mounted in a 1 inch diameter unanodized aluminium lens tube. A custom piece attached to the front of the lens tube held the blast shield at the designed 20° angle. Placing an EBT RCF at the back of the converter allowed to diagnose whether deuterons were able to penetrate the full length of the converter. A following 100 µm aluminium layer protected the RCF from light produced during the laser-target interaction. The lens tube assembly was mounted on a kinematic mirror mount to allow precision alignment on the laser forward axis using a vertical stage and the tip/tilt manipulation.

Figure 7.5.: Two converter design setups used during the experiment. Design #1 was used during shots 12355 and 12357 and design #2 was used during shot 12359 and 12365. Both stacks consist of a blast shield, angled at 20°, 6 mm of lithium, 6.25 or 11.25 mm of beryllium and RCFs inserted at different depths in the converter.

Design #1, implemented for the first two shots (12355 and 12357), uses a 6.25 mm thick beryllium layer. After shot 12357 deuteron signal was observed on the RCF layer at the back of the converter, indicating that not all impinging deuteron ions were fully stopped. To prevent this in future shots, the stack was extended in length and additional RCF layers were added to more closely track the deuteron beam pointing and profile within the converter. The resulting design #2, implemented for the two following shot (12359 and 12365), tracks the ion beam pointing directly after the lithium layer using an MD RCF followed by a 1.25 mm thick beryllium layer, another MD RCF and a 10 mm beryllium layer. To measure neutrons generated within the optimized converter and distinguish isotropic and directional neutron emission, a complex diagnostics setup was designed for the target area at the TPW laser facility.

7.6. Deuteron Beam-Catcher Overlap

As explained in Section 7.1, part of the accelerated deuteron beam, especially lower energy deuterons, are likely missing the converter the setup for this experiment. These deuterons can generate neutrons through interactions with other components of the setup. For simplicity we will only consider the emission of directional neutrons from the converter and the chamber wall to assess the contribution of both to a directional neutron beam. This is possible, since we can assume a constant background level due to complete fusion neutrons at any point in space. This assumption is based on the statistical nature of the complete fusion porcess with a constant emission probability in 4π. Directional neutrons generated in small components of the experimental setup, such as optical assemblies or motorization hardware, can additionally be neglected as the fraction of deuterons captured by these is much lower than what is captured by the converter or the chamber wall. Based on the achieved stability of the cryogenic planar deuterium jet target and the resulting deuteron acceleration, presented in Section 7.4, we will consider centered laser-target interactions distinguishing between two different cases: The deuteron beam is

1. centered on the converter, i.e. the target surface is normal to the laser beam,
2. partially missing the converter caused by a tilt of the target.

Figure 7.6 (schematic not to scale) illustrated the resulting deuteron-beam converter overlap for those two

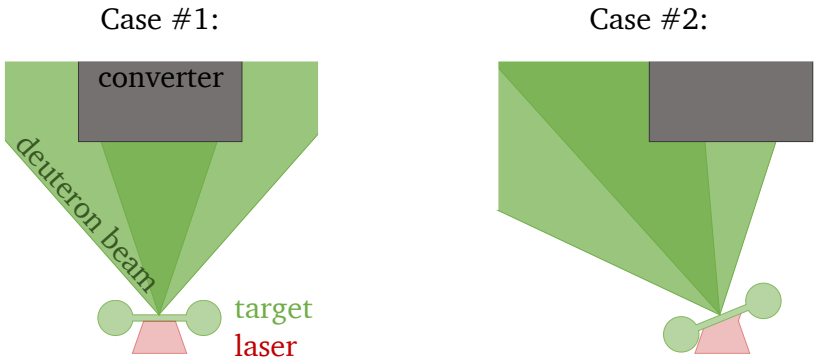

Figure 7.6.: Schematic (not to scale) of deuteron beam-converter overlap for different target orientations. In case #1 the target normal direction coincides with the laser forward direction and the high energy part (dark green) of the deuteron beam is predominantly stopped in the converter. In case #2 the target is rotated counter-clockwise and a large fraction of the high energy component of the deuteron beam is missing the converter.

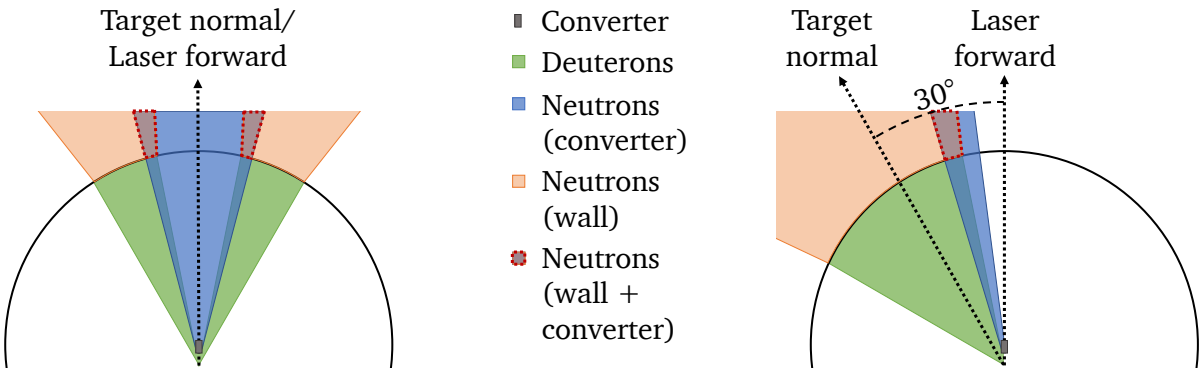

Figure 7.7.: Schematic of directional neutrons generated in the converter and in the chamber wall for a centered ion beam-converter interaction and coinciding target normal and laser forward direction (left) and ion beam pointing rotated counter clockwise by 30° (right). In the left scheme, the majority of the neutrons is generated in the converter (blue cone), while on the right, the majority of the neutrons is generated in the chamber wall (orange cone).

cases. A deuteron beam with a half opening angle of $\sim 30°$ is emitted normal to the target rear surface (light green cone) impinges on the converter (grey). The decreasing opening angle of the higher energy deuteron ions is illustrated by an exemplary narrow dark green cone, enclosing deuterons with energies above the threshold energy E_{thresh}. In case #1, the high energy component is predominantly captured by the converter. Lower energy deuterons at larger emission angles are missing the converter. In the second case, the high energy component is partially missing the converter.

Intuitively, one would assume that the emission direction and the flux of the directional neutrons will change depending on whether the high energy component of the deuteron beam is impinging on the converter or the chamber wall, as illustrated in Figure 7.7. The schematic identifies areas in which deuterons (green), neutrons from the converter (blue), neutrons from the wall (orange) and neutrons from both converter and wall (red dashed circumference) can be observed, based in case #1 or #2 of deuteron beam-converter overlap.

In the case #1 a large portion of the directional neutrons are generated within the converter. A smaller fraction of directional neutrons is generated in the wall to either side of the converter, which creates a small overlap of directional neutrons with different origin. In this scenario, the highest neutron flux is expected to be generated in the converter pointing in target normal direction. For a target rotated by 30°, case #2, the majority of directional neutrons in generated in the chamber wall with only a small fraction of directional neutrons produced in part of the converter.

It is important to be able to distinguish between the two origins of directional neutrons as the high fluxes of interest for material probing applications can only be efficiently achieved shortly behind the converter. Since the detection of neutrons is challenging within the target chamber, the setup presented in the next section will be used to identify the two different directional neutron beam components outside of the target chamber. It additionally has to be noted, that this simple concept can change from shot to shot and measured deuteron beam parameters will be used to adjust it for each individual shot.

7.7. Neutron Diagnostics Setup

A setup consisting of nTOF detectors and bubble detectors monitored the neutron emission around the target chamber at various angles and distances. The energy spectrum of the generated neutrons is measured at different angles from the laser forward direction. Neutron numbers were measured by bubble detectors mounted at various angles and distances in and out of the laser plane outside of the target chamber.

7.7.1. Neutron Time-of-Flight Detector Setup and Evaluation

Due to spatial constraints imposed by permanently installed shielding walls around the target chamber and a minimal required distance to TCC of 4 m, only specific angles from the laser forward direction were accessible. A 5 cm diameter hole was drilled through the shielding wall in laser forward direction to allow for the placement of one nTOF detector at 1.5°. Three additional nTOF detectors were positioned at 108, 111 and 113° from laser forward as shown in Figure 7.8 on the right. Precise distances and angles to TCC and the laser forward direction were determined post-experiment by implementing each nTOF detector in the 3D CAD model of the target area. Distances stated in Table 7.2 were further corrected to use the front of the converter stack as a reference point.

Three nTOF detectors with two separate designs, placed at 1.5, 108 and 113°, were supplied by the Texas Petawatt facility and one was supplied by TU Darmstadt, placed at 111°. The specifications and operation conditions of each individual detector are summarized in Table 7.2. A total of three different types of scintillators, EJ232Q, EJ200 and NE102, of different diameters and thicknesses were used.The scintillators were coupled to two different types of photomultiplier tubes, three Photonis XP2020 and a Hamamatsu R2059. Depending on distance to TCC and the response of the scintillator, different shielding materials and thicknesses. Consequently, it is not possible to directly compare the raw signal across detectors but will be limited to the shape and the cut-off energy of the measured neutron spectra.

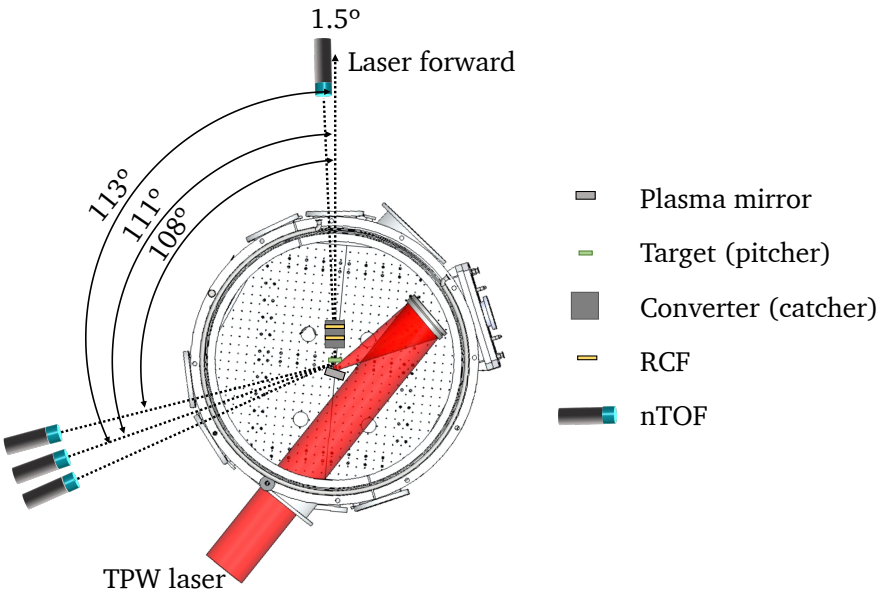

Figure 7.8.: Neutron time-of-flight detector setup to measure the neutron spectra at different angles. One nTOF was placed close to laser forward direction at 1.5° and three additional nTOF detectors were placed at 108, 111 and 113°.

angle (deg)	distance to TCC (m)	scintillator	PMT	Voltage (V)	shielding
1.5	5.7	EJ232Q (⌀ 4 cm, length 2 cm)	Photonis XP2020	-1650 (12355) / -1550 (12359)	24 cm Pb
108	7.19	EJ200 (⌀ 4.6 cm, length 4.9 cm)	Photonis XP2020	-1500	27 cm Pb
111	5.68	NE102 (⌀ 5 cm, length 8.5 cm)	Hamamatsu R2059	-1000	14 cm Pb
113	4.69	EJ232Q (⌀ 4 cm, length 2 cm)	Photonis XP2020	-1500	1.2 cm Cu (12355)/ 5 cm Pb (else)

Table 7.2.: nTOF detector setups at different angles from target normal and distances from TCC for the presented data shots. The nTOF detector at 1.5° was used with two different voltages during two individual shots and the shielding of the nTOF detector at 113° was changed after the first shot.

The raw data traces recorded by the nTOF detectors were evaluated by first fitting the gamma peak, caused by gamma radiation upon laser-target interaction, using a skewed Gaussian function given by

$$f(x) = A\, e^{\alpha\left(\mu - x + \frac{\alpha\sigma^2}{2}\right)} \left[1 - \mathrm{erf}\left(\frac{\mu - x + \alpha\sigma^2}{\sqrt{2}\sigma}\right)\right] \tag{7.2}$$

with the center of the Gaussian peak μ, the standard deviation σ, the amplitude A, the fit factor α and the error function erf. This fit serves two purposes, it is used for background subtraction to identify the neutron signal and to determine the reference time t_0 for the time of flight measurement and calculation of the energies of the detected neutrons. t_0 is determined by the global timing of the laser-target interaction. The gamma peak position in time on the oscilloscope trace is determined by using the generated fit and calculating the time at which the rising edge of the peak crosses the 10% threshold of the maximum value of the fit. For nTOF detectors placed multiple meters away from the target chamber, the obtained t_0 value needs to be additionally correct for the flight time of the gammas to the detector. After determination of t_0 time axis of the recorded trace can be converted to relative timing with respect to t_0, which in turn allows the assignment of a neutron energy to each data bin along the trace. The energy is calculated using the relativistic kinetic energy equation

$$E_{kin} = (\gamma - 1)mc^2 \quad \text{with} \quad \gamma = \frac{1}{\sqrt{1 - \frac{v^2}{c^2}}} \tag{7.3}$$

with the relativistic γ factor, the particle rest mass m, the speed of light c and the speed of the particle $v = d/t$ with the distance to the detector d and the flight time t. After energy conversion and background subtraction, the signal is divided by the derivative of the energy vector and the solid angle covered by the detector to obtain the signal in V/MeV/sr. For the analysis presented in this work, the representation in V/MeV/sr is sufficient. A future analysis task is the evaluation of a calibration measurement for each individual nTOF detector at a neutron source at Los Alamos National Laboratory, see Section 7.10.

7.7.2. Bubble Detector Setup and Evaluation

Twenty-two bubble detectors measure the neutron number at various locations and distances from TCC around the target chamber in and out of laser plane. Table 7.3 summarizes the distance and angle from laser forward for each bubble detector position. Equivalent to the distances and angles determination for the nTOF detectors, these two parameters were determined for each bubble detector position by implementing a detector placeholder in the 3D CAD model post experiment. For the data evaluation these distances were then corrected using the front of the converter as a reference. Bubble detector positions 1 - 20 were located in laser plane and 21 - 25 were located outside the laser plane. The locations are also indicated in Figure 7.9. A subset of bubble detectors, positions marked by a "*" symbol, was calibrated post experiment, by placing them next to a calibrated nTOF detector for an inertial confinement fusion experiment at the National Ignition Facility (NIF) at LLNL. The measured neutron number from the nTOF detector was then compared to the bubble counts in each bubble detectors. This way a sensitivity in terms of bubbles/mrem was calculated and used for the analysis of the data obtained during the experiment at the TPW laser facility presented here.

The bubble detector setup shown in Figure 7.9 serves multiple purposes. Bubble detectors mounted in laser plane, map the spatial emission as a function of angle from laser forward. This setup aims to distinguish between the quasi-isotropic and the directional neutron emission. Bubble detectors placed at different distances from the target chamber wall in laser forward direction, 1^{st} and 2^{nd} tier, are used to determine the primary source of neutrons within the setup. Additional bubble detectors are placed out of laser plane at selected angles roughly 90° from each other. This particular setup ca identify the scaling of the neutron flux outside of the laser plane to test the common assumption of rotational symmetric neutron fluxes.

No.	Angle to laser forward (deg)	Distance from TCC (cm)	Shots	No.	Angle to laser forward (deg)	Distance from TCC (cm)	Shots
1	-6	92	all	14*	10	131	> 12355
2	-14	80	all	15*	-13	126	> 12355
3	-27	80	all	16*	21	263	12355
4	-101	79	all	17*	7	210	12355
5	-148	80	all	18	4	199	≥ 12355
6	177	80	all	19	-3	185	≥ 12355
7	138	80	all	20*	-11	228	12355
8*	85	80	all	21	0	82	all
9	46	80	all	22	0	81	all
10	22	92	all	23	85	80	all
11*	13	80	all	24	177	80	all
12*	1	92	all	25	-100	80	all
13*	22	134	> 12355				

* calibrated detectors used

Table 7.3.: Summary of the angles and distances for different bubble detector positions with numbers corresponding to those shown in Figure 7.9. Positions with calibrated detectors are marked with a "*" symbol and occupation of the location is indicated by the 'Shots' column. Bubble detector positions 21 - 25 are located outside the laser plane, while all others are located in laser plane.

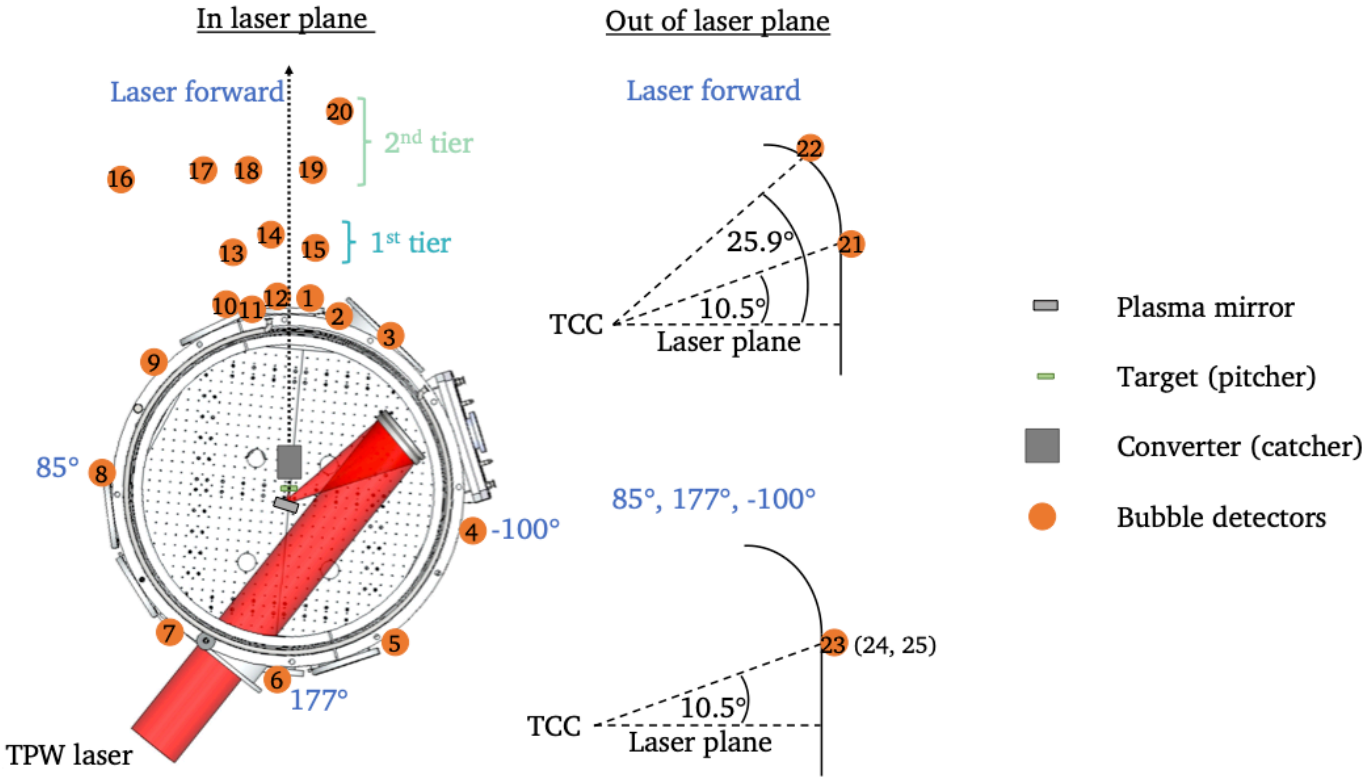

Figure 7.9.: Bubble detectors are positioned at various angles and distances around the target chamber in laser plane (left). Different tiers of bubble detectors, mounted at different distances from the target chamber, enable the identification of the dominant neutron source. Additional detectors are placed above the laser plane at selected angles (right) to enable the comparison with in plane detectors.

The bubble detector data obtained on shot is converted to deposited dose within the detector using the stated or calibrated sensitivity of each bubble detector. In a subsequent step, the measured dose is multiplied by the average bubble detector response from Jung et al. (Ref. 202) over the energy interval of interest, as shown in Section 6.2.2, and the square of the measured distance to the front of the converter for each bubble detector to obtain the neutron flux through each detector. The standard deviation of the average bubble detector response value is 20% within the energy range of interest. Statistical errors of the measurement, calculated by $\sqrt{N}/N$, are neglected as minimum values for neutrons impinging on the bubble detectors are at least 1×10^{10} or higher, which results in a statistical error of less than 1%. As a consequence, the error of the calculated neutron numbers and fluxes is given by the 20% error of the response of the bubble detector and for further evaluation, a 20% error is used as a measuring uncertainty for these values.

7.8. Dominant Neutron Generation within the Converter

The first considered scenario refers to an ion beam pointing close to the laser forward direction, as observed by the deuteron beam diagnostics. Below, a high neutron yield (12357) and a low neutron yield (12355) shot are analyzed and presented following the step of neutron generation. First the characteristics of the observed deuteron beam are analyzed which allows for an angle estimate of the deuteron beam pointing.

Both presented shots used converter design #1, see Section 7.5, with an RCF layer located at the end of the converter stack, corresponding to a deuteron energy of 50.2 MeV. Subsequently, the neutron generation data detected by the nTOF and bubble detectors is discussed. The first shot, 12357, will be used to explain the data evaluation of the RCF and the individual neutron diagnostics.

7.8.1. High Neutron Yield - Shot 12357

The Thomson parabolas positioned at 30 and 122° measured spectra with similar cut-off energies of 25 MeV (30°) and 24 MeV (122°) reaching peak fluxes around 10^{12} deuterons/MeV/sr. Figure 7.10 summarizes the deuteron acceleration results with the two Thomson parabola traces on the left and the RCF at a deuteron energy of 50.2 MeV behind the converter on the right. The deuteron beam trace on the RCF shows an approximately circular deuteron beam cross section and small intensity variations with an deposited doses up to 6 Gy. Furthermore the narrow, 7.4° opening angle, deuteron beam cross section with clear boundaries shows a slight offset from the center of the converter, indicated by the white cross, of a less than 5°.

The low cut-off energies and constant fluxes observed with the TPs at 30 and 122° and the confined high energy deuteron beam detected by the RCF in the converter indicate a centered laser-target interaction and a TNSA-like deuteron beam. The spectra observed at 30 and 122° are part of the 360° emission of deuterons, which has been observed in the past [122]. Based on the recorded data and the concept developed in Section 7.6 neutrons are expected to predominatly originate within the converter.

Figure 7.11 (a) shows the evaluated nTOF traces of only three of the four detectors as the nTOF detector in laser forward direction did not record any signal. Signals observed at 108 and 113° show a Maxwellian distribution with cut-off energies of 24 MeV. At 113° the trace is saturated between 15 and 5 MeV, which allows no conclusions about the shape of the spectrum, but a cut-off energy of 26 MeV can be determined. Based on the shape of the spectrum and the cut-off energy observed by the three different nTOF detectors, it is possible to estimate that all the neutron beam detected by each detector had similar properties in terms of neutron energies and flux distribution across those energies. This leads to the assumption of a uniform neutron generation at 108 - 113°.

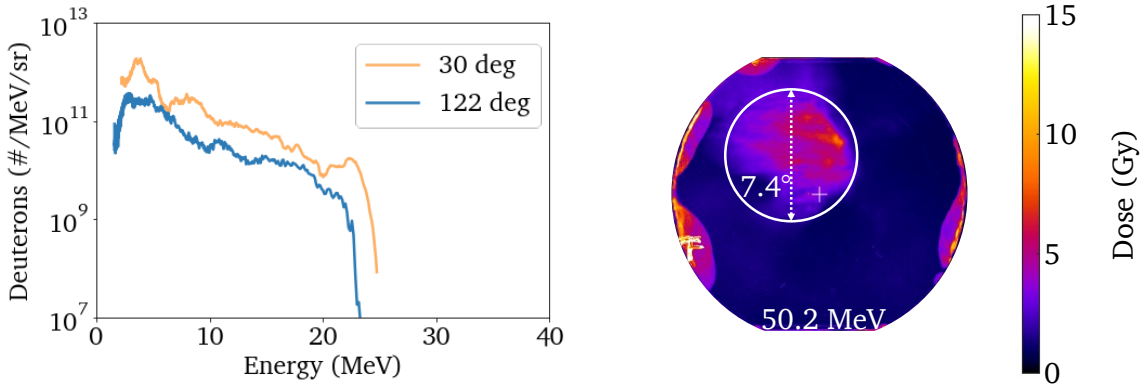

Figure 7.10.: Thomson parabola traces and dose imprint on converter RCF for shot 12357. Both Thomson parabolas show cut-off energies around 24 MeV and fluxes reaching 10^{22} deuterons/MeV/sr. The RCF shows a narrow (7.4°) deuteron beam at 50.2 MeV up to ~7 Gy.

The flux measured by the bubble detectors mounted in the laser plane on the chamber wall and the 1st and 2nd tier is displayed in Figure 7.11 (b). A red shaded band indicates the angles from laser forward direction that are covered by the 1 inch diameter cross-section of the converter at 4.75 cm from TCC. This region will be referred to as the 'shadow' of the converter going forward. The obtained data was fit using a Gaussian fit function (black) with the 1σ confidence interval shown in grey. The fit function is a standard Gaussian function

$$f(x) = A \cdot exp\left(-\frac{(x-x_0)^2}{2\sigma^2}\right) \tag{7.4}$$

with the amplitude A, the peak position x_0 and the standard deviation σ. The error for each data point was used to weight each point for the fit. The peak position and standard deviation of the fit are of interest to identify the directionality and emission characteristics of the generated neutrons. For the shown data set the peak position is $x_0 = 5.6$ and the standard deviation is $\sigma = 146$.

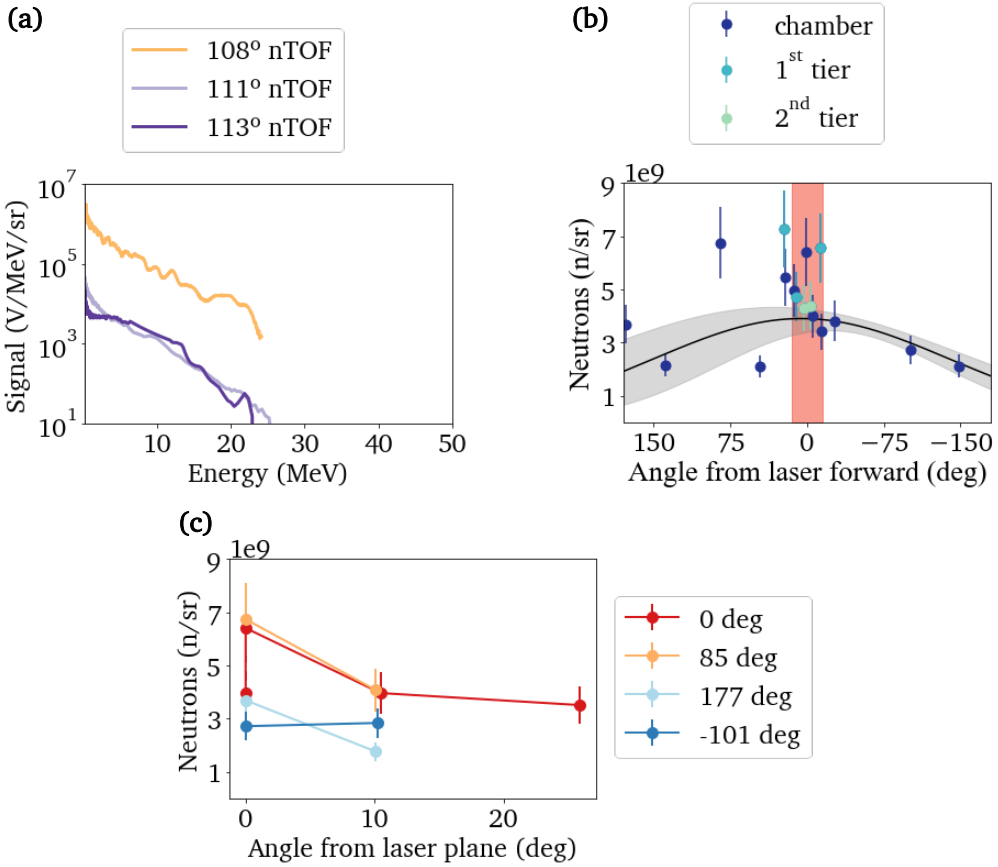

Figure 7.11.: Neutron generation results for shot 12357. (a) uncalibrated neutron spectra showing Maxwellian distributions with cut-off energies around 25 MeV. (b) Bubble detector radial map in laser plane with angles covered by converter (red) and a Gaussian fit (black) to the data with a 1 σ confidence interval shows higher neutron emission approaching laser forward direction. (c) Neutron fluxes measured outside of the laser plane are on average lower by a factor of two compared to their laser plane counter parts.

Low neutron fluxes around 3×10^9 neutrons/sr are observed outside of the shadow of the converter with the exception of three outliers at 22 and 85°. Within the shadow of the converter, neutron fluxes are consistently higher than the Gaussian fit, showing a high flux forward directed neutron beam component. Within this directional beam fluxes of on average 5.1×10^9 neutrons/sr are measured with small variations across all bubble detectors. The peak flux of 7.3×10^9 neutrons/sr is detected at 22° outside of the shadow of the converter.

Figure 7.11 (c) shows the out of plane bubble detectors with their in plane counter parts. Fluxes measured at the same angle from laser forward are plotted using the same color and are connected to guide the eye. Decreasing fluxes outside of the laser plane are observed for 0, 85 and 177° from laser forward. An average flux decrease of a factor 2 from the laser plane to 10° outside of the laser plane and a similar flux at 26° is observed. A slight increase within error bars is observed for -101° from laser forward direction.

This observed characteristics of the neutron emission , small x_0 value for the Gaussian fit and high neutron flux in laser forward direction, indicate that the majority of the high energy deuterons was incident on the converter. The close alignment of deuteron beam pointing and laser forward direction, as observed by the RCF is ideal for the generation of a high flux, directional neutron beam as the directional neutron beam can be predominantly attributed to break-up within the converter. An isotropic, 360° component generated a 4π background measured by all detectors. The neutron flux outliers at 22° suggest, that a larger fraction of the deuteron beam missed the converter, which is in agreement with the off-center deuteron trace observed on the RCF at the end of the converter. Measurements outside the laser plane further suggest, that it is not possible to assume isotropic neutron emission into 4π. To further investigate these conclusions it is essential to closely model the experimental conditions. Such simulations will be conducted in the future, see Section 7.10.

Using the overall average flux in laser plane, 4.4×10^9 neutrons/sr and at a minimum energy of 1 MeV based on the sensitivity drop off of the bubble detectors, a lower boundary for the conversion efficiency η from laser energy to neutrons can be estimated. The formula used for this purpose

$$\eta = \frac{\overline{\Phi}\cdot 4\pi\cdot\overline{E_n}}{E_L} \tag{7.5}$$

with the average neutron flux $\overline{\Phi}$, the average neutron energy $\overline{E_n}$ and the laser energy on target E_L. Using the average neutron properties and laser energy on target for this particular shot, the conversion efficiency from laser energy on target to neutrons is estimated as $\eta{=}1\times10^{-4}$. Addition measurements are required to estimate a more accurate conversion efficiency value in addition to the necessity of incorporating the detected neutron spectrum in the calculation.

7.8.2. Low Neutron Yield - Shot 12355

As a comparison to the previous shot, a low neutron yield shot is analysed to investigate whether a directional deuteron beam generation is dependent on the quality of the laser-target interaction. The ion data obtained for this shot includes only the deuteron spectra recorded by the 30° and 122° TPs, which are displayed in Figure 7.12, as no trace was observed on the RCF at the end of the converter. Peak fluxes for both TPs reach around 10^{12} deuterons/MeV/sr with cut-off energies of 21 MeV (122°) and 41 MeV (30°). This large change in cut-off energy suggests, that the angle between the ion beam emission direction and the laser forward direction was likely more than the 5° observed for shot 12357. However, the small difference in flux between the two TP spectra, especially for the low energy component, suggests, that the angle between the ion beam center axis and the laser forward direction is closer to 5° than to 30°.

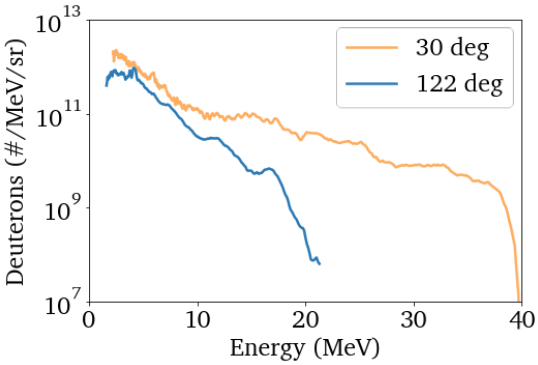

Figure 7.12.: Both Thomson parabolas for shot 12355 show fluxes reaching 10^{12} deuterons/MeV/sr with cut-off energies of 21 MeV (122°) and 41 MeV (30°).

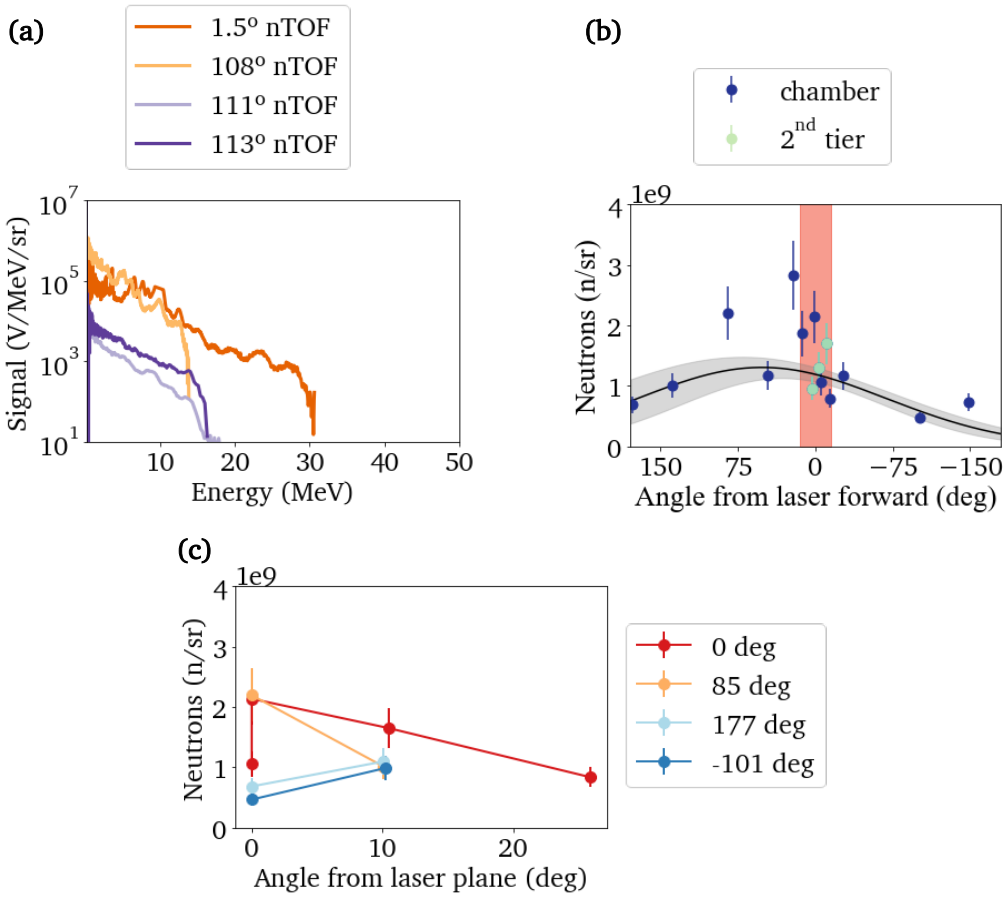

Figure 7.13.: (a) Uncalibrated neutron spectra for shot 12355 showing cut-off energies around 18 MeV at larger angles and 30 MeV at 1.5°. (b) Bubble detector radial map in laser plane displaying neutron flux. A gaussian fit (black) to the data with 1 σ confidence interval shows elevated neutron emission approaching laser forward direction. (c) Neutron fluxes measured outside of the laser plane with the laser plane counter parts. While 0 and 85° show lower fluxes outside the laser plane, higher fluxes outside the laser plane are observed at 177 and -101°.

The nTOF spectra displayed in Figure 7.13 (a) show a Maxwellian spectrum for all four detectors, with slight saturation around 10 MeV of the nTOF positioned at 1.5° and a more pronounced peaked structure towards lower energies. This could be an effect of a low number of incident neutrons. Measured cut-off energies are around 16 MeV (111 and 113°) and 14 MeV (108°) at larger angles from laser forward and almost double in laser forward direction at 31 MeV at 1.5°. The higher cut-off energy in laser forward direction indicates neutron production through deuteron breakup.

The in laser plane neutron flux measurement, Figure 7.13 (b), shows an average neutron flux of 1.3×10^{9} neutrons/sr, much lower flux than shot 12357. Using Equation 7.5 a conversion efficiency of 0.3×10^{-4} from laser energy to neutrons can be calculated. Similar to shot 12357 an elevated neutron flux is detected around the laser forward direction within the converter shadow, reaching a peak flux of 2.9×10^{9} neutrons/sr, and decreasing fluxes outside of that range. Overall good agreement between mesured fluxes at similar angles is observed, with one outlier from this trend is observed at 85°. The Gaussian fit to the data using Equation 7.4 yields a center position at 52° with a standard deviation of 121°.

Out of laser plane bubble detectors show a similar decrease in flux for the neutron fluxes measured in 85° and a much smaller decrease in laser forward direction (0°). This could be an indication that the ion beam and consequently the directional neutron beam was slightly pointing up out of the laser plane. An increase in flux measured outside the laser plane by almost a factor of two is shown at 177 and -101°. However, the overall measured fluxes are comparably low.

Although a much lower conversion efficiency from laser energy to neutrons is achieved for this shot compared to shot 12357, similar characteristics are observed for deuteron and neutron beam parameters. A larger shift of the deuteron beam pointing, away from the laser forward direction, can be seen by changed deuteron spectra and a shifted peak in the angular neutron flux map. This suggests, that a larger fraction of the deuteron beam missed the converter. However, even for lower laser energy to neutron conversion efficiency, the generation of a dominant, directional beam is still possible.

7.8.3. Primary Source Determination

This section will focus on the forward directed neutron beam component detected within and close to the shadow of the converter. Using the r^2 measurement, explained Section 6.2.4, their primary source is determined. This measurement will b evaluated for shot 12357, as it shows a much higher overall yield of neutrons. For the r^2 measurement, the total neutron numbers detected within each bubble detector are compared, which are calculated by multiplying the previously calculated flux with the solid angle of each detector.

Figure 7.14 shows the calculated neutron numbers at different distances from the front of the converter, while the colors of the data points encode the angle to the laser forward axis in degrees. The consistency with the expected decreasing neutron numbers for larger distances scaling with r^2 is quantified by using the fit function

$$f(x) = \frac{a}{x^2} + c \tag{7.6}$$

with the fit factors a and b and the distance variable x. The fit is shown as the black dashed line with the 1σ confidence interval indicated by the grey shaded area around the fit. The agreement of the data with the fit within error bars and the narrow confidence interval of the fit confirms, that the converter is the primary source of the neutrons detected by the bubble detectors in laser forward direction.

To cross-checking this result the calculated neutron flux using the distance to the converter for the subset of bubble detectors is plotted on the right in Figure 7.14 and are equally colored coded based on the angle to

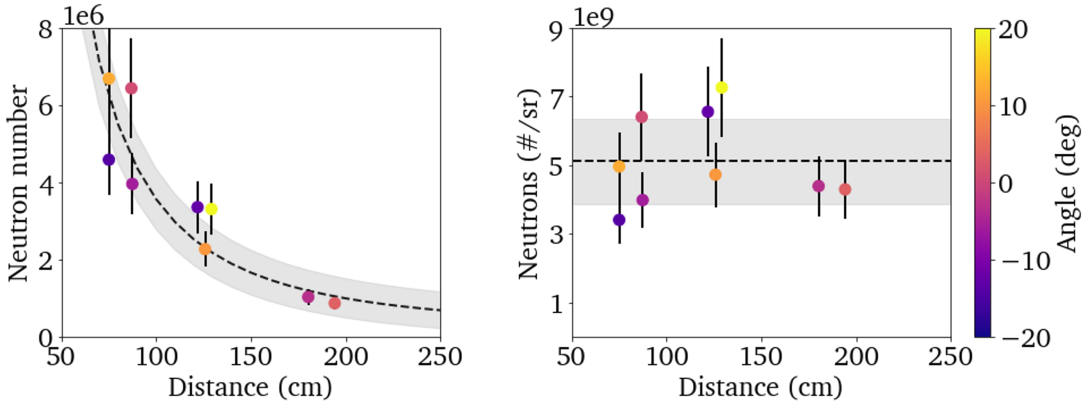

Figure 7.14.: Neutron numbers measured at different distances from laser forward (left). Neutron fluxes for the same set of bubble detectors (right). Angles of the detectors to laser forward are indicated by the color bar. The r^2 model decribes the dependence of the neutron numbers on the distance to the converter very well. On the right, the overlap of the calculated fluxes with the average neutron flux and the 1σ confidence interval confirms this conclusion.

the laser forward direction. The average flux of 5.1×10^9 neutrons/sr with a standard deviation of 1.25×10^9 neutrons/sr is shown by the dashed black line and the grey shaded area. Over half of the data points lie within the 1σ region of the average with their error bars overlapping with the calculated average value. For the values outside of the confidence interval, their error bars still show significant overlap with the confidence area. There does not seem to be an angular preference for higher or lower fluxes. This confirms, that the high flux forward directed neutron beam component for shot 12357 originated predominantly within the converter.

7.9. Dominant Neutron Generation within the Chamber Wall

The second considered scenario refers to a large fraction of the deuteron beam passing the converter, which can be determined based on the recorded deuteron beam data. Similar to the previous section a high neutron yield (12359) and a low neutron yield (12365) are analyzed and presented to investigate the influence of the quality of the laser-target on the neutron generation. Both presented shots used converter design #2 with RCF layers located at a depth corresponding to deuteron energies of 23.7, 31.6 and 66.1 MeV.

7.9.1. Partial Deuteron Beam Converter Overlap - Shot 12359

For this shot, both spectra show an overall semi-Maxwellian shape, which is expected for TNSA-like ion beams. The Thomson parabola at 30° measured a peak flux above 1×10^{12} deuterons/MeV/sr, higher by about an order of magnitude than the TP at 122°. The dip in the 30° TP spectrum is the result of a wire blocking part of the deflected ion beam before reaching the image plate detector. Deuteron cut-off energies reached 17 MeV (122°) and 38 MeV (30°).

The RCFs scans on the right hand side of Figure 7.15, equivalent to deuteron energies of 23.7 and 31.6 MeV, show a circular perimeter of the deuteron beam profile. Based on the perimeter and estimated center of the deuteron beam on the first RCF the deuteron beam pointing shift corresponds to around 10° and ∼50% of the accelerated deuteron beam is captured by the converter for energies above 23.7 MeV. The observed imprints on the RCFs paired with the observed deuteron spectra at different angles supports the assumption

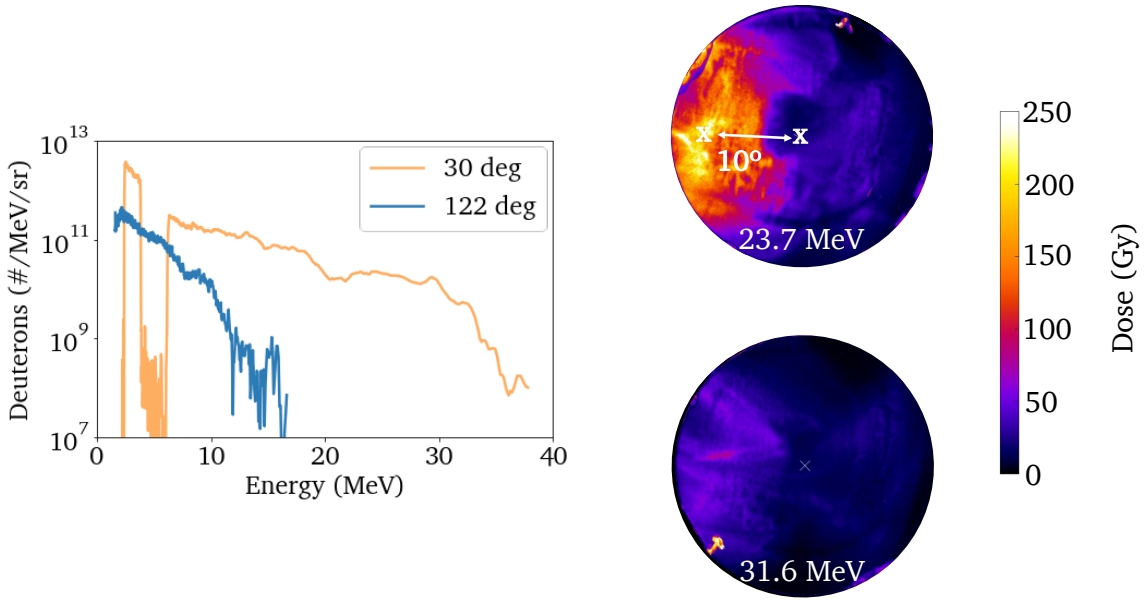

Figure 7.15.: Thomson parabola spectra at 30 and 122° from laser forward (left). A low deuteron peak flux of just above 10^{11} deuterons/MeV/sr and a cut-off energy of 17 MeV are observed at 122°. At 30° a peak flux one order of magnitude higher and a cut-off energy of 38 MeV was measured. The dip in the spectrum of the 30° TP was caused by a cable blocking the deflected beam on the way to the detector. The RCF images on the right show the deuteron beam at two different energies, 23.7 and 31.6 MeV. A round beam profile with an estimated offset of 10° is observed for both energies.

of a TNSA-like beam with only partial overlap of the deuteron beam with the converter. Since the full beam is not captured by the RCF a range of angles between deuteron beam pointing and laser forward direction can be narrowed down to 10 - 30°.

The neutron spectra measured at different angles are shown in Figure 7.16 (a). All four detectors show a Maxwellian spectrum, with a shallower slope at 1.5°. The nTOF in laser forward direction additionally shows a more prominent peaked modulation and reaches cut-off energies of 45 MeV, while the cut-off energies for the other three detectors are either 18 MeV (108 and 113°) or 23 MeV (111°). The high cut-off energies in laser forward direction indicate, that a significant amount of deuterons impinging on the generate neutrons through the breakup reaction.

The in laser plane angular neutron flux map, Figure 7.16 (b), shows a majority of the measured neutron fluxes under 2×10^9 neutrons/sr, contrary to the previously analyzed angular maps. It is important to note that, unlike for previous shots, a large spread and discrepancy is observed between detected fluxes in the forward direction, ranging from below 1×10^6 up to 5×10^6 neutrons/sr. A key feature of the angular map are the three bubble detectors at 15 and 22° from laser forward measuring neutron fluxes higher by a factor 2 than the otherwise detected.

The out of laser plane detectors consistently measured lower neutron fluxes compared to their in plane counterparts with almost constant flux for 10 and 26°. However it can be seen, that the difference between in plane and out of plane fluxes is less than previously observed. Additionally, the flux at 85° drops more significantly than for any other angles.

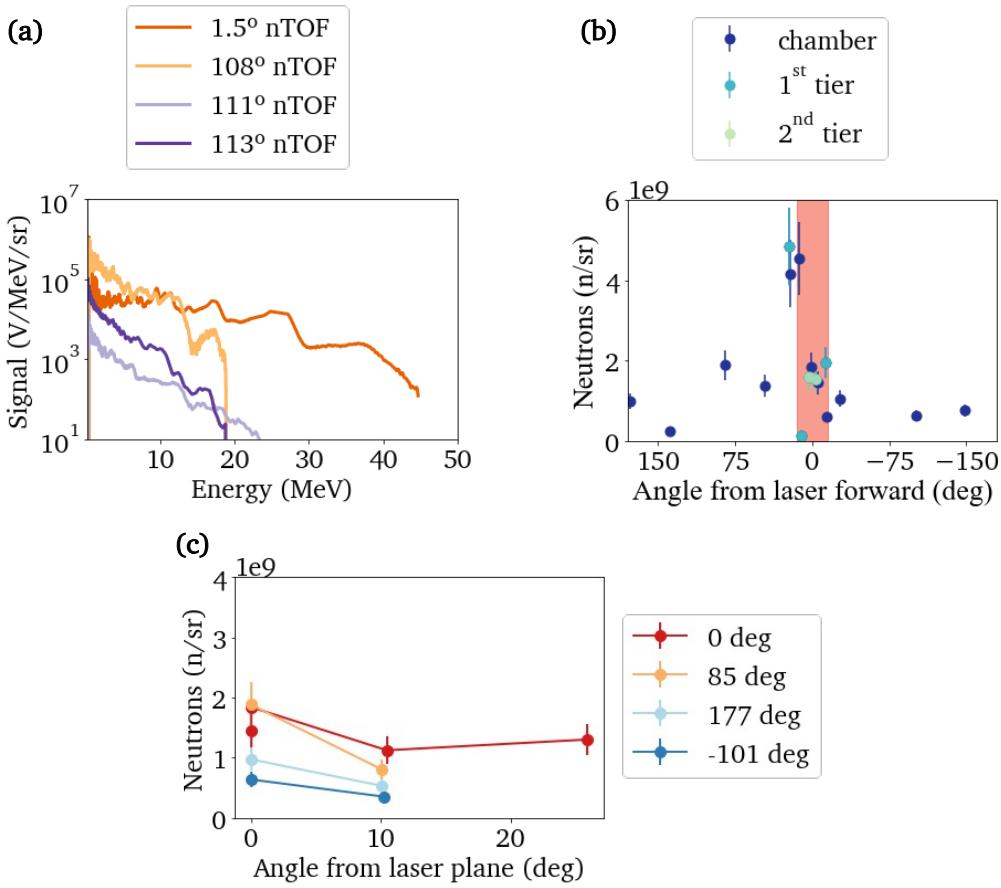

Figure 7.16.: Summary of neutron results of shot 12359. (a) nTOF spectra for all four angles show Maxwellian spectra with energies up to 18 MeV (108 and 113°), 23 MeV (111°) and 45 MeV (1.5°). (b) Angular plot of bubble detectors in laser plane at different distances form the chamber wall. The majority of the bubble detectors measured fluxes below 2×10^9 neutrons/sr with three outliers at 20°. (c) Out of plane bubble detectors measure consistently lower flux at all four angles.

The observed neutron parameters show, that a high energy directional neutron beam can be generated at decreased flux for a decreased deuteron beam-converter overlap. A significant contribution of neutrons generated in the chamber wall can be concluded from the large variation in detected neutron fluxes. Neutrons generated directly in front of bubble detectors mounted on the target chamber wall result in a higher calculated neutron flux. It is important to compare measured neutron fluxes with simulations, to fully understand the contributions from the converter and the chamber wall the the neutron flux measured at the individual detector positions.

7.9.2. Minimal Deuteron Beam Converter Overlap - Shot 12365

Figure 7.17 shows the deuteron beam data detected with the two Thomson parabola data shown on the left and the RCF data shown on the right. At 30° a peak flux around 10×10^{12} deuterons/MeV/sr and a cut-off energy of 36 MeV is reached. The dips in the spectrum are due to the implementation of a CR-39 diagnostic in front of the image plate for calibration purposes, for details of the CR-39 measurement see Section 4.2.3. The TP at 122° measured a flux of around 10×10^{11} deuterons/MeV/sr, lower by about one order of magnitude,

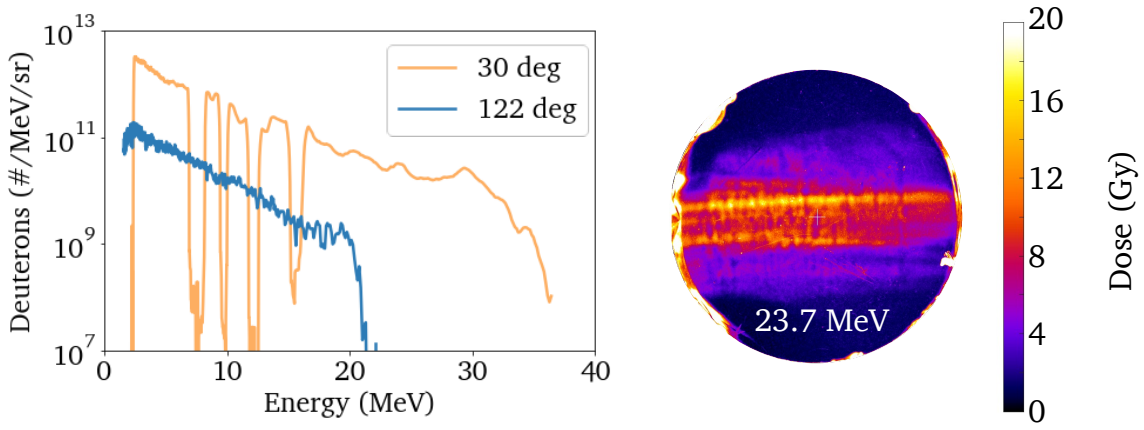

Figure 7.17.: Deuteron beam data for shot 12365. The Thomson parabola spectra (left) show semi-Maxwellian spectra with cut-off energies of 22 MeV (122°) and 36 MeV (30°). Observed dips in the spectrum recorded at 30° are due to a CR-39 inserted in front of the image plate for calibration purposes. The RCF detecting deuterons with 23.7 MeV on the right shows a band structure spanning across the full RCF which indicates an interaction with the rim of the jet target.

reaching cut-off energies around 22 MeV. Both spectra show a semi-Maxwellian distribution as expected for TNSA-like ion acceleration.

The imprint on the RCF shows a band of deuterons detected across the full width of the converter at 23.7 MeV. The width of the band on the RCF was determined for doses above 8 Gy, 3.4 mm top to bottom, and the full band, 12.8 mm top to bottom, corresponding to an opening angle of $\pm 2°$ and $\pm 7.7°$ respectively. These values can be compared to the emission profile measured for a 5 µm diameter cylindrical cryogenic hydrogen target by Obst-Huebl et al. ([122]), which shows high flux emission into $\pm 5°$ and extended emission into $\pm 10°$. The emission angles and deuteron spectra observed in this work agree well with data presented by Obst-Huebl et al. and we can therefore conclude, that the laser was predominantly interacting with the rim of the cryogenic jet.

Detected neutron spectra show a Maxwellian spectrum for all nTOF traces shown in Figure 7.18 (a). The nTOF detector in laser forward direction showed a noise dominated raw signal and is therefore not displayed here. Cut-off energies for the individual traces are 18 MeV (108°) and 20 MeV (111 and 113°). The bubble detector map in laser plane shows lowest fluxes detected in laser forward direction around 1×10^9 neutrons/sr. The bubble detectors mounted on the wall span a large flux region from 1×10^9 - 4×10^9 neutrons/sr giving no indication of a forward directed component. The reverse of the behavior compared to all other shots is observed, namely a higher flux outside of $\pm 15°$ from laser forward than in laser forward direction.

For the out of plane neutron flux measurement, we observe a clear trend towards lower fluxes for larger angles out of the laser plane for all four sampling locations. While some fluxes drop faster (85°), some drop less quickly (177° and -101°). This could be a direct result of the vertical confinement of the accelerated deuteron beam based on the laser interaction with the rim of the jet target.

The fluctuation across the whole bubble detector map paired with this inverse behavior suggests, that neutrons are generated in a multitude of locations with no clear dominant source of neutrons in the experimental setup and the absence of a directional neutron beam. Another argument in favor of this conclusion is the fact, that the nTOF at 1.5° showed no clear signal, indicating no significant neutron generation within the converter.

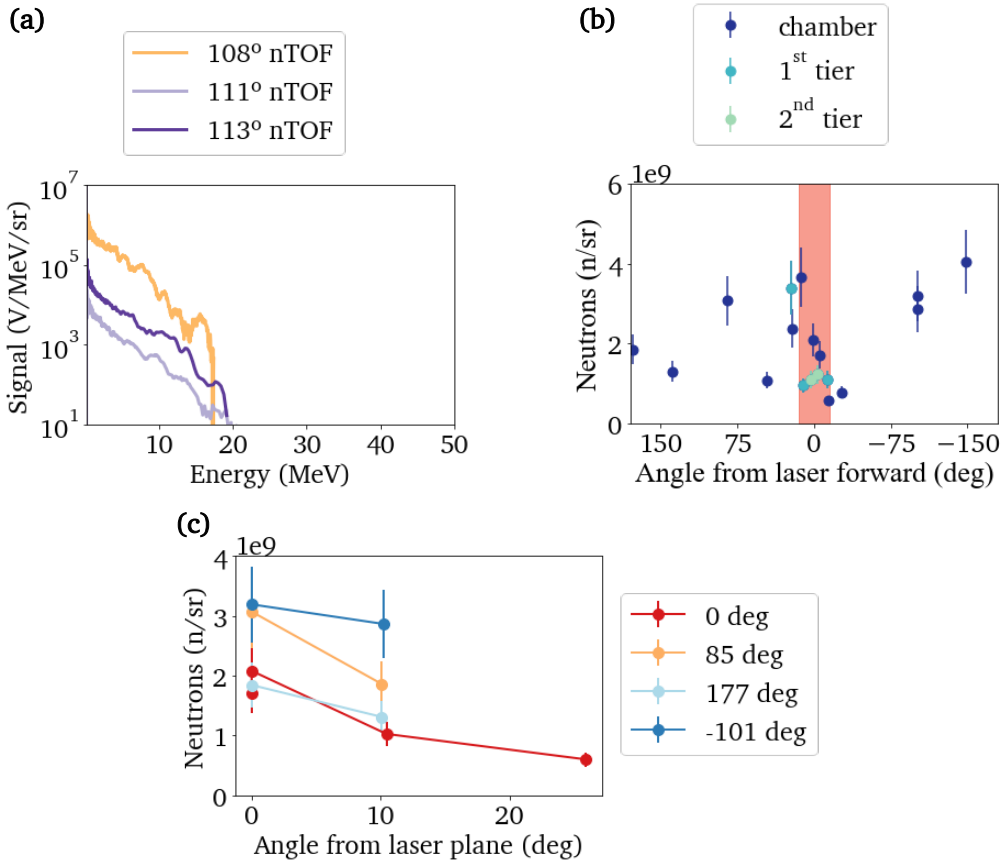

Figure 7.18.: Summary of collected neutron data from shot 12365. (a) nTOF spectra show cut-off energies around 18 and 20MeV, but no detectable signal in laser forward direction, supporting the hypothesis of no significant neutron generation of a directional neutron beam component in the converter. (b) Bubble detector map in laser plane as a function of angle show large spread of neutron fluxes at angles above 15° from laser forward. This supports the assumption of no significant neutron production in the converter, but predominant generation in the chamber wall leading to an overestimate of detected neutron fluxes. (c) The out of plane bubble detectors measure consistently lower fluxes outside of the laser plane.

7.9.3. Primary Source Determination

The conclusions drawn based on the experimental data can be further tested by determining the primary source of the generated neutrons through the r^2 method presented in Section 6.2.4. The neutron numbers and fluxes in laser forward direction at different distances from the target chamber wall are plotted in Figure 7.19 for shot 12359.

A large spread of neutron numbers detected is observed at various angles from laser forward in the left plot. The r^2 fit agrees with parts of the measured neutron numbers, but about half of the measured neutron numbers deviate significantly from the r^2 trend and are outside the 1σ confidence interval of the fit. Compared to the r2 fit in Section 7.8.3,a much wider confidence interval is observed for the overall fit, which indicated a decreased reliability of the converter as the primary source. This is further supported by the large variations in neutron fluxes shown on the right. The same bubble detectors that showed a deviation from the r^2 trend, show significantly different fluxes from the average flux (dashed line) and no overlap with the confidence

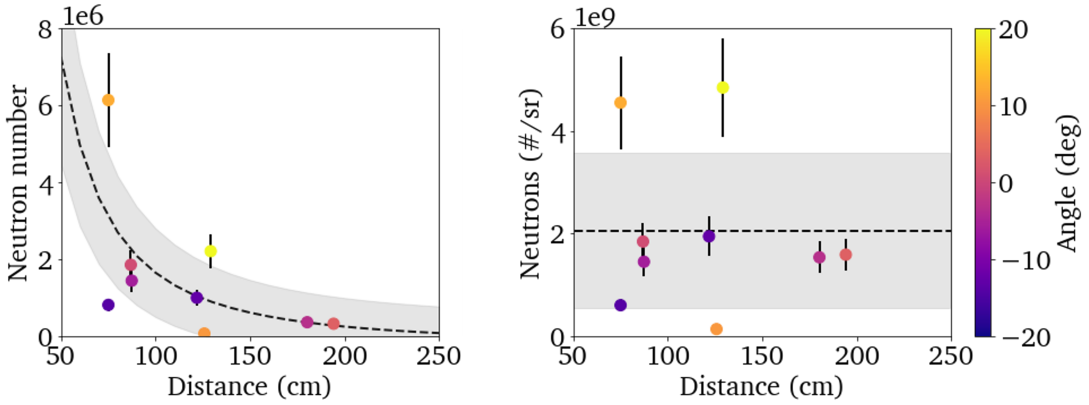

Figure 7.19.: R^2 measurement data for shot 12359. (left) The detected overall neutrons show a deviation from the r^2 trend (dashed line) and some data points are significantly outside the confidence interval of the fit. (right) The calculated neutron flux supports this hypothesis, showing large variation in the overall flux for all the bubble detectors taken into account.

interval. In conclusion, even in a partial beam-converter overlap, the converter can be the primary source of neutrons emitted into a certain angular subset of laser forward, in this case angles between 0 and 15°, but cannot be determined as the dominant source of the overall forward directed neutron beam.

7.10. Summary and Further Planned Analysis

Based on the results presented above, we can distinguish between three different scenarios

1. full ion beam converter overlap $\longrightarrow$ high flux directional neutron beam
2. partial ion beam converter overlap $\longrightarrow$ partially directional neutron beam
3. minimal ion beam converter overlap $\longrightarrow$ non-directional neutron beam .

In the first case neutron fluxes exceeding 6×10^9 neutrons/sr were measured in target normal direction with a clear separation between the directional and the isotropic neutron emission component. Furthermore the converter was identified as the dominant source of the forward directed neutron beam. For case 2 and 3 maximum neutron fluxes around 4×10^9 neutrons/sr are reached with a high uncertainty of the origin of the detected neutrons as the r^2 scaling showed. The analysis of the results presented above is in parts not yet complete. Outstanding tasks can be subdivided into data analysis tasks and simulation and interpretation tasks, which will be outlined in the following.

Two diagnostics still requiring further analysis are the RCFs within the converter and the nTOF detector traces. For the RCF layer, the remaining steps include the conversion of dose to detected deuteron numbers. Furthermore a correlation between the flux detected on the RCF and the neutron flux measured by the bubble detectors will be explored. For the nTOF detectors, a response calibration experiment, performed at the LANSCE neutron source at Los Alamos National Laboratory, will be analyzed. A cross-calibration with the neutron flux measurement of the bubble detectors will give insight in the validity of the calibration method. Furthermore, the effect of the shielding implemented in front of the nTOF detectors on the overall spectral shape and the measured cut-off energy has to be estimated. For this purpose 1D and 2D simulations, using simulation codes such as GEANT4 or equivalent, will be performed. Based on such simulations it will be

possible to draw conclusion about the neutron beam spectrum impinging on the shielding in front of the detector.

After completion of the experimental analysis of the obtained data, 3D simulations using simulation tools such as GEANT4 or equivalent, will model the experimental environment starting with the experimentally measured deuteron beam. The simulation will include the precise converter setup, the chamber wall and large components within the target chamber and the shielding wall of the target area. Detectors, nTOF and bubble detectors, will be positioned in the simulation at the exact position as implemented during the experiment. Equivalent to the experiment, the simulation will resolve the total neutron flux at the location of the bubble detectors and the flux as a function of energy at the location of the nTOF detectors. In addition to that, the simulation will resolve the origin of the detected neutrons, by creating different tags based on the generation location of the neutron. The converter and the chamber wall will be identified as potential sources. Based on the results of the simulation it will then be possible to compare the deconvolved neutron flux at the bubble detector locations with the conclusions drawn based on the experimental results, as presented earlier for the different scenarios of ion beam-converter overlap and dominant neutron sources.

7.11. Future Experiments

A future experiment will include multiple changes to target orientation, catcher design as well as detector placement. As the conversion efficiency from ions to neutrons strongly depends on the distance between the pitcher target and the catcher target, a follow up experiment will include a change of laser incident angle to 30-45° to be able to move the catcher closer to the target without any risk of damage. For this, studies to enhance the rotation-stability under comparable vacuum conditions are necessary to allow for enhance control over the cryogenic jet orientation. Simulations will be performed prior to the experiment to determine ideal positions and shielding material compositions for nTOF detectors prior to the experiment, which will allow for a more consistent and comparable configuration of each detector throughout the experiment.

The converter design will be changed to enable better ion beam tracking within and around the converter. This could include an ion imager mounted around the converter, preferably made of a scintillating material, to monitor the ion beam converter overlap by imaging the low energy component of the TNSA-like beam. Additionally, repetition-rate compatible options for deuteron tracking within the converter will be explored such as a cross pattern drilled through the converter disks. Using different types of scintillators emitting light of different wavelengths could then be used to simultaneously capture the signal of scintillators placed at different depths within the converter.

The bubble detector setup will be changed, by reducing the spacing between detectors for 90° either side of the laser forward direction, to be able to closely resolve the directional neutron beam generated during the interaction. A second tier of bubble detectors, away from the target chamber, will be installed directly behind the detectors mounted on the chamber wall. A third tier covering 5° either side of laser forward, will yield a more precise source estimation. More bubble detectors outside of the laser plane will allow to further investigate the flux scaling with the angle to the laser plane. Additional options of neutron detectors such as activation counters will be explored to add diversity and the ability to cross-check diagnostics.

8. Conclusion and Outlook

In this work the fundamental constituents necessary for the development of a high repetition-rate laser-driven neutron source are investigated. Key components to such sources are a high repetition-rate, high power laser system, a high repetition-rate compatible target system, an optimized converter design and an efficient and flexible deuteron and neutron detection platform. The technology for high repetition-rate Nd:glass-based high-repetition-rate PW laser systems, utilizing advanced cooling systems to allow for high-repetition-rate operation, already exists, leading to the commissioning of the L3 and L4 beamline at the Extreme Light Infrastructure (Dolní Břežany, Czech Republic) (ELI) in the Czech Republic or the high repetition-rate PW laser at the planned Matter in Extreme Conditions Upgrade (MEC-U) project at SLAC. Targetry systems on the other hand are still in their infancy facing challenges such as stability or debris generation. In the framework of this thesis, a robust ambient-temperature liquid microjet target delivery systems was developed for implementation at high repetition-rate, high power laser facilities. The first high-flux acceleration of deuterons from heavy water jets generated by this nozzle was demonstrated. Utilizing an already existing fast-replenishing cryogenic liquid jet target delivery system, a high repeitition-rate compatible platform for high flux, directional neutron beams was designed and implemented to demonstrate high conversion efficiency and investigate the emission characteristics of the laser-produced neutron beams.

The development of the robust converging liquid microjet target delivery system included the design and machining of a novel nozzle design made of tungsten to increase survivability and is presented in Chapter 3. As tungsten has a high melting temperature and tensile strength, it is an ideally suited material to survive the harsh conditions encountered in short-pulse laser-matter interaction experiments. Additionally, a target manipulation stage was designed to allow for all degrees of freedom including x-y-z-tip-tilt-rotation, to allow for precise positioning of the target at TCC and control of the ion beam pointing. For the purpose of target monitoring and enabling precise positioning of the target, a diagnostics setup, which can be implemented at any short-pulse laser facility, was developed. This target system was successfully fielded at the ALEPH laser at Colorado State University and at the Target Area 2 (TA2) of the Gemini laser at the Rutherford Appleton Laboratory (Didcot, UK) (RAL). The robust nozzles survived a combined number of over 1000 shots on target without any visible damage to the nozzles themselves or any observed degradation of the liquid target performance. Current efforts are focusing on a second iteration of this nozzle design exploring other materials in the process and optimizing the overall size of the nozzle assembly to give access to larger sections of the primary liquid jet sheet. Additional efforts are focusing on minimizing the foot print of the motorization unit and improving the design of the catcher and evacuation system to efficiently pump the residual liquid out of the target chamber.

For the purpose of deuteron acceleration, the developed platform was implemented at the ALEPH laser, where efficient deuteron acceleration was demonstrated at a repetition rate of 0.5 Hz from a 5 μm thick heavy water jet target. At full laser energy on target (5.5 J) deuteron acceleration was observed up to 4.4 MeV at a peak flux of 2×10^{11} deuterons/MeV/sr for 60 consecutive shots at 0.5 Hz. Such a source is of interest for the generation of neutrons with energies similar to deuterium-deuterium fusion neutrons at an energy of 2.45 MeV. Together with a data set acquired at lower laser energy on target (3.7 J), the shot-to-shot stability

was investigated for both data sets. Stable performance was observed for the lower laser energy on target with a stable shot-to-shot flux up to 60% of the cut-off energy of 1.25 MeV. Adding an additional data set at 1.5 J on target, the average spectra were calculated for 60 shots at 0.5 Hz to investigate the cut-off energy scaling with the laser energy incident on the target. The trend observed in this work promises a more favorable scaling with laser energy on target than standard TNSA scaling, making this target a promising platform to explore ion acceleration to high energies. A follow-up experiment at Colorado State University scheduled for March 2023 will investigate this scaling in more detail focusing on tuning laser parameters to achieve high ion energies and fluxes. This future experiment will additionally focus on improving the stability of the target and ion beam at higher laser energies on target and implement the neutron generation platform presented in Chapter 5 to explore the generation of directional neutron beams using ambient-temperature liquid jets as a pitcher target.

The neutron generation platform was developed in the framework of this thesis specifically for cyrogenic liquid jet targets, but can be adapted for any fast replenishing target system and is presented in Chapters 5 and 6 of this thesis. The converter setup is adaptable for different laser systems and experimental environments. This is achieved through the design of the neutron converter in a stacked configuration consisting of disks of materials, that can be stacked in the converter holder, a 1 inch diameter lens tube. Implementation of ion beam monitoring layers at different depths in the converter gives a guideline for the necessary thickness but also allows for precise adjustments of the placement of the converter or the pointing of the ion beam. For the presented configuration a combination of lithium and beryllium was chosen to maximize the neutron yield for a given energy spectrum of the incident deuteron beam. The suite of detectors presented in Chapter 6 characterizes the laser-driven deuteron and neutron beams and provides insights into the emission profile and energy spectra of both ion and neutron beams. Key component of the setup is an r^2 measurement to determine the primary source of neutrons within the target chamber. Paired with the angular emission characterization platform, this will ultimately enable the identification of dominant neutron production channels, which will enable understanding of the processes of neutron generation within the converter. Implementation of suitable detectors will allow the scaling of such experiments to high repetition rates to optimize the neutron production process on the way to achieving a laser-driven high peak and average flux neutron source.

Successful single-shot measurements implemented the described platform at the Texas Petawatt laser facility at the University of Texas at Austin using a cryogenic liquid deuterium jet. For an optimized ion beam-converter overlap, peak fluxes of 7.2×10^9 neutrons/sr were achieved in a directional neutron beam confined to $\pm20^\circ$. Evidence of the optimized ion beam-converter overlap was given by the ion beam spectra measured by the 30° and 122° Thomson parabolas and the RCF within the converter. Additional measurements with less ion beam-converter overlap, show the expected decrease in flux of a directional neutron beam component and resulted in predominant neutron generation in the target chamber wall. This was confirmed by our r^2 measurements, which show less agreement for the decreased overlap, but good agreement for the optimized ion beam-converter overlap. In a next step, the diagnostics around the target chamber and within the converter will be adapted to high repetition-rate operations using compatible detectors discussed in Chapter 6 that have been developed and demonstrated or are under active investigation. Inspiration for new, suitable detectors can be drawn from neutron detectors utilized at the National Ignition Facility (NIF) [270]. Imaging techniques such as penumberal imaging, previously demonstrated for source size imaging [28], or time of flight detectors using different types of scintillators (e.g., liquid scintillators), or different detection mechanisms such as Cherenkov detectors, will significantly broaden the capabilities of this setup in the future.

In conclusion, this work was able to demonstrate two key achievements essential for the development of a high repetition-rate laser-driven neutron source given by a stable source of deuterons generated at high repetition-rate and the generation of a high flux, directional neutron beam with conversion efficiencies matching or exceeding those of previous studies. Both target types, the ambient-temperature liquid jet target and the

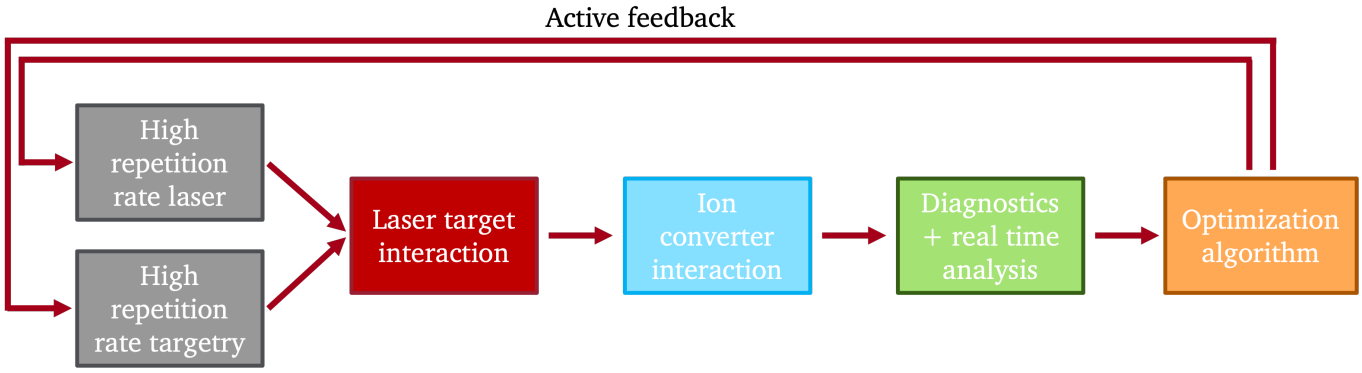

Figure 8.1.: Real time optimization relies on the high repetition-rate operation of a laser and targetry system, real time analysis opportunities for diagnostics, and the interpretation by the analysis and optimization algorithms. The algorithms will then send feedback to adjust the laser and targetry system to optimize the system based on observed particle beam properties.

cryogenic liquid jet target are suited to pursue the development of such a high-flux laser-driven neutron source. The developed platform is compatible with both targets and was successfully fielded for cryogenic liquid jets and will be tested with ambient-temperature liquid jet targets during the upcoming experiment at Colorado State University in March 2023.

In addition to the immediate application of the development of a high repetition-rate laser-driven neutron platform, this work also lays the foundations for testing optimization algorithms with the initial goal of optimizing the ion acceleration performance, which ultimately also benefits the laser-driven neutron source optimization efforts. A real-time optimization scheme is shown in Figure 8.1. The start and end point of such a system are the high repetition-rate laser and targetry systems. Starting with an initial set of parameters, the observed ion beam parameters are evaluated in real time and fed into an optimization algorithm. Such a system can be a more simple algorithm such as Bayesian optimization which aims at global optimization or use even more targeted machine learning techniques.

A system based on Bayesian optimization was implemented in a collaboration experiment between SLAC, the Imperial College London, the ELI Beamlines in the Czech Republic, the University of Michigan and the Queen's University Belfast in the UK at RAL to create a closed-loop system to optimize the proton acceleration

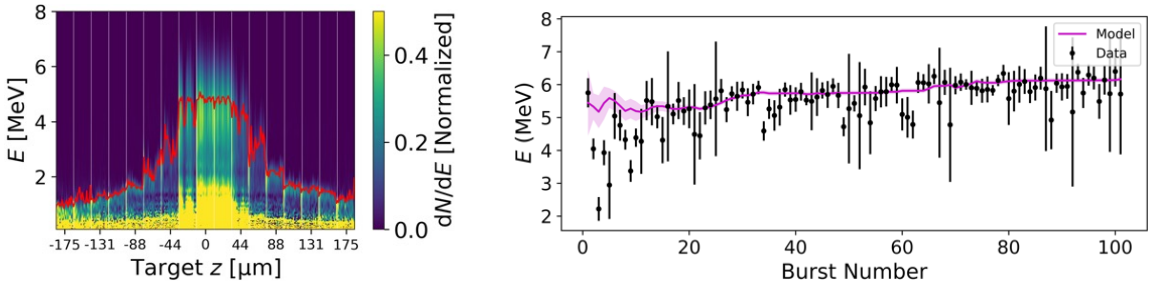

Figure 8.2.: Target z-position scan varying the distance to the focal plane of the laser (0 μm position) shows optimal performance close to the laser focal plane (left). On the right, the prediction of the model (purple) shows better prediction performance for higher training data quantities.

performance from the ambient-temperature liquid water jet target. Figure 8.2 shows an example of the cut-off energies of the proton beams accelerated from the liquid water jet target as a function of the target z-position with 0 corresponding to the laser focal plane. As can be seen, an optimum in ion acceleration energies is achieved close to the laser focal plane. Using this data, an initial model is updated to more accurately match observations. The obtained posterior model exhibits enhanced predictive capabilities with respect to the proton cut-off energies as seen on the right. Compared to also implemented Kapton tape drive targets, the liquid water jet showed stable proton acceleration with high proton cut-off energies and improved predictability of the optimization algorithm. Building on the experience from the experiment at RAL additional optimization techniques can be implemented using the data obtained by the ion and neutron diagnostics from the detection platform to generate predictions of behavior based on measured data and help guide the optimization of the experimental conditions and the platform itself.

In future experiments the versatile developed platform will be able to build on the experience gained in this thesis and will enable the detailed study of correlations between ion and neutron beam parameters and the dominant neutron-production mechanisms. Step-wise scaling of the operation of this neutron generation platform to high repetition rates will be enabled through consecutive experiments at current Ti:sapphire-based high-power laser facilities with increasing repetition rates such as the ALEPH laser at the Colorado State University [124], Gemini (RAL, UK, 1 shot/30 min) [52], Apollon (CNRS, France, 1 shot/min) [54, 55], or VEGA-2 (CLPU, Spain, 1 shot/s) [56]. This will prepare the ultimate test of this platform at high-repetition-rate PW lasers such as the L4 beamline at ELI in the Czech Republic or the planned Matter in Extreme Conditions Upgrade (MEC-U) project at SLAC for delivering the flux needed for applications in plasma physics, nuclear physics and material science.

List of Figures

List of Tables

Bibliography

[1] J. P. Gordon, H. J. Zeiger, and C. H. Townes, "The maser—new type of microwave amplifier, frequency standard, and spectrometer," Phys. Rev., vol. 99, pp. 1264–1274, Aug 1955.

[2] T. Maiman, "Stimulated Optical Radiation in Ruby," Nature, no. 187, pp. 493–494, 1960.

[3] D. Strickland and G. Mourou, "Compression of amplified chirped optical pulses," Optics Communications, vol. 56, no. 3, pp. 219–221, 1985.

[4] S. P. Hatchett, C. G. Brown, T. E. Cowan, E. A. Henry, J. S. Johnson, M. H. Key, J. A. Koch, A. B. Langdon, B. F. Lasinski, R. W. Lee, A. J. Mackinnon, D. M. Pennington, M. D. Perry, T. W. Phillips, M. Roth, T. C. Sangster, M. S. Singh, R. A. Snavely, M. A. Stoyer, S. C. Wilks, and K. Yasuike, "Electron, photon, and ion beams from the relativistic interaction of petawatt laser pulses with solid targets," Physics of Plasmas, vol. 7, no. 5, pp. 2076–2082, 2000.

[5] R. A. Snavely, M. H. Key, S. P. Hatchett, I. E. Cowan, M. Roth, T. W. Phillips, M. A. Stoyer, E. A. Henry, T. C. Sangster, M. S. Singh, S. C. Wilks, A. MacKinnon, A. Offenberger, D. M. Pennington, K. Yasuike, A. B. Langdon, B. F. Lasinski, J. Johnson, M. D. Perry, and E. M. Campbell, "Intense high-energy proton beams from petawatt-laser irradiation of solids," Phys. Rev. Lett., vol. 85, no. 14, pp. 2945–2948, 2000.

[6] S. C. Wilks, A. B. Langdon, T. E. Cowan, M. Roth, M. Singh, S. Hatchett, M. H. Key, D. Pennington, A. MacKinnon, and R. A. Snavely, "Energetic proton generation in ultra-intense laser–solid interactions," Physics of Plasmas, vol. 8, no. 2, pp. 542–549, 2001.

[7] M. Roth, T. E. Cowan, M. H. Key, S. P. Hatchett, C. Brown, W. Fountain, J. Johnson, D. M. Pennington, R. A. Snavely, S. C. Wilks, K. Yasuike, H. Ruhl, F. Pegoraro, S. V. Bulanov, E. M. Campbell, M. D. Perry, and H. Powell, "Fast ignition by intense laser-accelerated proton beams," Phys. Rev. Lett., vol. 86, no. 3, pp. 436–439, 2001.

[8] S. V. Bulanov, T. Z. Esirkepov, V. S. Khoroshkov, A. V. Kuznetsov, and F. Pegoraro, "Oncological hadron therapy with laser ion accelerators," Physics Letters A, vol. 299, no. 2-3, pp. 240–247, 2002.

[9] V. Malka, S. Fritzler, E. Lefebvre, E. d'Humières, R. Ferrand, G. Grillon, C. Albaret, S. Meyroneinc, J.-P. Chambaret, A. Antonetti, and D. Hulin, "Practicability of protontherapy using compact laser systems," Med. Phys., vol. 31, no. 6, pp. 1587–1592, 2004.

[10] T. Tajima, D. Habs, and X. Yan, "Laser Acceleration of Ions for Radiation Therapy," Rev. Accel. Sci. Technol., vol. 02, no. 01, pp. 201–228, 2009.

[11] S. D. Kraft, C. Richter, K. Zeil, M. Baumann, E. Beyreuther, S. Bock, M. Bussmann, T. E. Cowan, Y. Dammene, W. Enghardt, U. Helbig, L. Karsch, T. Kluge, L. Laschinsky, E. Lessmann, J. Metzkes, D. Naumburger, R. Sauerbrey, M. Schürer, M. Sobiella, J. Woithe, U. Schramm, and J. Pawelke, "Dose-dependent biological damage of tumor cells by laser-accelerated proton beams," New J. Phys., vol. 12, no. 8, p. 085003, 2010.

[12] K. Zeil, M. Baumann, E. Beyreuther, T. Burris-Mog, T. E. Cowan, W. Enghardt, L. Karsch, S. D. Kraft, L. Laschinsky, J. Metzkes, D. Naumburger, M. Oppelt, C. Richter, R. Sauerbrey, M. Schürer, U. Schramm, and J. Pawelke, "Dose-controlled irradiation of cancer cells with laser-accelerated proton pulses," App. Phys. B, vol. 110, pp. 437–444, Mar 2013.

[13] A. J. Mackinnon, P. K. Patel, M. Borghesi, R. C. Clarke, R. R. Freeman, H. Habara, S. P. Hatchett, D. Hey, D. G. Hicks, S. Kar, M. H. Key, J. A. King, K. Lancaster, D. Neely, A. Nikkro, P. A. Norreys, M. M. Notley, T. W. Phillips, L. Romagnani, R. A. Snavely, R. B. Stephens, and R. P. J. Town, "Proton Radiography of a Laser-Driven Implosion," Phys. Rev. Lett., vol. 97, no. 4, p. 045001, 2006.

[14] C. K. Li, F. H. Séguin, J. R. Rygg, J. A. Frenje, M. Manuel, R. D. Petrasso, R. Betti, J. Delettrez, J. P. Knauer, F. Marshall, D. D. Meyerhofer, D. Shvarts, V. A. Smalyuk, C. Stoeckl, O. L. Landen, R. P. J. Town, C. A. Back, and J. D. Kilkenny, "Monoenergetic-proton-radiography measurements of implosion dynamics in direct-drive inertial-confinement fusion," Phys. Rev. Lett., vol. 100, p. 225001, Jun 2008.

[15] S. Göde, C. Rödel, K. Zeil, R. Mishra, M. Gauthier, F.-E. Brack, T. Kluge, M. J. MacDonald, J. Metzkes, L. Obst, M. Rehwald, C. Ruyer, H.-P. Schlenvoigt, W. Schumaker, P. Sommer, T. E. Cowan, U. Schramm, S. Glenzer, and F. Fiuza, "Relativistic electron streaming instabilities modulate proton beams accelerated in laser-plasma interactions," Phys. Rev. Lett., vol. 118, p. 194801, May 2017.

[16] J. C. Fernández, J. J. Honrubia, B. J. Albright, K. A. Flippo, D. C. Gautier, B. M. Hegelich, M. J. Schmitt, M. Temporal, and L. Yin, "Progress and prospects of ion-driven fast ignition," Nucl. Fusion, vol. 49, no. 6, p. 065004, 2009.

[17] P. Antici, M. Fazi, A. Lombardi, M. Migliorati, L. Palumbo, P. Audebert, J. Fuchs, "Numerical study of a linear accelerator using laser-generated proton beams as a source," Journal of Applied Physics, vol. 104, no. 12, p. 124901, 2008.

[18] G. Aymar, T. Becker, S. Boogert, M. Borghesi, R. Bingham, C. Brenner, P. N. Burrows, O. C. Ettlinger, T. Dascalu, S. Gibson, et al., "Lhara: The laser-hybrid accelerator for radiobiological applications," Frontiers in Physics, vol. 8, 2020.

[19] L. Perkins, B. Logan, M. Rosen, M. Perry, T. D. de la Rubia, N. Ghoniem, T. Ditmire, P. Springer, and S. Wilks, "The investigation of high intensity laser driven micro neutron sources for fusion materials research at high fluence," Nuclear Fusion, vol. 40, p. 1, jan 2000.

[20] G. Noguere, F. Cserpak, C. Ingelbrecht, A. Plompen, C. Quetel, and P. Schillebeeckx, "Non-destructive analysis of materials by neutron resonance transmission," Nuclear Instruments and Methods in Physics Research Section A: Accelerators, Spectrometers, Detectors and Associated Equipment, vol. 575, no. 3, pp. 476–488, 2007.

[21] M. Roth, D. Jung, K. Falk, N. Guler, O. Deppert, M. Devlin, A. Favalli, J. Fernandez, D. Gautier, M. Geissel, R. Haight, C. E. Hamilton, B. M. Hegelich, R. P. Johnson, F. Merrill, G. Schaumann, K. Schoenberg, M. Schollmeier, T. Shimada, T. Taddeucci, J. L. Tybo, F. Wagner, S. A. Wender, C. H. Wilde, and G. A. Wurden, "Bright laser-driven neutron source based on the relativistic transparency of solids," Phys. Rev. Lett., vol. 110, p. 044802, Jan 2013.

[22] F. Treffert, C. B. Curry, T. Ditmire, G. D. Glenn, H. J. Quevedo, M. Roth, C. Schoenwaelder, M. Zimmer, S. H. Glenzer, and M. Gauthier, "Towards high-repetition-rate fast neutron sources using novel enabling technologies," Instruments, vol. 5, p. 38, Dec 2021.

[23] T. M. Spinka and C. Haefner, "High average-power ultrafast lasers," Optics & Photonics News, 2017.

[24] K. Nakamura, H.-S. Mao, A. J. Gonsalves, H. Vincenti, D. E. Mittelberger, J. Daniels, A. Magana, C. Toth, and W. P. Leemans, "Diagnostics, control and performance parameters for the bella high repetition rate petawatt class laser," IEEE Journal of Quantum Electronics, vol. 53, no. 4, pp. 1–21, 2017.

[25] A. Bayramian, R. Bopp, M. Borden, B. Deri, R. DesJardin, J. M. Di Nicola, M. Drouin, A. Erlandson, S. Fulkerson, J. Jarboe, G. Johnson, H. Zhang, B. Heidl, J. Horner, K. Kasl, D. Kim, E. Koh, J. Lusk, C. Marshall, D. Mason, T. Mazanec, J. Naylon, J. Nissen, K. Primdahl, B. Rus, M. Scanlan, K. Schaffers, T. Simon, T. Spinka, J. Stanley, C. Stolz, S. Telford, and C. Haefner, "High energy, high average power, dpssl system for next generation petawatt laser systems," in 2016 Conference on Lasers and Electro-Optics (CLEO), pp. 1–2, 2016.

[26] C. B. Curry, C. Schoenwaelder, S. Goede, J. B. Kim, M. Rehwald, F. Treffert, K. Zeil, S. H. Glenzer, and M. Gauthier, "Cryogenic liquid jets for high repetition rate discovery science," J. Vis. Exp., vol. 159, p. e61130, 2020.

[27] D. P. Higginson, J. M. McNaney, D. C. Swift, T. Bartal, D. S. Hey, R. Kodama, S. Le Pape, A. Mackinnon, D. Mariscal, H. Nakamura, N. Nakanii, K. A. Tanaka, and F. N. Beg, "Laser generated neutron source for neutron resonance spectroscopy," Physics of Plasmas, vol. 17, no. 10, p. 100701, 2010.

[28] N. Guler, P. Volegov, A. Favalli, F. E. Merrill, K. Falk, D. Jung, J. L. Tybo, C. H. Wilde, S. Croft, C. Danly, O. Deppert, M. Devlin, J. Fernandez, D. C. Gautier, M. Geissel, R. Haight, C. E. Hamilton, B. M. Hegelich, D. Henzlova, R. P. Johnson, G. Schaumann, K. Schoenberg, M. Schollmeier, T. Shimada, M. T. Swinhoe, T. Taddeucci, S. A. Wender, G. A. Wurden, and M. Roth, "Neutron imaging with the short-pulse laser driven neutron source at the trident laser facility," Journal of Applied Physics, vol. 120, no. 15, p. 154901, 2016.

[29] D. Brown, T. Gozani, R. Loveman, J. Bendahan, P. Ryge, J. Stevenson, F. Liu, and M. Sivakumar, "Application of pulsed fast neutrons analysis to cargo inspection," Nuclear Instruments and Methods in Physics Research Section A: Accelerators, Spectrometers, Detectors and Associated Equipment, vol. 353, no. 1, pp. 684–688, 1994.

[30] L. Gray and J. Read, "Treatment of cancer by fast neutrons," Nature, vol. 152, p. 53, 1943.

[31] Y. B. Melnichenko and G. D. Wignall, "Small-angle neutron scattering in materials science: Recent practical applications," Journal of Applied Physics, vol. 102, no. 2, 2007.

[32] S. N. Chen, F. Negoita, K. Spohr, E. d'Humières, I. Pomerantz, and J. Fuchs, "Extreme brightness laser-based neutron pulses as a pathway for investigating nucleosynthesis in the laboratory," Matter and Radiation at Extremes, vol. 4, no. 5, p. 054402, 2019.

[33] P.-H. Rebut, "Iter: the first experimental fusion reactor," Fusion Engineering and Design, vol. 30, no. 1, pp. 85–118, 1995.

[34] K. Ikeda, "Iter on the road to fusion energy," Nucl. Fusion, vol. 50, p. 014002, 2009.

[35] S. Ciattaglia, G. Federici, L. Barucca, A. Lampasi, S. Minucci, and I. Moscato, "The european demo fusion reactor: Design status and challenges from balance of plant point of view," in 2017 IEEE International Conference on Environment and Electrical Engineering and 2017 IEEE Industrial and Commercial Power Systems Europe (EEEIC / I CPS Europe), pp. 1–6, 2017.

[36] L. J. Reinders, Post-ITER: DEMO and Fusion Power Plants, pp. 455–484. Springer International Publishing, 2021.

[37] G. J. Russell, J. S. Gilmore, H. Robinson, G. L. Legate, A. Bridge, R. J. Sanchez, R. J. Brewton, R. Woods, and I. H. G. Hughes, "LANSCE target system performance," Advanced Neutron Sources, pp. 483–496, 1988.

[38] International Atomic Energy Agency (IAEA), "Research reactor details - lena, triga ii pavia." http://www-naweb.iaea.org/napc/physics/research_reactors/database/RR%20Data%20Base/datasets/report/Italy%20(Italian%20Republic)%20%20Research%20Reactor%20Details%20-%20LENA,%20TRIGA%20II%20PAVIA.htm, March 2009.

[39] R. Kodama, P. A. Norreys, K. Mima, A. E. Dangor, R. G. Evans, H. Fujita, Y. Kitagawa, K. Krushelnick, T. Miyakoshi, N. Miyanaga, T. Norimatsu, S. J. Rose, T. Shozaki, K. Shigemori, A. Sunahara, M. Tampo, K. A. Tanaka, Y. Toyama, T. Yamanaka, and M. Zepf, "Fast heating of ultrahigh-density plasma as a step towards laser fusion ignition," Nature, vol. 412, no. 6849, pp. 798–802, 2001.

[40] R. Betti and O. Hurricane, "Inertial-confinement fusion with lasers," Nature Phys., vol. 12, pp. 435–448, 2016.

[41] P. B. Radha, R. Betti, T. R. Boehly, J. A. Delettrez, D. H. Edgell, V. N. Goncharov, I. V. Igumenshchev, J. P. Knauer, J. A. Marozas, F. J. Marshall, R. L. McCrory, D. D. Meyerhofer, S. P. Regan, T. C. Sangster, W. Seka, S. Skupsky, A. A. Solodov, C. Stoeckl, W. Theobald, J. A. Frenje, D. T. Casey, C. K. Li, and R. D. Petrasso, "Inertial confinement fusion using the omega laser system," IEEE Transactions on Plasma Science, vol. 39, no. 4, pp. 1007–1014, 2011.

[42] S. H. Glenzer, B. J. MacGowan, P. Michel, N. B. Meezan, L. J. Suter, S. N. Dixit, J. L. Kline, G. A. Kyrala, D. K. Bradley, D. A. Callahan, E. L. Dewald, L. Divol, E. Dzenitis, M. J. Edwards, A. V. Hamza, C. A. Haynam, D. E. Hinkel, D. H. Kalantar, J. D. Kilkenny, O. L. Landen, J. D. Lindl, S. LePape, J. D. Moody, A. Nikroo, T. Parham, M. B. Schneider, R. P. J. Town, P. Wegner, K. Widmann, P. Whitman, B. K. F. Young, B. V. Wonterghem, L. J. Atherton, and E. I. Moses, "Symmetric inertial confinement fusion implosions at ultra-high laser energies," Science, vol. 327, no. 5970, pp. 1228–1231, 2010.

[43] A. B. Zylstra, O. A. Hurricane, D. A. Callahan, A. L. Kritcher, J. E. Ralph, H. F. Robey, J. S. Ross, C. V. Young, K. L. Baker, D. T. Casey, T. Döppner, L. Divol, M. Hohenberger, S. Le Pape, A. Pak, P. K. Patel, R. Tommasini, S. J. Ali, P. A. Amendt, L. J. Atherton, B. Bachmann, D. Bailey, L. R. Benedetti, L. Berzak Hopkins, R. Betti, S. D. Bhandarkar, J. Biener, R. M. Bionta, N. W. Birge, E. J. Bond, D. K. Bradley, T. Braun, T. M. Briggs, M. W. Bruhn, P. M. Celliers, B. Chang, T. Chapman, H. Chen, C. Choate, A. R. Christopherson, D. S. Clark, J. W. Crippen, E. L. Dewald, T. R. Dittrich, M. J. Edwards, W. A. Farmer, J. E. Field, D. Fittinghoff, J. Frenje, J. Gaffney, M. Gatu Johnson, S. H. Glenzer, G. P. Grim, S. Haan, K. D. Hahn, G. N. Hall, B. A. Hammel, J. Harte, E. Hartouni, J. E. Heebner, V. J. Hernandez, H. Herrmann, M. C. Herrmann, D. E. Hinkel, D. D. Ho, J. P. Holder, W. W. Hsing, H. Huang, K. D. Humbird, N. Izumi, L. C. Jarrott, J. Jeet, O. Jones, G. D. Kerbel, S. M. Kerr, S. F. Khan, J. Kilkenny, Y. Kim, H. Geppert Kleinrath, V. Geppert Kleinrath, C. Kong, J. M. Koning, J. J. Kroll, M. K. G. Kruse, B. Kustowski, O. L. Landen, S. Langer, D. Larson, N. C. Lemos, J. D. Lindl, T. Ma, M. J. MacDonald, B. J. MacGowan, A. J. Mackinnon, S. A. MacLaren, A. G. MacPhee, M. M. Marinak, D. A. Mariscal, E. V. Marley, L. Masse, K. Meaney, N. B. Meezan, P. A. Michel, M. Millot, J. L. Milovich, J. D. Moody, A. S. Moore, J. W. Morton, T. Murphy, K. Newman, J. M. G. Di Nicola, A. Nikroo, R. Nora, M. V. Patel, L. J. Pelz, J. L. Peterson, Y. Ping, B. B. Pollock, M. Ratledge, N. G. Rice, H. Rinderknecht, M. Rosen, M. S. Rubery, J. D. Salmonson, J. Sater, S. Schiaffino, D. J. Schlossberg, M. B. Schneider, C. R. Schroeder, H. A. Scott, S. M. Sepke, K. Sequoia, M. W. Sherlock, S. Shin, V. A. Smalyuk, B. K. Spears, P. T. Springer, M. Stadermann, S. Stoupin, D. J. Strozzi, L. J. Suter, C. A. Thomas, R. P. J. Town, E. R. Tubman,

C. Trosseille, P. L. Volegov, C. R. Weber, K. Widmann, C. Wild, C. H. Wilde, B. M. Van Wonterghem, D. T. Woods, B. N. Woodworth, M. Yamaguchi, S. T. Yang, and G. B. Zimmerman, "Burning plasma achieved in inertial fusion," Nature, vol. 601, no. 7894, pp. 542–548, 2022.

[44] A. L. Kritcher, C. V. Young, H. F. Robey, C. R. Weber, A. B. Zylstra, O. A. Hurricane, D. A. Callahan, J. E. Ralph, J. S. Ross, K. L. Baker, D. T. Casey, D. S. Clark, T. Döppner, L. Divol, M. Hohenberger, L. B. Hopkins, S. Le Pape, N. B. Meezan, A. Pak, P. K. Patel, R. Tommasini, S. J. Ali, P. A. Amendt, L. J. Atherton, B. Bachmann, D. Bailey, L. R. Benedetti, R. Betti, S. D. Bhandarkar, J. Biener, R. M. Bionta, N. W. Birge, E. J. Bond, D. K. Bradley, T. Braun, T. M. Briggs, M. W. Bruhn, P. M. Celliers, B. Chang, T. Chapman, H. Chen, C. Choate, A. R. Christopherson, J. W. Crippen, E. L. Dewald, T. R. Dittrich, M. J. Edwards, W. A. Farmer, J. E. Field, D. Fittinghoff, J. A. Frenje, J. A. Gaffney, M. G. Johnson, S. H. Glenzer, G. P. Grim, S. Haan, K. D. Hahn, G. N. Hall, B. A. Hammel, J. Harte, E. Hartouni, J. E. Heebner, V. J. Hernandez, H. Herrmann, M. C. Herrmann, D. E. Hinkel, D. D. Ho, J. P. Holder, W. W. Hsing, H. Huang, K. D. Humbird, N. Izumi, L. C. Jarrott, J. Jeet, O. Jones, G. D. Kerbel, S. M. Kerr, S. F. Khan, J. Kilkenny, Y. Kim, H. Geppert-Kleinrath, V. Geppert-Kleinrath, C. Kong, J. M. Koning, M. K. G. Kruse, J. J. Kroll, B. Kustowski, O. L. Landen, S. Langer, D. Larson, N. C. Lemos, J. D. Lindl, T. Ma, M. J. MacDonald, B. J. MacGowan, A. J. Mackinnon, S. A. MacLaren, A. G. MacPhee, M. M. Marinak, D. A. Mariscal, E. V. Marley, L. Masse, K. Meaney, P. A. Michel, M. Millot, J. L. Milovich, J. D. Moody, A. S. Moore, J. W. Morton, T. Murphy, K. Newman, J. M. G. Di Nicola, A. Nikroo, R. Nora, M. V. Patel, L. J. Pelz, J. L. Peterson, Y. Ping, B. B. Pollock, M. Ratledge, N. G. Rice, H. Rinderknecht, M. Rosen, M. S. Rubery, J. D. Salmonson, J. Sater, S. Schiaffino, D. J. Schlossberg, M. B. Schneider, C. R. Schroeder, H. A. Scott, S. M. Sepke, K. Sequoia, M. W. Sherlock, S. Shin, V. A. Smalyuk, B. K. Spears, P. T. Springer, M. Stadermann, S. Stoupin, D. J. Strozzi, L. J. Suter, C. A. Thomas, R. P. J. Town, C. Trosseille, E. R. Tubman, P. L. Volegov, K. Widmann, C. Wild, C. H. Wilde, B. M. Van Wonterghem, D. T. Woods, B. N. Woodworth, M. Yamaguchi, S. T. Yang, and G. B. Zimmerman, "Design of inertial fusion implosions reaching the burning plasma regime," Nature Physics, vol. 18, no. 3, pp. 251–258, 2022.

[45] K. L. Lancaster, S. Karsch, H. Habara, F. N. Beg, E. L. Clark, R. Freeman, M. H. Key, J. A. King, R. Kodama, K. Krushelnick, K. W. D. Ledingham, P. McKenna, C. D. Murphy, P. A. Norreys, R. Stephens, C. Stöeckl, Y. Toyama, M. S. Wei, and M. Zepf, "Characterization of 7li(p,n)7be neutron yields from laser produced ion beams for fast neutron radiography," Physics of Plasmas, vol. 11, no. 7, pp. 3404–3408, 2004.

[46] L. Willingale, G. M. Petrov, A. Maksimchuk, J. Davis, R. R. Freeman, A. S. Joglekar, T. Matsuoka, C. D. Murphy, V. M. Ovchinnikov, A. G. R. Thomas, L. Van Woerkom, and K. Krushelnick, "Comparison of bulk and pitcher-catcher targets for laser-driven neutron production," Physics of Plasmas, vol. 18, no. 8, p. 083106, 2011.

[47] A. Favalli, N. Guler, D. Henzlova, S. Croft, K. Falk, D. C. Gautier, K. D. Ianakiev, M. Iliev, S. Palaniyappan, M. Roth, J. C. Fernandez, and M. T. Swinhoe, "Characterizing laser-plasma ion accelerators driving an intense neutron beam via nuclear signatures," Scientific Reports, vol. 9, no. 1, p. 2004, 2019.

[48] W. I. Linlor, "Ion energies produced by laser giant pulse," Applied Physics Letters, vol. 3, no. 11, pp. 210–211, 1963.

[49] S. J. Gitomer, R. D. Jones, F. Begay, A. W. Ehler, J. F. Kephart, and R. Kristal, "Fast ions and hot electrons in the laser–plasma interaction," The Physics of Fluids, vol. 29, no. 8, pp. 2679–2688, 1986.

[50] A. Maksimchuk, S. Gu, K. Flippo, D. Umstadter, and A. Y. Bychenkov, "Forward ion acceleration in thin films driven by a high-intensity laser," Physical Review Letters, vol. 84, no. 18, pp. 4108–4111, 2000.

[51] V. Bagnoud, B. Aurand, A. Blazevic, S. Borneis, C. Bruske, B. Ecker, U. Eisenbarth, J. Fils, A. Frank,

E. Gaul, S. Goette, C. Haefner, T. Hahn, K. Harres, H. M. Heuck, D. Hochhaus, D. H. H. Hoffmann, D. Javorková, H. J. Kluge, T. Kuehl, S. Kunzer, M. Kreutz, T. Merz-Mantwill, P. Neumayer, E. Onkels, D. Reemts, O. Rosmej, M. Roth, T. Stoehlker, A. Tauschwitz, B. Zielbauer, D. Zimmer, and K. Witte, "Commissioning and early experiments of the phelix facility," Applied Physics B, vol. 100, no. 1, pp. 137–150, 2010.

[52] C. J. Hooker, S. Blake, O. Chekhlov, R. J. Clarke, J. L. Collier, E. J. Divall, K. Ertel, P. S. Foster, S. J. Hawkes, P. Holligan, B. Landowski, W. J. Lester, D. Neely, B. Parry, R. Pattathil, M. Streeter, and B. E. Wyborn, "Commissioning the astra gemini petawatt ti:sapphire laser system," in 2008 Conference on Lasers and Electro-Optics and 2008 Conference on Quantum Electronics and Laser Science, pp. 1–2, 2008.

[53] V. Yanovsky, V. Chvykov, G. Kalinchenko, P. Rousseau, T. Planchon, T. Matsuoka, A. Maksimchuk, J. Nees, G. Cheriaux, G. Mourou, and K. Krushelnick, "Ultra-high intensity- 300-tw laser at 0.1 hz repetition rate.," Opt. Express, vol. 16, pp. 2109–2114, Feb 2008.

[54] D. Papadopoulos, J. Zou, C. Le Blanc, G. Chériaux, P. Georges, F. Druon, G. Mennerat, P. Ramirez, L. Martin, A. Fréneaux, and et al., "The apollon 10 pw laser: experimental and theoretical investigation of the temporal characteristics," High Power Laser Science and Engineering, vol. 4, p. e34, 2016.

[55] K. Burdonov, A. Fazzini, V. Lelasseux, J. Albrecht, P. Antici, Y. Ayoul, A. Beluze, D. Cavanna, T. Ceccotti, M. Chabanis, A. Chaleil, S. N. Chen, Z. Chen, F. Consoli, M. Cuciuc, X. Davoine, J. P. Delaneau, E. d'Humières, J.-L. Dubois, C. Evrard, E. Filippov, A. Freneaux, P. Forestier-Colleoni, L. Gremillet, V. Horny, L. Lancia, L. Lecherbourg, N. Lebas, A. Leblanc, W. Ma, L. Martin, F. Negoita, J.-L. Paillard, D. Papadopoulos, F. Perez, S. Pikuz, G. Qi, F. Quéré, L. Ranc, P.-A. Söderström, M. Scisciò, S. Sun, S. Vallières, P. Wang, W. Yao, F. Mathieu, P. Audebert, and J. Fuchs, "Characterization and performance of the apollon short-focal-area facility following its commissioning at 1 pw level," Matter and Radiation at Extremes, vol. 6, no. 6, p. 064402, 2021.

[56] M. Huault, G. Zeraouli, J. G. Ajates, J. Apiñaniz, E. García, I. Hernández, S. Malko, C. Méndez, J. A. Perez, J. D. Pisonero, C. Salgado, X. Vaisseau, O. Varela, G. Gatti, L. Volpe, L. Roso, R. Fedosejevs, A. Longman, R. Shepherd, and W. T. Hill, "Commissioning experiments of vega-2 at centro de láseres pulsados (clpu)," in Frontiers in Optics 2017, p. FM2B.4, Optical Society of America, 2017.

[57] J. W. Yoon, C. Jeon, J. Shin, S. K. Lee, H. W. Lee, I. W. Choi, H. T. Kim, J. H. Sung, and C. H. Nam, "Achieving the laser intensity of 5.5×1022 w/cm2 with a wavefront-corrected multi-pw laser," Opt. Express, vol. 27, pp. 20412–20420, Jul 2019.

[58] J. W. Yoon, Y. G. Kim, I. W. Choi, J. H. Sung, H. W. Lee, S. K. Lee, and C. H. Nam, "Realization of laser intensity over 10^{23}w/cm^2," Optica, vol. 8, pp. 630–635, May 2021.

[59] L. Ranc, C. L. Blanc, N. Lebas, L. Martin, J.-P. Zou, F. Mathieu, C. Radier, S. Ricaud, F. Druon, and D. Papadopoulos, "Improvement in the temporal contrast in the tens of ps range of the multi-pw apollon laser front-end," Opt. Lett., vol. 45, pp. 4599–4602, Aug 2020.

[60] D. Kaganovich, J. R. Penano, M. H. Helle, D. F. Gordon, B. Hafizi, and A. Ting, "Origin and control of the subpicosecond pedestal in femtosecond laser systems," Opt. Lett., vol. 38, pp. 3635–3638, Sep 2013.

[61] N. Didenko, A. Konyashchenko, A. Lutsenko, and S. Tenyakov, "Contrast degradation in a chirped-pulse amplifier due to generation of prepulses by postpulses," Opt. Express, vol. 16, pp. 3178–3190, Mar 2008.

[62] A. Bayramian, P. Armstrong, E. Ault, R. Beach, C. Bibeau, J. Caird, R. Campbell, B. Chai, J. Dawson, C. Ebbers, A. Erlandson, Y. Fei, B. Freitas, R. Kent, Z. Liao, T. Ladran, J. Menapace, B. Molander, S. Payne, N. Peterson, M. Randles, K. Schaffers, S. Sutton, J. Tassano, S. Telford, and E. Utterback, "The mercury project: A high average power, gas-cooled laser for inertial fusion energy development," Fusion Science and Technology, vol. 52, no. 3, pp. 383–387, 2007.

[63] Z. Ye, C. Liu, B. Tu, K. Wang, Q. Gao, C. Tang, and Z. Cai, "Kilowatt-level direct-'refractive index matching liquid'-cooled Nd:YLF thin disk laser resonator," Optics Express, vol. 24, no. 2, p. 1758, 2016.

[64] E. Sistrunk, T. Spinka, A. Bayramian, S. Betts, R. Bopp, S. Buck, K. Charron, J. Cupal, R. Deri, M. Drouin, A. Erlandson, E. S. Fulkerson, J. Horner, J. Horacek, J. Jarboe, K. Kasl, D. Kim, E. Koh, L. Koubikova, R. Lanning, W. Maranville, C. Marshall, D. Mason, J. Menapace, P. Miller, P. Mazurek, A. Naylon, J. Novak, D. Peceli, P. Rosso, K. Schaffers, D. Smith, J. Stanley, R. Steele, S. Telford, J. Thoma, D. VanBlarcom, J. Weiss, P. Wegner, B. Rus, and C. Haefner, "All diode-pumped, high-repetition-rate advanced petawatt laser system (HAPLS)," 2017 Conference on Lasers and Electro-Optics, CLEO 2017 - Proceedings, vol. 2017-Janua, pp. 1–2, 2017.

[65] B. Rus, P. Bakule, D. Kramer, G. Korn, J. T. Green, J. Nóvak, M. Fibrich, F. Batysta, J. Thoma, J. Naylon, T. Mazanec, M. Vítek, R. Barros, E. Koutris, J. Hřebíček, J. Polan, R. Baše, P. Homer, M. Košelja, T. Havlíček, A. Honsa, M. Novák, C. Zervos, P. Korous, M. Laub, and J. Houžvička, "ELI-Beamlines laser systems: status and design options," in High-Power, High-Energy, and High-Intensity Laser Technology; and Research Using Extreme Light: Entering New Frontiers with Petawatt-Class Lasers (G. Korn, L. O. Silva, and J. Hein, eds.), vol. 8780, p. 87801T, International Society for Optics and Photonics, SPIE, 2013.

[66] P. Gibbon, Short Pulse Laser Interactions with Matter: An Introduction. Imperial College Press, 2005.

[67] H. R. Varma, M. F. Ciappina, N. Rohringer, and R. Santra, "Above-threshold ionization in the x-ray regime," Phys. Rev. A, vol. 80, p. 053424, Nov 2009.

[68] T. D. Märk and G. D. Dunn, Electron Impact Ionization. Springer Verlag Wien, 1. ed. ed., 1985.

[69] P. McKenna, D. Neely, R. Bingham, and D. Jaroszynski, Laser-Plasma Interactions and Applications. Springer Heidelberg, 2013. Scottish Graduate Series.

[70] E. Esarey, P. Sprangle, and J. Krall, "Laser acceleration of electrons in vacuum," Phys. Rev. E, vol. 52, pp. 5443–5453, Nov 1995.

[71] F. F. Chen, Introduction to Plasma Physics and Controlled Fusion. Springer, ed. 3 ed., 2016.

[72] W. L. Kruer and K. Estabrook, "J x B heating by very intense laser light," The Physics of Fluids, vol. 28, no. 1, pp. 430–432, 1985.

[73] T. Liseykina, P. Mulser, and M. Murakami, "Collisionless absorption, hot electron generation, and energy scaling in intense laser-target interaction," Physics of Plasmas, vol. 22, no. 3, p. 033302, 2015.

[74] S. Jiang, A. G. Krygier, D. W. Schumacher, K. U. Akli, and R. R. Freeman, "Effects of front-surface target structures on properties of relativistic laser-plasma electrons," Phys. Rev. E, vol. 89, p. 013106, Jan 2014.

[75] S. C. Wilks, W. L. Kruer, M. Tabak, and A. B. Langdon, "Absorption of ultra-intense laser pulses," Phys. Rev. Lett., vol. 69, pp. 1383–1386, Aug 1992.

[76] K. B. Wharton, S. P. Hatchett, S. C. Wilks, M. H. Key, J. D. Moody, V. Yanovsky, A. A. Offenberger, B. A. Hammel, M. D. Perry, and C. Joshi, "Experimental Measurements of Hot Electrons Generated by Ultraintense ($> 10^{19} W/\mathrm{cm}^2$) Laser-Plasma Interactions on Solid-Density Targets," Phys. Rev. Lett., vol. 81, pp. 822–825, Jul 1998.

[77] E. L. Clark, K. Krushelnick, J. R. Davies, M. Zepf, M. Tatarakis, F. N. Beg, A. Machacek, P. A. Norreys, M. I. K. Santala, I. Watts, and A. E. Dangor, "Measurements of energetic proton transport through magnetized plasma from intense laser interactions with solids," Phys. Rev. Lett., vol. 84, pp. 670–673, Jan 2000.

[78] J. Fuchs, P. Antici, E. D'Humières, E. Lefebvre, M. Borghesi, E. Brambrink, C. a. Cecchetti, M. Kaluza, V. Malka, M. Manclossi, S. Meyroneinc, P. Mora, J. Schreiber, T. Toncian, H. Pépin, and P. Audebert, "Laser-driven proton scaling laws and new paths towards energy increase," Nat. Phys., vol. 2, no. 1, pp. 48–54, 2006.

[79] A. P. L. Robinson, M. Zepf, S. Kar, R. G. Evans, and C. Bellei, "Radiation pressure acceleration of thin foils with circularly polarized laser pulses," New Journal of Physics, vol. 10, no. 1, p. 013021, 2008.

[80] L. Yin, B. J. Albright, B. M. Hegelich, and J. C. Fernández, "Gev laser ion acceleration from ultrathin targets: The laser break-out afterburner," Laser and Particle Beams, vol. 24, no. 2, p. 291–298, 2006.

[81] A. Henig, S. Steinke, M. Schnürer, T. Sokollik, R. Hörlein, D. Kiefer, D. Jung, J. Schreiber, B. M. Hegelich, X. Q. Yan, J. Meyer-ter Vehn, T. Tajima, P. V. Nickles, W. Sandner, and D. Habs, "Radiation-pressure acceleration of ion beams driven by circularly polarized laser pulses," Phys. Rev. Lett., vol. 103, p. 245003, Dec 2009.

[82] D. Haberberger, S. Tochitsky, F. Fiuza, C. Gong, R. A. Fonseca, L. O. Silva, W. B. Mori, and C. Joshi, "Collisionless shocks in laser-produced plasma generate monoenergetic high-energy proton beams," Nat. Phys., vol. 8, pp. 95–99, jan 2012.

[83] F. Fiuza, A. Stockem, E. Boella, R. A. Fonseca, L. O. Silva, D. Haberberger, S. Tochitsky, C. Gong, W. B. Mori, and C. Joshi, "Laser-driven shock acceleration of monoenergetic ion beams," Phys. Rev. Lett., vol. 109, p. 215001, Nov 2012.

[84] R. Mishra, F. Fiuza, and S. Glenzer, "Enhanced ion acceleration in transition from opaque to transparent plasmas," New Journal of Physics, vol. 20, no. 4, p. 043047, 2018.

[85] P. L. Poole, L. Obst, G. E. Cochran, J. Metzkes, H. P. Schlenvoigt, I. Prencipe, T. Kluge, T. Cowan, U. Schramm, D. W. Schumacher, and K. Zeil, "Laser-driven ion acceleration via target normal sheath acceleration in the relativistic transparency regime," New Journal of Physics, vol. 20, no. 1, 2018.

[86] A. Higginson, R. J. Gray, M. King, R. J. Dance, S. D. Williamson, N. M. Butler, R. Wilson, R. Capdessus, C. Armstrong, J. S. Green, S. J. Hawkes, P. Martin, W. Q. Wei, S. R. Mirfayzi, X. H. Yuan, S. Kar, M. Borghesi, R. J. Clarke, D. Neely, and P. McKenna, "Near-100 MeV protons via a laser-driven transparency-enhanced hybrid acceleration scheme," Nature Communications, vol. 9, no. 1, 2018.

[87] H. Daido, M. Nishiuchi, and A. S. Pirozhkov, "Review of laser-driven ion sources and their applications," Reports on Progress in Physics, vol. 75, p. 056401, apr 2012.

[88] P. Mora, "Plasma expansion into a vacuum," Phys. Rev. Lett., vol. 90, p. 185002, May 2003.

[89] M. Borghesi, "Laser-driven ion acceleration: State of the art and emerging mechanisms," Nuclear Instruments and Methods in Physics Research Section A: Accelerators, Spectrometers, Detectors and

Associated Equipment, vol. 740, pp. 6 – 9, 2014. Proceedings of the first European Advanced Accelerator Concepts Workshop 2013.

[90] M. Roth and M. Schollmeier, "Ion Acceleration - Target Normal Sheath Acceleration," Proceedings of the CAS-CERN Accelerator School: Plasma Wake Acceleration, November 2014.

[91] P. Mora, "Collisionless expansion of a gaussian plasma into a vacuum," Physics of Plasmas, vol. 12, no. 11, p. 112102, 2005.

[92] P. Mora, "Thin-foil expansion into a vacuum," Phys. Rev. E, vol. 72, p. 056401, Nov 2005.

[93] J. Fuchs, P. Antici, E. d'Humières, E. Lefebvre, M. Borghesi, E. Brambrink, C. A. Cecchetti, M. Kaluza, V. Malka, M. Manclossi, S. Meyroneinc, P. Mora, J. Schreiber, T. Toncian, H. Pépin, and P. Audebert, "Laser-driven proton scaling laws and new paths towards energy increase," Nature Physics, vol. 2, no. 1, pp. 48–54, 2006.

[94] T. Ceccotti, A. Lévy, H. Popescu, F. Réau, P. D'Oliveira, P. Monot, J. P. Geindre, E. Lefebvre, and P. Martin, "Proton acceleration with high-intensity ultrahigh-contrast laser pulses," Phys. Rev. Lett., vol. 99, p. 185002, Oct 2007.

[95] K. Zeil, S. D. Kraft, S. Bock, M. Bussmann, T. E. Cowan, T. Kluge, J. Metzkes, T. Richter, R. Sauerbrey, and U. Schramm, "The scaling of proton energies in ultrashort pulse laser plasma acceleration," New J. Phys., vol. 12, no. 4, p. 045015, 2010.

[96] F. Wagner, O. Deppert, C. Brabetz, P. Fiala, A. Kleinschmidt, P. Poth, V. A. Schanz, A. Tebartz, B. Zielbauer, M. Roth, T. Stöhlker, and V. Bagnoud, "Maximum proton energy above 85 mev from the relativistic interaction of laser pulses with micrometer thick ch_2 targets," Phys. Rev. Lett., vol. 116, p. 205002, May 2016.

[97] J. Schreiber, F. Bell, and Z. Najmudin, "Optimization of relativistic laser–ion acceleration," High Power Laser Science and Engineering, vol. 2, p. e41, 2014.

[98] C. Perego, A. Zani, D. Batani, and M. Passoni, "Extensive comparison among target normal sheath acceleration theoretical models," Nuclear Instruments and Methods in Physics Research Section A: Accelerators, Spectrometers, Detectors and Associated Equipment, vol. 653, no. 1, pp. 89–93, 2011. Superstrong 2010.

[99] J. Schreiber, F. Bell, F. Grüner, U. Schramm, M. Geissler, M. Schnürer, S. Ter-Avetisyan, B. M. Hegelich, J. Cobble, E. Brambrink, J. Fuchs, P. Audebert, and D. Habs, "Analytical model for ion acceleration by high-intensity laser pulses," Phys. Rev. Lett., vol. 97, p. 045005, Jul 2006.

[100] C.M. Brenner, J.S. Green, A.P.L. Robinson, D.C. Carroll, B. Dromey, P.S. Foster, S. Kar, Y.T. Li, K. Markey, C. Spindloe, M.J.V. Streeter, M. Tolley, C.-G. Wahlström, M.H. Xu, M. Zepf, P. McKenna and D. Neely, "Dependence of laser accelerated protons on laser energy following the interaction of defocused, intense laser pulses with ultra-thin targets," Laser and Particle Beams, vol. 29, no. 3, p. 345–351, 2011.

[101] R. A. Simpson, G. G. Scott, D. Mariscal, D. Rusby, P. M. King, E. Grace, A. Aghedo, I. Pagano, M. Sinclair, C. Armstrong, M. J.-E. Manuel, A. Haid, K. Flippo, L. Winslow, M. Gatu-Johnson, J. A. Frenje, D. Neely, S. Kerr, G. J. Williams, S. Andrews, R. Cauble, K. Charron, R. Costa, B. Fischer, S. Maricle, B. Stuart, F. Albert, N. Lemos, A. Mackinnon, A. MacPhee, A. Pak, and T. Ma, "Scaling of laser-driven electron and proton acceleration as a function of laser pulse duration, energy, and intensity in the multi-picosecond regime," Physics of Plasmas, vol. 28, no. 1, p. 013108, 2021.

[102] M. Zimmer, S. Scheuren, T. Ebert, G. Schaumann, B. Schmitz, J. Hornung, V. Bagnoud, C. Rödel, and M. Roth, "Analysis of laser-proton acceleration experiments for development of empirical scaling laws," Phys. Rev. E, vol. 104, p. 045210, Oct 2021.

[103] M. Rehwald et al., "Ultra-short pulse laser acceleration of protons to 80 mev from cryogenic hydrogen jets tailored to near-critical density," Nature Physics, *In review*.

[104] F. Kroll, F.-E. Brack, C. Bernert, S. Bock, E. Bodenstein, K. Brüchner, T. E. Cowan, L. Gaus, R. Gebhardt, U. Helbig, L. Karsch, T. Kluge, S. Kraft, M. Krause, E. Lessmann, U. Masood, S. Meister, J. Metzkes-Ng, A. Nossula, J. Pawelke, J. Pietzsch, T. Püschel, M. Reimold, M. Rehwald, C. Richter, H.-P. Schlenvoigt, U. Schramm, M. E. P. Umlandt, T. Ziegler, K. Zeil, and E. Beyreuther, "Tumour irradiation in mice with a laser-accelerated proton beam," Nature Physics, vol. 18, no. 3, pp. 316–322, 2022.

[105] P. McKenna, K.W.D. Ledingham, I. Spencer, T. McCany, R.P. Singhal, C. Ziener, P.S. Foster, E.J. Divall, C.J. Hooker, D. Neely, A.J. Langley, R.J. Clarke, P.A. Norreys, K. Krushelnick, E.L. Clark, "Characterization of multiterawatt laser-solid interactions for proton acceleration," Review of Scientific Instruments, vol. 73, no. 12, pp. 4176–4184, 2002.

[106] T. Nayuki, Y. Oishi, T. Fujii, K. Nemoto, T. Kayoiji, Y. Okano, Y. Hironaka, K. Nakamura, K. Kondo, and K. Ueda, "Thin tape target driver for laser ion acceleration," Review of Scientific Instruments, no. 73, p. 3293, 2003.

[107] F. P. Condamine, N. Jourdain, J.-C. Hernandez, M. Taylor, H. Bohlin, A. Fajstavr, T. M. Jeong, D. Kumar, T. Laštovička, O. Renner, and S. Weber, "High-repetition rate solid target delivery system for PW-class laser–matter interaction at ELI Beamlines," Review of Scientific Instruments, vol. 92, p. 063504, jun 2021.

[108] J. B. Kim, S. Göde, and S. H. Glenzer, "Development of a cryogenic hydrogen microjet for high-intensity, high-repetition rate experiments," Rev. Sci. Inst., vol. 87, no. 11, pp. 1–4, 2016.

[109] C. B. Curry, C. A. S. Dunning, M. Gauthier, H.-G. J. Chou, F. Fiuza, G. D. Glenn, Y. Y. Tsui, M. Bazalova-Carter, and S. H. Glenzer, "Optimization of radiochromic film stacks to diagnose high-flux laser-accelerated proton beams," Review of Scientific Instruments, vol. 91, p. 093303, sep 2020.

[110] P.L. Poole, C.D. Andereck, D.W. Schumacher, R.L. Daskalova, S. Feister, K.M. George, C. Willis, K.U. Akli, E.A. Chowdhury, "Liquid crystal films as on-demand, variable thickness (50–5000nm) targets for intense lasers," Physics of Plasmas, vol. 21, no. 6, p. 063109, 2014.

[111] B. Ha, D.P. DePonte, J.G. Santiago, "Device design and flow scaling for liquid sheet jets," Phys. Rev. Fluids, vol. 3, p. 114202, Nov 2018.

[112] J.T. Morrison, S. Feister, K.D. Frische, D.R. Austin, G.K. Ngirmang, N.R. Murphy, C. Orban, E.A. Chowdhury, W.M. Roquemore, "MeV proton acceleration at kHz repetition rate from ultra-intense laser liquid interaction," New Journal of Physics, vol. 20, p. 022001, feb 2018.

[113] J.D. Koralek, J.B. Kim, P. Brůža, C.B. Curry, Z. Chen, H.A. Bechtel, A.A. Cordones, P. Sperling, S. Toleikis, J.F. Kern, S.P. Moeller, S.H. Glenzer, D.P. DePonte, "Generation and characterization of ultrathin free-flowing liquid sheets," Nature Communications, vol. 9, no. 1353, 2018.

[114] B. Aurand, E. Aktan, K.M. Schwind, R. Prasad, M. Cerchez, T. Toncian, O. Willi, "A laser-driven droplet source for plasma physics applications," Laser and Particle Beams, vol. 38, no. 4, p. 214–221, 2020.

[115] C. J. Crissman, M. Mo, Z. Chen, J. Yang, D. A. Huyke, S. H. Glenzer, K. Ledbetter, J. P. F. Nunes, M. L.

Ng, H. Wang, X. Shen, X. Wang, and D. P. DePonte, “Sub-micron thick liquid sheets produced by isotropically etched glass nozzles,” Lab on a Chip, vol. 22, no. 7, pp. 1365–1373, 2022.

[116] F. Treffert, G. D. Glenn, H.-G. J. Chou, C. Crissman, C. B. Curry, D. P. DePonte, F. Fiuza, N. J. Hartley, B. Ofori-Okai, M. Roth, S. H. Glenzer, and M. Gauthier, “Ambient-temperature liquid jet targets for high-repetition-rate hed discovery science,” Physics of Plasmas, vol. 29, no. 12, p. 123105, 2022.

[117] V. Sanjay and A. K. Das, “Formation of liquid chain by collision of two Laminar jets,” Physics of Fluids, vol. 29, no. 11, 2017.

[118] J. W. Bush and A. E. Hasha, “On the collision of laminar jets: Fluid chains and fishbones,” Journal of Fluid Mechanics, vol. 511, pp. 285–310, 2004.

[119] S. Jung, S. D. Hoath, G. D. Martin, and I. M. Hutchings, “Atomization patterns produced by the oblique collision of two Newtonian liquid jets,” Physics of Fluids, vol. 22, no. 4, pp. 1–10, 2010.

[120] J. B. Kim, S. Göde, and S. H. Glenzer, “Development of a cryogenic hydrogen microjet for high-intensity, high-repetition rate experiments,” Rev. Sci. Inst., vol. 87, p. 11, 2016.

[121] M. Gauthier, J. B. Kim, C. B. Curry, B. Aurand, E. J. Gamboa, S. Göde, C. Goyon, A. Hazi, S. Kerr, A. Pak, A. Propp, B. Ramakrishna, J. Ruby, O. Willi, G. J. Williams, C. Rödel, and S. H. Glenzer, “High-intensity laser-accelerated ion beam produced from cryogenic micro-jet target,” Rev. Sci. Inst., vol. 87, no. 11, pp. 13–16, 2016.

[122] L. Obst, S. Göde, M. Rehwald, F.-E. Brack, J. Branco, S. Bock, M. Bussmann, T. E. Cowan, C. B. Curry, F. Fiuza, M. Gauthier, R. Gebhardt, U. Helbig, A. Huebl, U. Hübner, A. Irman, L. Kazak, J. B. Kim, T. Kluge, S. Kraft, M. Loeser, J. Metzkes, R. Mishra, C. Rödel, H.-P. Schlenvoigt, M. Siebold, J. Tiggesbäumker, S. Wolter, T. Ziegler, U. Schramm, S. H. Glenzer, and K. Zeil, “Efficient laser-driven proton acceleration from cylindrical and planar cryogenic hydrogen jets,” Scientific Reports, vol. 7, no. 1, p. 10248, 2017.

[123] J. J. Fendley, “Measurement of refractive index using a michelson interferometer,” Physics Education, vol. 17, p. 209, sep 1982.

[124] Y. Wang, S. Wang, A. Rockwood, B. M. Luther, R. Hollinger, A. Curtis, C. Calvi, C. S. Menoni, and J. J. Rocca, “0.85 pw laser operation at 3.3 hz and high-contrast ultrahigh-intensity λ = 400 nm second-harmonic beamline,” Opt. Lett., vol. 42, pp. 3828–3831, Oct 2017.

[125] F. Treffert, C. B. Curry, H.-G. J. Chou, C. J. Crissman, D. P. DePonte, F. Fiuza, G. D. Glenn, R. C. Hollinger, R. Nedbailo, J. Park, C. Schoenwaelder, H. Song, S. Wang, J. J. Rocca, M. Roth, S. H. Glenzer, and M. Gauthier, “High-repetition-rate, multi-mev deuteron acceleration from converging heavy water microjets at laser intensities of 10^{21} w/cm2,” Applied Physics Letters, vol. 121, no. 7, p. 074104, 2022.

[126] M. Gauthier, C. B. Curry, S. Göde, F.-E. Brack, J. B. Kim, M. J. MacDonald, J. Metzkes, L. Obst, M. Rehwald, C. Rödel, H.-P. Schlenvoigt, W. Schumaker, U. Schramm, K. Zeil, and S. H. Glenzer, “High repetition rate, multi-mev proton source from cryogenic hydrogen jets,” Applied Physics Letters, vol. 111, no. 11, p. 114102, 2017.

[127] L. Obst-Huebl, T. Ziegler, F.-E. Brack, J. Branco, M. Bussmann, T. E. Cowan, C. B. Curry, F. Fiuza, M. Garten, M. Gauthier, S. Göde, S. H. Glenzer, A. Huebl, A. Irman, J. B. Kim, T. Kluge, S. D. Kraft, F. Kroll, J. Metzkes-Ng, R. Pausch, I. Prencipe, M. Rehwald, C. Roedel, H.-P. Schlenvoigt, U. Schramm,

and K. Zeil, “All-optical structuring of laser-driven proton beam profiles,” Nature Communications, vol. 9, no. 1, p. 5292, 2018.

[128] A. Huebl, M. Rehwald, L. Obst-Huebl, T. Ziegler, M. Garten, R. Widera, K. Zeil, T. E. Cowan, M. Bussmann, U. Schramm, and T. Kluge, “Spectral control via multi-species effects in PW-class laser-ion acceleration,” Plasma Physics and Controlled Fusion, vol. 62, p. 124003, oct 2020.

[129] C. Bernert, S. Assenbaum, F.-E. Brack, T. E. Cowan, . B. Curry, M. Garten, L. Gaus, M. Gauthier, S. Göde, I. Goethel, S. H. Glenzer, T. Kluge, S. Kraft, F. Kroll, M. Kuntzsch, J. Metzkes-Ng, M. Loeser, L. Obst-Huebl, M. Rehwald, H.-P. Schlenvoigt, C. Schoenwaelder, U. Schramm, M. Siebold, F. Treffert, T. Ziegler, K. Zeil, “Off-harmonic optical probing of high intensity laser plasma expansion dynamics in solid density hydrogen jets,” Scientific Reports, vol. 12, p. 7287, 2022.

[130] A. Alejo, D. Gwynne, D. Doria, H. Ahmed, D. Carroll, R. Clarke, D. Neely, G. Scott, M. Borghesi, and S. Kar, “Recent developments in the thomson parabola spectrometer diagnostic for laser-driven multi-species ion sources,” Journal of Instrumentation, vol. 11, pp. C10005–C10005, oct 2016.

[131] K. A. Tanaka, T. Yabuuchi, T. Sato, R. Kodama, Y. Kitagawa, T. Takahashi, T. Ikeda, Y. Honda, and S. Okuda, “Calibration of imaging plate for high energy electron spectrometer,” Review of Scientific Instruments, vol. 76, no. 1, p. 013507, 2005.

[132] P. Bolton, M. Borghesi, C. Brenner, D. Carroll, C. De Martinis, F. Fiorini, A. Flacco, V. Floquet, J. Fuchs, P. Gallegos, D. Giove, J. Green, S. Green, B. Jones, D. Kirby, P. McKenna, D. Neely, F. Nuesslin, R. Prasad, S. Reinhardt, M. Roth, U. Schramm, G. Scott, S. Ter-Avetisyan, M. Tolley, G. Turchetti, and J. Wilkens, “Instrumentation for diagnostics and control of laser-accelerated proton (ion) beams,” Physica Medica, vol. 30, no. 3, pp. 255–270, 2014.

[133] J. L. Wiza, “Microchannel Plate Detectors,” Nuclear Instruments and Methods, 1979.

[134] Glenn F. Knoll, Radiation detection and measurement. New York: Wiley, 4. ed. ed., 2010.

[135] Hamamatsu Photonics K.K., MCP (Microchannel Plate) and MCP Assembly. January 2016.

[136] Hamamatsu Photonics, “Handbook Chapter 10 MCP-PMT,” 2007.

[137] N Serman & S. Singer, “Intensifying Screen, Cassettes and Screen Films.” `http://www.columbia.edu/itc/hs/dental/sophs/material/screens.pdf`. Accessed: 2017-01-29.

[138] J. Miyahara, K. Takahashi, Y. Amemiya, N. Kamiya, and Y. Satow, “A new type of x-ray area detector utilizing laser stimulated luminescence,” Nuclear Instruments and Methods in Physics Research Section A: Accelerators, Spectrometers, Detectors and Associated Equipment, vol. 246, no. 1, pp. 572–578, 1986.

[139] A. Mančić, J. Fuchs, P. Antici, S. A. Gaillard, and P. Audebert, “Absolute calibration of photostimulable image plate detectors used as (0.5–20mev) high-energy proton detectors,” Review of Scientific Instruments, vol. 79, no. 7, p. 073301, 2008.

[140] I. W. Choi, C. M. Kim, J. H. Sung, I. J. Kim, T. J. Yu, S. K. Lee, Y.-Y. Jin, K. H. Pae, N. Hafz, and J. Lee, “Absolute calibration of a time-of-flight spectrometer and imaging plate for the characterization of laser-accelerated protons,” Measurement Science and Technology, vol. 20, p. 115112, oct 2009.

[141] T. Bonnet, M. Comet, D. Denis-Petit, F. Gobet, F. Hannachi, M. Tarisien, M. Versteegen, and M. M. Aleonard, “Response functions of fuji imaging plates to monoenergetic protons in the energy range 0.6–3.2 mev,” Review of Scientific Instruments, vol. 84, no. 1, p. 013508, 2013.

[142] G. Boutoux, D. Batani, F. Burgy, J.-E. Ducret, P. Forestier-Colleoni, S. Hulin, N. Rabhi, A. Duval, L. Lecherbourg, C. Reverdin, K. Jakubowska, C. I. Szabo, S. Bastiani-Ceccotti, F. Consoli, A. Curcio, R. De Angelis, F. Ingenito, J. Baggio, and D. Raffestin, "Validation of modelled imaging plates sensitivity to 1-100 kev x-rays and spatial resolution characterisation for diagnostics for the "petawatt aquitaine laser"," Review of Scientific Instruments, vol. 87, no. 4, p. 043108, 2016.

[143] N. Rabhi, D. Batani, G. Boutoux, J.-E. Ducret, K. Jakubowska, I. Lantuejoul-Thfoin, C. Nauraye, A. Patriarca, A. Saïd, A. Semsoum, L. Serani, B. Thomas, and B. Vauzour, "Calibration of imaging plate detectors to mono-energetic protons in the range 1-200 mev," Review of Scientific Instruments, vol. 88, no. 11, p. 113301, 2017.

[144] A. Mančićć, J. Fuchs, P. Antici, S. A. Gaillard, and P. Audebert, "Absolute calibration of photostimulable image plate detectors used as (0.5–20mev) high-energy proton detectors," Rev. Sci. Inst., vol. 79, no. 7, p. 073301, 2008.

[145] D. Nikezic and K.N. Yub, "Formation and growth of tracks in nuclear track materials," Mater. Sci. Eng. R Rep, vol. 46, p. 51–123, 2004.

[146] J. Strehlow, P. Forestier-Colleoni, C. McGuffey, M. Bailly-Grandvaux, T. S. Daykin, E. McCary, J. Peebles, G. Revet, S. Zhang, T. Ditmire, M. Donovan, G. Dyer, J. Fuchs, E. W. Gaul, D. P. Higginson, G. E. Kemp, M. Martinez, H. S. McLean, M. Spinks, H. Sawada, and F. N. Beg, "The response function of fujifilm bas-tr imaging plates to laser-accelerated titanium ions," Review of Scientific Instruments, vol. 90, no. 8, p. 083302, 2019.

[147] B. Cartwright, E. Shirk, and P. Price, "A nuclear-track-recording polymer of unique sensitivity and resolution," Nuclear Instruments and Methods, vol. 153, no. 2, pp. 457–460, 1978.

[148] T. W. Jeong, P. K. Singh, C. Scullion, H. Ahmed, P. Hadjisolomou, C. Jeon, H. Yun, K. F. Kakolee, M. Borghesi, S. Ter-Avetisyan Sci. Rep., vol. 7, p. 2152, 2017.

[149] K. Zeil, J. Metzkes, T. Kluge, M. Bussmann, T. E. Cowan, S. D. Kraft, R. Sauerbrey, B. Schmidt, M. Zier, and U. Schramm, "Robust energy enhancement of ultrashort pulse laser accelerated protons from reduced mass targets," Plasma Physics and Controlled Fusion, vol. 56, no. 8, p. 084004, 2014.

[150] M. Noaman-ul-Haq, H. Ahmed, T. Sokollik, Y. Fang, X. Ge, X. Yuan, L. Chen, "Parametric scalings of laser driven protons using a high repetition rate tape drive target system," Nuclear Instruments and Methods in Physics Research Section A: Accelerators, Spectrometers, Detectors and Associated Equipment, vol. 909, pp. 164–167, 2018. 3rd European Advanced Accelerator Concepts workshop (EAAC2017).

[151] M. Schollmeier, Optimization and control of laser-accelerated proton beams. PhD thesis, Technische Universität Darmstadt, 2008.

[152] B. Hou, J. Nees, J. Easter, J. Davis, G. Petrov, A. Thomas, and K. Krushelnick, "Mev proton beams generated by 3 mj ultrafast laser pulses at 0.5 khz," Applied Physics Letters, vol. 95, no. 10, p. 101503, 2009.

[153] T. Fujii, Y. Oishi, T. Nayuki, Y. Takizawa, K. Nemoto, T. Kayoiji, K. Horioka, Y. Okano, Y. Hironaka, K. G. Nakamura, and K.-i. Kondo, "Mev-order proton and carbon ion acceleration by irradiation of 60 fs tw laser pulses on thin copper tape," Applied Physics Letters, vol. 83, no. 8, pp. 1524–1526, 2003.

[154] I. Spencer, K. W. D. Ledingham, P. McKenna, T. McCanny, R. P. Singhal, P. S. Foster, D. Neely, A. J. Langley, E. J. Divall, C. J. Hooker, R. J. Clarke, P. A. Norreys, E. L. Clark, K. Krushelnick, and J. R. Davies,

"Experimental study of proton emission from 60-fs, 200-mj high-repetition-rate tabletop-laser pulses interacting with solid targets," Phys. Rev. E, vol. 67, p. 046402, Apr 2003.

[155] A. S. Pirozhkov, M. Mori, A. Yogo, H. Kiriyama, K. Ogura, A. Sagisaka, J.-L. Ma, S. Orimo, M. Nishiuchi, H. Sugiyama, T. Z. Esirkepov, S. V. Bulanov, H. Okada, S. Kondo, S. Kanazawa, Y. Nakai, A. Akutsu, T. Motomura, M. Tanoue, T. Shimomura, M. Ikegami, T. Shirai, Y. Iwashita, A. Noda, I. W. Choi, S. K. Lee, J. Lee, Y. Oishi, T. Kimura, T. Tajima, and H. Daido, "Laser-driven proton acceleration and plasma diagnostics with j-karen laser," Proc. Soc. Photo-Opt. Instrum. Eng., vol. 7354, 2009.

[156] M. Noaman-ul Haq, H. Ahmed, T. Sokollik, L. Yu, Z. Liu, X. Yuan, F. Yuan, M. Mirzaie, X. Ge, L. Chen, and J. Zhang, "Statistical analysis of laser driven protons using a high-repetition-rate tape drive target system," Phys. Rev. ST Accel. Beams, vol. 20, no. 4, p. 041301, 2017.

[157] S. Göde, C. Rödel, K. Zeil, R. Mishra, M. Gauthier, F.-E. Brack, T. Kluge, M. J. MacDonald, J. Metzkes, L. Obst, M. Rehwald, C. Ruyer, H.-P. Schlenvoigt, W. Schumaker, P. Sommer, T. E. Cowan, U. Schramm, S. Glenzer, and F. Fiuza, "Relativistic electron streaming instabilities modulate proton beams accelerated in laser-plasma interactions," Phys. Rev. Lett., vol. 118, p. 194801, May 2017.

[158] M. Noaman-ul-Haq, T. Sokollik, H. Ahmed, J. Braenzel, L. Ehrentraut, M. Mirzaie, L.-L. Yu, Z.M. Sheng, L.M. Chen, M. Schnürer, J. Zhang, "Controlling laser driven protons acceleration using a deformable mirror at a high repetition rate," Nuclear Instruments and Methods in Physics Research Section A: Accelerators, Spectrometers, Detectors and Associated Equipment, vol. 883, pp. 191–195, 2018.

[159] B. Aurand, S. Grieser, T. Toncian, E. Aktan, M. Cerchez, L. Lessmann, R. Prasad, A. Khoukaz, and O. Willi, "A multihertz, kiloelectronvolt pulsed proton source from a laser irradiated continuous hydrogen cluster target," Physics of Plasmas, vol. 26, no. 7, p. 073102, 2019.

[160] Y. Gershuni, D. Roitman, I. Cohen, E. Porat, Y. Danan, M. Elkind, A. Levanon, R. Louzon, D. Reichenberg, A. Tsabary, E. Urisman, S. Vaisman, and I. Pomerantz, "A gatling-gun target delivery system for high-intensity laser irradiation experiments," Nuclear Instruments and Methods in Physics Research Section A: Accelerators, Spectrometers, Detectors and Associated Equipment, vol. 934, pp. 58–62, 2019.

[161] P. Puyuelo-Valdes, D. de Luis, J. Hernandez, J. I. Apiñaniz, A. Curcio, J. L. Henares, M. Huault, J. A. Pérez-Hernández, L. Roso, G. Gatti, and L. Volpe, "Implementation of a thin, flat water target capable of high-repetition-rate MeV-range proton acceleration in a high-power laser at the CLPU," Plasma Physics and Controlled Fusion, vol. 64, p. 054003, mar 2022.

[162] A. Stockem Novo, M. C. Kaluza, R. A. Fonseca, L. O. Silva, "Optimizing laser-driven proton acceleration from overdense targets," Scientific Reports, vol. 6, p. 29402, 2016.

[163] A. J. Mackinnon, Y. Sentoku, P. K. Patel, D. W. Price, S. Hatchett, M. H. Key, C. Andersen, R. Snavely, and R. R. Freeman, "Enhancement of proton acceleration by hot-electron recirculation in thin foils irradiated by ultraintense laser pulses," Phys. Rev. Lett., vol. 88, p. 215006, May 2002.

[164] D. Neely, P. Foster, A. Robinson, F. Lindau, O. Lundh, A. Persson, C.-G. Wahlström, and P. McKenna, "Enhanced proton beams from ultrathin targets driven by high contrast laser pulses," Appl. Phys. Lett., vol. 89, no. 2, p. 021502, 2006.

[165] A. T. Yue, M. S. Dewey, D. M. Gilliam, G. L. Greene, A. B. Laptev, J. S. Nico, W. M. Snow, and F. E. Wietfeldt, "Improved determination of the neutron lifetime," Phys. Rev. Lett., vol. 111, p. 222501, Nov 2013.

[166] I. Anderson, C. Andreani, J. Carpenter, G. Festa, G. Gorini, C.-K. Loong, and R. Senesi, "Research opportunities with compact accelerator-driven neutron sources," Physics Reports, vol. 654, pp. 1–58, 2016. Research opportunities with compact accelerator-driven neutron sources.

[167] U. Rücker, T. Cronert, J. Voigt, J. P. Dabruck, P. E. Doege, J. Ulrich, R. Nabbi, Y. Beßler, M. Butzek, M. Büscher, C. Lange, M. Klaus, T. Gutberlet, and T. Brückel, "The jülich high-brilliance neutron source project," The European Physical Journal Plus, vol. 131, no. 1, p. 19, 2016.

[168] B. Ludewigt, R. Wells, and J. Reijonen, "High-yield d t neutron generator," Nuclear Instruments & Methods in Physics Research Section B-beam Interactions With Materials and Atoms, vol. 261, pp. 830–834, 2006.

[169] SERC - Carlton College, "Instrumental Neutron Activation Analysis (INAA)." https://serc.carleton.edu/research_education/geochemsheets/techniques/INAA.html. Accessed: 10/17/2022.

[170] S. Wender and L. Dominik, "Los alamos high-energy neutron testing handbook," 2019.

[171] G. Ericsson, "Advanced neutron spectroscopy in fusion research," Journal of Fusion Energy, vol. 38, no. 1, pp. 330–335, 2019.

[172] N. Schunck and L. M. Robledo, "Microscopic theory of nuclear fission: a review," Reports on Progress in Physics, vol. 79, p. 116301, oct 2016.

[173] J. M. Carpenter and C.-K. Loong, Elements of Slow-Neutron Scattering. Cambridge University Press, 2015.

[174] P. W. Lisowski, C. D. Bowman, G. J. Russell, and S. A. Wender, "The los alamos national laboratory spallation neutron sources," Nuclear Science and Engineering, vol. 106, no. 2, pp. 208–218, 1990.

[175] R. Garoby, A. Vergara, H. Danared, I. Alonso, E. Bargallo, B. Cheymol, C. Darve, M. Eshraqi, H. Hassanzadegan, A. Jansson, I. Kittelmann, Y. Levinsen, M. Lindroos, C. Martins, Ø. Midttun, R. Miyamoto, S. Molloy, D. Phan, A. Ponton, E. Sargsyan, T. Shea, A. Sunesson, L. Tchelidze, C. Thomas, M. Jensen, W. Hees, P. Arnold, M. Juni-Ferreira, F. Jensen, A. Lundmark, D. McGinnis, N. Gazis, J. W. II, M. Anthony, E. Pitcher, L. Coney, M. Gohran, J. Haines, R. Linander, D. Lyngh, U. Oden, H. Carling, R. Andersson, S. Birch, J. Cereijo, T. Friedrich, T. Korhonen, E. Laface, M. Mansouri-Sharifabad, A. Monera-Martinez, A. Nordt, D. Paulic, D. Piso, S. Regnell, M. Zaera-Sanz, M. Aberg, K. Breimer, K. Batkov, Y. Lee, L. Zanini, M. Kickulies, Y. Bessler, J. Ringnér, J. Jurns, A. Sadeghzadeh, P. Nilsson, M. Olsson, J.-E. Presteng, H. Carlsson, A. Polato, J. Harborn, K. Sjögreen, G. Muhrer, and F. Sordo, "The european spallation source design," Physica Scripta, vol. 93, p. 014001, dec 2017.

[176] G. J. Russell, "Spallation physics - an overview," 1CANS-XI International Collaboration on Advanced Neutron Sources, 1990.

[177] F. Goldenbaum, "The physics of spallation processes - theory, experiments and applications," 2004.

[178] O. M. Mannion, K. M. Woo, A. J. Crilly, C. J. Forrest, J. A. Frenje, M. G. Johnson, V. Y. Glebov, J. P. Knauer, Z. L. Mohamed, M. H. Romanofsky, C. Stoeckl, W. Theobald, and S. P. Regan, "Reconstructing 3d asymmetries in laser-direct-drive implosions on omega," Review of Scientific Instruments, vol. 92, no. 3, p. 033529, 2021.

[179] G. McCracken and P. Stott, "Chapter 7 - inertial-confinement fusion," in Fusion (Second Edition) (G. McCracken and P. Stott, eds.), pp. 67–81, Boston: Academic Press, second edition ed., 2013.

[180] J. D. Lawson, "Some criteria for a power producing thermonuclear reactor," Proceedings of the Physical Society. Section B, vol. 70, p. 6, jan 1957.

[181] O. A. Hurricane, D. A. Callahan, D. T. Casey, P. M. Celliers, C. Cerjan, E. L. Dewald, T. R. Dittrich, T. Döppner, D. E. Hinkel, L. F. B. Hopkins, J. L. Kline, S. Le Pape, T. Ma, A. G. MacPhee, J. L. Milovich, A. Pak, H. S. Park, P. K. Patel, B. A. Remington, J. D. Salmonson, P. T. Springer, and R. Tommasini, "Fuel gain exceeding unity in an inertially confined fusion implosion," Nature, vol. 506, no. 7488, pp. 343–348, 2014.

[182] R. Betti, A. R. Christopherson, B. K. Spears, R. Nora, A. Bose, J. Howard, K. M. Woo, M. J. Edwards, and J. Sanz, "Alpha heating and burning plasmas in inertial confinement fusion," Phys. Rev. Lett., vol. 114, p. 255003, Jun 2015.

[183] O. A. Hurricane, P. T. Springer, P. K. Patel, D. A. Callahan, K. Baker, D. T. Casey, L. Divol, T. Döppner, D. E. Hinkel, M. Hohenberger, L. F. Berzak Hopkins, C. Jarrott, A. Kritcher, S. Le Pape, S. Maclaren, L. Masse, A. Pak, J. Ralph, C. Thomas, P. Volegov, and A. Zylstra, "Approaching a burning plasma on the nif," Physics of Plasmas, vol. 26, no. 5, p. 052704, 2019.

[184] P. Boillat, E. Lehmann, P. Trtik, and M. Cochet, "Neutron imaging of fuel cells – recent trends and future prospects," Current Opinion in Electrochemistry, vol. 5, no. 1, pp. 3–10, 2017.

[185] R. F. Barth, A. H. Soloway, and R. G. Fairchild, "Boron neutron capture therapy for cancer," Scientific American, vol. 263, no. 4, pp. 100–107, 1990.

[186] S. Nakai, K. Mima, Y. Kato, K. Tanaka, Y. Ikeda, H. Azechi, K. Miyanaga, M. Nakai, M. Perlado, and R. G. Arrabal, "Industrial applications of laser neutron source," Journal of Physics: Conference Series, vol. 244, p. 042027, aug 2010.

[187] J. Alvarez, J. Fernández-Tobias, K. Mima, S. Nakai, S. Kar, Y. Kato, and J. Perlado, "Laser driven neutron sources: Characteristics, applications and prospects," Physics Procedia, vol. 60, pp. 29–38, 2014.

[188] A. Benuzzi-Mounaix, M. Koenig, G. Huser, B. Faral, D. Batani, E. Henry, M. Tomasini, B. Marchet, T. A. Hall, M. Boustie, T. De Rességuier, M. Hallouin, F. Guyot, D. Andrault, and T. Charpin, "Absolute equation of state measurements of iron using laser driven shocks," Physics of Plasmas, vol. 9, no. 6, pp. 2466–2469, 2002.

[189] V. W. YUAN, Temperature Measurements In Dynamically-Loaded Systems Using Neutron Resonance Spectroscopy (NRS) At LANSCE, pp. 138–145. 2002.

[190] V. W. Yuan, J. D. Bowman, D. J. Funk, G. L. Morgan, R. L. Rabie, C. E. Ragan, J. P. Quintana, and H. L. Stacy, "Shock temperature measurement using neutron resonance spectroscopy," Phys. Rev. Lett., vol. 94, p. 125504, Mar 2005.

[191] M. N. H. Comsan, "Spallation neutron sources for science and technology." `http://www.iaea.org/inis/collection/NCLCollectionStore/_Public/43/099/43099436.pdf`, 2011.

[192] I. Pomerantz, E. McCary, A. R. Meadows, A. Arefiev, A. C. Bernstein, C. Chester, J. Cortez, M. E. Donovan, G. Dyer, E. W. Gaul, D. Hamilton, D. Kuk, A. C. Lestrade, C. Wang, T. Ditmire, and B. M. Hegelich, "Ultrashort pulsed neutron source," Phys. Rev. Lett., vol. 113, p. 184801, Oct 2014.

[193] D. P. Higginson, L. Vassura, M. M. Gugiu, P. Antici, M. Borghesi, S. Brauckmann, C. Diouf, A. Green, L. Palumbo, H. Petrascu, S. Sofia, M. Stardubtsev, O. Willi, S. Kar, F. Negoita, and J. Fuchs, "Temporal narrowing of neutrons produced by high-intensity short-pulse lasers," Phys. Rev. Lett., vol. 115, p. 054802, Jul 2015.

[194] B. Rus, P. Bakule, D. Kramer, J. Naylon, J. Thoma, M. Fibrich, J. T. Green, J. C. Lagron, R. Antipenkov, J. Bartonícek, F. Batysta, R. Baše, R. Boge, S. Buck, J. Cupal, M. A. Drouin, M. Ďurák, B. Himmel, T. Havlícek, P. Homer, A. Honsa, M. Horáček, P. Hríbek, J. HubáCek, Z. Hubka, G. Kalinchenko, K. Kasl, L. Indra, P. Korous, M. KoSelja, L. Koubíková, M. Laub, T. Mazanec, A. Meadows, J. Novák, D. Peceli, J. Polan, D. Snopek, V. Sobr, P. Trojek, B. Tykalewicz, P. Velpula, E. Verhagen, S. Vyhlídka, J. Weiss, C. Haefner, A. Bayramian, S. Betts, A. Erlandson, J. Jarboe, G. Johnson, J. Horner, D. Kim, E. Koh, C. Marshall, D. Mason, E. Sistrunk, D. Smith, T. Spinka, J. Stanley, C. Stolz, T. Suratwala, S. Telford, T. Ditmire, E. Gaul, M. Donovan, C. Frederickson, G. Friedman, D. Hammond, D. Hidinger, G. Chériaux, A. Jochmann, M. Kepler, C. Malato, M. Martinez, T. Metzger, M. Schultze, P. Mason, K. Ertel, A. Lintern, C. Edwards, C. Hernandez-Gomez, and J. Collier, "ELI-beamlines: progress in development of next generation short-pulse laser systems," in Research Using Extreme Light: Entering New Frontiers with Petawatt-Class Lasers III (G. Korn and L. O. Silva, eds.), vol. 10241, p. 102410J, International Society for Optics and Photonics, SPIE, 2017.

[195] S. Borneis, T. Laštovička, M. Sokol, T.-M. Jeong, F. Condamine, O. Renner, V. Tikhonchuk, H. Bohlin, A. Fajstavr, J.-C. Hernandez, and et al., "Design, installation and commissioning of the eli-beamlines high-power, high-repetition rate hapls laser beam transport system to p3," High Power Laser Science and Engineering, vol. 9, p. e30, 2021.

[196] L. Disdier, J.-P. Garconnet, G. Malka, and J.-L. Miquel, "Fast neutron emission from a high-energy ion beam produced by a high-intensity subpicosecond laser pulse," Phys. Rev. Lett., vol. 82, pp. 1454–1457, Feb 1999.

[197] J. M. Yang, P. McKenna, K. W. D. Ledingham, T. McCanny, L. Robson, S. Shimizu, R. P. Singhal, M. S. Wei, K. Krushelnick, R. J. Clarke, D. Neely, and P. A. Norreys, "Neutron production by fast protons from ultraintense laser-plasma interactions," Journal of Applied Physics, vol. 96, no. 11, pp. 6912–6918, 2004.

[198] D. P. Higginson, J. M. McNaney, D. C. Swift, G. M. Petrov, J. Davis, J. A. Frenje, L. C. Jarrott, R. Kodama, K. L. Lancaster, A. J. Mackinnon, H. Nakamura, P. K. Patel, G. Tynan, and F. N. Beg, "Production of neutrons up to 18 mev in high-intensity, short-pulse laser matter interactions," Physics of Plasmas, vol. 18, no. 10, p. 100703, 2011.

[199] A. Maksimchuk, A. Raymond, F. Yu, G. M. Petrov, F. Dollar, L. Willingale, C. Zulick, J. Davis, and K. Krushelnick, "Dominant deuteron acceleration with a high-intensity laser for isotope production and neutron generation," Applied Physics Letters, vol. 102, no. 19, p. 191117, 2013.

[200] C. Zulick, F. Dollar, V. Chvykov, J. Davis, G. Kalinchenko, A. Maksimchuk, G. M. Petrov, A. Raymond, A. G. R. Thomas, L. Willingale, V. Yanovsky, and K. Krushelnick, "Energetic neutron beams generated from femtosecond laser plasma interactions," Applied Physics Letters, vol. 102, no. 12, p. 124101, 2013.

[201] M. Storm, S. Jiang, D. Wertepny, C. Orban, J. Morrison, C. Willis, E. McCary, P. Belancourt, J. Snyder, E. Chowdhury, W. Bang, E. Gaul, G. Dyer, T. Ditmire, R. R. Freeman, and K. Akli, "Fast neutron production from lithium converters and laser driven protons," Physics of Plasmas, vol. 20, no. 5, p. 053106, 2013.

[202] D. Jung, K. Falk, N. Guler, O. Deppert, M. Devlin, A. Favalli, J. C. Fernandez, D. C. Gautier, M. Geissel, R. Haight, C. E. Hamilton, B. M. Hegelich, R. P. Johnson, F. Merrill, G. Schaumann, K. Schoenberg, M. Schollmeier, T. Shimada, T. Taddeucci, J. L. Tybo, S. A. Wender, C. H. Wilde, G. A. Wurden, and

M. Roth, “Characterization of a novel, short pulse laser-driven neutron source,” Phys. Plasmas, vol. 20, p. 056706, 2013.

[203] I. Pomerantz, J. Blakeney, G. Dyer, L. Fuller, E. Gaul, D. Gautier, D. Jung, A. Meadows, R. Shah, C. Wang, J. Fernandez, T. Ditmire, and B. Hegelich, “Laser driven neutron generation at the texas petawatt,” in CLEO: 2013, p. QTh3A.4, Optica Publishing Group, 2013.

[204] C. M. Brenner, S. R. Mirfayzi, D. R. Rusby, C. Armstrong, A. Alejo, L. A. Wilson, R. Clarke, H. Ahmed, N. M. H. Butler, D. Haddock, A. Higginson, A. McClymont, C. Murphy, M. Notley, P. Oliver, R. Allott, C. Hernandez-Gomez, S. Kar, P. McKenna, and D. Neely, “Laser-driven x-ray and neutron source development for industrial applications of plasma accelerators,” Plasma Physics and Controlled Fusion, vol. 58, p. 014039, nov 2015.

[205] S. Kar, A. Green, H. Ahmed, A. Alejo, A. P. L. Robinson, M. Cerchez, R. Clarke, D. Doria, S. Dorkings, J. Fernandez, S. R. Mirfayzi, P. McKenna, K. Naughton, D. Neely, P. Norreys, C. Peth, H. Powell, J. A. Ruiz, J. Swain, O. Willi, and M. Borghesi, “Beamed neutron emission driven by laser accelerated light ions,” New J. Phys., vol. 18, p. 053002, 2016.

[206] A. Kleinschmidt, V. Bagnoud, O. Deppert, A. Favalli, S. Frydrych, J. Hornung, D. Jahn, G. Schaumann, A. Tebartz, F. Wagner, G. Wurden, B. Zielbauer, and M. Roth, “Intense, directed neutron beams from a laser-driven neutron source at phelix,” Phys. Plasmas, vol. 25, pp. 3–8, 2018.

[207] M. Avrigeanu and V. Avrigeanu, “Assessment of deuteron-induced reaction mechanisms at low and medium energies,” EPJ Web of Conferences, vol. 2, no. 01004, 2010.

[208] M. Boselli and A. Diaz-Torres, “Unambiguous separation of low-energy fusion processes of weakly bound nuclei,” Journal of Physics G: Nuclear and Particle Physics, vol. 41, p. 094001, jul 2014.

[209] H. Wang, H. Otsu, N. Chiga, S. Kawase, S. Takeuchi, T. Sumikama, S. Koyama, H. Sakurai, Y. Watanabe, S. Nakayama, D. S. Ahn, H. Baba, S. D. Chen, K. Chikaato, M. L. Cortés, N. Fukuda, A. Hirayama, R. Hosoda, T. Isobe, S. Kawakami, Y. Kondo, S. Kubono, Y. Maeda, S. Masuoka, S. Michimasa, I. Murray, R. Nakajima, T. Nakamura, K. Nakano, M. Nishimura, T. Ozaki, A. Saito, T. Saito, H. Sato, Y. Shimizu, S. Shimoura, P. A. Söderström, Y. Soudo, X. H. Sun, J. Suwa, D. Suzuki, H. Suzuki, H. Takeda, M. Takechi, Y. Togano, T. Tomai, H. Yamada, M. Yasuda, and K. Yoshida, “Enhancement of element production by incomplete fusion reaction with weakly bound deuteron,” Communications Physics, vol. 2, no. 1, p. 78, 2019.

[210] J. J. Griffin, “Statistical model of intermediate structure,” Phys. Rev. Lett., vol. 17, pp. 478–481, Aug 1966.

[211] M. Blann, “Extensions of griffin’s statistical model for medium-energy nuclear reactions,” Phys. Rev. Lett., vol. 21, pp. 1357–1360, Oct 1968.

[212] E. Gadioli and E. Gadioli Erba, “Pre-equilibrium emission,” Nuclear Instruments and Methods, vol. 146, no. 1, pp. 265–277, 1977.

[213] J. Randrup and R. Vandenbosch, “Pre-equilibrium neutron emission in the nucleon exchange transport model,” Nuclear Physics A, vol. 474, no. 1, pp. 219–239, 1987.

[214] G. M. Petrov, D. P. Higginson, J. Davis, T. B. Petrova, C. McGuffey, B. Qiao, and F. N. Beg, “Generation of energetic (>15 mev) neutron beams from proton- and deuteron-driven nuclear reactions using short pulse lasers,” Plasma Physics and Controlled Fusion, vol. 55, no. 10, p. 105009, 2013.

[215] J. R. Oppenheimer and M. Phillips, "Note on the transmutation function for deuterons," Phys. Rev., vol. 48, pp. 500–502, Sep 1935.

[216] C. L. Fink, B. L. Cohen, J. C. van der Weerd, and R. J. Petty, "Nemets effect in deuteron breakup by heavy nuclei," Phys. Rev., vol. 185, pp. 1568–1576, Sep 1969.

[217] R. Serber, "The production of high energy neutrons by stripping," Phys. Rev., vol. 72, pp. 1008–1016, Dec 1947.

[218] T. Ye, Y. Watanabe, and K. Ogata, "Analysis of deuteron breakup reactions on ^{7}Li for energies up to 100 mev," Phys. Rev. C, vol. 80, p. 014604, Jul 2009.

[219] D. Brown, M. Chadwick, R. Capote, A. Kahler, A. Trkov, M. Herman, A. Sonzogni, Y. Danon, A. Carlson, M. Dunn, D. Smith, G. Hale, G. Arbanas, R. Arcilla, C. Bates, B. Beck, B. Becker, F. Brown, R. Casperson, J. Conlin, D. Cullen, M.-A. Descalle, R. Firestone, T. Gaines, K. Guber, A. Hawari, J. Holmes, T. Johnson, T. Kawano, B. Kiedrowski, A. Koning, S. Kopecky, L. Leal, J. Lestone, C. Lubitz, J. Márquez Damián, C. Mattoon, E. McCutchan, S. Mughabghab, P. Navratil, D. Neudecker, G. Nobre, G. Noguere, M. Paris, M. Pigni, A. Plompen, B. Pritychenko, V. Pronyaev, D. Roubtsov, D. Rochman, P. Romano, P. Schillebeeckx, S. Simakov, M. Sin, I. Sirakov, B. Sleaford, V. Sobes, E. Soukhovitskii, I. Stetcu, P. Talou, I. Thompson, S. van der Marck, L. Welser-Sherrill, D. Wiarda, M. White, J. Wormald, R. Wright, M. Zerkle, G. Žerovnik, and Y. Zhu, "Endf/b-viii.0: The 8th major release of the nuclear reaction data library with cielo-project cross sections, new standards and thermal scattering data," Nuclear Data Sheets, vol. 148, pp. 1 – 142, 2018. Special Issue on Nuclear Reaction Data.

[220] A. Koning, D. Rochman, J.-C. Sublet, N. Dzysiuk, M. Fleming, and S. van der Marck, "Tendl: Complete nuclear data library for innovative nuclear science and technology," Nuclear Data Sheets, vol. 155, pp. 1 – 55, 2019. Special Issue on Nuclear Reaction Data.

[221] S. Nakayama, O. Iwamoto, Y. Watanabe, and K. Ogata, "Jendl/deu-2020: deuteron nuclear data library for design studies of accelerator-based neutron sources," Journal of Nuclear Science and Technology, vol. 58, no. 7, pp. 805–821, 2021.

[222] A. Hermanne, F. Tarkanyi, and S. Takacs, "Activation cross sections for production of 7be by proton and deuteron induced reactions on 9be: Protons up to 65mev and deuterons up to 50mev," Applied Radiation and Isotopes, vol. 90, pp. 203–207, 2014.

[223] L. Generalov, S. Abramovich, and S. Selyankina, "Activation measurements of the integral cross sections of reactions 7li(p,n0+n1)7be(gs), 6li(d,n0+n1)7be(gs), 7li(d,2n)7be(gs), 65cu(p,n)65zn, 65cu(d,2n)65zn, 63cu(d,g)65zn," Bull. Russ. Acad. Sci. Phys., vol. 81, pp. 644–657, 2017.

[224] Osetinskij, G.M. and Sikora, B. and Tyke, Y. and Fryshchin, B., "The investigation of li-7(d,n)be-8 reaction," Joint Inst. for Nucl. Res., Dubna Reports, vol. 5143, 1970.

[225] A. J. Koning and D. Rochman Nucl. Data Sheets, vol. 113, no. 2841-2934, 2012.

[226] C. Nelson, F. Purser, P. Von Behren, and H. Newson, "Neutron spectra from deuteron and proton bombardment of thick lithium targets: potential for neutron therapy," Phys. Med. Biol., pp. 39–46, Jan 1978.

[227] M. Hagiwara, T. Itoga, N. Kawata, N. Hirabayashi, T. Oishi, T. Yamauchi, M. Baba, M. Sugimoto, and T. Muroga, "Measurement of neutron emission spectra in li(d,xn) reaction with thick and thin targets for 40-mev deuterons," Fusion Science and Technology, vol. 48, no. 3, pp. 1320–1328, 2005.

[228] S. Ménard, M. Mirea, F. Clapier, N. Pauwels, J. Proust, C. Donzaud, D. Guillemaud-Mueller, I. Lhenry, A. C. Mueller, J. A. Scarpaci, and O. Sorlin, "Fast neutron forward distributions from c, be, and u thick targets bombarded by deuterons," Phys. Rev. ST Accel. Beams, vol. 2, p. 033501, Mar 1999.

[229] U. Fischer, S. Simakov, A. Konobeyev, P. Pereslavtsev, and P. Wilson, "Neutronics and nuclear data for the ifmif neutron source," Fusion Engineering and Design, vol. 63-64, pp. 493–500, 2002.

[230] U. Fischer, M. Avrigeanu, P. Pereslavtsev, S. Simakov, and I. Schmuck, "Evaluation and validation of d–li cross section data for the ifmif neutron source term simulation," Journal of Nuclear Materials, vol. 367-370, pp. 1531–1536, 2007. Proceedings of the Twelfth International Conference on Fusion Reactor Materials (ICFRM-12).

[231] Y. L. Parfenova and M. V. Zhukov, "Study of deuteron breakup in light targets at intermediate energies," Eur. Phys. J. A, vol. 12, pp. 191–197, 2001.

[232] M. Zimmer, Laser Driven Neutron Sources - a Compact Approach to Non-Destructive Material Analysis. PhD thesis, Technische Universität Darmstadt, 2020.

[233] J. F. Ziegler, M. D. Ziegler, and J. P. Biersack, "Srim – the stopping and range of ions in matter (2010)," Nuclear Instruments and Methods in Physics Research Section B: Beam Interactions with Materials and Atoms, vol. 268, no. 11, pp. 1818 – 1823, 2010.

[234] Glenn F. Knoll, Radiation detection and measurement. New York: Wiley, 4. ed. ed., 2010.

[235] W. Wesch and E. Wendler, Ion Beam Modification of Solids : Ion-Solid Interaction and Radiation Damage. Springer, 2016.

[236] W. L. McLaughlin, M. Al-Sheikhly, D. F. Lewis, A. Kovács and L. Wojnárovits, "Radiochromic solid-state polymerization reaction," ACS Symposium Series, Americal Chemical Society, 1996.

[237] Deric P. Jones, Biomedical Sensors. Momentum Press, 2010.

[238] "Gafchromic^{TM}." MD-V3 box booklet.

[239] M. Borghesi, A. Schiavi, D. Campbell, M. Haines, O. Willi, A. Mackinnon, P. Patel, M. Galimberti, and L. Gizzi, "Proton imaging detection of transient electromagnetic fields in laser-plasma interactions (invited)," Review of Scientific Instruments, vol. 74, no. 3, pp. 1688–1693, 2003.

[240] D. Hey, M. Key, A. Mackinnon, A. MacPhee, P. Patel, R. Freeman, L. Van Woerkom, and C. Castaneda, "Use of gafchromic film to diagnose laser generated proton beams," Review of Scientific Instruments, vol. 79, no. 5, p. 053501, 2008.

[241] J. Green, M. Borghesi, C. Brenner, D. Carroll, N. Dover, P. Foster, P. Gallegos, S. Green, D. Kirby, and K. Kirkby, "Scintillator-based ion beam profiler for diagnosing laser-accelerated ion beams," Laser Acceleration of Electrons, Protons, and Ions; and Medical Applications of Laser-Generated Secondary Sources of Radiation and Particles, vol. 8079, no. May 2011, p. 807919, 2011.

[242] K. Schwind, E. Aktan, R. Prasad, M. Cerchez, D. Eversheim, O. Willi, and B. Aurand, "An online beam profiler for laser-accelerated protons," Review of Scientific Instruments, vol. 90, no. 5, 2019.

[243] M. Huault, D. De Luis, J. Apiñaniz, M. De Marco, C. Salgado, N. Gordillo, C. Gutiérrez Neira, J. Pérez-Hernández, R. Fedosejevs, and G. Gatti, "A 2D scintillator-based proton detector for high repetition rate experiments," High Power Laser Science and Engineering, vol. 7, pp. 8–13, 2019.

[244] J. Metzkes, K. Zeil, S. Kraft, L. Karsch, M. Sobiella, M. Rehwald, L. Obst, H.-P. Schlenvoigt, and U. Schramm, "An online, energy-resolving beam profile detector for laser-driven proton beams," Review of Scientific Instruments, vol. 87, no. 8, 2016.

[245] N. P. Dover, M. Nishiuchi, H. Sakaki, M. A. Alkhimova, A. Y. Faenov, Y. Fukuda, H. Kiriyama, A. Kon, K. Kondo, K. Nishitani, K. Ogura, T. A. Pikuz, A. S. Pirozhkov, A. Sagisaka, M. Kando, and K. Kondo, "Scintillator-based transverse proton beam profiler for laser-plasma ion sources," Review of Scientific Instruments, vol. 88, no. 7, 2017.

[246] M. Hesse, T. Ebert, M. Zimmer, S. Scheuren, G. Schaumann, and M. Roth, "Spatially resolved online particle detector using scintillators for laser-driven particle sources," Review of Scientific Instruments, vol. 92, no. 9, p. 093302, 2021.

[247] M. J.-E. Manuel, H. Tang, B. K. Russell, L. Willingale, A. Maksimchuk, J. S. Green, E. L. Alfonso, J. Jaquez, L. Carlson, D. Neely, and T. Ma, "Enhanced spatial resolution of Eljen-204 plastic scintillators for use in rep-rated proton diagnostics," Review of Scientific Instruments, vol. 91, p. 103301, oct 2020.

[248] P. Rinar, Neutron Interaction with Matter, p. 357. U.S. Nuclear Regulatory Commission, 1991.

[249] H. Ing, R. A. Noulty, and T. D. McLean, "Bubble detectors—a maturing technology," Radiation Measurements, vol. 27, no. 1, pp. 1 – 11, 1997.

[250] V. P. Skripov, "Metastable liquids," Halsted Press, p. 128, 1974.

[251] C. Bell, N. Oberle, W. Rohsenow, N. Todreas, and C. Tso, "Radiation-induced boiling in superheated water and organic liquids," Nuclear Science and Engineering, vol. 53, no. 4, pp. 458–465, 1974.

[252] F. Smecka and M. Hajek, "Neutronendosimetrie mit bubbledetektoren," 2007.

[253] R. H. Olsher, T. D. McLean, M. W. Mallett, L. L. Romero, R. T. Devine, and J. M. Hoffman, "High-energy response of passive dosemeters in use at LANL," Radiation Protection Dosimetry, vol. 126, pp. 326–332, 05 2007.

[254] W. Rosenstock, J. Schulze, T. Köble, G. Kruzinski, P. Thesing, G. Jaunich, and H. Kronholz, "Estimation of Neutron Energy Spectra with Bubble Detectors: Potential and Limitations," Radiation Protection Dosimetry, vol. 61, pp. 133–136, 08 1995.

[255] H. Ing, "Neutron measurements using bubble detectors — terrestrial and space," Radiation Measurements, vol. 33, no. 3, pp. 275 – 286, 2001. Prediction and Measurements of Secondary Neutrons in Space.

[256] M. S. Plesset and S. A. Zwick, "The growth of vapor bubbles in superheated liquids," Journal of Applied Physics, vol. 25, no. 493, 1954.

[257] G. F. Knoll, Radiation Detection and Measurement, vol. 3. 2000.

[258] R. T. Kouzes, A. T. Lintereur, and E. R. Siciliano, "Progress in alternative neutron detection to address the helium-3 shortage," Nuclear Instruments and Methods in Physics Research Section A: Accelerators, Spectrometers, Detectors and Associated Equipment, vol. 784, pp. 172 – 175, 2015. Symposium on Radiation Measurements and Applications 2014 (SORMA XV).

[259] W. Petry, "Neutrons for industry," EPJ Web of Conferences, vol. 104, p. 01001, 2015.

[260] M. Berger, J. Hubbell, S. Seltzer, J. Chang, J. Coursey, R. Sukumar, D. Zucker, and K. Olsen, "Xcom:

Photon cross sections database," NIST Standard Reference Database 8 (XGAM), pp. NBSIR 87–3597, 2010.

[261] Y. Hongwei, THE N-P SCATTERING CROSS SECTION FROM 90 KEV TO 1.8 MEV. PhD thesis, University of Kentucky, 2015.

[262] J. Lee, J. Nishiyama, J.-I. Hori, R. Kimura, T. Sako, A. Yamada, and T. Sano, "Neutron total cross section measurements of polyethylene using time-of-flight method at kurns-linac," Journal of Nuclear Science and Technology, vol. 57, no. 1, pp. 1–8, 2020.

[263] N. Campbell and V. Francis, "A theory of valve and circuit noise," Journal of the Institution of Electrical Engineers - Part III: Radio and Communication Engineering, vol. 93, pp. 45–52(7), January 1946.

[264] G. Zhong, K. Li, L. Hu, H. Cao, R. Zhou, S. Lin, B. Hong, Z. Huo, H. Zhang, M. Xiao, M. Zhou, R. Zhang, L. Huang, J. Huang, T. Fan, and Y. Zhang, "Development of a wide-range neutron flux monitoring system in EAST," Journal of Instrumentation, vol. 15, pp. P05011–P05011, may 2020.

[265] B. J. Lewis, M. B. Smith, H. Ing, H. R. Andrews, R. Machrafi, L. Tomi, T. J. Matthews, L. Veloce, V. Shurshakov, I. Tchernykh, and N. Khoshooniy, "Review of bubble detector response characteristics and results from space," Radiation Protection Dosimetry, vol. 150, pp. 1–21, 09 2011.

[266] P. Antici, J. Fuchs, E. d'Humières, E. Lefebvre, M. Borghesi, E. Brambrink, C. A. Cecchetti, S. Gaillard, L. Romagnani, Y. Sentoku, T. Toncian, O. Willi, P. Audebert, and H. Pépin, "Energetic protons generated by ultrahigh contrast laser pulses interacting with ultrathin targets," Physics of Plasmas, vol. 14, no. 3, p. 030701, 2007.

[267] C. G. Freeman, G. Fiksel, C. Stoeckl, N. Sinenian, M. J. Canfield, G. B. Graeper, A. T. Lombardo, C. R. Stillman, S. J. Padalino, C. Mileham, T. C. Sangster, and J. A. Frenje, "Calibration of a thomson parabola ion spectrometer and fujifilm imaging plate detectors for protons, deuterons, and alpha particles," Review of Scientific Instruments, vol. 82, no. 7, p. 073301, 2011.

[268] A. Alejo, S. Kar, H. Ahmed, A. G. Krygier, D. Doria, R. Clarke, J. Fernandez, R. R. Freeman, J. Fuchs, A. Green, J. S. Green, D. Jung, A. Kleinschmidt, C. L. S. Lewis, J. T. Morrison, Z. Najmudin, H. Nakamura, G. Nersisyan, P. Norreys, M. Notley, M. Oliver, M. Roth, J. A. Ruiz, L. Vassura, M. Zepf, and M. Borghesi, "Characterisation of deuterium spectra from laser driven multi-species sources by employing differentially filtered image plate detectors in thomson spectrometers," Review of Scientific Instruments, vol. 85, no. 9, p. 093303, 2014.

[269] V. Lelasseux and J. Fuchs, "Modelling energy deposition in tr image plate detectors for various ion types," Journal of Instrumentation, vol. 15, p. P04002, apr 2020.

[270] V. Y. Glebov, D. D. Meyerhofer, T. C. Sangster, C. Stoeckl, S. Roberts, C. A. Barrera, J. R. Celeste, C. J. Cerjan, L. S. Dauffy, D. C. Eder, R. L. Griffith, S. W. Haan, B. A. Hammel, S. P. Hatchett, N. Izumi, J. R. Kimbrough, J. A. Koch, O. L. Landen, R. A. Lerche, B. J. MacGowan, M. J. Moran, E. W. Ng, T. W. Phillips, P. M. Song, R. Tommasini, B. K. Young, S. E. Caldwell, G. P. Grim, S. C. Evans, J. M. Mack, T. J. Sedillo, M. D. Wilke, D. C. Wilson, C. S. Young, D. Casey, J. A. Frenje, C. K. Li, R. D. Petrasso, F. H. Séguin, J. L. Bourgade, L. Disdier, M. Houry, I. Lantuejoul, O. Landoas, G. A. Chandler, G. W. Cooper, R. J. Leeper, R. E. Olson, C. L. Ruiz, M. A. Sweeney, S. P. Padalino, C. Horsfield, and B. A. Davis, "Development of nuclear diagnostics for the national ignition facility (invited)," Review of Scientific Instruments, vol. 77, no. 10, p. 10E715, 2006. and references therin.

Acknowledgments

First of all I would like to thank my advisor Prof. Dr. Markus Roth at TU Darmstadt. Thank you for agreeing to supervisor my Master's thesis and PhD thesis projects abroad. I am grateful for the opportunities you helped me create, for supporting me every step of the way and for always taking the time, despite the unforgiving time difference, if I needed advise.

I would also like to thank my advisor at SLAC, Prof. Dr. Siegfried Glenzer, for allowing me to work as a part of his division for the last five years. Thank you for supporting and motivating me at times when I needed to be reminded to be confident in my knowledge and skills.

Over the last five years as part of the HEDS division at SLAC, I have met some of the smartest, most inspiring people and I will be forever grateful to have had the pleasure to work with everyone. I would like to especially thank the core of team short pulse Maxence Gauthier, Chandra Curry, Chris Schönwälder and Griffin Glenn. Without all of you, experiments would have only been half the fun. As hard as some of the days were, we all managed to pull through together. Living in Airbnb's and exploring new places together during our experiments made everything so much more bearable and enjoyable. Maxence, our epic walks in fresh snow in the middle of the night are still one of my favorite memories from our experiment at CSU. Chandra, I will miss our meal prep adventures and trash TV evenings wherever we went. Chris, we basically grew up together as PhD students. I am grateful you brought a piece of home into the crazy place SLAC can sometimes be. Griffin, I have relied on you heavily the past weeks and months and I am grateful for all the work you have put in, it means a lot to me.

I am grateful to have had the opportunity to work with each and everyone of my colleagues. You have set the bar really high and I am sad that I will leave. I would like to take the opportunity to thank some of my colleagues who are particularly important to me. Thank you Adrien Descamps for all the bike rides, and no I will never be as fast as you, delicious pastries and endless laughs. I will always be grateful for all the evenings you cooked dinner for me during times I was too preoccupied with science to take care of myself. Thank you Ben Ofori-Okai for always taking the time to talk to me about literally anything and sometimes knowing better than I did, that I actually wanted to talk. Finally I would like to thank three amazing ladies, thank you Emma McBride, Anna Grassi and Meriam Berboucha. You inspire me every day to chase my goals and have fun doing it.

In addition to my group at SLAC, I would also like to take the opportunity to thank my group at TU Darmstadt for letting me invade and occupy office space whenever I was in Darmstadt. Special thanks are due to Gabriel Schaumann, who was always available to help me figure out TU Darmstadt's bureaucracy. And finally, thank you to a colleague and my friend Tina Ebert for introducing me to the field of plasma physics. I am grateful for uncountable coffee chats and zoom calls and that we managed to stay in touch over the years. I am excited that we will soon live and work in the same place again.

I would also like to thank those who have worked hard to make the experiments presented in this thesis possible. Thank you to Todd Ditmire's team and the staff of the Texas Petawatt laser, Mike Donovan, Michael

Spinks, Hernan Quevedo and Grant Richmond, for all the support throughout our experiment in 2019. Additional thanks are due to Jorge Rocca's team at the ALEPH laser at CSU, Reed Hollinger, Ryan Nedbailo, Jaebum Park, Huanyu Song and Shoujun Wang. Thank you for helping us realize a challenging experiment during COVID in 2021.

To my home away from home. Thank you to all my past and current house mates and honorary house mates at Broma Verde: David, Molly, Paul, Manny, Jessica, Van, Dan, Katina, Gaby, Sam, Bhavesh, Divya, Justeen, Tucker, Melanie and Joaquin. You guys are my family in the US and I feel blessed to live in such a great house with such a unique and tight-knit community. You keep me grounded and made me look forward to coming back every time I leave. Thank you for numerous family dinners, weekend hiking trips, bike rides, climbing adventures, an epic greek wedding, Tahoe skiing trips and just spending time together every week.

Thank you to one of my oldest friends in the bay, Ankit. Thank you for letting me crash at your place and invade your flat whenever I needed to and for reminding me to not push myself to my limit every single time. I would also like to thank Ellie for many fun bike rides, evening climbing session and lots of great conversations over good food and beers. I am so glad we grew so close over the past years. I would also like to thank Tané, James and their amazing little daughter for making me part of your family. You have taught me to be true to myself and enjoy every single day without excuses and regrets.

And finally I want to thank my amazing family, my dad, my mum and my sibling, Lukas and Viktoria. For you, I strive to be the best version of myself every single day. You motivate me and support me in a way I could have never imagined. You never allow me to doubt myself but instead always give me the strength and confidence to believe in myself and my dreams.

Curriculum Vitae

Education

2015 - 2017	**Master of Science Physics**, *Technische Universität Darmstadt*, Graduation: 10/27/2017 Master's thesis: Interaction of intense, charged Ion Beams with Matter: Energy-Loss Measurements and Thomson Parabola Design
2012 - 2015	**Bachelor of Science Physics**, *Technische Universität Darmstadt*, Graduation: 08/31/2015 Bachelor's thesis: Improvement of the Time Resolution of HPGermanium Detectors using Pulse Shape Analysis
2011	**A-Levels**, *Siebengebirgsgymnasium* Bad Honnef

Professional Experience

since 01/2018	**Research Assistant**, *SLAC National Accelerator Laboratory*, USA High Energy Density Science Division
09/2016 - 10/2017	**Research Assistant**, *Lawrence Berkeley National Laboratory*, USA Accelerator Technology and Applied Physics Division
05/2014 - 04/2016	**Research Assistant**, *Gesellschaft für Schwerionenforschung (GSI)*, Darmstadt Gammaspectroscopy Group

Awards

2021	**LaserNetUS - Colorado State University** Grant to continue study of high repetition-rate laser driven neutron sources
2019	**LaserNetUS - Colorado State University** Grant to conduct experiment of high repetition-rate laser driven neutron sources
2019	**Studienstiftung des Deutschen Volkes** PhD student scholarship
2016	**Gerhard Herzberg Gesellschaft** des Fachbereichs Physik der TU Darmstadt, Sholarship and membership

Peer-reviewed Publications

13. C. Bernert, ..., F. Treffert et al., "Transient laser-induced breakdown of dielectrics in ultra-relativistic laser-solid interactons", Physical Review Applied, *Accepted*
12. X. Jiao, ..., F. Treffert et al., "High deuteron and neutron yields from the interaction of a petawatt laser with a cryogenic deuterium jet", Frontiers in Physics, *Accepted*
11. F. Treffert et al., "Ambient-temperature liquid jet targets for high-repetition-rate HED discovery science", Phys. Plasmas 29, 123105 (2022), doi: 10.1063/5.0097857
10. F. Treffert et al., "High-repetition-rate, multi-MeV deuteron acceleration from converging heavy water microjets at laser intensities of 10^{21} W/cm^2", Appl. Phys. Lett. 121:74104 (2022), doi: 10.1063/5.0098973
9. C. Bernert, ..., F. Treffert, et al., "Off-harmonic optical probing of high intensity laser plasma expansion dynamics in solid density hydrogen jets", Scientific Reports 12(1):7287 (2022), doi: 10.1038/s41598-022-10797-6
8. L. B. Fletcher, ..., F. Treffert, et al., "Investigation of hard x-ray emissions from terawatt laser-irradiated foils at the Matter in Extreme Conditions instrument of the Linac Coherent Light Source", JINST 17(04):T04004 (2022), doi: 10.1088/1748-0221/17/04/T04004
7. L. Gaus, ..., F. Treffert, et al., "Probing ultrafast laser plasma processes inside solids with resonant small angle X-ray scattering", Phys. Rev. Research 3, 043194 (2021), doi: 10.1103/PhysRevResearch.3.043194
6. F. Treffert et al., "Towards High-Repetition-Rate Fast Neutron Sources Using Novel Enabling Technologies", Instruments 5, 38 (2021), doi: 10.3390/instruments5040038
5. M. Hohenberger, ..., F. Treffert, et al., "Developing “inverted-corona” fusion targets as high-fluence neutron sources", Rev. Sci. Inst. 92, 033544 (2021), doi: 10.1063/5.0040877
4. Z. Chen, ..., F. Treffert, et al., "Ultrafast Multi-Cycle Terahertz Measurement of the Electrical Conductivity in Strongly Excited Solids", Nature Comm. 12, 1638 (2021), doi: 10.1038/s41467-021-21756-6
3. C. B. Curry, ..., F. Treffert et al., "Cryogenic Liquid Jets for High Repetition-Rate Discovery Science", JoVE 159, 61130 (2020), doi: 10.3791/61130
2. F. Treffert et al., "Design and Implementation of a Thomson Parabola for Fluence Dependent Energy-Loss Measurements at the Neutralized Drift Compression eXperiment", Rev. Sci. Inst. 89, 103302 (2018), doi: 10.1063/1.5030541
1. P. A. Seidl, ..., F. Treffert, et al., "Irradiation of Materials with Short, Intense Ion pulses at NDCX-II", Laser and Particle Beams, 35(2), 373-378 (2017), doi: 10.1017/S0263034617000295

Peer-reviewed Publications In Review or Submitted

3. M. Rehwald, ..., F. Treffert et al., "Ultra-short pulse laser acceleration of protons to 80 MeV from cryogenic hydrogen jets tailored to near-critical density", Nature Physics, *In Review*
2. B. Loughran, ..., F. Treffert et al., "Automated control and optimisation of laser driven ion acceleration", High Power Laser Science and Engineering, *In Review*
1. X. Nuo, ..., F. Treffert et al., "Versatile tape-drive target for high-repetition rate laser-driven proton acceleration", High Power Laser Science and Engineering, *Submitted*

Oral Contributions

2022 Invited PS&T Seminar at PPPL (talk, virtual), "Towards high repetition-rate laser-driven neutron sources using fast replenishing jet targets"

2022 LaserNetUS Annual Meeting (talk), "Towards high repetition-rate laser-driven neutron sources using ambient-temperature liquid jet targets"

2022 Invited Seminar at HEDS Center at LLNL (talk), "High Repetition-Rate Laser-Driven Particle Generation - Towards High Flux Fast Neutron Sources"

2022 Physics of Quantum Electronics, Snowbird USA (talk, invited), "High Repetition-Rate Laser-Driven Ion and Neutron Beam Sources Employing Micron-Scale Converging Liquid Jet Targets"

2021 American Physical Society - Division of Plasma Physics, virtual (talk), "Towards high repetition-rate neutron beam generation using micron-scale converging heavy water jet targets"

2021 LaserNetUS Annual Meeting, virtual (talk), "Development of high-repetition-rate neutron source using micron-sized converging heavy water jet targets"

2020 High Temperature Plasma Diagnostics, virtual (poster), "Absolute flux calibration of neutron time-of-flight detectors using high energy neutron beams at LANSCE"

2020 American Physical Society - Division of Plasma Physics, virtual (poster), "Absolute flux calibration of neutron time-of-flight detectors for laser-generated neutron beam experiments"

2018 6^{th} High Power Laser Workshop, SLAC, Menlo Park USA (poster), "High-intensity laser hole boring of solid-density wires at the MEC end-station"

2018 7^{th} Target Fabrication Workshop, Darmstadt Germany (talk), "Developement of cryogenic low-Z jets for laser-driven ion acceleration"

2018 International Conference on Plasma Sciences (ICOPS), Denver USA (poster), "First Energy-Loss Measurements of Intense Pulsed Ion Beams In Matter using a Thomson Parabola at NDCX-II"

2017 Invited Seminar at HEDS Division at SLAC (talk), "Energy-Loss Measurements of Intense Pulsed Ion Beams in Si (SiO_2) using a Thomson Parabola at NDCX-II"

A. Appendix

A.1. LaserNetUS Experiment Proposal Cycle 4 March 2023

LaserNetUS Proposal, Cycle 4

Title of Proposed Experiment: High repetition-rate, quasi-directional fast neutron source using converging D_2O microjets

Principal Investigator:
Franziska Treffert
High Energy Density Science Division
SLAC National Accelerator Laboratory
Visiting Scientist, PhD Student
2575 Sand Hill Road, M/S 72
Menlo Park, CA 94025
Email: treffert@slac.stanford.edu
Phone: +1 (650) 926-4408

Abstract

Short, intense bursts of neutrons with MeV energies are desirable for damage cascade studies, probing of radioactive materials, and high precision fast neutron imaging. These neutron beams can be efficiently driven by high power short pulse lasers. While the peak flux of these beams is high due to the favorable scaling of neutron beam peak brightness with laser intensity, the average flux has historically been limited by low laser repetition rates. The advent of high repetition-rate petawatt lasers paves the way towards record average neutron fluxes. In this work we propose a study of high repetition-rate neutron generation using an ultra-thin heavy water sheet target and a neutron converter material in a pitcher-catcher geometry. The ALEPH petawatt laser interacts with a heavy water sheet, accelerating a beam of deuterons that in turn generates a fast neutron beam after interacting with a converter target. An optimal heavy water sheet thickness to maximize the flux of accelerated deuterons has been identified using 2D particle-in-cell (PIC) simulations. The laser-accelerated deuterons and the neutron beam will be diagnosed using high-repetition-rate-compatible ion and neutron detectors described herein. These measurements will be compared with predictions from simulations to provide deeper insights into laser-driven neutron beam generation mechanisms and to advance this platform towards maturity for applications.

Tentative Research Team

Name	Email	Institution
F. Treffert	treffert@slac.stanford.edu	HEDS/SLAC and Technische Universität Darmstadt
G. D. Glenn (thesis work)	gdglenn@slac.stanford.edu	HEDS/SLAC and Stanford
M. Gauthier	gauthier@slac.stanford.edu	HEDS/SLAC
C. B. Curry	ccurry@slac.stanford.edu	HEDS/SLAC
C. Schoenwaelder	schchris@slac.stanford.edu	HEDS/SLAC and Universität Erlangen-Nurnberg
C. Crissman	christopher.crissman@westpoint.edu	USMA at West Point
J. Chou	jasonhc@slac.stanford.edu	HEDS/SLAC and Stanford
D. Deponte	deponte@slac.stanford.edu	LCLS/SLAC

M. Roth	markus.roth@physik.tu-darmstadt.de	Technische Universität Darmstadt
F. Fiuza	fiuza@slac.stanford.edu	HEDS/SLAC
S. H. Glenzer	glenzer@slac.stanford.edu	HEDS/SLAC and Stanford

This team combines extensive experience in fielding short-pulse laser experiments, developing ambient temperature and cryogenic jet target delivery systems[1,2] and diagnostics, and designing and running state-of-the-art simulations. Most members of the team have significant experience with large-scale facilities like the Titan Laser at JLF, the Texas Petawatt Laser at UT Austin, the Draco 150 TW and Petawatt laser at HZDR, the NIF, the OMEGA and OMEGA EP lasers, the Vulcan Petawatt laser at RAL, the ALEPH laser at CSU, the 100 TW ELFIE laser at LULI, and FLASH at DESY. Our team has pioneered the use of 2D and 3D particle-in-cell (PIC) codes for the *ab initio* study of laser-plasma interactions using synthetic diagnostics. These large-scale simulations, performed with realistic experimental conditions, allow us to design experiments and interpret experimental results.

Scientific Case

Neutron beams are highly applicable in fusion energy research[3], fundamental physics research[4], materials science[5], homeland security[6], and medicine[7]. As a complementary diagnostic to X-rays, neutron scattering is ideally suited to resolve atomic properties of low-Z materials, where X-rays suffer from low interaction cross-sections. While X-ray and electron-based measurements rely on interactions with the atomic electron cloud governed by the electromagnetic force, neutrons have point-like interactions with the nuclei through the strong force[8]. At present, standard large-scale facilities like spallation sources and nuclear reactors can produce neutron beams with the flux (10^{15} n/cm^2-sec) needed for most applications[8], but generally require substantial accumulation times to obtain high-quality measurements. In addition, their pulse duration (100s of ns) limits their utility to studies of slowly evolving systems. High-intensity laser-matter interactions, by contrast, generate very large instantaneous neutron fluxes but presently have demonstrated average fluxes lower than those of standard neutron sources. However, platforms combining high repetition-rate (HRR) petawatt (PW)-class laser drivers and novel HRR-compatible targets promise to address this limitation, suggesting high average flux fast neutron sources for both fundamental HED science and the applications above are within reach.

During the interaction of a high-power laser with an over-critical target, neutrons can be produced directly by fusion processes in the hot target plasma or indirectly when a converter material is bombarded by an energetic laser-accelerated ion beam. Neutrons generated in fusion reactions are quasi-monoenergetic, but are emitted isotropically and limited to specific energies (e.g. 2.45 MeV for D-D fusion). By contrast, indirect neutron generation methods have the potential to produce directed neutron beams with a broader energy spectrum. These properties are realized when a high-intensity laser irradiates a “pitcher” target and accelerates a deuteron-dominated ion beam, which is then directed into a “catcher” or “converter” target. The incident ion beam energy spectrum is convolved with energy-dependent cross sections for neutron-producing reactions such as deuteron breakup and stripping reactions to produce a broadband neutron energy spectrum. Additionally, conservation of momentum and deuteron scattering in the converter target lead to a quasi-directional neutron beam with a slightly broader angular distribution than the incident deuteron beam.

Experiments in the pitcher-catcher configuration have demonstrated neutron beams with up to 10^{10} neutrons per steradian[9-13], but the average neutron flux achievable using these platforms has been limited by the low repetition rate of the laser drivers and target replenishment

systems. The recent proliferation of PW-class laser systems operating at HRR[14,15] thus removes one of the primary constraints on the production of directed neutron beams with high average fluxes and cutoff energies. By contrast, the development of targets well-suited to producing these beams remains an active area of investigation.

Previous studies have sought to develop quickly replenishing targets, but to date these targets have primarily been used to produce D-D fusion neutrons[16-19]. Such sources are limited in their utility for applications due to the monoenergetic and isotropic nature of their neutron emission. By contrast, targets that accelerate deuterons via the target normal sheath acceleration (TNSA) and enhanced TNSA mechanisms[20] are effective drivers of the spatially constrained neutron beams necessary for applications in fundamental and applied science.

At SLAC, we have developed an ambient-temperature planar microjet target[1,21] that is well-suited for use as an HRR-compatible pitcher target for neutron generation. Custom tungsten microfluidic nozzles deliver optically flat heavy water (D_2O) sheets with mm-scale transverse dimensions and thicknesses tunable from tens of nm to tens of μm. In recent experiments at the ALEPH laser at Colorado State University and the Gemini laser at Rutherford Appleton Laboratories (UK), we used the jet to stably accelerate proton and deuteron beams to MeV energies at Hz-scale repetition rates across hundreds or thousands of shots (see attached progress report).

To further explore the use of this jet as a pitcher target for laser-driven neutron generation, we have performed 2D particle-in-cell (PIC) OSIRIS[22,23] simulations of the laser-target interaction using realistic laser parameters (400 nm, 45 fs, 10 J, 1.2 μm FWHM, 6.5×10^{21} W/cm^2). The target thickness was varied across a range (0.25 μm to 1 μm) that can be realized experimentally using our liquid jet target, and the energy spectrum of deuterons accelerated from the target was extracted. As shown in Figure 1, the simulations identify a clear optimum target thickness for the production of high-energy ions. The neutron generation cross-section of typical neutron converter materials increases with incident ion energy, so these results will guide an experimental target thickness scan to optimize the deuteron and neutron beams. Additionally, these simulations have identified changes in the ion beam spatial distribution as a function of target thickness, which will also be studied to clarify the role of advanced acceleration mechanisms and maximize ion beam coupling into the neutron converter target.

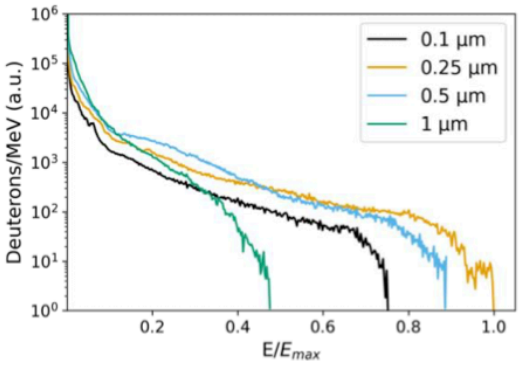

Figure 1: Deuteron spectra extracted from 2D PIC simulations of the ALEPH laser interacting with planar D_2O targets of various thicknesses.

In this experiment, we will bridge the gap between previous demonstrations of isotropic neutron sources at HRR and high-flux directed neutron sources at low repetition rates. This platform is predicted to achieve neutron numbers of 1×10^6 neutrons/J, exceeding previous demonstrations using HRR-compatible isotropic neutron sources by up to two orders of magnitude. At HRR (~1 Hz) operation, this source will produce an average neutron flux up to 10^4 neutrons/cm^2/s. This experiment will lay the groundwork for future scaling to higher laser energy on target and higher repetition rates by characterizing the source in detail. To clarify the specific ion acceleration mechanisms at work, we will measure the deuteron beam spatial profile and energy spectrum using a scintillator-based ion imager and HRR-compatible Thomson parabola ion spectrometers at multiple angles. Bubble detectors and calibrated neutron time of flight detectors will characterize the energy spectrum, flux, and spatial distribution of the neutron beam to yield insights into the neutron generation mechanisms. Follow-up experiments will allow this platform to match or even exceed the average neutron fluxes of

directed neutron sources utilizing high power single-shot laser systems. In all, this experiment will significantly advance the state of the art in producing the directed, high-maximum-energy, HRR neutron beams necessary for both frontier HED science and the societal applications of laser-driven neutron sources.

Experimental Procedure

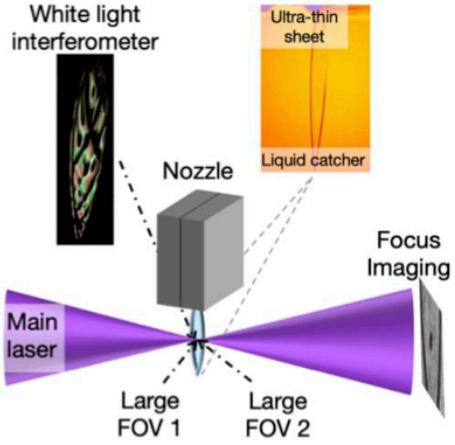

Figure 2: A schematic of the planar D_2O liquid jet and nozzle, the primary laser, and necessary imaging lines.

The proposed experiment will systematically investigate laser-driven neutron generation in the pitcher-catcher geometry using a liquid heavy water microjet irradiated by a high-intensity, high-contrast laser. The setup, shown in Figure 2, is based on our previous experience with this target platform at FLASH (DESY, Germany), the UED facility at SLAC, the ALEPH laser at CSU, and the Gemini TA2 laser at RAL (UK). It incorporates reflectometry and large field of view imaging measurements to characterize and monitor the dimensions, position, and thickness of the jet in real time. The laser will be focused using an f/2 parabola onto the first sheet below the microfluidic jet nozzle at a 45° angle of incidence. A motorized focus imaging system in the laser forward direction enables optimization of the focal spot under vacuum before each shot series.

Ion and neutron diagnostics will supplement the setup in and out of the laser plane. Two MCP-based Thomson parabolas (TPs) will be positioned at 0° (target normal) and 22.5° relative to the target normal direction. An HRR-compatible ion imager with an aperture to allow simultaneous operation with the TPs will be installed to resolve the spatial distribution of the ion beam. After initial characterization of the ion beam, the ion imager will be removed and the converter target inserted. Neutrons generated during the interaction will be detected using neutron time-of-flight detectors (nTOFs) at various angles in the laser plane. A bubble detector array on the upper hemisphere of the target chamber will facilitate reconstruction of the isotropic component of neutron emission.

For the proposed experiment we request a minimum of 1 week of dedicated set-up time for target installation and vacuum system modifications followed by 3 consecutive experimental weeks. During the setup week, minimal facility support and no laser is required. A week-by-week breakdown of the schedule is shown in Table 1 below. The experiment will be conducted mainly at HRR (0.5-2.5 Hz) scanning laser intensity and target thickness.

Set-up	Liquid jet assembly setup/characterization; vacuum system modifications and testing
Week 1	Laser path setup and alignment, probe imaging setup for precision target alignment, ion/neutron diagnostic setup
Week 2	Diagnostic setup and test shots on Cu/CD_2 targets Target thickness scan with deuteron beam
Week 3	Target thickness scan with neutron-generating converter at HRR utilizing the heavy water jet

Table 1: Proposed experimental schedule

Experiment Readiness

Our experiment advances an experimental platform that has been successfully fielded at multiple facilities in the US and abroad, including the ALEPH laser facility at CSU. We are preparing for a collaborative experiment at RAL in the fall of 2022 in which we will perform additional development of our nozzles and diagnostics. We will be prepared for a LaserNetUS experiment using this platform by November 2022.

Technical Feasibility

Laser Facility Requirements

Main laser system:
The ALEPH 400 nm laser will be focused on target using an f/2 parabola. Maximum laser energy, shortest pulse length, and pulse contrast of 10^{-12} are required. Bursts of at least 60 shots at constant maximum energy and 2.5 Hz repetition rate would be ideal to obtain sufficient statistics. For precise diagnostic alignment a fixed laser focal position at target chamber center (TCC) is preferred.

Secondary laser(s):
A low energy probe beam, around 10 mJ, is required during the experiment to monitor and align the water jet target pre-shot.

Experimental Equipment and Diagnostics

Alignment and calibration targets:
Vertical wires (Cu) of various diameters (10-100 μm) and CD_2 foils will be used for calibration purposes and will be fabricated by our team prior to the experiment. No special storage or sample preparation requirements.

Ambient temperature water jet:
SLAC will provide the custom tungsten microfluidic chips used to create the jet. PEEK tubing with 1 mm ID is used for liquid transport into the chamber through a custom CF 2.75" flange. By changing the liquid flow rates the thickness and dimensions of the sheet can be tuned in situ[1]. Optimal parameters create up to five planar liquid sheets of 0.5 x 5 mm^2 maximum area. The typical flow rate of several mL/min enables repetition rates exceeding 10 Hz.

For accurate positioning, the jet assembly uses 6-axis motorization which will be provided by SLAC as required. The hardware needed to operate the liquid jet source will be provided by our team at SLAC: see Ref. 24 for more information on the full operation procedure. The thickness gradient across the liquid sheets facilitates studies of the deuteron and neutron yield as a function of thickness.

Vacuum requirements and system modifications:
During jet operation, the chamber pressure is dominated by the liquid water vapor and is approximately 10^{-3} mBar. To compensate for the gas load, a supplemental turbo pump provided by SLAC will be installed on an ISO 200 flange available on the target chamber. A total pumping speed at low vacuum of 1,100 L/min is needed to safely turn on turbo pumps. Additionally, we will require at least three cold traps: one in the vacuum chamber, one on the liquid catcher line,

and one between the SLAC-provided turbo pump and the scroll pump**.** We will also implement a vacuum isolation window based on a design described in Ref. 25 that was successfully fielded on the ALEPH system in our previous LaserNetUS experiment during Cycle 2 to protect the compressor from the water vapor in the target chamber.

Liquid jet catcher system:
A liquid catcher system intercepts the jet around 6 mm below the liquid jet nozzle and evacuates the majority of the injected water. A combination of differential and gravity-assisted pumping and a cold trap ensures efficient operation. The copper catcher body is heated significantly above 100°C using heating elements to create the pressure differential.

Calibrated neutron time-of-flight scintillators:
Neutron energy distributions in the laser plane will be measured at various angles and distances from TCC using calibrated neutron time-of-flight (nTOF) scintillators[26]. The scintillators are coupled to photomultipliers and are only sensitive to fast neutrons above 1 MeV.

Neutron bubble detectors:
The angular emission profile of the neutrons will be detected with an array of high sensitivity bubble detectors, mapping the upper hemisphere above the laser plane. They will be installed directly on the chamber wall. The bubble detectors will be calibrated directly before or after the experiment at the National Ignition Facility or using a radiation source at UT Austin.

Thomson parabola ion spectrometers:
SLAC HEDS can provide two Thomson parabola ion spectrometers (TPs) coupled with calibrated micro-channel plates[27]. The TPs will be installed at 0º (target normal) and 22.5º relative to the target normal direction respectively. The TPs are in external vacuum housings and separated from the target chamber by a gate valve. Differential pumping stages or Kapton windows will be installed to maintain high vacuum despite the gas load in the target chamber. These TPs have been successfully calibrated and fielded by our team in our previous campaigns at MEC, HZDR, and CSU.

Ion imager:
SLAC HEDS will provide an HRR-compatible scintillator-based ion beam imager to characterize the spatial profile and pointing stability of the laser-accelerated deuteron beam at the repetition rate of the laser. Radiochromic film (RCF) will be installed on selected shots to cross-calibrate the ion imager[28].

X-ray scintillators:
Two plastic X-ray scintillators will be installed on the wall of the target chamber. The X-ray scintillators are a sensitive HRR diagnostic to monitor the quality of the laser-plasma interaction. The X-ray scintillators have been used successfully at MEC[29], Titan, and the Texas Petawatt.

White light thin film interferometry:
A fiber-coupled tungsten halogen white light source is used to measure and monitor the thickness of the liquid jet[1]. The spectral reflectance curve of a sub-micron film of liquid strongly depends on the thickness of the sheet. Comparison with calculated spectra enables precise thickness determination of the planar water sheet.

References:

[1] J. Koralek et al., Nat. Commun. 9, 1 (2018)
[2] M. Gauthier et al., Rev. Sci. Instrum. 87, 11 (2016)
[3] L. Perkins et al., Nucl. Fusion 40, 1 (2000)
[4] D. P. Higginson et al., Phys. Plasmas 17, 100701 (2010)
[5] G. Noguere et al., Nucl. Instrum. Methods Phys. Res., Sect. A 575, 476 (2007)
[6] D. R. Brown et al., Nucl. Instrum. Methods Phys. Res., Sect. A 353, 684 (1994)
[7] L. Gray and J. Read, Nature 152, 53 (1943)
[8] S. C. Vogel and H. Priesmeyer, Rev, Mineral. Geochem. 63, (2006)
[9] M. Roth et al., Phys. Rev. Lett. 110, 044802 (2013)
[10] A. Favalli et al., Scientific Reports 9 (2019)
[11] D. Jung et al., Phys. Plasmas 20, 056706 (2013)
[12] A. Higginson et al., Phys. Plasmas 18, 100703 (2011)
[13] A. Kleinschmidt et al., Phys. Plasmas 25, 053101 (2018)
[14] D. N. Papadopoulos et al., Opt. Lett. 42, 3530-3533 (2017)
[15] F. Batysta et al., Proc. SPIE 11034, 110340C (2019)
[16] D. Hilscher et al., Phys. Rev. E 64, 016414 (2001)
[17] S. Ter-Avetisyan et al., Phys. Plasmas 12, 012702 (2005)
[18] T. Ditmire et al., Nature 398, 6727 (1999)
[19] J. Hah et al., Appl. Phys. Lett. 109, 144102 (2016)
[20] R. Mishra et al., New J. Phys. 20, 043047 (2018)
[21] B. Ha et al., Phys. Rev. Fluids 3, 114202 (2018)
[22] R. A. Fonseca et al., Lect. Notes Comput. Sci. 2331, 342 (2002)
[23] R. A. Fonseca et al., Plasma Phys. Controlled Fusion 50, 124034 (2008).
[24] J. P. F. Nunes et al., Struct. Dyn. 7, 024301 (2020)
[25] B Aurand et al., New J. Phys. 22 033025 (2020)
[26] F. Treffert et al., Rev. Sci. Instrum. (In prep.)
[27] F. Treffert et al., Rev. Sci. Instrum. (In prep.)
[28] C. Curry et al., Rev. Sci. Instrum. 91, 093303 (2020)
[29] L. B. Fletcher et al., JINST, submitted